



Incremental Virtual Prototyping of Electromechanical Actuators for Position Synchronization

Jian Fu

► To cite this version:

Jian Fu. Incremental Virtual Prototyping of Electromechanical Actuators for Position Synchronization. Mechanical engineering [physics.class-ph]. INSA de Toulouse, 2016. English. NNT : 2016ISAT0008 . tel-01511290

HAL Id: tel-01511290

<https://theses.hal.science/tel-01511290>

Submitted on 20 Apr 2017

HAL is a multi-disciplinary open access archive for the deposit and dissemination of scientific research documents, whether they are published or not. The documents may come from teaching and research institutions in France or abroad, or from public or private research centers.

L'archive ouverte pluridisciplinaire **HAL**, est destinée au dépôt et à la diffusion de documents scientifiques de niveau recherche, publiés ou non, émanant des établissements d'enseignement et de recherche français ou étrangers, des laboratoires publics ou privés.



THÈSE

En vue de l'obtention du

DOCTORAT DE L'UNIVERSITÉ DE TOULOUSE

Délivré par :

Institut National des Sciences Appliquées de Toulouse (INSA de Toulouse)

Discipline ou spécialité :

Génie Mécanique, Mécanique des Matériaux

Présentée et soutenue par :

Jian FU

Le mercredi 6 Juillet 2016

Titre :

Prototypage Virtuel Incrémental des Actionneurs Electromécanique
pour la Synchronisation en Position

JURY

Geneviève DAUPHIN-TANGUY, Professeur, Ecole Centrale de Lille, Rapporteur
Jesús FELEZ, Professeur, Universidad Politécnica de Madrid, Rapporteur
Jean-Charles MARE, Professeur, INSA de Toulouse, Examineur
Ion HAZYUK, Maître de Conférences, INSA de Toulouse, Examineur
Yongling FU, Professeur, Beihang University, Invité

Ecole doctorale :

Mécanique, Energétique, Génie civil, Procédés (MEGEP)

Unité de recherche :

Institut Clément Ader (ICA, CNRS UMR 5312)

Directeur(s) de Thèse :

Jean-Charles MARE

Université fédérale de Toulouse Midi-Pyrénées
Institut National des Sciences Appliquées de Toulouse
Institut Clément Ader (CNRS UMR 5312)

Incremental Virtual Prototyping of Electromechanical Actuators for Position Synchronization

Doctoral Thesis

Prepared by: Jian FU
Supervisor: Prof. Jean-Charles MARE
Reviewers: Prof. Geneviève DAUPHIN-TANGUY
Prof. Jesús FELEZ
Examiner: Mcf. Ion HAZYUK
Inviter: Prof. Yongling FU

Toulouse
July 2016

Abstract

In the aerospace field, the concepts based on extended use of electricity in “More Electric Aircraft” (MEA) and even “All Electric Aircraft” (AEA), electromechanical actuators (EMAs) are increasingly being implemented in place of conventional hydraulic servo actuators (HSAs). When EMAs are used for safety-critical actuation applications like flight controls, some specific issues related to thermal balance, reflected inertia, parasitic motion due to compliance, response to failure (jamming and free-run) and synchronization of EMAs driving independent loads cannot be ignored. The simulation-aided design process can efficiently support the assessment and validation of the concepts fixing these issues. For that, virtual prototypes of EMAs at system-level have to be developed in a structured way that meets the engineers’ needs. Unfortunately, the physical effects governing the EMAs behavior are multidisciplinary, coupled and highly nonlinear. Although numerous multi-domain and system-level simulation packages are now available in the market of simulation software, the modelling process and the engineers’ needs are rarely addressed as a whole because of lack of scientific approaches for model-based architecting, multi-purpose incremental modelling and model implementation for efficient numerical simulation. In this thesis, the virtual prototyping of EMAs is addressed using the Bond-Graph formalism. New approaches are proposed to enable incremental modelling of EMAs that provides models supporting control design, energy consumption and thermal analysis, calculation of reaction forces, power network pollution simulation, prediction of response to faults and influence of temperature. The case of preliminary design of EMAs position synchronization is used to highlight the interests and advantages of the proposed process and models of EMAs.

Keywords: *Bond-Graph, More Electric Aircraft, Power-by-Wire, EMA, Energy Losses, Response to Faults, Synchronization*

Acknowledgements

First of all, I am grateful to China Scholarship Council (CSC) for providing me with 40 months of financial grant and support for my doctoral studies in France.

I would like to express my sincere gratitude to my supervisor, Mr. Jean-Charles MARE, at INSA-Toulouse, Institut Clément Ader (ICA). I am indebted to him for his guidance and help during my PhD thesis. His rigorous research attitude and good work ethics will have an everlasting impact on my life.

I would also like to specially thank Mr. FU Yongling, in Beihang University, for his instructive advice during my M.S and first year of PhD in Beihang. I am deeply grateful for his recommendation, which gave me the opportunity to pursue my PhD degree in France.

I would also like to express my thanks to Mr. Ion HAZYUK, in INSA-Toulouse, ICA, for his discussion and contribution towards my thesis. I would like to thank Mr. Nicolas LAURIEN and Mr. Stéphane ORIEUX, for their assistance and suggestions during the experimental tests in my PhD.

I am also deeply indebted to all my Chinese and international friends in the laboratory of ICA, for their help, encouragement and friendship during my Ph.D studies.

Finally, the last words are for my family. In the most difficult time, during the mid of my Ph.D study, my father was no more. I would especially like to thank my mother for her continued support and encouragement during these tough moments of my overseas study, and she is indeed a great mother. I dedicate this thesis to my father in heaven, thank you very much!

Contents

Nomenclature	I
Introduction	1
Chapter 1 State of the Art	7
1.1 Flight Control Actuators.....	7
1.2 Safety Critical Requirements and Position Synchronization	13
1.3 Virtual Prototyping Methodology	21
1.4 Performance Requirements	26
1.5 Conclusion of Chapter 1	27
References.....	27
 Chapter 2 Individual EMA Controller Design	31
2.1 Individual EMA System Description.....	31
2.2 Linear Virtual Prototype	35
2.3 Power Limitation and Saturation Effects	42
2.4 Motor Current Loop Effects.....	45
2.5 Imperfections due to Mechanical Compliances	53
2.6 Force Feedback Compensation for Position Control	62
2.7 Conclusion of Chapter 2	71
References.....	72
 Chapter 3 Power Drive Electronics and Motor	73
3.1 Physical Effects in Power Drive Electronics (PDE)	73
3.2 Physical Effects at Electric Motor (EM)	85
3.3 Incremental Virtual Prototyping.....	95
3.4 Numerical Simulation and Analysis.....	104
3.5 Conclusion of Chapter 3	111
References.....	112

Chapter 4 Mechanical Power Transmission	115
4.1 Power Screw Mechanism	116
4.2 1-DoF Integrated Model.....	119
4.3 2-DoF Decomposition Model	131
4.4 Model Implementation	148
4.5 Numerical Simulation and Analysis	156
4.5 Conclusion of Chapter 4.....	167
References	168
 Chapter 5 Test Bench and Preliminary Study of Position Synchronization.....	 171
5.1 Description of the Test Bench	171
5.2 Preliminary Study of Position Synchronization	181
5.3 Validation of Overall Twin-Parallel EMAs Virtual Prototype.....	191
5.4 Conclusion of Chapter 5.....	201
References	202
 Conclusion.....	 205
 List of Publications	 209
 Appendix	 211
Appendix A BLDC vs.PMSM Used for EMAs	211
Appendix B SKF Bearing Loss Model	217
 Résumé	 221

Nomenclature

Parameters

Θ_0	Reference Temperature	[°C]
β	Conduction Loss Model Parameter	[-]
ε_m	Temperature Dependency of Material Magnet	[1/°C]
ε_r	Temperature Dependency of Resistance	[1/°C]
γ	Steinmetz Constant	[-]
λ	Cogging Factor	[-]
μ_b	Constant Coefficient of Bearing Friction	[-]
μ_m	Magnetic Permeability	[H/m]
τ_{hp}	High Pass Filter Time Constant	[s]
τ_{lp}	Low Pass Filter Time Constant	[s]
τ_i	Motor Current PI controller Time Constant	[s]
$\hat{\omega}_n$	Desired Natural Frequency	[rad/s]
ξ	Desired Damping Factor	[-]
a	Conduction Voltage Drop Model Parameter	[V]
A_s	Effective Area of Core	[m ²]
a_{sw}	Switching Loss Curve Fitting Constant	[J]
b	Conduction Voltage Drop Model Parameter	[V]
b_{sw}	Switching Loss Curve Fitting Constant	[-]
B_m	Peak Value of the Magnetic Flux Density	[T]
c	Conduction Voltage Drop Model Parameter	[-]
C_N	Motor Rated Torque	[Nm]
d_e	Damping Factor in Compliance	[N/m/s]
d_m	Bearing Mean Diameter	[m]
E_{roff}	Reference Turn-off Energy Losses of IGBT/Diode	[J]
E_{ron}	Reference Turn-on Energy Losses of IGBT/Diode	[J]
F_{cl}	Coulomb Friction Force of Friction Loss Model	[N]
F_{st}	Stribeck Friction Force	[N]
F_{jam}	Jamming Force in Advance Friction Model	[N]
f_{hp}	High Pass Filter Frequency	[Hz]
f_{lp}	Low Pass Filter Frequency	[Hz]
f_p	Resonance Frequency	[Hz]
f_{sw}	Switching Frequency	[Hz]
f_v	Viscous Friction Coefficient	[Nm/rad/s]
I_r	Rated Current for IGBT/Diode	[A]
I_{ref}	Switch Current at Reference Condition	[A]
J_L	Load Inertia	[kgm ²]
J_m	Motor Rotor Inertia	[kgm ²]
K_m	Motor Torque Constant	[Nm/A] or [V/rad/s]
k_a	Anchorage Stiffness Between EMA Housing and Airframe	[N/m]

k_e	Pure Spring Stiffness of Nut-screw	[N/m]
k_{ed}	Eddy Current Constant	[-]
k_{eq}	Equivalent Stiffness of EMA	[N/m]
k_n	Nut-screw Stiffness	[N/m]
k_s	Structural Stiffness	[N/m]
k_t	Transmission Stiffness Between EMA rod and Load	[N/m]
K_{t0}	Motor Torque Constant at Reference Temperature	[Nm/A]
K_f	Force Feedback Controller Proportional Gain	[Nm/N]
K_{hp}	High Pass Filter Gain	[-]
k_{hy}	Hysteresis Constant	[-]
K_{lp}	Low Pass Filter Gain	[-]
K_{ii}	Motor Current Loop Integral Gain	[V/A/s]
K_{ip}	Motor Current Loop Proportional Gain	[V/A]
K_p	Position Controller Proportional Gain	[rad/s/m]
$K_{p\omega}$	Speed Synchronization Controller Proportional Gain	[Nm/rad/s]
K_{pr}	Position Synchronization Controller Proportional Gain	[Nm/m]
K_{ir}	Position Synchronization Controller Integral Gain	[Nm/ms]
K_{dr}	Position Synchronization Controller Derivative Gain	[Nm/m/s]
K_v	Velocity Controller Proportional Gain	[Nm/rad/s]
l	Lever Arm Length	[m]
l_m	Effective Magnetic Path Length	[m]
L_m	Motor Windings Inductance	[H]
M_m	Mass Reflected at Load by Motor Rotor Inertia	[kg]
M_s	Equivalent Surface Mass	[kg]
M_t	Mass of the EMA Rod	[kg]
N	Number of Turns in the Coil of Motor	[-]
n_p	Motor Number of Pole Pairs	[-]
p	Lead of Roller Screw	[m]
R_m	Motor Windings Resistance	[Ω]
R_{on0}	On State Resistance for IGBT/Diode at Reference Temperature	[Ω]
R_{on}	On State Resistance for IGBT/Diode	[Ω]
R_{s0}	Motor winding resistance at Reference Temperature	[Ω]
\hat{t}_s	Desired Response Time	[s]
U_0	Static Forward Voltage Drop by IGBG/Diode	[V]
U_{ref}	Switch Voltage at Reference Condition	[V]
U_s	Electric Power Supply	[V]
x_0	Backlash or equivalent preload parameter in Compliance Model	[m]
x^*_0	Backlash or equivalent preload parameter by wear	[m]
x_w	Wear Parameter	[m]

Variables

Θ	Temperature	[°C]
Θ_1	Actual Operating Temperature	[°C]
α	Duty Cycle for Control Motor Power Drive	[-]
α_ω	Motor Velocity Saturation Ratio	[-]
α_c	Torque Saturation Ratio	[-]
ε_ω	Velocity Difference Between Two EMAs Motor Rotor	[rad/s]

ε_p	Static Error Under Step Demand	[m]
ε_v	Tracking Error Under Ramp Demand	[m]
ε_d	Static Disturbance Error	[m]
γ_L	Loads Synchronization Error	[m]
γ_L	Rods Synchronization Error	[m]
θ	Degree	[°]
θ_m	Motor Rotor Angle Position	[°]
θ_s	Surface Deflection Angle	[°]
τ_c	Current Loop Time Constant	[s]
τ_e	Motor Electric Time Constant	[s]
ω	Rotation Velocity	[rad/s]
ω_b	Support Bearing Rotational Velocity	[rad/s]
ω_c	Current Loop Break Frequency	[rad/s]
ω_i	Motor Current Loop Nature Frequency	[rad/s]
ω_m	Motor Rotor Velocity	[rad/s]
ω_{rmax}	Maximum Velocity Reference From Position Controller	[rad/s]
ω_n	Nature Frequency	[rad/s]
ω_{nr}	Relative Rotational Velocity Between Nut and Bearings	[rad/s]
ω_r	Velocity Reference From Position Controller	[rad/s]
ξ	Damping Factor	[-]
ξ_i	Current Loop Damping Factor	[-]
ψ	Magnetic Flux	[Wb]
B	Magnetic Flux Density	[T]
C	Torque	[Nm]
C^*	Torque Reference Demand for Electric Motor	[Nm]
C_{ad}	Aerodynamic Torque on Surface	[Nm]
C_{axl}	Torque Loss Due to Axial Load	[Nm]
C_{b0}	Load Independent Bearing Friction Moment	[Nm]
C_{b1}	Load dependent Bearing Friction Moment	[Nm]
C_{bl}	Bearing Friction Torque	[Nm]
C_{cg}	Motor Compliance Torque (Cogging Torque)	[Nm]
C_d	Motor Dissipative Torque	[Nm]
C_{drag}	Frictional Moment of Lubrication Loss of Bearing	[Nm]
C_{ed}	Equivalent Eddy Current Torque Losses	[Nm]
C_{em}	Motor Electromagnetic Torque	[Nm]
C_{fm}	Motor Friction Torque	[Nm]
C_{hy}	Equivalent Hysteresis Torque Loss	[Nm]
C_j	Inertia Torque of MPT	[Nm]
C_m	Torque of Motor Shaft	[Nm]
C_{oil}	Torque Loss Due to Oil of Bearing	[Nm]
C_r	Motor Torque Reference From Velocity Controller	[Nm]
C_{rad}	Torque Loss Due to Radial Load of Bearing	[Nm]
C_{rmax}	Maximum Torque Reference From Velocity Controller	[Nm]
C_{rr}	Rolling Frictional Moment of Bearing Loss	[Nm]
C_s	Position Synchronization Controller Compensate Torque	[Nm]
C_{seal}	Frictional Moment of Seals	[Nm]
C_{sl}	Sliding Frictional Moment of Bearing Loss	[Nm]
E_d	Conduction Energy Losses of IGBT/Diode	[J]

E_{sw}	Switching Energy Losses of IGBT/Diode	[J]
E_{doff}	Switching Turn-off Energy Losses of Diode	[J]
E_{don}	Switching Turn-on Energy Losses of Diode	[J]
E_{toff}	Switching Turn-off Energy Losses of IGBT	[J]
E_{ton}	Switching Turn-on Energy Losses of IGBT	[J]
f_i	Current Loop Frequency	[Hz]
f_s	Undamped Natural Frequency	[Hz]
F	Force	[N]
F_c	Compliance Contact Force	[N]
F_d	Damping Force of Compliance	[N]
F_e	Elastic Force of Compliance	[N]
F_{ex}	External Force Disturbance	[N]
F_f	Friction Force in Mechanical Power Transmission	[N]
F_f^*	Friction Force with Jamming	[N]
F_L	EMA Load Force	[N]
F_{LA}	EMA_A Load Disturbance Force	[N]
F_{LB}	EMA_B Load Disturbance Force	[N]
F_r	Force Output form EMA Rod	[N]
F_s	EMA Output Force	[N]
H	Magnetic Field Strength	[A/m]
i_d	Operating Current for IGBT/Diode	[A]
I_d	Average Current Flowing Through the IGBT/Diode	[A]
I_{in}	Switch Input Current	[A]
I_m	Electric Motor Current	[A]
I_{mw}	Motor Windings Current	[A]
I_s	Electric Current Supply	[A]
I_{sw}	Equivalent Current Leak by Switching in IGBT/Diode	[A]
J_n	Nut-screw inertia	[kgm ²]
K_t	Motor Torque Constant During Operation	[Nm]
P_{bl}	Bearing Power Losses	[W]
P_{co}	Copper Loss	[W]
P_{cd}	Conduction Power Losses of IGBT/Diode	[W]
P_d	Power Loss by Compliance Damping	[W]
P_{ed}	Eddy Current Loss	[W]
P_f	Friction Power Loss	[W]
P_{hy}	Hysteresis Constant	[W]
P_{sw}	Switching Power Losses	[W]
R_{mw}	Motor winding resistance	[Ω]
R_{on1}	On State Resistance for IGBT/Diode at Operating Temperature	[Ω]
\dot{S}	Entropy Flow	[J/K/s]
t_d	IGBT/Diode Conduction Time	[s]
t_s	Response Time	[s]
t_{cs}	Motor Current Loop Response Time	[s]
U_{co}	Voltage Drop Due to Copper Loss	[V]
U_d	Voltage Drop by IGBT/Diode	[V]
U_m	Electric Motor Voltage	[V]
v_b	Support Bearing Translational Velocity	[m/s]
V_{ce}	IGBT Voltage	[V]

V_d	Diode Voltage	[V]
V_e	Linear Velocity of EMA Rod	[m/s]
V_{ex}	External Linear Velocity	[m/s]
v_r	Relative Linear Velocity in Nut-screw	[m/s]
v_s	EMA Output Linear Velocity	[m/s]
v_{sr}	Relative Translational Velocity Between Screw and Bearings	[m/s]
x	Linear Displacement	[m]
X_c	Position Command	[m]
X_{ca}	EMA_A Position Command	[m]
X_{cb}	EMA_B Position Command	[m]
X_e	EMA Rod Displacement	[m]
X_r	EMA Reference Control Setpoint	[m]
x_r	Relative Deformation by Compliance	[m]
X_s	Surface Equivalent Linear Displacement	[m]
X_{sa}	EMA_A Surface Equivalent Linear Displacement	[m]
X_{sb}	EMA_B Surface Equivalent Linear Displacement	[m]
X_t	EMA Rod Displacement	[m]
X_{ta}	EMA_A Rod Displacement	[m]
X_{tb}	EMA_B Rod Displacement	[m]

Abbreviation

A/C	Aircraft Control
AEA	All Electric Aircraft
bemf	Back Electromotive Force
BLDC	Brushless Direct Current Motor
CCS	Cross-Coupled Synchronization
DC	Direct Current
DoF	Degree of Freedom
EBHA	Electro Backup Hydrostatic Actuator
EHA	Electro-Hydrostatic Actuator
EM	Electric Motor
EMA	Electromechanical Actuator
FBW	Fly By Wire
FBWL	Fly By Wireless
FBL	Fly By Light
FC	Flight Control
FCC	Flight Control Computer
FOC	Field-Oriented Control
HIL	Hardware In-the-Loop
HMA	Hydro-Mechanical Actuator
HSA	Hydraulic Servo Actuator
HMU	Health Minor and Usage
IGBT	Insulated Gate Bipolar Transistor
ITAE	Integral of Time-weighted Absolute Error
LVDT	Linear Variable Displacement Transducer
MBSE	Model-Based System Engineering
MEA	More Electric Aircraft

MIMO	Multiple Input Multiple Output
MOSFET	Metal-Oxide-Semiconductor Field-Effect Transistor
MPT	Mechanical Power Transmission
NS	Nut-Screw
PbW	Power-by-Wire
PCU	Power Control Unit
PDE	Power Drive Electronics
PID	Proportional–Integral–Derivative
PMSM	Permanent Magnet Synchronous Motor
PWM	Pulse Width Modulation
RC	Resistance-Capacitance
SIL	Software In-the-Loop
THS	Trimmable Horizontal Stabiliser
TRAS	Thrust Reverser Actuation System
XPC	Real Time Control Computer

Introduction

In recent years, the increase in fuel costs, the environmental footprints and the emergence of new competitors have driven the aerospace industry to introduce step changes towards greener, safer and cheaper air transport [1]. The concepts based on extended use of electricity in “More Electric Aircraft” (MEA) and even “All Electric Aircraft” (AEA) have logically defined the technological shift towards “greening” aviation operations, using the electric power networks to replace conventional hydraulic networks [2][3]. Currently, numerous research activities strive to widen the use of electrical power networks for electrically supplied power users (Power-by-Wire or PbW) in replacement of the conventional hydraulic, pneumatic and mechanical power networks [4]. At the same time, PbW actuators have become sufficiently mature to be introduced in the latest commercial programmes:

- Electro-hydrostatic actuators (EHAs) as backup actuators for primary and secondary flight controls in Airbus A380 / A400M / A350,
- Electromechanical actuators (EMAs) as frontline actuators for a few secondary flight controls and for landing gear braking in Boeing B787.

Although they remove the central hydraulic power distribution, EHAs still use hydraulics locally to keep the major advantages of conventional actuators regarding secondary functions (back-driving, overload protection, damping) and response to failure (easy hydraulic declutch and extremely low risk of jamming). EMAs, however, remove both central and local hydraulic circuits by transmitting the motor power to the load through mechanical reducers (e.g. gearbox, nut-screw, etc.). Nevertheless, EMAs are not yet sufficiently mature to replace conventional hydraulic servo-actuators (HSA) in normal mode for safety-critical functions such as primary flight controls. Several technical challenges still need to be taken up: weight and size constraints for integration, voltage spikes and current transients affecting the pollution and stability of the electrical network, heat rejection for actuator thermal balance,

reduced reflected inertia for dynamic performance, increased service life and fault tolerance or resistance (e.g. for jamming or free-run) for safety [5][6]. In particular, introducing more or all electrical actuation by using EMAs raises new challenges:

a) Heat Rejection

It is well known that the temperature of motor windings and power electronics is a key element affecting service life and reliability. Thus, thermal balance is an important issue for PbW actuation. In HSAs, the heat generated by energy losses is taken away by the fluid returning to the reservoir. Conversely, the heat in PbW actuators has to be rejected locally to the surroundings or to a heatsink. The simulation of lumped-parameter models can provide a detailed view of the temperature and heat flow fields [7][8]. Unfortunately, these methods are too time-consuming for modelling and simulation at system level. In addition, they cannot be used in the early design phases because they are too detailed and they require numerous parameters that are not yet known in these phases. The heat generated in EMAs comes from a multiplicity of sources: electronic (switching and conduction losses), electrical (copper losses), magnetic (iron losses) and mechanical (friction losses). It is very interesting to accurately quantify this heat during a reference flight cycle because it determines the operating temperature of the actuator's components.

b) Response to Failure

Safety-critical functions like primary flight controls have to show extremely low failure rates (e.g. 10^{-9} per flight hour). This is achieved through redundancy by installing multiple channels. However, each channel must be fail-safe to enable the remaining channels to operate correctly. In EMAs, this requirement introduces another challenge, when jamming and free-run faults of mechanical components are considered. In HSAs, a fail-safe response to failure (free, damped or frozen) is easily obtained at low mass and low cost by resorting to bypass valves, restrictors, piloted check valves or isolation valves. Unfortunately, it is no longer possible to transpose the needs from the hydraulic domain to EMAs where clutches, brakes, dampers and torque limiters may be required. Virtual prototyping at system-level therefore becomes very interesting, not only to support conceptual design but also to verify

the control and reconfiguration strategies.

c) Pollution of Electrical Supply

The control of power of electrical machines (e.g. actuator motor) is based on high frequency on/off switching (e.g. 8 to 16 kHz) of power semi-conductors through pulse width modulation (PWM). Although power is controlled with very low energy losses, it generates high transients in the electrical supply bus and can affect the stability of the electrical network. Moreover, regenerative currents need to be managed properly under aiding-load conditions. This is another reason why model-based systems engineering (MBSE) of PbW actuators calls for more realistic models.

d) Motivation of the Research Work

However, with the constant efforts of aviation, on recently developed commercial airplanes and future aircraft program will certainly rely on more increasing use of electrical power, and EMAs will be more involved on the next generation aircraft. The first concept is that EMA will work together with HSA or EHA as a hybrid redundancy structure to drive single surface for primary flight control application, such as aileron. This redundant structure has been investigated with consideration of force equalization in much academic research works [9-11].

This thesis has been conducted at Laboratory Institut Clement Ader, Institut National des Sciences Appliquées de Toulouse (INSA-Toulouse). It can be seen and the logical continuation of former defended Ph.D studies that were related to the modelling, simulation and control of electrically powered actuators for aerospace applications:

-WANG Lijian, “Force Equalization for Active/Active Redundant Actuation System Involving Servo-hydraulic and Electro-mechanical Technologies”, INSA-Toulouse, France Thesis, 2012.

-QI Haitao, “Research on Actuation System Architecture of More Electric Aircraft and Electro-Hydrostatic Actuator (EHA)”, Beihang University, Codirected by INSA-Toulouse and Beihang University, China Thesis, 2010.

-KARAM Wissam, “Investigation into the electromechanical actuator when used for high performance force control”, INSA-Toulouse, France Thesis, 2007.

-NFONGUEM Gustave, “Contribution to the development of a more electrical actuator – inverse modelling mechanical components specific to an aerospace application”, INSA-Toulouse, France Thesis, 2006.

On its side, the present research work addresses the case where 2 EMAs drive separately 2 independent loads (flight control surfaces) that shall be position-synchronized at any time. This typically corresponds to secondary flight control, such as flaps, slats, or to thrust reverser applications. The conventional position synchronization strategy is centralized via a mechanical shaft system. It is heavy, bulky and not flexible. Individual loads offer new opportunities for distributed actuation that requires synchronization control strategies.

According to the above mentioned needs and challenges, the present thesis intends to propose incremental models of EMAs and their components to support the various engineering needs appearing during the development and integration of actuation systems. The typical application that will be addressed is presented on Fig. 1.

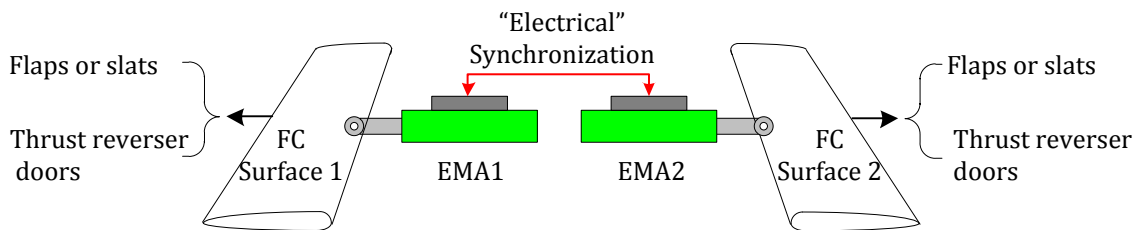


Fig. 1 “Electrical” synchronization structure of EMAs for thesis study

All above considerations highlight the interest of developing high fidelity virtual prototype with a transverse view of the physical domains involved in EMAs for position synchronization. A model-based and simulation-driven approach can unquestionably provide engineers with efficient means to address all these critical issues as a whole. In particular, it will facilitate and accelerate the assessment of innovative architectures and concepts [12][13], and also their technological embodiments. This thesis will make wide use of the Bond-Graph methodology for graphical and qualitative modelling. Bond-Graph modelling [14][15] explicitly displays the

multidisciplinary energy transfers, and the structure and the calculation scheme for simulation. Incidentally, it facilitates the design of a model structure that enables incremental (or even decremental) modelling. The thesis is organized as follows:

In **chapter 1**, state of the art of actuation for flight control is firstly introduced and the objectives, requirements and methodology of virtual prototyping of EMAs for position synchronization are presented. In **chapter 2**, the individual EMA controller with position/velocity/force loops is designed on the basis of the linear approach. The saturation (torque and velocity), motor current loop and compliances effects are considered. In **chapter 3**, the incremental virtual prototypes of power drive electronics (PDE) and electric motor (EM) of EMA are built respectively, with resort to Bond-Graph formalism. Multi-level of models are implemented and tested in the LMS-AMESim, and the numerical simulation and results are analyzed. In **chapter 4**, the virtual prototyping of mechanical power transmission (MPT) of EMA is also addressed with an incremental approach, the physical effects are progressively introduced. The one degree of freedom (1-DoF) and two degrees of freedom (2-DoF) models are proposed, implemented and tested in LMS-AMESim. In **chapter 5**, the test bench configuration is presented for next experimental study. The preliminary position synchronization of EMAs is addressed, a proportional–integral–derivative cross-coupled synchronization (PID-CCS) controller is proposed. Then, the proposed models (linear or advanced) of EMAs are integrated and simulated to illustrate how they can support the assessment of the PID-CCS control strategy. In **the end**, the general conclusions summarizes the main proposals and achievements of this research work, and gives perspectives for further development of system-level virtual prototyping and position synchronizing.

Reference

- [1] X. Roboam, B. Sareni, and A. D. Andrade, "More electricity in the air: Toward optimized electrical networks embedded in more-electrical aircraft," *Industrial Electronics Magazine, IEEE*, vol. 6, pp. 6-17, 2012.
- [2] J. A. Rosero, J. A. Ortega, E. Aldabas, and L. Romeral, "Moving towards a more electric aircraft," *Aerospace and Electronic Systems Magazine, IEEE*, vol. 22, pp. 3-9, 2007.

- [3] S. L. Botten, C. R. Whitley, and A. D. King, "Flight control actuation technology for next-generation all-electric aircraft," *Technology Review Journal*, vol. 8, pp. 55-68, 2000.
- [4] I. Chakraborty, D. N. Mavris, M. Emeneth, and A. Schneegans, "A methodology for vehicle and mission level comparison of More Electric Aircraft subsystem solutions: Application to the flight control actuation system," *Proceedings of the Institution of Mechanical Engineers, Part G: Journal of Aerospace Engineering*, vol. 229, pp. 1088-1102, 2015.
- [5] X. Yu and Y. Zhang, "Design of passive fault-tolerant flight controller against actuator failures," *Chinese Journal of Aeronautics*, vol. 28, pp. 180-190, 2// 2015.
- [6] M. Todeschi, "Airbus-EMAs for flight controls actuation system-perspectives," presented at the International Conference on Recent Advances in Aerospace Actuation Systems and Components (R3ASC), Toulouse, France, 2010.
- [7] W. Takebayashi and Y. Hara, "Thermal design tool for EHA," in *International Conference on Recent Advances in Aerospace Actuation Systems and Components (R3ASC)*, Toulouse, France, 2004, pp. 15-20.
- [8] E. Faugère, J.-C. Maré, C. Changenet, F. Ville, and D. Delloue, "Coupling mechanical and thermal lumped parameters models for the preliminary design of power transmissions driven by thermal issues," in *28th International Congress on Aerospace Sciences (ICAS)*, Brisbane, Australia, 2012, pp. 3690-3700.
- [9] L. Wang and J.-C. Maré, "A force equalization controller for active/active redundant actuation system involving servo-hydraulic and electro-mechanical technologies," *Proceedings of the Institution of Mechanical Engineers, Part G: Journal of Aerospace Engineering*, vol. 228, pp. 1768-1787, 2014.
- [10] W. Karam and J.-C. Maré, "Force control of a roller-screw electromechanical actuator for dynamic loading of aerospace actuators," in *International Conference on Fluid Power and Motion Control*, 2008.
- [11] W. Ur Rehman, S. Wang, X. Wang, L. Fan, and K. A. Shah, "Motion synchronization in a dual redundant HA/EHA system by using a hybrid integrated intelligent control design," *Chinese Journal of Aeronautics*, 2016.
- [12] I. Chakraborty and D. N. Mavris, "Integrated Assessment of Aircraft and Novel Subsystem Architectures in Early Design," presented at the 54th AIAA Aerospace Sciences Meeting (SciTech), San Diego, California, USA, 2016.
- [13] J. Liscouët, J.-C. Maré, and M. Budinger, "An integrated methodology for the preliminary design of highly reliable electromechanical actuators: Search for architecture solutions," *Aerospace Science and Technology*, vol. 22, pp. 9-18, 2012.
- [14] G. Dauphin-Tanguy, A. Rahmani, and C. Sueur, "Bond graph aided design of controlled systems," *Simulation Practice and Theory*, vol. 7, pp. 493-513, 12/15/ 1999.
- [15] W. Borutzky, "Bond graph modelling and simulation of multidisciplinary systems – An introduction," *Simulation Modelling Practice and Theory*, vol. 17, pp. 3-21, 1// 2009.

Chapter 1

State of the Art

The thesis focuses on virtual prototyping of electromechanical actuators for position synchronization in aerospace application. The complex, numerous and cross-linked parasitic effects of electromechanical actuator are incrementally modeled with the support of Bond-Graph formalism. The state of the art of aerospace actuation will be firstly introduced. The innovations and developments of electrically powered actuators, especially electromechanical actuators, for recent aircraft even for next generation of more electric aircraft application are presented. For safety critical actuation applications like flight control, the safety issues and reliability requirements are of particular importance. For this reason, the redundancy configurations will be presented. The following part will address the common active/active mode of operation for actuators with its main issue for electromechanical actuators: the position synchronization. Then, the incremental modelling approach, considering with priority the engineering needs and the physical effects, will be introduced as it has been used extensively in the present work.

1.1 Flight Control Actuators

The new generation of aircraft will use almost exclusively electric power distribution networks. For this reason, the actuators should evolve to take advantage of this development, in terms of performance, weight and maintenance.

1.1.1 Power Distribution

In aeronautics, as in all types of aircrafts, we can define the primary and secondary power systems [1]. The primary power is to ensure the movement of the aircrafts (propulsion, traction, lift, etc.). The secondary power relates to other power systems (air conditioning, flight controls, landing gears, fuel, anti/de-ice, etc.).

In today's commercial aircraft, primary power is created by the main engines. It comes from the combustion of aviation fuel in a gas turbine that produces reaction forces (jet aircrafts) or a mechanical rotational power (turbo-propellers). For example, in the Airbus A330, the propulsion power is typically 40 MW [2].

The secondary power is essentially derived from primary energy. It is used to supply the aircraft no-propulsive systems. On a conventional commercial airplane, there are generally four types of energy networks: pneumatic, mechanical, hydraulic and electric. In Airbus A330, as shown in Tab. 1-1, the total "non-propulsive" power is about 1.74 MW [2].

Table 1-1 Various secondary powers in an Airbus A330

Power types	Application systems
Pneumatic : 1,200kW	air conditioning, cabin pressurization, anti/de-icing, etc.
Mechanical : 100kW	secondary power generators (hydraulic pumps and electric generators), etc.
Hydraulic : 240kW	flight controls, landing gear, brakes, thrust reverse, etc.
Electric : 200kW	avionics, de-icing, lighting, cabin system, etc.

1.1.2 Flight Control of Civil Aircraft

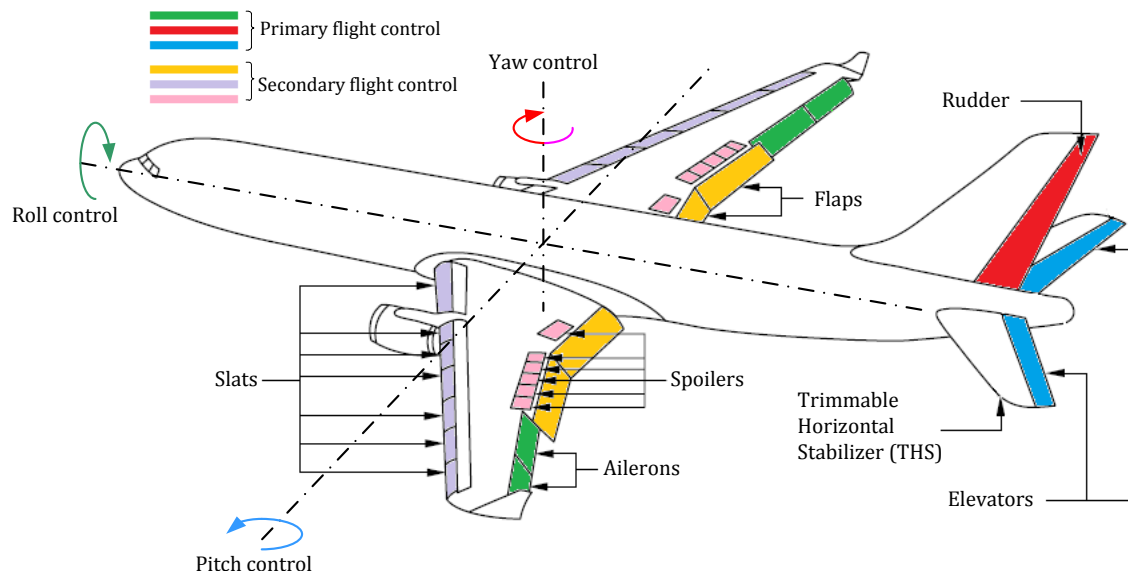


Fig.1-1 Flight control of an Airbus A330 [3]

In an aircraft, the flight control system aims at acting on the trajectory of the aircraft (primary) and on the aerodynamic configuration (secondary) by moving control surfaces

from the commands given by the pilot (or autopilot) [4]. Flight Control system includes all the components between the cockpit control units and control surfaces. Figure 1-1 shows the flight control architecture of an Airbus A330 [3].

Primary Flight Control: The primary flight controls are used to control the evolution of the aircraft around its reference axis during the flight [4]: the rudder or rudder for yaw control, the ailerons and spoilers for roll control, and the elevators and the trimmable horizontal stabilizer (THS) for pitch control.

Second Flight Control: The secondary flight controls allow changing the aerodynamic configuration of the aircraft during landing and takeoff phases: Flaps and slats for lifting, spoilers for the trail, airbrakes.

1.1.3 Actuators Technology Innovations

Actuator servo control is used to position a flight control surface to follow a setpoint. This is a key element in the flight control of an aircraft. As illustrated in Fig. 1-2, it is historically hydraulic powered by an external centralized hydraulic system or via an electromechanical pump associated with a local hydraulic power generation.

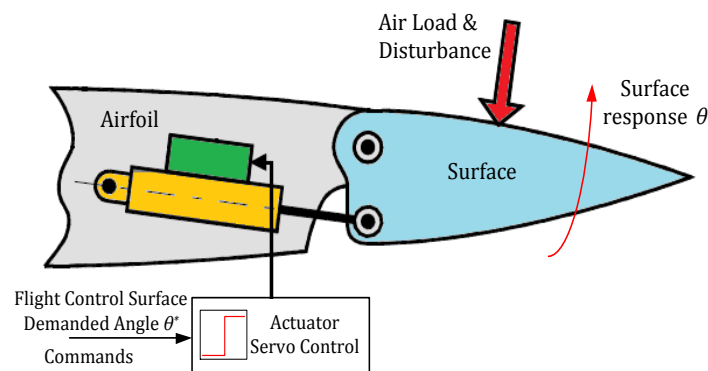


Fig.1-2 Schematic of actuator servo-control

Actuator used for aerospace applications first appeared in earlier 1940. Until now, it has gone through many times of innovation and updating. The development history and future tendency are summarized in Tab. 1-2.

Table 1-2 Summary of actuator technology development [3]

Decade	Actuator	Signaling	Powering
~-1940s	Null	Mechanical Cables	Human Mechanical
1950s	Hydro-Mechanical Actuator (HMA)	Mechanical Cables	Human Mechanical + Hydraulic Assist
1960s	HMA (with stability augmentation)	Mechanical Cables	Hydraulic
1980s	Hydraulic Servo Actuator (HSA)	Electric Wires (Fly-By-Wire)	Hydraulic
2000s	HSA & Electrically powered Actuator (Electro-hydrostatic actuator(EHA), Electromechanical actuator (EMA))	Electric Wires (FBW)	Electric + Hydraulic (Power-By-Wire)
2020s?	EHA & EMA	Electric Wires (FBW)	Electric (PBW)
	EHA & EMA	Optical Fiber Cables (Fly-By-Light, FBL)	Electric (PBW)
	EMA	Optical Fiber Cables (Fly-By-Light, FBL)	Electric (PBW)
2030s?	EMA	Wireless Protocol (Fly-By-Wireless, FBWL)	Electric (PBW)

As the rapid growth of air traffic market in recent years, man-made CO₂ emissions into the atmosphere increased largely by civil aviation. The aircraft industry has to face both economic and environmental issues [5]. Currently, an interim and attractive solution is towards “More Electric Aircraft” (MEA) using more electric power technological advancements for non-propulsive systems of aircrafts. On this basis, today’s aircraft actuation systems prefer power-by-wire (PBW) and have centered on novel approaches to design and develop electrically powered actuators.

Currently, aircraft manufacturers are still in an intermediate step. The latest generation of commercial aircraft such as the Airbus A380 or A350 is an example since they have a mixed the type of power supply to the flight controls. By suppressing one hydraulic circuit over three in favor of electrical networks; it was possible to significantly reduce the weight of the aircraft (5%, for the A380) [6]. This approach has resulted in a new generation of PBW actuators of EHAs or electro backup hydrostatic (EBHA) types.

Across the Atlantic, the latest project from Boeing, the 787, is also intended to be the "most electric" aircraft, as said by the MOOG Company that provides 21 flight control surface actuators, all hydraulically power excepted 4 EMAs for spoilers [7].

Undoubtedly, the next airliners will see an increase in the use of electrical power. The Airbus A380/A350 and Boeing 787 are paving the way to the future single-aisle, medium-haul. Three reasons explain this tendency [8]:

(1) First, the permanent objective is to reduce the overall weight of the aircraft - thus its fuel consumption. In fact, the use of electrical instead of hydraulic systems provides flexibility in terms of design, integration and power management.

(2) Secondly, this same design flexibility offers significant potential for personalization and adaptation of systems to the customer needs.

(3) Finally, maintenance promises to be more efficient because the electrical circuits can be tested and diagnosed more easily. The maintenance actions are expected to be reduced.

However, there is no question in near future of replacing the hydraulic networks and generators by electric wire and electric motors: the announced rule of electric power is a revolution that engages the power architecture of the aircraft to achieve substantial gains. Yet the introduction of major technological breakthroughs in commercial aviation is a process that lasts for many years [4].

Nowadays, beyond the well-known HSAs, the new uses have three different concepts of PBW actuators for flight controls: EHAs, EBHAs and EMAs [9].

(a) Hydraulic Servo Actuator (HSA)

HSAs are powered by hydraulic power and controlled by a servo valve, displayed in Fig. 1-3 (a). The power transfer is metered by introduction of hydraulic variable resistors between the constant pressure hydraulic source of and cylinder. When the HSA is not active, a mode select valve forces the actuator to operate in a damping mode.

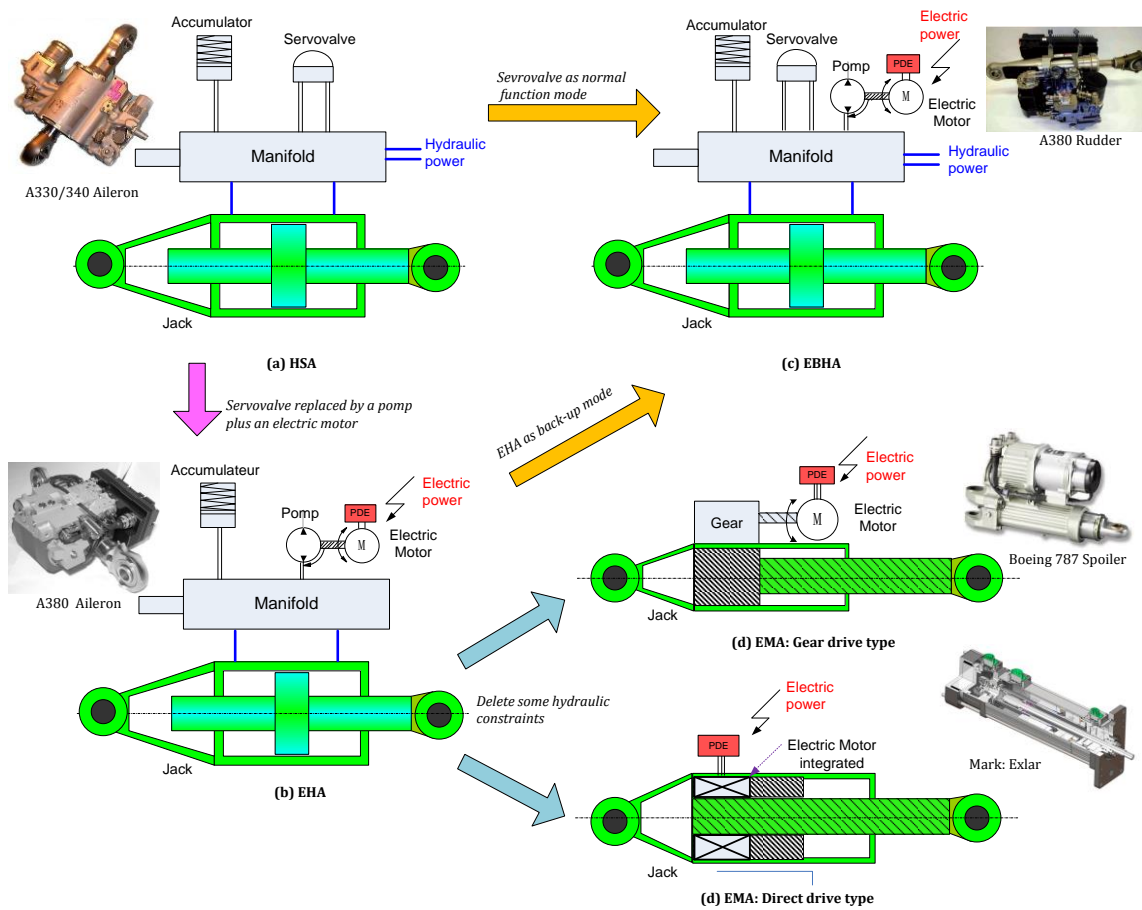


Fig.1-3 Different actuators for flight controls

(b) Electro-hydrostatic Actuator (EHA)

In the last decades, numbers of investigations explored EHAs technologies and achieved deep understanding studies. Unlike the HSAs, for control flight surfaces, EHAs use internally a hydraulic power generation that removes the need for a centralized hydraulic power distribution. Thus, EHAs have their own fluid reservoir. A high-speed electric motor drives at variable speed a fixed displacement hydraulic pump, the speed of the motor controlling functionally the load velocity, as the servovalve current does in HSAs, as per Fig. 1-3 (b). The EHAs are used on elevators and ailerons for the A380 and A 350 as backup actuators [10]. In this figure, the electronic control box is integrated in the actuator package.

(c) Electro Backup Hydrostatic Actuator (EBHA)

The EBHA appeared for reasons of safety: it has a compact structure but provides an effective dissimilar redundancy solution regarding the sources of power. As shown in Fig. 1-3 (c), an EBHA implements a hybrid power architecture and combines the EHA structure for backup

and an HAS structure for normal mode. The EHA and HAS are sharing a same jack and the working mode is changed by a selector valve. In recent aerospace applications, the rudder and some spoilers for the A380 are driven (among others) by EBHAs.

(d) Electromechanical Actuator (EMA)

EMAs compared to EHAs, eliminate all the hydraulic circuits, as show the successful applications in Boeing 787 for a few secondary flight controls. The use of EMAs is pursued not only because of its clean energy but also for fuel consumption reduction and maintenance cost reduction for aircraft actuation systems. Hence, EMAs technologies are crucial for the ultimate goal to the achievement of the All Electric Aircraft.

Currently, two types of linear EMAs are regarded for flight control applications: geared and direct drive. As shown in Fig. 1-3 (d), when the nut screw is directly driven by the electric motor, the EMA is so-called direct drive. When an intermediate reduced in introduced, the EMA becomes a geared EMA. Whatever the type of EMAs, the electric energy is converted into mechanical one by a rotary electric motor which transfers the mechanic power to the control surface through an optional gearbox and a nut-screw mechanism. Direct drive EMAs cancel the gear reduction and offer a high potential for geometrical integration of the nut-screw reducer and the electric motor. Although the required motor torque is higher than in a geared EMA, direct-drive EMAs seem to be lighter and more compact.

1.2 Safety-Critical Requirements and Position Synchronization

The safety issues a very demanding for the design and operation of commercial aircrafts. When it comes to perform critical functions, such as primary flight controls, the reliability aspects become more preponderant. Therefore, one most important issue of reliability requirements is to ensure the actuation system provides the right level of failure rate and the right response to failure [11]. For example, especially in EMAs, the most feared events come generally from the jamming susceptibility of mechanical power transmissions, the short circuit in electric motor windings and power drive electronics.

1.2.1 Redundancy Configuration

In order to meet these safety issues and reliability requirements for today's aircraft design, the flight control actuation systems have to be redundant. The dual redundant actuation configuration is considered here and summarized in three common arrangements [12], as shown in Fig. 1-4, the internal redundancy, the actuator redundancy and the surface redundancy.

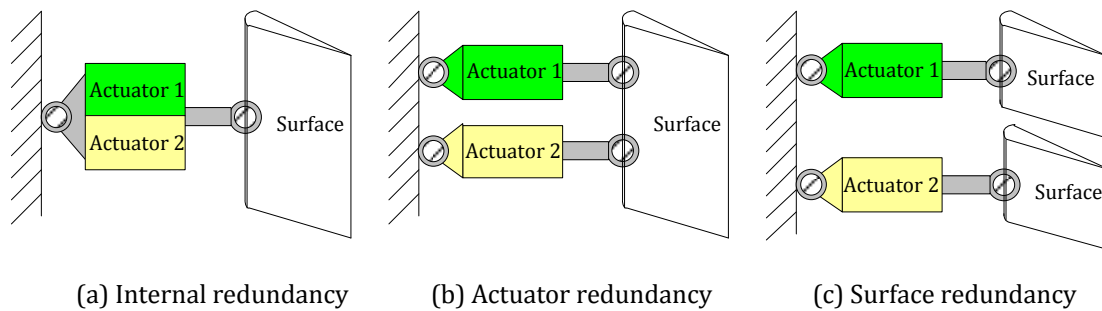


Fig.1-4 Examples of redundancy configuration to control surface

The different redundant configurations impact the design objectives to reduce the probability of “loss of control” of the driven surface:

(a) Internal redundancy

A single actuator jack integrates multiple power paths to drive a single actuator arm. This redundant configuration is applied on fighters or helicopters. However, it is unable to completely avoid the presence of common failure points and just tolerates a failure in the power path.

(b) Actuator redundancy

That is the most common and simplest apparent solution for fault tolerance. A single moving surface is driven by two or multiple actuators. When actuators operate in active/damping mode, only one actuator is in charge of the positioning function while the other operates as a damper. The roles are reversed in case of failure of the active channel. While in active/active mode, both actuators equally drive the load, so “force fighting” may occur and produce additional stress or energy consumption. For primary flight control systems of today's commercial aircraft (e.g. both A380 and B787), no single surface is driven by a single actuator. The actuators are involved into dissimilar redundant (e.g. HSA/EHA) or similar redundant

(e.g. HSA/HSA) [13].

(c) Surface redundancy

When multiple surfaces available perform a same control mission, for example, surface of spoilers or slats are used for reducing lift as well as increasing drag. Therefore, each moving surface can employ a single actuator. In case of failure, the actuator can be locked in failed position or return to a defined position. And the remaining surfaces are normally operated.

Today, advanced technologies are developed in electrical and electronics domains, which provide a wider use of PbW actuators. Because of maturity and response to failure, PbW does not enable removing all conventional actuators (e.g. HSA). But nowadays in aerospace industry for new generation aircraft design, the electrically supplied actuators, especially EMAs, are being more and more considered.

From a more academic viewpoint, using EMA in the area of aerospace application considering the safety-critical functions, there has been much research focused on internal redundancy, Fig. 1-4 (a). The fault-tolerant and fault bypassing methods have been proposed in EMA electric drives and power paths design [13]. Also in our laboratory, Institute Clément Ader (ICA), from 2001 we began to take interest in the EMA technology, then in 2006, Dr. G.NFONGUEM did thesis defense with a contribution to the development of more electric actuators for THS [14]. Then Dr. W. KARAM and Dr. L.J WANG focused on the development of a hybrid redundant configuration of an HSA and an EMA actuation test bench, corresponding to the Fig. 1-4 (b) arrangement. Dynamic force generators were designed with resort to different modeling levels of EMA mechanical components [15]. In addition, force equalization strategies were studied when HSA and EMA operate in active/active mode to drive a single load [3].

The present thesis focuses on EMA technologies for safety-critical functions, according to the surface redundancy arrangement, Fig. 1-4 (c). The main progress concerns the development of advanced system-level virtual prototypes of EMA for position synchronization of independent loads. Due to the different natural dynamics and external loads, the two

independent loads tend to have a different position, which is not acceptable when applied to symmetrical surfaces control for spoilers, slats or even thrust reversers doors (or transcowls). Therefore, one of the main interests of this thesis is to enable addressing virtually the response to failure, in order to verify that the safety requirements are met for position synchronized EMAs.

1.2.2 Position Synchronization in Aerospace Application

At present for aerospace application, in position synchronization is the key technology and is well applied for some different functions.

(a) Application to Thrust Reverser Actuation System (TRAS)

The thrust reverser actuation system is used in many turbine engines for aircraft to assist in reducing the horizontal speed of the aircraft after touch-down, reducing wear on the brakes and enabling shorter landing distance [16]. This action allows sending the air flow generated by the reactor forward and develops a forward force during the landing phase. Nowadays, some different thrust reverser types can be found in aircrafts, as shown in Fig. 1-5.



a) Bucket type
(Source: Fokker70, KLM)



b) Clamshell door type
(Source: Airbus A320, Easyjet)



c) Translating cowl type
(Source: Airbus A380, AirFrance)

Fig.1-5 Different thrust reverser types

Taking an example of Airbus A340-600, the thrust reverser is supplied with constant pressure hydraulic power from onboard hydraulic network. For each engine, the function of thrust reverser is achieved by translating two panels (translating cowl or transwcol type) that produce the reversal of the air flow (a right panel and left panel of the engine). Each panel is driven by three actuators and bonded to the nacelle engine so as to provide a motorized

sliding connection. Furthermore, in order to reduce the risk of jamming, the three jacks are mechanically synchronized and connected by using two flexible shafts, as shown in Fig. 1-6. The mechanical position synchronization helps to both halves of the thrust reverser and lock the system in flight.

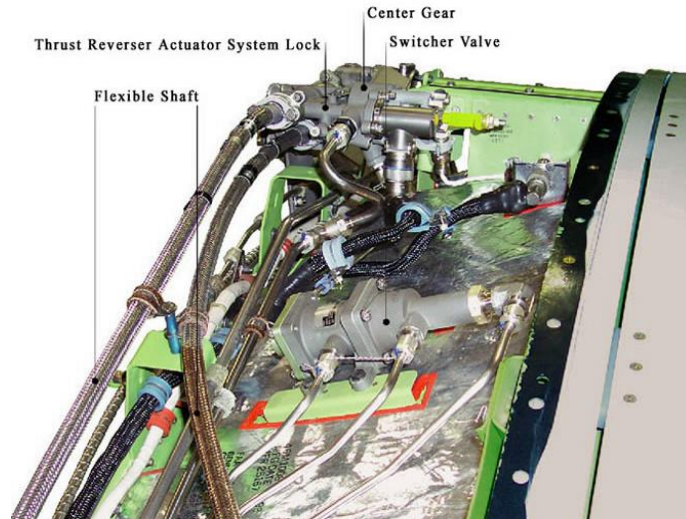


Fig.1-6 Mechanical synchronization in thrust reverser by using flexible shaft [17]

(b) Application to Secondary Flight Control Actuation System

The flaps and slats are the most common devices in high lift actuation system for aircraft secondary flight control. They must always be extended and retracted identically on both left and right wings to maintain the symmetry of flight, as displayed in Fig. 1-7.

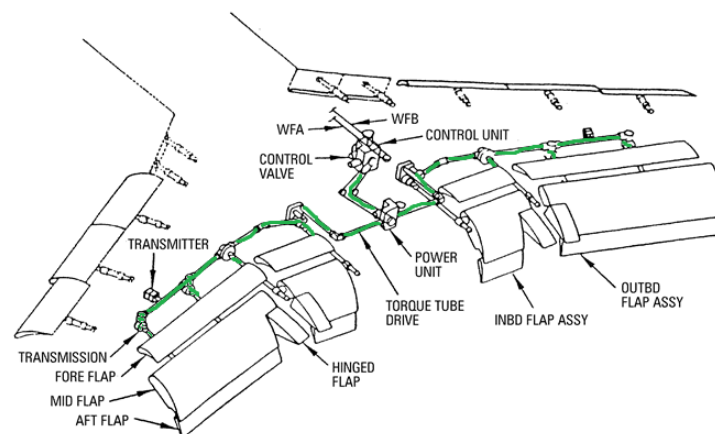


Fig.1-7 Boeing 737 wings drive system [18]

Figure 1-8 shows a conventional architecture of a flap actuation system, due to the permanent coupling, the entire flap or slat system movements must be position-synchronized and usually

centrally-controlled by a power control unit (PCU), which is usually redundant (using centralized hydraulic and/or electric power). The power is transmitted to drive a mechanical shaft, which transmits motor to the loads through several gear boxes (BGB, KGB), rotary hinges and actuators. For security consideration, wing tip brakes (WTB) are used to perform the functions of position holding for shaft system or gear box failures. Meanwhile, several torque limiting devices (STL) are needed with the function of protection against the excessive loads of the wing or the actuator in case of jamming faults. In addition, for health minoring and usage (HMU) consideration, several sensors for system control, cockpit display and failure detection (FPPU, IPPU, APPUs) are available.

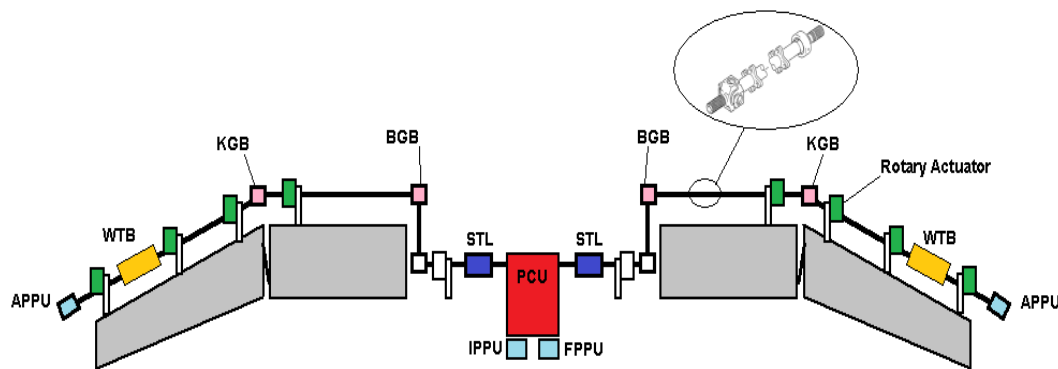


Fig.1-8 Architecture of a conventional flap drive system of Airbus A330/A 340 [19]

(c) Application to Tiltrotor Aircraft Conversion Actuation System

Position synchronization applications also can be found in today's most recent tiltrotor aircrafts, such as V22 Osprey, XV-15 and AW609/BA609. They are also be called the vectored-thrust aircraft that takes off and lands vertically like a helicopter but converts to airplane mode while in flight [20], seen Fig. 1-9.



(a).Helicopter mode

(b). Conversion mode

(c). Airplane mode

Fig.1-9 Tiltrotor aircrafts of AW609/BA609 [Source: Google photo]

For position synchronization, V22 Osprey, XV-15 and AW609/BA609 have the similar functions, which have a pylon conversion actuation system for angular positioning and synchronising their two engine nacelles to switch from one mode to another (helicopter /airplane) [20]. In order to ensure high reliability and safety requirements, the conversion actuators usually have multi-redundant architectures. For example, as the principle of the AW609/BA609 conversion actuator is shown in Fig. 1-10.

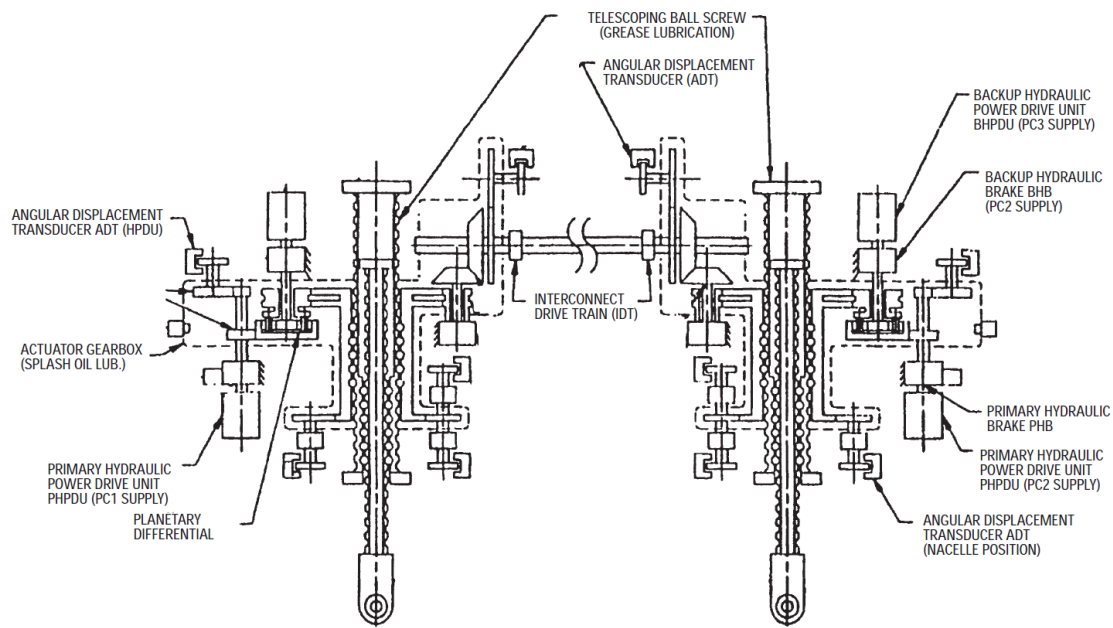


Fig.1-10 Functional schematic of AW609/BA 609 conversion system [20]

Each conversion actuator is supplied with different and independent power networks. In addition, the conversion actuator consists of a two-stage, telescopic ball-screw that is driven by a planetary gear differential with two inputs: a primary hydraulic drive unit or a backup unit. The synchronizing motion of the wing on each side of the aircraft is mechanically linked via an elastic cross shaft located in the leading edge of the wing. The position synchronization is also monitored electronically to ensure synchronous operation even if in case of failure in the power path [20, 21].

1.2.3 Interests of Future “Electrical” Position Synchronization

In early very small aircraft system and today’s some industry process system, the position synchronization was performed hydraulically (e.g. using flow dividers) or by dedicated

strategies that elaborate the control signal of each actuator servovalve [22]. The example of secondary flight controls, have shown how synchronization is achieved mechanically. However, although the mechanical synchronization is mature, the potential failure of mechanical shaft or actuator may cause the entire flap or slat high lift system to jam and the overall function to be lost. So the mechanical synchronization is not a very flexible configuration and has a large number of components, is heavy and requires significant installation space. For next generation aircraft, “electrical” position synchronization has a great interest, in particular with distributed control of PbW actuators, such as EMAs.

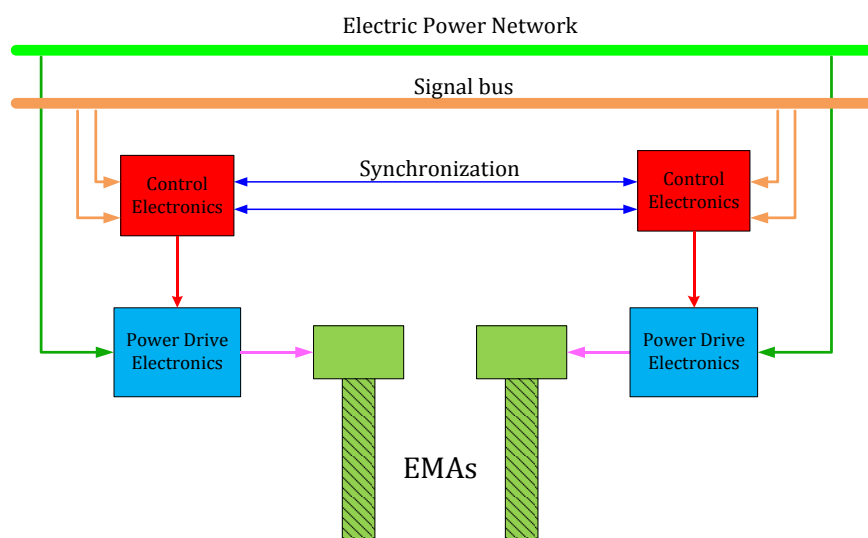


Fig.1-11 Concept of “electrical” synchronization of EMAs for thrust reverser actuation system

Figure 1-11 shows a concept of “electrical” synchronization of EMAs for thrust reverser actuation system in future more electric aircraft [23]. The thrust reverser includes two doors individually driven by two electromechanical actuators (EMAs). The control law for position synchronization of the two doors of the TRAS is implemented in the control electronic units that pilot the power drive electronics (PDE) associated with each EMA motor. The electronic control units of the actuators can also exchange data between each other via an electrical connection. The control units are in charge of generating the movement sequence of the two doors, to regulate the position and to synchronize the doors’ position in any case. This electrically solution is more flexible and facilitates the realization of the position synchronization function.

In addition, “electrical” position synchronization also can be developed in the field of secondary flight control actuation system by introducing a concept of “distributed actuation system”. Different from the previously presented conventional high lift system, each surfaces, flap or slat, is driven by an independent EMA. This concept potentially enables different positions to be ordered for each actuator in order to improve the quality of flight. Figure 1-12 gives an example of application coming from the research project DEAWS (Distributed, Electrically Actuated Wing System) [24].

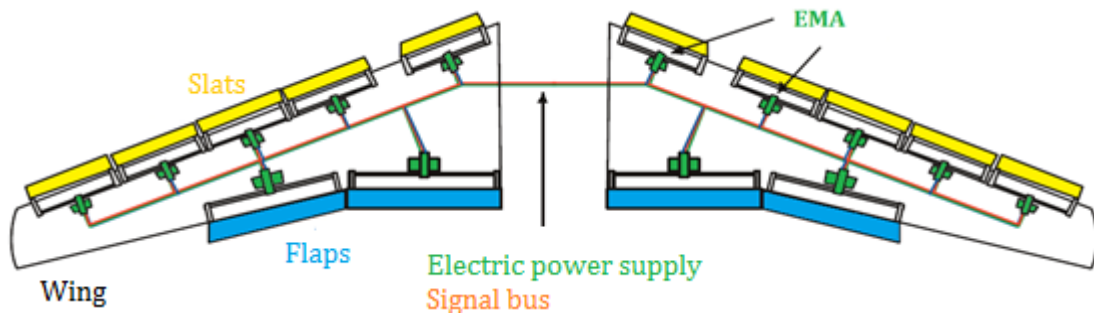


Fig.1-12 Concept of electrical synchronization of EMAs for flaps and slats [24]

All surfaces of left wing and right wing are mechanically independent and their position synchronization is fully electric [25]. The other project NEFS (New track integrated Electrical Flap Drive System) [26] is based on the similar configuration. Its main objective is to firstly simplify the synchronization control while optimizing the power architecture. The second objective is to develop a distributed electrical flap drive system that is completely integrated into the flap support structure.

This thesis aims at contributing to the assessment of electrical position synchronization by means of realistic simulation. Because of safety critical requirements, the position synchronization methodology needs to be validated and verified in the presence of faults. Therefore, a full model of electrical position synchronization of EMAs for independent load control is a key step and needs to be firstly addressed. It will facilitate the next step that will be addressed, that deals with the real validation with a generic test bench.

1.3 Virtual Prototyping Methodology

As previously presented, the electrical synchronization of EMAs will be a great challenge in

future aircraft. Fig. 1-13 shows the architecture of two EMAs driving independent surfaces under independent dynamic load. Each actuator is individually controlled and position synchronization will be added between the two EMA controllers. Considering the importance of response to faults for a safety critical application, it is of prior importance to develop virtual and real test means with progressive transition between simulated and real worlds through hardware in-the-loop (HIL) and software in-the-loop (SIL). Therefore, in the frame of this thesis, it is firstly needed to develop a virtual prototype of these two EMAs to virtually evaluate the position synchronization strategy on the full model before implementing the real controller and running real tests.

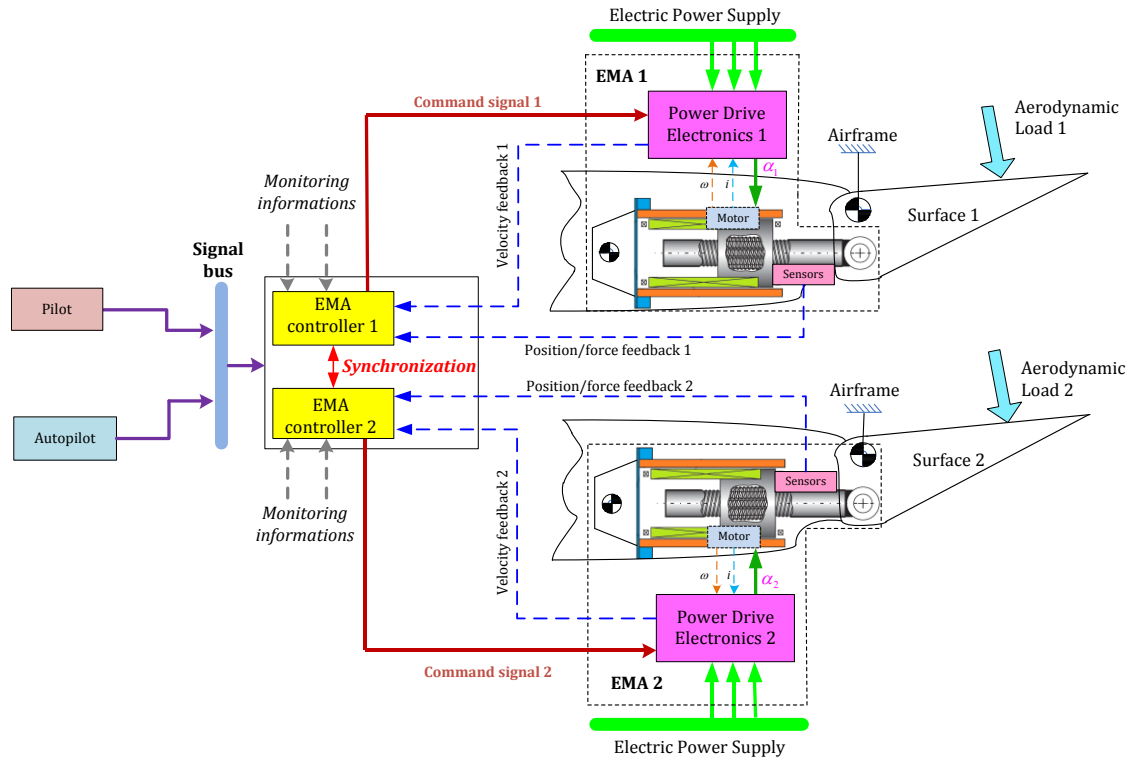


Fig.1-13 Architecture of electrical synchronization of EMAs for thesis study

The present application involves two identical EMAs. Therefore, virtual prototyping of individual EMA is firstly needed, which can support system-level design, development, integration and monitoring. However, there is a huge requirement for realistic models, which include the architecting (functional, conceptual then technological), sizing and specification of sub-systems (preliminary then detailed), and their integration, verification and validation (virtual then real) [27]. All these considerations motivated the work in this thesis, which has

the main objective of developing and implementing models that reproduce with realism the multi-domain cross-link disciplines. The models shall meet the system-level engineering needs and the associated constraints. In particular generic models shall be developed with progressive complexity and with same interfaces in order to make them easily replaceable.

1.3.1 Cross-linked Multi-domain Disciplines

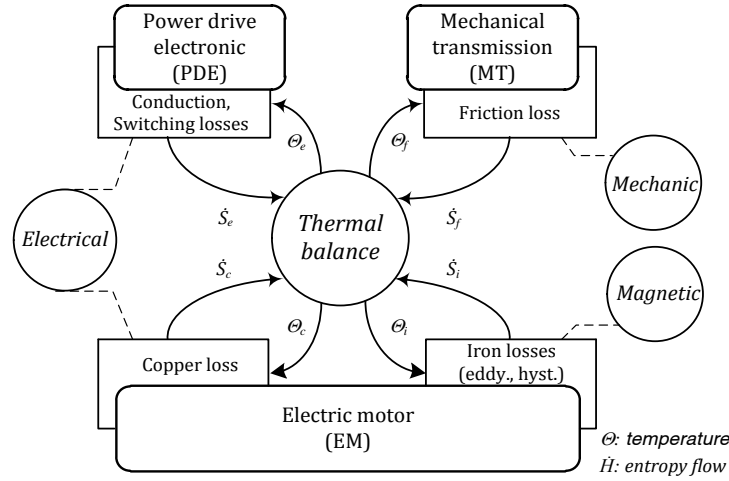


Fig.1-14 Multi-domain coupling of EMA system

Virtual prototyping of EMA system requires multidisciplinary approaches for preliminary power sizing and performance evaluation. The thermal effect is a key effect that drives sizing, performance and lifespan. Unlike a HSA, the heat generated by energy losses in EMAs has to be dissipated (or stored) at the actuator level, excepted in very specific applications where the actuator can be cooled by a dedicated liquid circuit. These energy losses come from switching in transistors (commutation losses), resistance of wires/windings and power electronics (copper and conduction losses), eddy currents and magnetic hysteresis (iron losses) in the motor, and friction losses between moving bodies. Most of these losses govern the thermal balance of the EMA as the heat they produce must be dissipated toward the local environment. Moreover, the sensitivity of energy losses to actual temperature may produce snowball effects that cannot be ignored. All these effects induce a strong multidisciplinary coupling among physical domains, as depicted by Fig. 1-14. The virtual prototype to be developed shall reproduce with realism the physical effects and their coupling in electric, magnetic, thermal and mechanical domains.

1.3.2 Model Architectures versus Engineering Needs

A lumped-parameters model suits well the need for system-level virtual prototyping. The model depends strongly on the needs of the current engineering task, the best model never being the most detailed one. For this reason, it is important to properly select the physical effects to be considered in order to get the right level of model complexity for model architecting. Meanwhile, the virtual prototyping of realistic consideration to physical effects has now become a practice way to work towards multiplicity of engineering needs, such as analysis of natural dynamics, thermal balance, energy losses, closed-loop controlled performance, component sizing, weight reduction, back-drivability, damping, soft endstop, tolerance or reconfiguration and faults to failure, etc. [27, 28]. However, these engineering needs require different cross-linked physical effects to be considered with different accuracy levels: indeed, the model complexity has to be adapted to the need in order to make simulation as rapid and as robust as possible [29].

Table 1-3 Model architectures of EMA power devices vs. engineering needs

Model Architectures	Engineering needs								
	Functional	Power sizing	Thermal balance	Natural dynamics	Stability accuracy	Consumed energy	Failure response	Load propagation	Reliability
PDE									
perfect transformer	Y	Y	Y	Y	Y	Y	Y	Y	Y
dynamic torque function	Y	N/A	N/A	P	Y	N/A	N/A	N/A	N/A
power source with losses	N/A	Y	Y	N/A	N/A	Y	P	N/A	N/A
EM									
perfect converter	Y	Y	Y	Y	Y	Y	Y	Y	Y
with power losses	N/A	Y	Y	Y	Y	Y	N/A	N/A	N/A
advanced model	N/A	Y	Y	P	P	Y	N/A	P	N/A
MPT									
perfect transformer	Y	Y	Y	Y	Y	Y	Y	Y	Y
with friction losses	N/A	Y	Y	Y	Y	Y	Y	P	P
with compliances	N/A	P	N/A	P	P	N/A	P	P	P
with faults injections	N/A	N/A	N/A	N/A	p	N/A	Y	N/A	Y

Note: Y means yes; P means possibly but depending on relative level; N/A means not applicable.

Typically, the EMA model can be developed for simulation aided conceptual design (architectures and function), control design, thermal balance, mean and peak power drawn,

etc. Since the level of detail is not obviously identical for each component of the EMA, it is proposed to decompose the EMA into three package models: Power Drive Electronics (PDE), Electric Motor (EM) and Mechanical Power Transmission (MPT) that also correspond to the physical elements of the EMA. Table 1-3 links the engineering tasks to the physical effects to be considered, following the proposed decomposition.

This approach requires the components' models to be made replaceable, whether each physical effect is considered or not.

1.3.3 Incremental Multi-level Modeling Based on Bond-Graph

There are two main options to develop a model of a system. The decremental approach consists in making the most complex model first then simplifying or reducing the model. The incremental approach is opposite. It consists in increasing progressively the model complexity. This second approach has been selected because it is consistent with the Systems Engineering process. Thus, we propose to use the incremental approach for each component which is associated with a dedicated package model. In any package, the models complexity is progressively increased but the interfaces of the models (signal and power ports) remain unchanged to ensure models' replaceability (as far as possible). In addition, it has been found important for an industrial use of the proposed models to develop them from combining and adapting the models that are available in the standard libraries of the commercial simulation software. In that way, risk and time are saved because the submodels are (supposed to be) tested, validated, documented, supported and numerically robust.

However the physical effects are always multi-domain cross-linked. Making the models balanced (in particular energetically) is an important target for assessing coupled effects (e.g. EMA temperature rise due to losses of power electronics). For this reason, using the Bond-Graph formalism is particularly interesting for model structure definition. By the above analysis based on Bond-Graph theory [30], the disciplines involved by EMA study in cross-linked multi-domains are shown in Fig. 1-15.

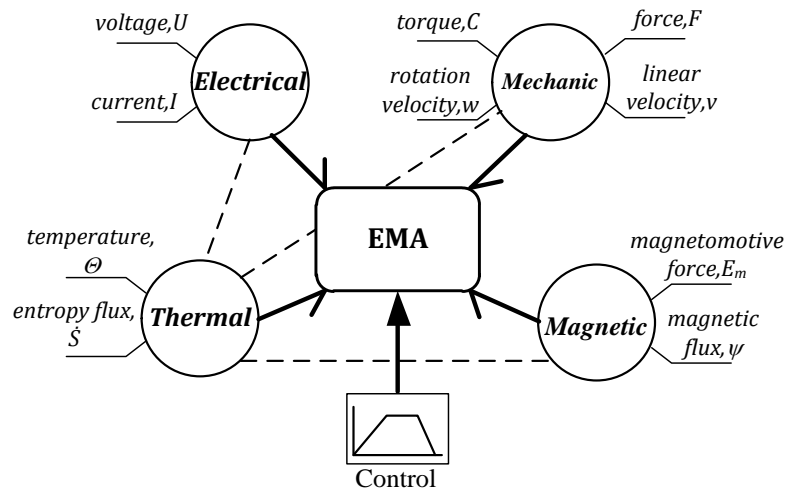


Fig.1-15 Multidisciplinary domain Bond-Graph power flow coupling in EMAs

According to the Bond-Graph formalism, the power bond is represented by a half arrow in order to distinguish it from signal flows and power flows. Each bond transports power as the product of two power variables which involves some different physical quantities as given in Tab. 1-4. The effort and the flow correspond to variables which product makes power.

Table 1-4 Bond-Graph variables

Physical domain	Effort(e)	Flow(f)
Electrical	Voltage(V)	Current(i)
Mechanic(rotation)	Torque(C)	Angular velocity(ω)
Mechanic(translation)	Force(F)	Velocity(v)
Magnetic	Magneto-motive force(E_m)	Magnetic flux(ψ)
Thermal	Temperature(Θ)	Entropy flow (\dot{S})

1.4 Performance Requirements

According to the former discussions, the EMA model to be developed shall meet the following requirements [27]:

➤ R1) Control design: the model shall enable the pursuit and rejection performances to be assured for individual EMA. It shall also enable the position synchronization function to be assessed, including in the presence of faults in the mechanical transmission of the actuator (other sources of faults are out of scope of the present work and have already generated huge quantity of research work).

- R2) Realism and Balance: The model shall reproduce, with a system-level view, the key physical effects should be considered. The model shall be balanced (mechanically, energetically, etc.).
- R3) Incremental and Progressivity: the model shall enable incremental modelling (including progressive levels with relevant complexity in response to the current engineering need).
- R4) Interface and Replaceability: The model shall have standard interfaces that are conserved throughout modelling levels. As far as possible, the model shall be made of a combination of generic sub-models that can be re-used for other modelling purposes.
- R5) Faults: the model shall enable ageing effects or faults to be simulated.
- R6) Causality: the model shall be developed to admit various causalities, which are consistent with in today's causal and non-causal simulation environments.

1.5 Conclusion of Chapter 1

The present chapter firstly introduced developments of actuation for flight controls with a special focus on power distribution, architectures and innovative technologies. Then the safety-critical requirements have been presented and the redundancy and need for position synchronization (including application examples) also have been introduced. The final part has been dedicated to the modelling and simulation needs for system-level virtual prototyping. It has been proposed to develop the models to meet the engineering needs, and to follow an incremental approach considering multi-domain physical effects, that need the support of the Bond-Graph formalism. A set of requirements have been generated that will be used along the thesis for EMAs applications.

References

- [1] O. Langlois, E. Foch, X. Roboam, and H. Piquet, "De l'avion plus électrique à l'avion tout électrique: état de l'art et prospective sur les réseaux de bord," *J3eA*, vol. 4, p. 001, 2005.
- [2] P. Wheeler, "The more electric aircraft: Why aerospace needs power electronics?," in *Proc. of the 13th Conf. on Power Electronics and Applications (EPE'09)*, 2009, pp. 1-30.
- [3] L. Wang, "Force equalization for active/active redundant actuation system involving servo-

- hydraulic and electro-mechanical technologies," Université de Toulouse, INSA Toulouse, 2012.
- [4] J. A. Weimer, "The role of electric machines and drives in the more electric aircraft," in *Electric Machines and Drives Conference, 2003. IEMDC'03. IEEE International*, 2003, pp. 11-15 vol.1.
 - [5] X. Roboam, B. Sareni, and A. D. Andrade, "More electricity in the air: Toward optimized electrical networks embedded in more-electrical aircraft," *Industrial Electronics Magazine, IEEE*, vol. 6, pp. 6-17, 2012.
 - [6] P. M. Churn, C. J. Maxwell, N. Schofield, D. Howe, and D. J. Powell, "Electro-hydraulic actuation of primary flight control surfaces," in *IEEE Colloquium on All Electric Aircraft (Digest No. 260)*, London, UK, 1998, pp. 3/1-3/5.
 - [7] C. Adams, "A380: 'More Electric' Aircraft," *Avionics Magazine*, vol. 25, pp. 44-48, 2001.
 - [8] S. J. Cutts, "A collaborative approach to the More Electric Aircraft," in *Power Electronics, Machines and Drives, 2002. International Conference on (Conf. Publ. No. 487)*, 2002, pp. 223-228.
 - [9] X. Le Tron, "Airbus, A380 Flight Controls Overview," ed, 2007.
 - [10] D. Van Den Bossche, "The A380 flight control electrohydrostatic actuators, achievements and lessons learnt," in *25th Congress of the International Council of the Aeronautical Sciences (ICAS)*, Hamburg, Germany, 2006, p. 1.
 - [11] A. Garcia, J. Cusido, J. Rosero, J. Ortega, and L. Romeral, "Reliable electro-mechanical actuators in aircraft," *Aerospace and Electronic Systems Magazine, IEEE*, vol. 23, pp. 19-25, 2008.
 - [12] J. W. Bennett, G. J. Atkinson, B. C. Mecrow, and D. J. Atkinson, "Fault-Tolerant Design Considerations and Control Strategies for Aerospace Drives," *IEEE Transactions on Industrial Electronics*, vol. 59, pp. 2049-2058, 2012.
 - [13] O. Cochoy, U. B. Carl, and F. Thielecke, "Integration and control of electromechanical and electrohydraulic actuators in a hybrid primary flight control architecture," in *International Conference on Recent Advances in Aerospace Actuation Systems and Components (R3ASC)*, Toulouse, 2007, pp. 1-8.
 - [14] G. Nfonguem, "Contribution au développement d'actionneurs plus électriques: modélisation inverse et composants mécaniques spécifiques à une application aéronautique," Toulouse, INSA, 2006.
 - [15] W. Karam, "Générateurs de forces statiques et dynamiques à haute puissance en technologie électromécanique," INSA Toulouse, Université de Toulouse, 2007.
 - [16] M. A. Siddiqui and M. S. Haq, "Review of Thrust Reverser Mechanism used in Turbofan Jet Engine Aircraft," *International Journal of Engineering*, vol. 6, pp. 717-726, 2013.
 - [17] F. google. (2012). *DC-10 Thrust Reverser Safety Enhancement*.
 - [18] M. Tursini, G. Fabri, E. Loggia, and M. Villani, "Parallel positioning of twin EMAs for Fault-Tolerant flap applications," in *Electrical Systems for Aircraft, Railway and Ship Propulsion (ESARS), 2012*, 2012, pp. 1-6.
 - [19] M. Recksiek, "Advanced high lift system architecture with distributed electrical flap actuation," in *Workshop on Aviation System Technology (AST)*, Hamburg, Germany, 2009.

- [20] T. Ford, "Tiltrotor progress," *Aircraft Engineering and Aerospace Technology*, vol. 71, pp. 42-47, 1999.
- [21] E. B. Carlson, "Optimal tiltrotor aircraft operations during power failure," University of Minnesota, 1999.
- [22] C. Wang, Z. Jiao, S. Wu, and Y. Shang, "An experimental study of the dual-loop control of electro-hydraulic load simulator (EHLS)," *Chinese Journal of Aeronautics*, vol. 26, pp. 1586-1595, 12// 2013.
- [23] B. MacIsaac and R. Langton, *Gas Turbine Propulsion Systems*: John Wiley & Sons, 2011.
- [24] J. W. Bennett, "Fault Tolerant Electromechanical Actuators for Aircraft," 2010.
- [25] M. Christmann, S. Seemann, and P. Jänker, "Innovative Approaches to Electromechanical Flight Control Actuators and Systems," in *International Conference on Recent Advances in Aerospace Actuation Systems and Components (R3ASC)*, Toulouse, 2010, pp. 17-23.
- [26] F. Claeysen, P. Jänker, R. LeLetty, O. Sosniki, A. Pages, G. Magnac, *et al.*, "New Actuators for Aircraft, Space and Military Applications," in *Proceedings of ACTUATOR 2010, 12th International Conference on New Actuators*, 2010, pp. 324-330.
- [27] J.-C. Maré, "Requirement-based system-level simulation of mechanical transmissions with special consideration of friction, backlash and preload," *Simulation Modelling Practice and Theory*, vol. 63, pp. 58-82, 4// 2016.
- [28] J.-C. Maré, "Best practices in system-level virtual prototyping - application to mechanical transmission in electromechanical actuators," in *5th International Workshop on Aircraft System Technologies*, Hamburg, 2015.
- [29] J.-C. Maré and J. Fu, "Best practices in modelling and simulation applied to aerospace electromechanical actuators," presented at the 2015 European Aerospace Engineering Conference, Toulouse, 2015.
- [30] D. C. Karnopp, D. L. Margolis, and R. C. Rosenberg, *System dynamics: modeling, simulation, and control of mechatronic systems*, 5th ed. New York: John Wiley & Sons, 2012.

Chapter 2

Individual EMA Controller Design

As mentioned in chapter 1, the objective of the thesis is to develop knowledge models for model-based synthesis of synchronized position control of twin EMAs driving independent loads. The performance evaluation of individual EMA position control is important and synchronization position is a further objective. Therefore, the first step is to design the position controller for individual EMA. The linear approach is used first, on basis on conventional multiple feedback structure for cascade controller. However, given the aerospace application, several constraints should be considered with care during the controller design. This concerns in particular the torque and velocity saturations and the parasitic mechanical compliances coming from the actuator itself or from the airframe and the driven load (non-infinite anchorage and attachment stiffness). The proposed complete individual position controller is validated in a first step using a realistic virtual prototype.

2.1 Individual EMA System Description

This study deals with a direct drive type linear EMA. In such an “in-line” EMA, the motor rotor is integrated with the rotating part of the nut-screw. The absence of gear reduction saves weight and offers a high potential of geometrical integration. This design is attractive for aerospace applications because the actuator is compact and easily integrated within the airframe when the available geometrical envelope is reduced. The schematic of such an EMA is described by Fig. 2-1. When applied to flight controls the load is the flight control surface on which the aerodynamic forces apply. This schematic is also valid for landing gear actuation applications. In this case the load is the landing gear leg for extension/retraction or the turning tube for steering.

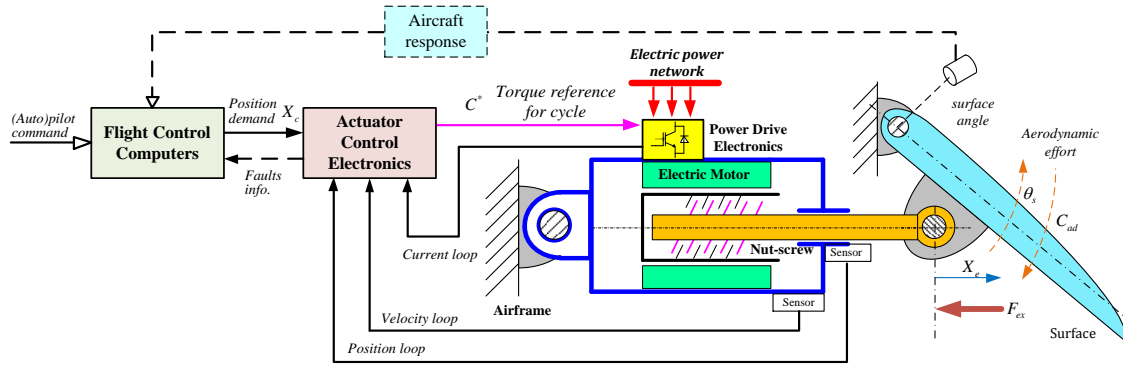


Fig. 2-1 Schematic architecture of an EMA actuation system

The electric power comes from the aircraft power network. Power delivered to the driven load is metered by the power drive electronics (PDE) according to the command reference signal. The electric power is transformed into mechanical power by a rotary electric motor which transfers the mechanic power to the control surface directly through a nut-screw mechanism. The individual EMA actuation system has two inputs. One is functional: the motor torque demand C^* . The other is an external force disturbance F_{ex} that comes essentially from the aerodynamic torque on the surface C_{ad} created by the airflow on the control surface. The output of the actuator is the linear displacement X_c , which produces the surface deflection angle θ_s thanks to the lever arm effect produced by the 3-arm kinematics of the actuator integration (the actuator is kinematically equivalent to a piloted-length arm).

2.1.1 Basic Components

In this study, it is considered that the flight control EMA consists of the following components:

- an aircraft control (A/C) unit which performs a closed loop position control,
- a power drive electronics (PDE) which meters the power delivered to the motor from the electric supply,
- an electric motor (DC or 3-phase BLDC/PMSM) that transforms power between the electrical and the mechanical rotational domains,
- a nut-screw (NS) mechanical transmission that transforms power between the high speed/low torque rotational and the low velocity/high force translational domains,

- sensors of current, speed, position and eventually force to load,
- a flight control surface which transforms power between rod translation and surface rotation, through a lever arm effect.

2.1.2 Control Structure

The EMA is a position servoloop that shall follow the pilot or autopilot demand (pursuit) and reject the disturbance (regulation) that is generated by the aerodynamic actions. The common way to control the EMA is to use a cascade structure. It involves three basic loops: the current (inner) loop, the velocity (middle) loop and the position (outer) loop. If needed, a force sensor can be inserted between the EMA rod and the flight control surface in order to meet the rejection performance through an additional force feedback [1]. The controller design is generally based on the linear approach and involves proportional and integral serial correctors. However, a particular attention has to be paid to the structural compliances and to the power saturations (voltage and current). This part of our research work has been reported in [2].

As EMAs naturally include the above mentioned sensors for the position control loop, it becomes possible to develop and implement Health and Usage Monitoring (HUM) functions. Health monitoring is currently investigated to prevent a hard failure (e.g. jamming, free-run or motor-windings short-circuit) and to allow on-condition maintenance. On its side, usage monitoring enables the designers to get experience feedback on the real service of the EMA components to better adapt the design rules and the scheduled maintenance intervals. For this reason, the motor control electronics is usually also in charge of running the HUM algorithms and to report the EMA faults to the FCCs.

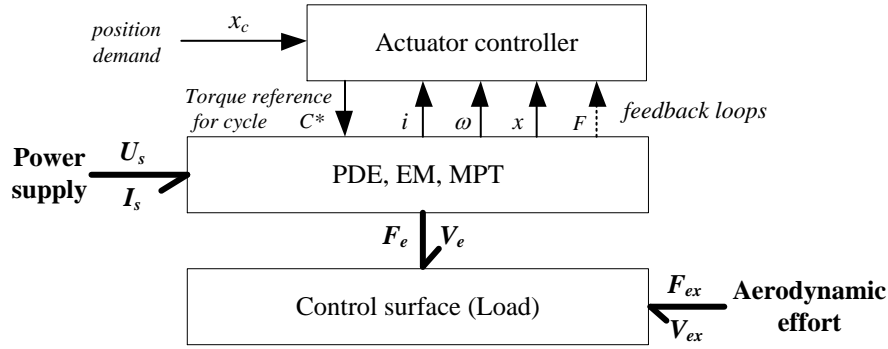


Fig. 2-2 Synoptic control structure of EMA system

The synoptic control structure of the EMA is shown in Fig. 2-2 where signal and power flows are explicitly differentiated. According to the Bond-Graph formalism, power flows are represented using a half-arrow which carries the two power variables (e.g. voltage and current, force and velocity). Full arrows indicate a signal flow which carries only one type of information.

In order to facilitate integration, the actuator uses its own position sensor to perform the position control loop. This sensor measures the rod extension relative to the actuator housing, usually with a linear variable displacement transducer (LVDT). However, a load angular position sensor is also generally installed but is it used only for monitoring purposes. The motor angular position and velocity can be measured by an integrated resolver (PMSM motors) or by on-off Hall sensors (BLDC motors). An equivalent linear EMA system with the conventional cascade control architecture is displayed in Fig. 2-3.

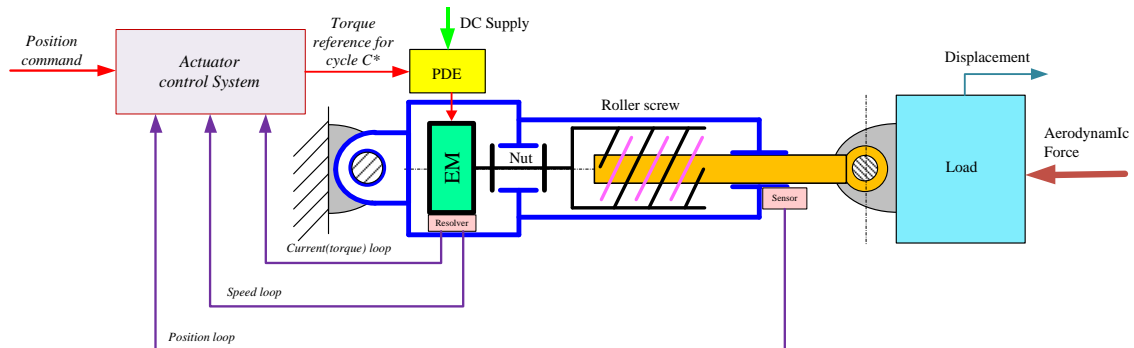


Fig. 2-3 Control structure for a linear EMA system

2.2 Linear Virtual Prototype

As done conventionally, the linear approach enables the control designer to employ the open-loop model of the system under study (the EMA) to set the controller parameters in order to get the desired closed-loop performance (rapidity, stability, accuracy).

2.2.1 Simplifications and Assumptions

The challenge of modelling for control design consists in balancing simplicity and realism. In the following approach, the objective is to get an analytical model that enables getting formally the contribution of each control loop to the closed-loop performance. In order to get a low order model of EMA the simplifications and assumptions are considered consequently:

- The bandwidth of the PDE and the current loop of the motor are much higher (typically 500Hz-1KHz) as compared to the position and velocity loops, so it can be neglected here in a first approach.
- There is no parasitic compliance inside the actuator and all the structure compliances are neglected.
- Motor and nut-screw inertia are merged into a single lumped inertia, while the rod mass is neglected.
- Friction effects are neglected. This can be seen as the worst case for stability as all the damping effect has to be created “electrically” by the velocity feedback.
- The backlash and preload in the EMA kinematics are neglected.
- Power limitations and saturations are neglected.
- The digital signal effects (delay, sampling, quantizing, etc.) are neglected.

The schematic of EMA simplified model with its control system is shown in Fig. 2-4. However, when the current loop is ignored, the input of the motor (actually its mechanical part) becomes the electromagnetic torque C_{em} . If torque saturation of the motor is not considered, the electromagnetic torque C_{em} is equal to the command signal C^* elaborated by of the velocity controller.

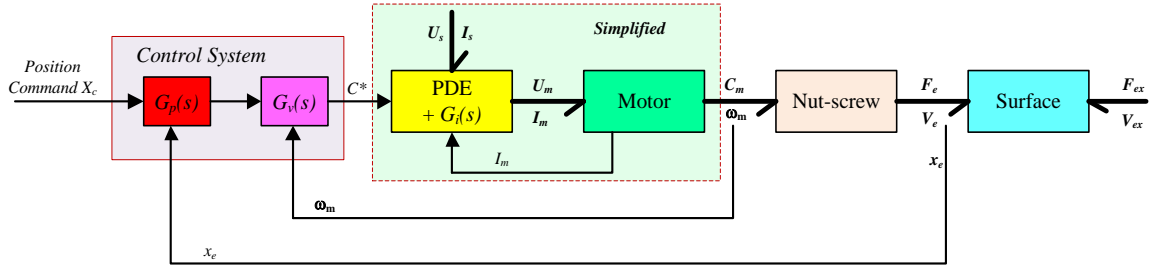


Fig. 2-4 Simplified EMA model by word Bond-Graph

2.2.2 Conventional Controller Design

(1) Open Loop Model

The torque balance at the motor shaft is:

$$C_m = C_{em} - J_m \dot{\omega}_m \quad (2.1)$$

C_m	Torque output of motor shaft [Nm]	C_{em}	Motor electromagnetic torque [Nm]
J_m	Motor rotor inertia [kgm ²]	ω_m	Motor angular velocity [rad/s]

The mechanical power transferred from rotational motion into translational one through the nut-screw is:

$$\begin{cases} V_e = \frac{p}{2\pi} \omega_m \\ F_e = \frac{2\pi}{p} C_m \end{cases} \quad (2.2)$$

V_e	EMA output linear velocity [m/s]	p	Lead of roller screw [m]
F_e	EMA output force [N]		

The surface dynamics equation can be expressed as:

$$F_e - F_{ex} = M_s \ddot{X}_s \quad (2.3)$$

F_{ex}	Aerodynamic action force [N]	M_s	Equivalent flight surface mass [kg]
X_s	Equivalent surface linear displacement [m]		

For small angular displacements of the surface (aileron) around the neutral position, it can be assumed that:

$$X_s = X_e \quad (2.4)$$

X_e EMA rod displacement [m]

Applying Laplace transform to the upper equations (2.1) to(2.4), the displacement X_s can be expressed as:

$$X_s(s) = \frac{\frac{2\pi}{p} C^*(s) - F_{ex}(s)}{\left(\frac{4\pi^2}{p^2} J_m + M_s \right) s^2} \quad (2.5)$$

s Laplace variable [-]

It is worth mentioning that equation (2.5) shows that even a small motor inertia will reflect a huge equivalent mass (because p is very small) at the EMA rod level, which strongly affects the system dynamic performance:

$$M_m = \frac{4\pi^2}{p^2} J_m \quad (2.6)$$

M_m Mass reflected at load level by the motor
rotor inertia [kg]

Also equation (2.5) shows that the open loop of the EMA linear model is a second order system, with a double pole at origin (double integrator). The absence of damping is explained by the deliberate omission of the viscous friction, which corresponds to the worst case scenario regarding stability. The equivalent block diagram of the open loop EMA linear model can be presented in Fig. 2-5, where $H_a(s)$ is the adjusting transfer function; $H_d(s)$ is the disturbance transfer function.

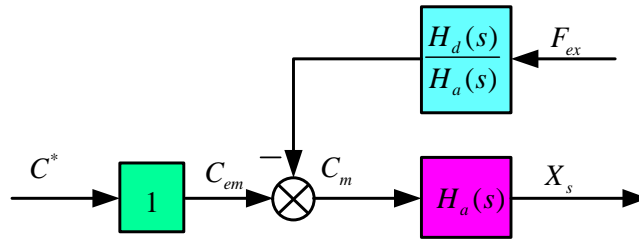


Fig. 2-5 Bloc diagram of open loop EMA linear model

Then equation (2.5) is expressed as:

$$X_s = H_a(s)C^* - H_d(s)F_{ex} \quad (2.7)$$

The adjusting chain transfer function $H_a(s)$:

$$H_a(s) = \frac{X_s}{C^*} = \frac{1}{\frac{p}{2\pi} \left(M_s + \frac{4\pi^2}{p^2} J_m \right) s^2} \quad (2.8)$$

The adjusting chain transfer function $H_d(s)$:

$$H_d(s) = \frac{X_s}{F_{ex}} = \frac{1}{\left(M_s + \frac{4\pi^2}{p^2} J_m \right) s^2} \quad (2.9)$$

(2) Cascade Controller

On the basis of the EMA open-loop linear model analysis, (no damping and poor natural dynamics), a simple proportional position controller cannot meet the closed-loop requirements. One of the common ways to get around this problem is to design a proportional derivative (PD) position controller, as illustrated in Fig. 2-6.

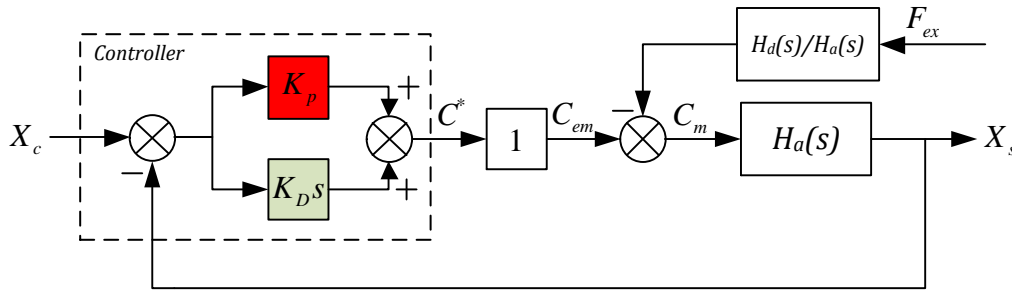


Fig. 2-6 PD position controller for EMA closed-loop control

Another way for EMA closed-loop control design is to introduce a speed loop, as in Fig. 2-7.

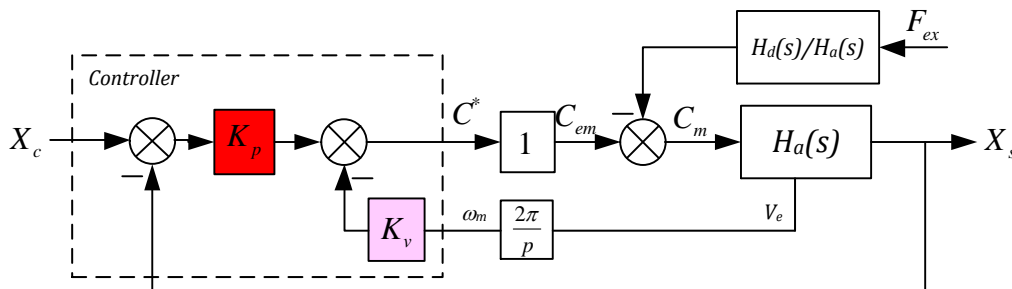


Fig. 2-7 Speed feedback controller for EMA closed-loop control

$$X_s(s) = \frac{X_c(s) - \frac{p}{2\pi K_p} F_{ex}(s)}{\frac{1}{K_p} \left(\frac{pM_s}{2\pi} + \frac{2\pi J_m}{p} \right) s^2 + \frac{2\pi K_v}{pK_p} s + 1} \quad (2.10)$$

X_c	EMA position command [m]	K_p	Position controller gain [Nm/m]
K_v	Velocity controller gain [Nm/(rad/s)]		

2.2.3 Performance Requirements

Generally, the regarded performance requirements for closed-loop control systems are mainly:

- ✓ Stability
- ✓ Rapidity
- ✓ Accuracy for position pursuit and rejection of airload disturbance.

For second order systems, the dynamic performance is completely characterized by two parameters: the damping ratio ξ and the natural angular frequency ω_n . In the present case, they can be expressed as:

$$\begin{cases} \xi = \frac{K_v}{\sqrt{K_p}} \frac{1}{\sqrt{\frac{p^3}{2\pi^3} (M_s + M_m)}} \\ \omega_n = \frac{\sqrt{K_p}}{\sqrt{\frac{p}{2\pi} (M_s + M_m)}} \end{cases} \quad (2.11)$$

ξ	Damping factor [-]	ω_n	Natural frequency [rad/s]
-------	--------------------	------------	---------------------------

For a set of required dynamic performance, imposed by the parameters $\hat{\xi}$ and $\hat{\omega}_n$, the control parameters K_p and K_v , can be obtained from above equation (2.11) as:

$$\begin{cases} K_p = \hat{\omega}_n^2 \frac{p}{2\pi} (M_s + M_m) \\ K_v = 2\hat{\xi}\hat{\omega}_n \left(\frac{p}{2\pi} \right)^2 (M_s + M_m) \end{cases} \quad (2.12)$$

$\hat{\xi}$	Desired damping factor [-]	$\hat{\omega}_n$	Desired natural frequency [rad/s]
-------------	----------------------------	------------------	-----------------------------------

For a second order system, when the desired damping ratio equals 0.707, a compromise is got between stability and rapidity. The system is stable with an overshoot about of 5% that minimizes the response time t_s at $\pm 5\%$

$$\text{if } \hat{\xi} = 0.707 \Rightarrow \hat{t}_s = \frac{2.9}{\hat{\omega}_n} \quad (2.13)$$

t_s Response time [s] |

In the frequency domain this maximizes the bandwidth without resonance.

Moreover, from equation (2.10) it follows that for a step set-point input, the system static error is zero. The same conclusion can be drawn from the fact that there is a pure integrator in the outer open loop.

$$\varepsilon_p = 0 \quad (2.14)$$

ε_p Static error under step demand [m] |

The tracking error under ramp demand is given by:

$$\varepsilon_v = \frac{2\pi K_v}{p K_p} V_r \quad (2.15)$$

ε_v Tracking error under ramp demand [m] | V_r Ramp velocity demand [m/s]

In addition, the position error under constant airload disturbance can be expressed as:

$$\varepsilon_d = \frac{p}{2\pi K_p} F_{ex} \quad (2.16)$$

ε_d Static disturbance error [m] |

Therefore, for the disturbance rejection point of view, the closed-loop EMA behaves at low frequency, in response to airload and a constant position demand, as an equivalent spring having a stiffness of:

$$k_e = \frac{2\pi K_p}{p} \quad (2.17)$$

$$K'_p \quad \text{Position controller gain considering saturations [(rad/s)/m]} \quad \left| \quad K'_v \quad \text{Velocity controller gain considering saturations [Nm/(rad/s)]} \right.$$

When the set-point amplitude is X_c and the control system is unsaturated, the speed and torque reference are given as:

$$\begin{cases} \omega_r = K'_p (X_c - X_s) \\ C_r = [K'_p (X_c - X_s) - \omega_m] K'_v \end{cases} \quad (2.19)$$

$$\omega_r \quad \text{Velocity reference from position controller [rad/s]} \quad \left| \quad C_r \quad \text{Torque reference from velocity controller [Nm]} \right.$$

This helps defining reference values of torque and speed for analyzing the effect of saturations. Therefore, the maximum velocity ω_{rmax} and torque C_{rmax} are defined by the given input magnitude X_{cmax} as:

$$\begin{cases} \omega_{rmax} = K'_p X_{cmax} \\ C_{rmax} = K'_p K'_v X_{cmax} \end{cases} \quad (2.20)$$

$$\omega_{rmax} \quad \text{Maximum velocity reference from position controller [(rad/s)/m]} \quad \left| \quad C_{rmax} \quad \text{Maximum torque reference from velocity controller [Nm]} \right.$$

In order to evaluate the influence of these saturations on the closed loop performance, the importance of speed saturation and torque saturation are defined by the ratio α_ω and α_c as:

$$\alpha_\omega = \frac{\omega_{lim}}{\omega_{rmax}} \in [0, 100\%] \quad (2.21)$$

$$\alpha_c = \frac{C_{lim}}{C_{rmax}} \in [0, 100\%] \quad (2.22)$$

$$\begin{array}{ll} \omega_{lim} & \text{Velocity saturation for motor safety [rad/s]} \\ \alpha_\omega & \text{Motor velocity saturation ratio [-]} \end{array} \quad \left| \quad \begin{array}{ll} C_{lim} & \text{Torque saturation for motor safety [Nm]} \\ \alpha_c & \text{Torque saturation ratio [-]} \end{array} \right.$$

A torque saturation ratio of 10% means that the saturation setting C_{lim} represents a tenth of the maximal unsaturated torque while 100% means that there is no torque saturation. The same holds for the speed saturation.

2.3.2 Example and Numerical Simulation

The speed and torque saturation ratios were varied. For each value of the saturation ratios,

different values of the motor rotor inertia, the lead of nut-screw and the desired closed-loop natural frequency were tested as well. The models with and without saturations (no speed, no torque saturations) were simulated as a function of the speed saturation and torque saturations to trace:

-The impact on the response time. This impact is quantified by calculating $\log(t_{ss}/t_{su})$ where t_{ss} is the response time with saturation and t_{su} is the response time without saturation, as it can be seen in Fig. 2-10.

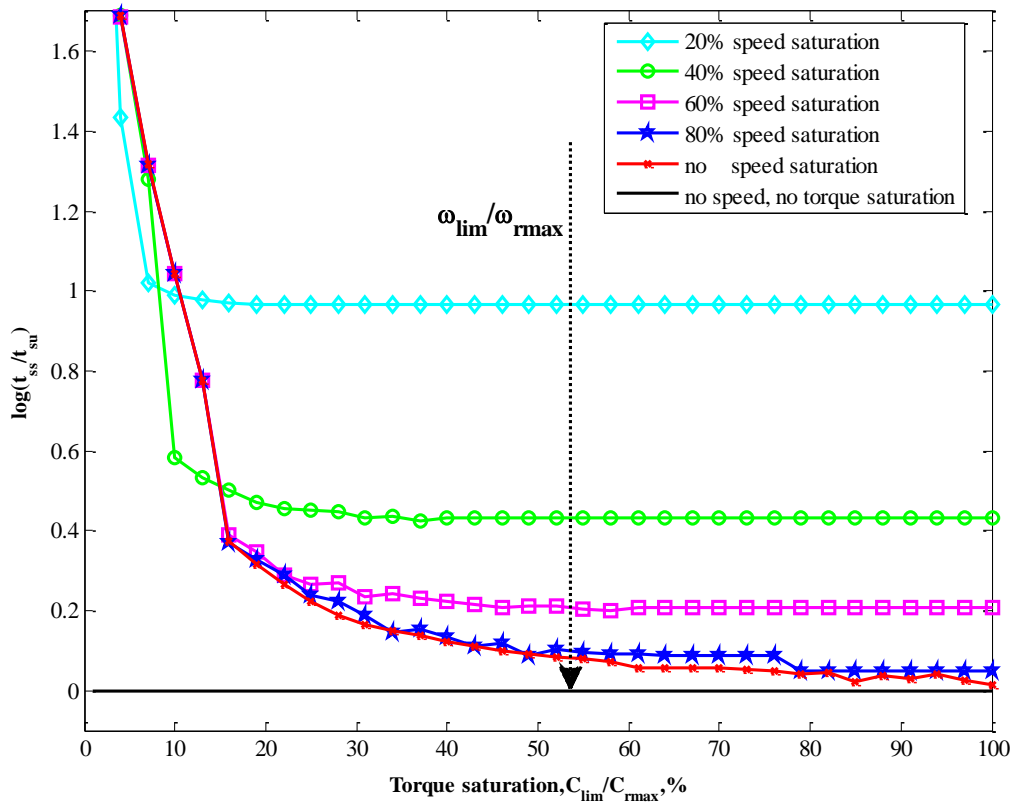


Fig. 2-10 Dimensionless response time depending on torque and speed saturations

-The impact on first overshoot. This impact is quantified by calculating $\log(\sigma_{ps}/\sigma_{pu})$ where σ_{ps} is the first overshoot with saturation and σ_{pu} is the first overshoot without saturation, displayed in Fig. 2-11.

It turns out that inertia, nut-screw lead and the closed-loop natural frequency do not have any impact on the curves presented in Fig. 2-10 and Fig. 2-11 (K'_p and K'_v are automatically recalculated for the new set of parameters according to Eq. (2.18) that applies for unsaturated EMA).

Figure 2-10 and Figure 2-11 show that in the absence of torque saturation ($\alpha_c = 100\%$) the overshoot decreases and the response time increases when speed saturation becomes more important (low speed saturation ratios). When $\alpha_\omega = 40\%$, overshoot reduces by 45% while response time increases by 53%. The effect of torque saturation starts to influence the response time for torque saturation ratio $\alpha_c < 0.5$ and becomes significant for $\alpha_c < 0.2$. Even in the absence of speed saturation, the response time is increased by 46% when the torque saturation ratio is 15%.

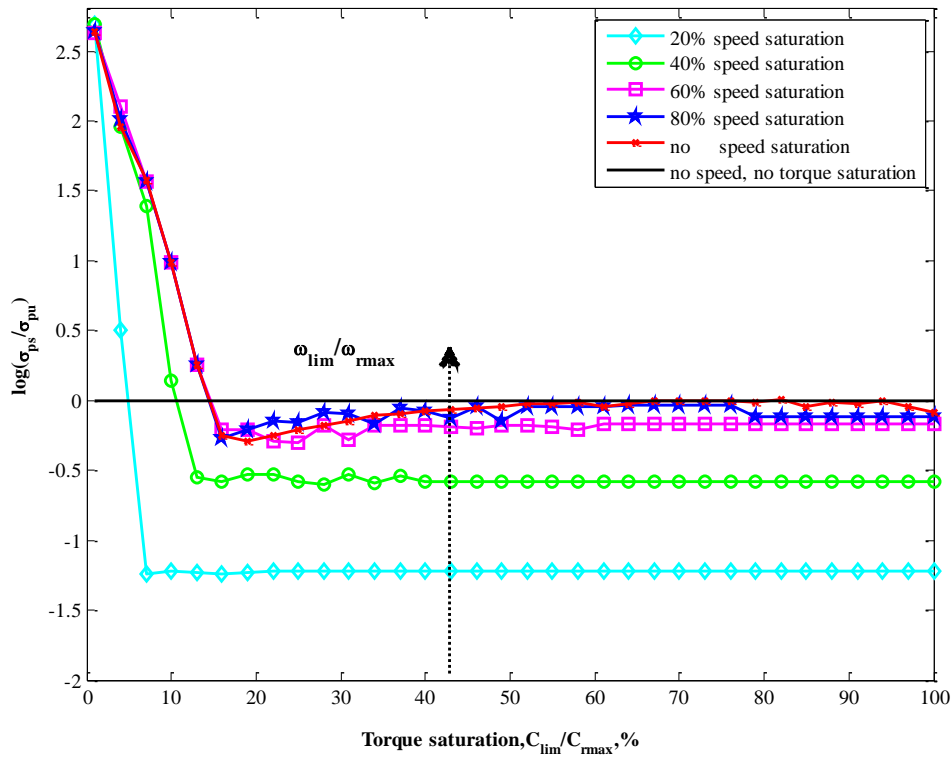


Fig. 2-11 Dimensionless first overshoot depending on torque and speed saturation

In practice, these plots provide useful information for preliminary design to assess the impact of speed and torque saturations for a given magnitude of the position step demand.

2.4 Motor Current Loop Effects

In previous sections, the electric motor in EMA was assumed to act as a perfect power transformer; the imperfections of resistance and inductance are neglected. Also, the inner current loop which is implemented in the power drive electronics was assumed to behave as a unity gain.

2.4.1 Motor Electrical Effects

Nowadays, highly efficient and reliable electrical technologies are available in EMAs for aerospace applications, that use 3-phase motors (BLDC or PMSM) [3]. Both BLDC and PMSM can be simplified as an equivalent brushed DC motor for simulation and analysis purposes. The electromotive force balance equations concerning the motor electrical circuit is

$$U_m = U_{em} + R_m I_m + L_m \frac{dI_m}{dt} \quad (2.23)$$

U_m	Electric motor voltage [V]	U_{em}	Back-electromotive force (EMF) [V]
I_m	Electric motor current [A]	R_m	Motor windings resistance [Ω]
L_m	Motor windings inductance [H]		

The torque balance referred to the motor shaft is

$$C_m = C_{em} - J_m \frac{d\omega_m}{dt} - C_{fm} \quad (2.24)$$

C_m	Motor output torque [Nm]	C_{em}	Motor electromagnetic torque [Nm]
C_{fm}	Motor friction torque [Nm]		

The back electromotive force and the electromagnetic torque are given by

$$E_m = K_m \omega_m \quad (2.25)$$

$$C_{em} = K_m I_m \quad (2.26)$$

K_m	Motor torque constant [Nm/A] or [V/(rad/s)]
-------	---------------------------------------------

2.4.2 Motor Current Loop and PI Controller

The structure of field-oriented control (FOC) of 3-phase motors is displayed on Fig. 2-12 which shows the direct and inverse Park transforms [4], used to change between the 3 phases space and the d-q space.

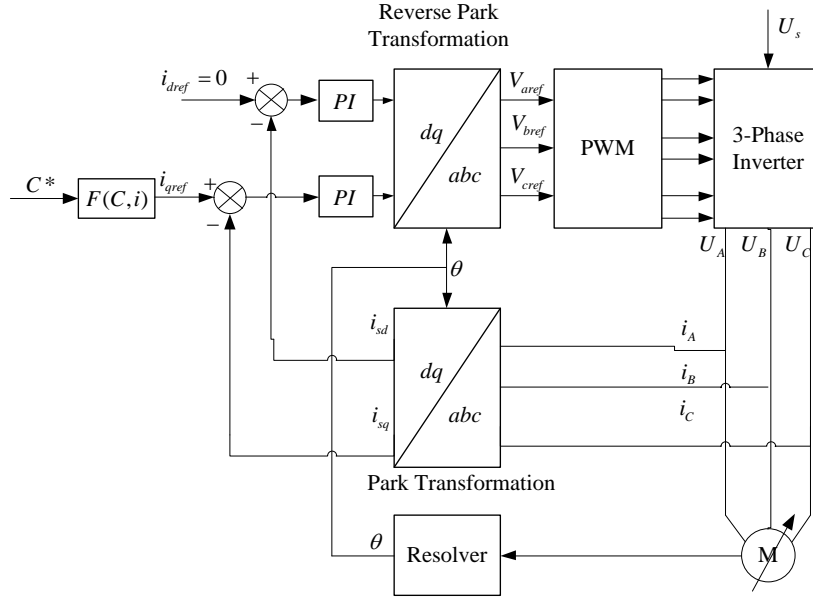


Fig. 2-12 Schematic diagram of FOC control for 3-phase motor

Proportional plus integral (PI) controllers are used to perform the current loops. The bandwidth of the current loop is much higher than the one in the speed and position loops. For this reason, the dynamics of the current loop can be neglected for preliminary studies [5], assuming the effective motor current I_m equals the demanded current I^* .

In a more detailed approach, the current loop is introduced by considering an equivalent brushed DC motor with rotor windings that can be described by a first order transfer function $G_m(s)$:

$$G_m(s) = \frac{I_m}{U_m} = \frac{1}{R_m + L_m s} \quad (2.27)$$

The motor electric time constant can be given as:

$$\tau_e = \frac{L_m}{R_m} \quad (2.28)$$

The current controller $G_i(s)$ by using PI structure, is given in the Laplace domain by:

$$G_i(s) = K_{ip} + \frac{K_{ii}}{s} \quad (2.29)$$

The current controller time constant can be given as:

$$\tau_i = \frac{K_{ip}}{K_{ii}} \quad (2.30)$$

K_{ip}	Current controller proportional gain [V/A]	K_{ii}	Current controller integral gain [V/As]
τ_e	Motor electric time constant [s]	τ_i	Current controller time constant [s]

Therefore, for EMA system, the control block diagram for the current loop and electrical circuit of the motor can be simplified as shown in Fig. 2-13.

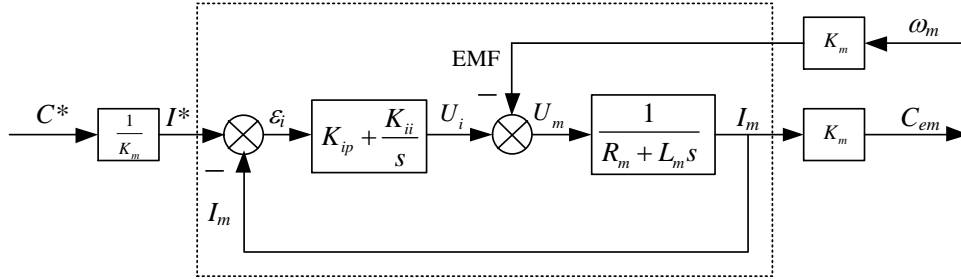


Fig. 2-13 Simplified block diagram of current loop of the motor

On the basis of block diagram in Fig. 2-13, the voltage balance equation of motor current loop can be written as:

$$(I^* - I_m)(K_{ip} + \frac{K_{ii}}{s}) - K_m \omega_m = I_m (R_m + L_m s) \quad (2.31)$$

I^* Reference current command [A]

In practice, the conventional motor control method to avoid current loop overshoot, which causes the large current that impacts the power drive electronics (PDE), is usually to set an over damped system for the current loop. In this case the PI coefficients are designed to satisfy the following relationship:

$$\frac{K_{ip}}{K_{ii}} = \tau_i = \tau_e = \frac{L_m}{R_m} \quad (2.32)$$

Thus, the closed loop function of current loop for motor becomes

$$I_m(s) = \frac{1}{1 + \frac{R_m}{K_{ii}} s} I^* - \frac{K_m s}{K_{ii} (1 + \frac{R_m}{K_{ii}} s)(1 + \tau_e s)} \omega_m(s) \quad (2.33)$$

For pursuit performance, when the disturbance ω_m is zero, the current loop can be considered as a first order transfer function, with an equivalent time constant expressed as:

$$\tau_c = \frac{1}{\omega_c} = \frac{R_m}{K_{ii}} \quad (2.34)$$

τ_c Current loop time constant [s] | ω_c Current loop break frequency [rad/s]

Thus, with PI controller, the step response of the current loop should be monotonically increasing, without overshoot and with a response time t_{cs} of about:

$$t_{cs} = 3\tau_c = \frac{3R_m}{K_{ii}} \quad \text{or} \quad \frac{3L_m}{K_{ip}} \quad (2.35)$$

t_{cs} Current loop response time [s]

In addition, considering the current control input $I^*=0$, based on the Final Value Theorem, the static error due to velocity disturbance step (value of ω_{m0}) is:

$$\lim_{t \rightarrow \infty} I_m = \lim_{s \rightarrow 0} s \frac{-K_m s}{K_{ii} (1 + \frac{R_m}{K_{ii}} s)(1 + \tau_e s)} \frac{\omega_{m0}}{s} = 0 \quad (2.36)$$

ω_{m0} Velocity disturbance step Value [rad/s]

Remark: From the above Eq.(2.36), it is known that the disturbance ω_m in current loop at low frequency can be ignored. However, the high dynamic effect cannot be neglected because of τ_c and τ_e .

Applying the Initial Value Theorem to calculate the initial current produced by a velocity step at null current demand gives a null value when Eq. (2.33) is used. In order to estimate the peak value of the current error, the following assumption is made. In practice, the setting of the PI current controller makes the current closed loop time constant τ_c far smaller than the motor electric time constant τ_e . Therefore when $I^*=0$, the motor velocity disturbance in equation (2.33) can be estimated assuming:

$$I_m(s) \approx \frac{-K_m s}{K_{ii} (1 + \tau_e s)} \omega_m(s) |_{I^*=0} \quad (2.37)$$

Also for a step input of motor velocity, the initial disturbance error can be expressed as:

$$\lim_{t \rightarrow 0} I_m = \lim_{s \rightarrow \infty} s \frac{-K_m s}{K_{ii} (1 + \tau_e s)} \frac{\omega_{m0}}{s} = \frac{K_m}{K_{ip}} \omega_{m0} \quad (2.38)$$

(as far as the PI current controller is set to make $\frac{R_m}{K_{ii}} \ll \tau_e$)

Equation (2.38) shows that with current PI controller there will be an initial error due to the motor velocity disturbance. It can be reduced by increasing the controller gain K_{ip} , but cannot be eliminated. Therefore, in practice, a velocity feedforward controller, or back emf compensation, is introduced to eliminate this effect [6].

2.4.3 Example and Numerical Simulation

The proposed rules of current PI coefficients setting have been verified through simulation of the EMA model in the MATLAB-Simulink environment, according to the structure of Fig. 2-13. An example from Exlar EMA, the motor parameters are shown in Tab. 4-6.

Table 4-6. EMA motor parameters [7]

Parameter	Value	Parameter	Value
Motor windings resistance R_m (Ω)	1.77	Motor torque constant K_m (Nm/A)	1.65
Motor winding inductance L_m (H)	$6.78 \cdot 10^{-3}$		

From Tab. 4-6, the motor electric time constant τ_e gives 3.8 ms, and the current PI controller gains K_{ip} and K_{ii} can be set to satisfy the rule in equation. (2.32). However, different combinations of K_{ip} and K_{ii} are possible for the same $\tau_i = 3.8$ ms. For simulation study, the motor current step demand I^* is 6 A at $t = 0.01$ s, and the motor velocity step as the perturbation occurred at $t = 0.1$ s with value $\omega_{m0} = 1000$ rpm (104.7 rad/s).

In the following, a numerical simulation is carried out in order to study the effects of K_{ip} and K_{ii} on the motor velocity. A first simulation used a set of current controller gains $K_{ip} = 67.8$ V/A, $K_{ii} = 1.77 \cdot 10^4$ Vs⁻¹/A (for $\tau_i = \tau_e = 3.8$ ms). Then, other 2 simulations were run where K_{ip} and K_{ii} were set to be 5 times bigger and 5 times smaller than the ones used in the first simulation, but which had the same $\tau_i = 3.8$ ms.

Figure 2-14 shows that greater K_{ip} and K_{ii} make the current response faster, which is also verified theoretically by Eq. (2.35). Greater K_{ip} and K_{ii} also make better rejection of the motor velocity disturbance, which is agreement with the Eq. (2.38).

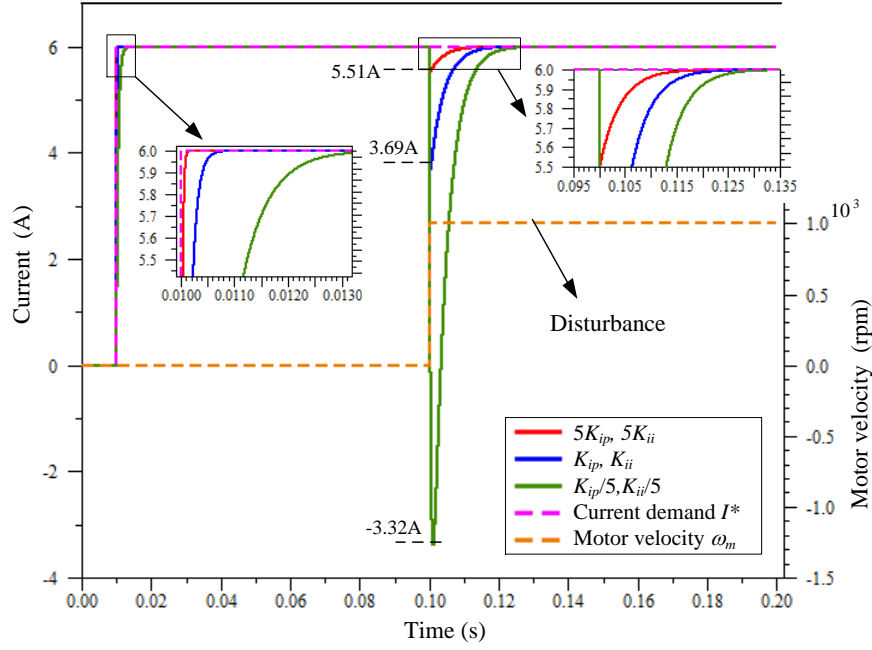


Fig. 2-14 Motor current response under different current PI controller gains

Next, the robustness of the current control is considered with respect to the variation of the electric resistance of the motor windings. Actually, the copper has a temperature coefficient of resistivity of about $3.9 \cdot 10^{-3}/^{\circ}\text{C}$ [8]. This means that for a temperature elevation of 100°C the resistance of a copper winding will change by 39%. The variation of motor resistance will change the electric time constant τ_e , so the latter will not match anymore the time constant τ_i of the current controller. Consequently, this may change the dynamics of the current loop given in Eq. (2.33). In order to assess the impact of the motor resistance variation, we conducted a simulation study based on the same current, I^* , and velocity, ω_m , excitations as above. Considering the initial value of R_m at initial temperature of 25°C , when the operating temperature varies from -40°C to 90°C , the R_m varies in the range of about -25% to +25%.

Simulation results in Fig. 2-15 firstly show that with the increase of the operating temperature in the EMA, the current loop time response becomes smaller, but the peak value due to disturbance rejection is slightly smaller as well. When the operating temperature is much lower, the current loop has an overshoot and a slightly greater peak value for disturbance rejection. Secondly, at operating temperature of 25°C , according to the Eq. (2.38), the estimated peak current produced by a step velocity of 1000 rpm ($\omega_{m0} = 104.7 \text{ rad/s}$) is -2.55 A. It makes the current dropping from 6 A to 3.45 A. The simulation value is 3.69 A.

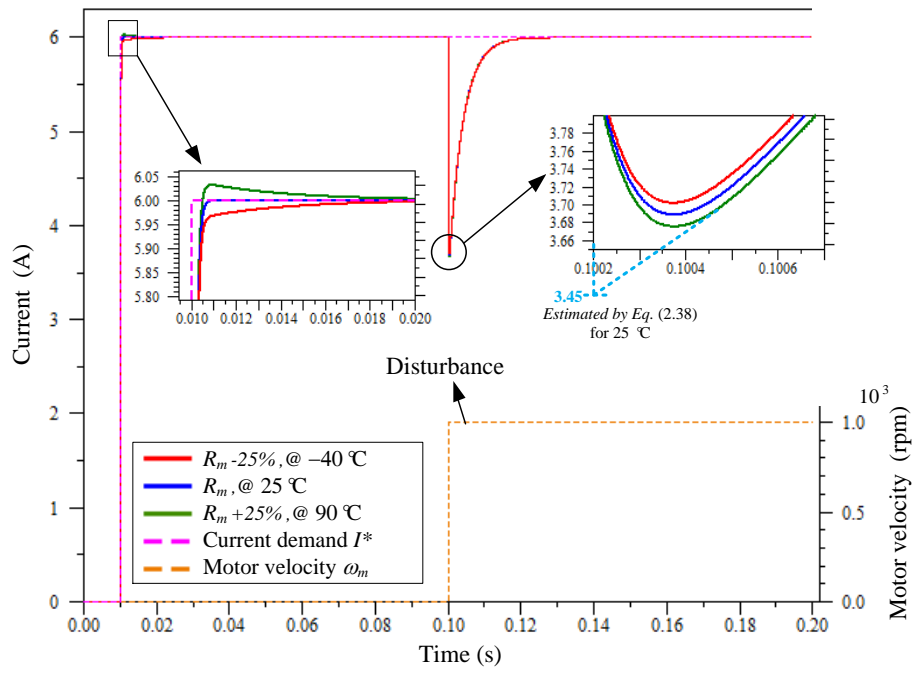


Fig. 2-15 Temperature sensitivity to motor current loop

Both Fig. 2-14 and Fig. 2-15 show that the current loop performance can be seriously affected by motor velocity disturbance, even for small values of velocity amplitudes such as of 1000 rpm (30% of the nominal speed). Therefore, the back emf compensation should be regarded in current loop for motor control.

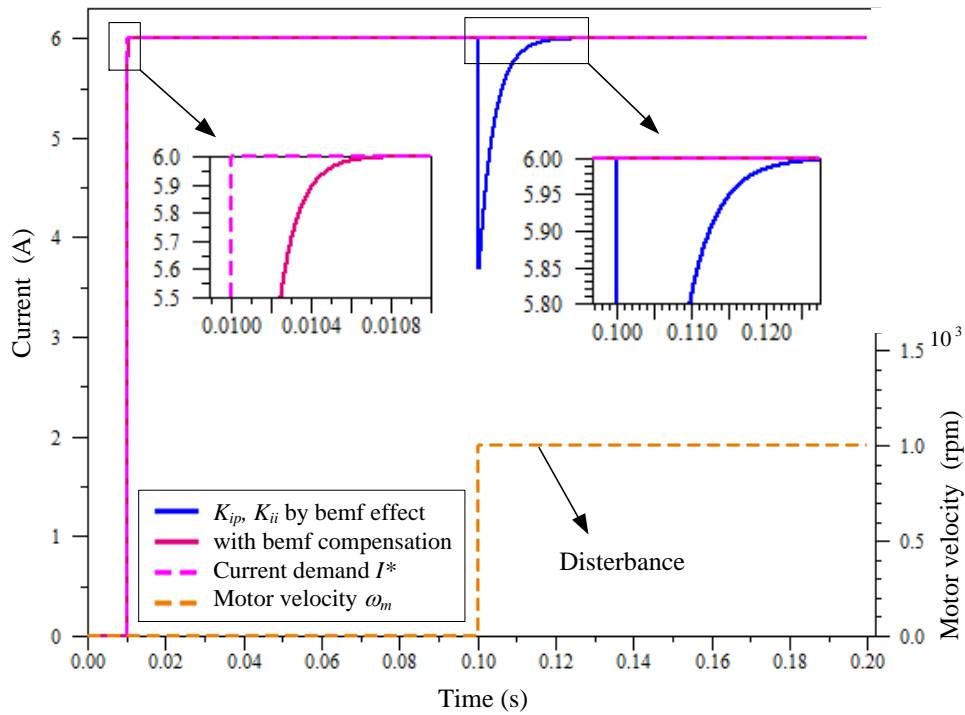


Fig. 2-16 Motor current PI controller with bemf compensation

A numerical simulation is used to verify the back emf compensation. Figure 2-16 shows interest of back emf compensation, the current response is stable and has no static error under velocity disturbance. However, the response time is not affected by the back emf compensation.

2.4.4 Limitations in the Implementation of the Current Loop

As shown in the former sections, it is interesting to increase the P gain of the current loop while keeping the I gain set to verify equation (2.32) in order to get better dynamics and accuracy. Using the results obtained with the linear model from equation (2.33), it seems to indicate that there is no limit in this augmentation. However, it has to be kept in mind that the current is altered by additional effects, essentially coming from:

- The digital realization of the controller (sampling, quantization and calculation delay effects)
- The filtering of the measured current in the feedback line (phase lag).
- Temperature variation (e.g. the windings resistance varies by $\pm 25\%$ for $\pm 65^\circ\text{C}$ temperature change) and magnetic saturation.

Because they lower the closed loop stability, these effects obviously limit the possibility of removing, by setting huge current controller gains, the parasitic effects of motor resistance, inductance and back emf.

2.5 Imperfections due to Mechanical Compliances

In any hardware, there are many technological imperfections that impact performance. In the case of EMA, these imperfections are due to digital control (sampling, quantization and computer time cost), measurement (sensors, signal conditioning and filtering), compliance effects (kinematics is not infinitely stiff), mechanical friction (in motor and mechanical power transmission). Among them, parasitic compliances can modify significantly the performance of the real EMA actuation system [9], that is far from that predicted by the simplified linear model presented in section 2.2.

When dealing with EMA actuation system control and design, many analysis and research

work uses a linear first or at most second order system to represent the EMA. Thus, the EMA inner compliance (i.e. nut-screw) and outer compliances (the anchorage to airframe and the transmission to load) are all neglected. In the following, the compliances are considered in a way that enables the designer to investigate their effect on EMA performance. In this attempt, the structural diagram of EMA is proposed in Fig. 2-17. The main sources of compliance are introduced by adding the anchorage (k_a) and transmission (k_t) stiffness coming from the aircraft structure and the global stiffness of the EMA internal mechanical transmission (k_n) that merge the contributions of the nut-screw, the bearing and joints.

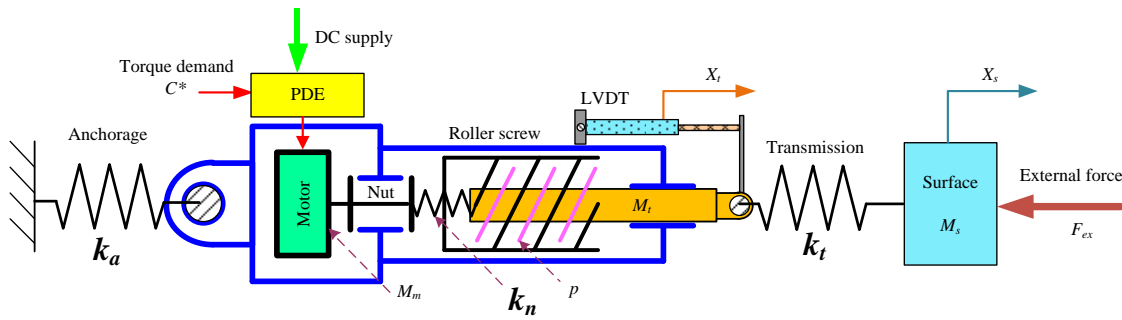


Fig. 2-17 EMA configuration with structural compliances

In order to analyze the compliances effects for EMA control system, the worst case of system stability is addressed by considering that there is no structural damping. In these conditions some oscillations of the control surface and the EMA appear from the combination of masses (M_m , M_t and M_s) and stiffness (k_a , k_n and k_t). To simplify the analysis, the anchorage and transmission stiffness can be considered as a series connection to make a single structural stiffness (k_s) [10], expressed as:

$$k_s = \frac{k_a k_t}{k_a + k_t} \quad (2.39)$$

k_s	Structural stiffness [N/m]	k_a	Anchorage stiffness [N/m]
k_t	Transmission stiffness [N/m]	k_n	Nut-screw Stiffness [N/m]

2.5.1 Closed-loop Transfer Function

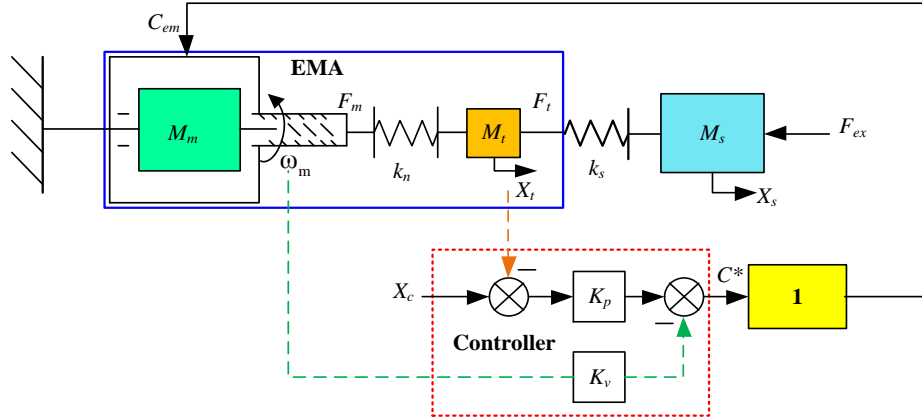


Fig. 2-18 Equivalent schematic of position controlled EMA with compliances

In this section, the effects of the torque and speed saturations are not considered. The considered control structure is still based on that depicted by Fig. 2-8. The equivalent schematic diagram with the controller is shown in Fig. 2-18. Because of existing structural compliance k_s , the EMA rod displacement X_t is not equal to surface displacement X_s . For integration and reliability purposes, the feedback signal for the position control loop is the extension X_t of the EMA that is usually measured with a LVDT position sensor.

The torque open-loop model of the EMA has two inputs (torque demand C^* and external disturbance force F_{ex}) and one output (the rod displacement X_t). Due to the higher order of the model, it is more convenient to use a state space representation than a transfer function. So the input vector is $\mathbf{u} = [C^* \ F_{ex}]^T$, the output variable is $y = X_t$. The state vector is of dimension 6. It is selected to be $\mathbf{x} = [\omega_m \ F_m \ V_t \ F_t \ V_s \ X_t]^T$ because its elements have a physical meaning and can be easily accessed in the model through sensors (for some of them). The state-space model using Laplace transformation is therefore given by

$$\begin{cases} sX_t(s) = AX_t(s) + BU(s) \\ Y(s) = CX_t(s) \end{cases} \quad (2.40)$$

where,

$$A = \begin{bmatrix} 0 & -\frac{2\pi}{pM_m} & 0 & 0 & 0 & 0 \\ \frac{pk_n}{2\pi} & 0 & -k_n & 0 & 0 & 0 \\ 0 & \frac{1}{M_t} & 0 & -\frac{1}{M_t} & 0 & 0 \\ 0 & 0 & k_s & 0 & -k_s & 0 \\ 0 & 0 & 0 & \frac{1}{M_s} & 0 & 0 \\ 0 & 0 & 1 & 0 & 0 & 0 \end{bmatrix}, \quad B = \begin{pmatrix} \frac{4\pi^2}{p^2 M_m} & 0 & 0 & 0 & 0 & 0 \\ 0 & 0 & 0 & 0 & \frac{1}{M_s} & 0 \end{pmatrix}^T \quad (2.41)$$

$$C = (0 \ 0 \ 0 \ 0 \ 0 \ 1), \quad D = (0 \ 0) \quad (2.42)$$

Consequently, the output X_t can be expressed by

$$X_t(s) = C(sI - A)^{-1}BU \quad (2.43)$$

where I is unitary matrix.

According to equations (2.41) to (2.42) the open-loop transfer of rod displacement in response to torque demand C^* and load disturbance F_{ex} is of 6th order:

$$X_t(s) = \frac{2\pi pk_n k_s \left(\frac{M_s}{k_s} s^2 + 1 \right) C^*(s) - p^2 k_n k_s \left(\frac{M_m}{k_n} s^2 + 1 \right) F_{ex}(s)}{p^2 M_m M_s M_t s^6 + [p^2 k_n M_s M_t + p^2 M_m k_s M_t + p^2 M_m M_s (k_n + k_s)] s^4 + [p^2 k_n k_s M_t + p^2 (M_m + M_s) k_n k_s] s^2} \quad (2.44)$$

In practice, the mass of actuator body (dozens of kg) and the rod (a few kg) are very small compared to the mass effect that the motor rotor reflects at the load level through the mechanical transmission. For this reason, they can be neglected for preliminary design. Then, introducing pure position and velocity controller gains K_p and K_v respectively, the closed-loop transfer function for position pursuit ($F_{ex} = 0$) is given by:

$$\frac{X_t(s)}{X_c(s)} = \frac{2\pi p \frac{k_n k_s}{k_n + k_s} K_p \left(\frac{M_s}{k_s} s^2 + 1 \right)}{p^2 M_m M_s s^4 + 4\pi^2 M_s K_v s^3 + [p^2 \frac{k_n k_s}{k_n + k_s} (M_m + M_s) + 2\pi p M_s \frac{k_n}{k_n + k_s} K_p] s^2 + 4\pi^2 \frac{k_n k_s}{k_n + k_s} K_v s + 2\pi p \frac{k_n k_s}{k_n + k_s} K_p} \quad (2.45)$$

The characteristic equation $D(s)$ of the closed loop system becomes:

$$D(s) = p^2 M_m M_s s^4 + 4\pi^2 M_s K_v s^3 + [p^2 \frac{k_n k_s}{k_n + k_s} (M_m + M_s) + 2\pi p M_s \frac{k_n}{k_n + k_s} K_p] s^2 + 4\pi^2 \frac{k_n k_s}{k_n + k_s} K_v s + 2\pi p \frac{k_n k_s}{k_n + k_s} K_p \quad (2.46)$$

For rod displacement, the closed-loop transfer function for load rejection ($X_c = 0$) at the rod level is:

$$\frac{X_t(s)}{F_{ex}(s)} = \frac{p^2 M_m \frac{k_n}{k_n + k_s} s^2 + 4\pi^2 K_v \frac{k_n}{k_n + k_s} s + p^2 \frac{k_n k_s}{k_n + k_s}}{D(s)} \quad (2.47)$$

As the position of interest at aircraft level is that of the control surface (X_s), the associated closed-loop transfer function for position pursuit ($F_{ex} = 0$) becomes

$$\frac{X_s(s)}{X_c(s)} = \frac{2\pi p \frac{k_n k_s}{k_n + k_s} K_p}{D(s)} \quad (2.48)$$

and the closed-loop transfer function for load rejection ($X_c = 0$) is

$$\frac{X_s(s)}{F_{ex}(s)} = \frac{p^2 M_m s^2 + 4\pi^2 K_v s + p^2 \frac{k_n k_s}{k_n + k_s} + 2\pi p \frac{k_n}{k_n + k_s} K_p}{D(s)} \quad (2.49)$$

2.5.2 Stability Analysis

System stability is the most important issue when the EMA control parameters are set on the basis of a 2nd order model, that of equation (2.10). In order to investigate the impact of parasitic compliances, it is proposed to apply this setting (K_p , K_v) to the fourth-order model, equation (2.46). The stability of the system in the presence of compliances can therefore be studied by using Routh Criterion [11]. The first column of the Routh table is:

$$\left\{ p^2 M_m M_s \quad 4\pi^2 M_s K_v \quad p^2 M_s k_{eq} + \frac{2\pi p M_s K_p k_n}{k_n + k_s} \quad p k_{eq} + \frac{2\pi K_p k_n}{k_n + k_s} - 2\pi K_p \quad 2\pi p k_{eq} K_p \right\} \quad (2.50)$$

Where:

$$k_{eq} = \frac{k_n k_s}{k_n + k_s} \quad (2.51)$$

The system stability is ensured if all the entries in the first column of the Routh table are positive. Satisfying this condition leads to the following single constraint:

$$k_n > \frac{2\pi}{p} K_p \quad (2.52)$$

Equation (2.52) indicates that the EMA proportional gain K_p is upper bounded by the compliance k_n .

Substituting equations (2.12) and (2.13) into equation (2.52) enables checking whether or not the specified response time \hat{t}_s is consistent with the compliance k_n and the total translating mass (M_m plus M_s):

$$\hat{t}_s > \frac{1}{2.9} \sqrt{\frac{M_s + M_m}{k_n}} \quad (2.53)$$

The combination of equation (2.52) with equations (2.47) and (2.49) give the position error for rod and for surface under constant external load (rejection function):

$$\varepsilon_{dt} = \lim_{s \rightarrow 0} s X_s(s) = \frac{p F_{ex}}{2\pi K_p} > \frac{F_{ex}}{k_n} \quad (2.54)$$

$$\varepsilon_{ds} = \lim_{s \rightarrow 0} s X_s(s) = \left(\frac{p}{2\pi K_p} + \frac{1}{k_s} \right) F_{ex} > \left(\frac{1}{k_n} + \frac{1}{k_s} \right) F_{ex} \quad (2.55)$$

ε_{dt} Static rod position error [m]		ε_{ds} Static surface position error [m]
--------------------------------------------------	--	------------------------------------------------------

These two equations clearly indicate that the low frequency stiffness of the actuator when operated in closed loop cannot be greater than:

- k_n if the rod displacement is considered,
- k_{eq} if the translated surface displacement X_s is considered.

The undamped natural frequency of the surface can be calculated as:

$$f_s = \frac{1}{2\pi} \sqrt{\frac{k_{eq}}{M_s}} \quad (2.56)$$

2.5.3 Example and Numerical Simulation

Comparing the above equations (2.54) and (2.55), it shows that the structural compliance k_s will reduce the closed loop system stiffness and increase the static error under load disturbance. In order to verify these design rules of Eqs.(2.52) and (2.53), the EMA is simulated with and without mechanical compliances. The performance target and the EMA parameters are listed in Table 4-5 and the simulation results are plotted in Fig. 2-19.

Table 4-5 EMA desired mission and mechanism parameters

Parameter	Value	Parameter	Value
Desired response time at +/- 5% \hat{t}_s (s)	0.05	Nut-screw stiffness k_n (N/m)	$3 \cdot 10^8$
Desired maximum first overshoot $\hat{\sigma}_p$ (-)	5%	Structural stiffness k_s (N/m)	$5 \cdot 10^7$
Surface equivalent mass M_s (kg)	600	Lead of roller-screw p (mm)	2.54
Motor inertia J_m (kgm ²)	0.00171		

A position step command $X_c = 10$ mm for flight surface is applied at $t = 0.1$ s, which is followed by a 10 kN external aerodynamic force step occurring at $t = 1$ s as load disturbance. For tracking performance at surface level, the second order model (perfectly rigid), predicts a response time of 0.05 s, a first overshoot of 5%. When compliances are considered in the model, the response time is doubled (0.1 s) and the surface oscillates for a long time. It has to be kept in mind that no structural damping is considered. Therefore, the surface damping only comes from the action of the EMA control loop that feels the oscillatory motion of the surface through the reaction force it applies on the EMA rod.

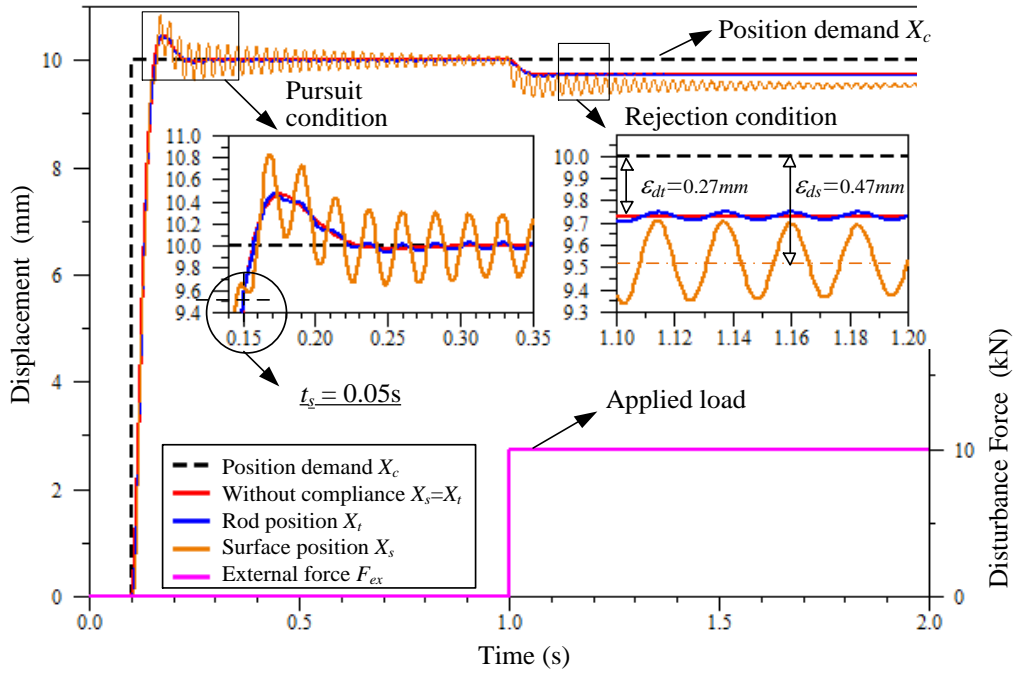


Fig. 2-19 Comparison of position pursuit and rejection performance without/with compliances

The disturbance rejection performance is also very different. The static disturbance error calculated from the second order model is $\varepsilon_{dt} = 0.27$ mm and becomes $\varepsilon_{ds} = 0.47$ mm in the presence of compliances. Of course this comes from the structural stiffness k_s that acts outside the position control loop. The simulation responses are consistent with the theoretical results given by equations (2.54) and (2.55).

The interest of the preliminary design rules proposed above can also be illustrated by considering the EMA response in the frequency domain. In this attempt:

- the control parameters are set for the same response time target ($\hat{t}_s = 0.05$ s) and the structural stiffness is set to $k_s = 5 \cdot 10^7$ N/m;

- the closed-loop frequency response of EMA surface displacement is plotted in the Bode planes (position pursuit and load rejection) when the compliances are considered or not, i.e using the 4th order or the 2nd order model;

- the responses are compared for 5 different values of nut-screw stiffness. The nut-screw stiffness k_n is varied in a ratio of 0.04, 0.2, 1, 5 and 25 times of k_s , ($k_n = 2 \cdot 10^6$ to $1.25 \cdot 10^9$ N/m). The responses are plotted in Fig. 2-20 for position pursuit and in Fig. 2-21 for disturbance rejection.

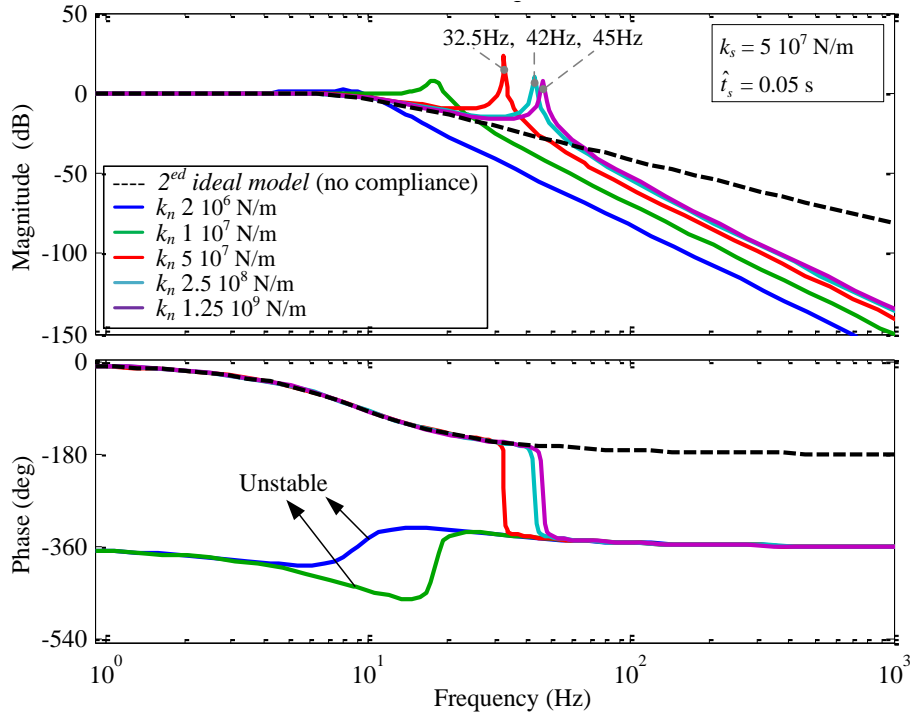


Fig. 2-20 Bode graph of surface position pursuit without/with compliance effects

Both figures show that firstly there is no resonant peak for the response of the rigid EMA model (the black dotted line). Considering the preliminary design rule, equation (2.52), the target response time of 50 ms can be achieved without stability issues only if the nut-screw stiffness k_n is higher than $3.75 \cdot 10^7$ N/m (equivalent stiffness of 2nd ideal model without compliance, equation (2.17)). This is confirmed by Fig. 2-21 and Fig. 2-21 where the EMA position control for the pursuit and load rejection becomes unstable for the nut-screw stiffness k_n lower than $3.75 \cdot 10^7$ N/m. It is important to remark that for higher values of k_n , although the position control loop is stable, the EMA has a tendency to produce resonance at a frequency of 32 Hz, 42 Hz and 45 Hz, which corresponds to equation (2.56). Once again, the resonance factor will be lowered in practice due to the structural damping and to the friction at rod/surface and airframe/surface joints.

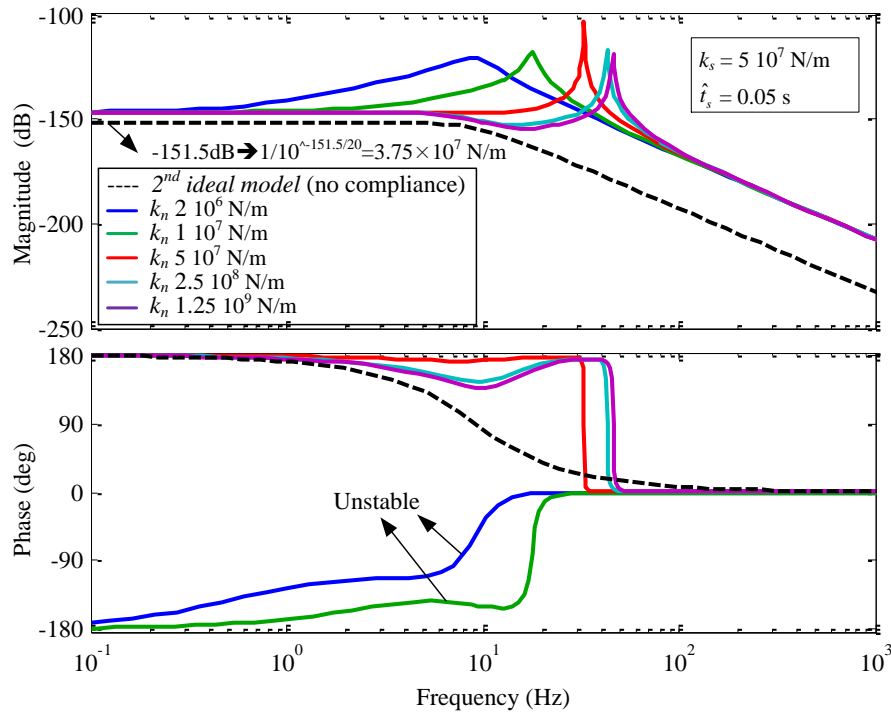


Fig. 2-21 Bode diagram of surface load rejection without/with compliance effects

2.6 Force Feedback Compensation for Position Control

As shown in Fig.2-20, 2-21 and 2-22, based on the development for EMA position controller, although a good performance can be reached on the EMA rod displacement, because of compliances, the effects of resonance on the driven load (surface) is serious. Many researches on this topic have been conducted for thrust vector control (TVC) applications. Force feedback was implemented and tested on EMAs of Vega launcher, where it effectively reacted to external force disturbances, [10]. The stability analysis of such control loop has been carried out in [12]. Another publication, [13], reported the theoretical results in frequency domain: they achieved a 20 dB reduction of the resonant peak as compared to classical control loops. Thus, force feedback is a good solution to deal with the resonance problem in EMA systems. However, for the design of this controller, accurate values of the compliances are necessary.

2.6.1 Simple Force Controller Design

In order to better damp the load, an effective method consists in incorporating a force feedback as displayed in red on Fig. 2-22. This figure illustrates the concept of the force

feedback compensation loop. Usually, the force controller is implemented as a pure propositional gain (K_f [Nm/N]). Its function is to reduce equivalent back-driving force from the structure compliance and to improve the EMA dynamics performance.

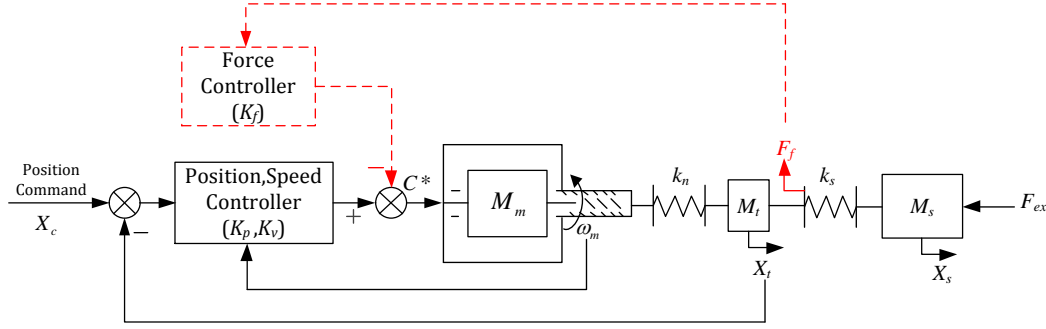


Fig. 2-22: Force feedback of the load to reduce the compliances effects

Based on the control structure of a perfect rigid model of EMA in Fig. 2-8, a combined force controller (feedback compensated) is described in Fig. 2-23. It shows that the combination of the position K_p , velocity K_v and force feedback K_f controllers occur at the torque (current) demand to the electric model. The force feedback force F_f can be physically measured (if available) with the load cell, and can be fed into the force controller.

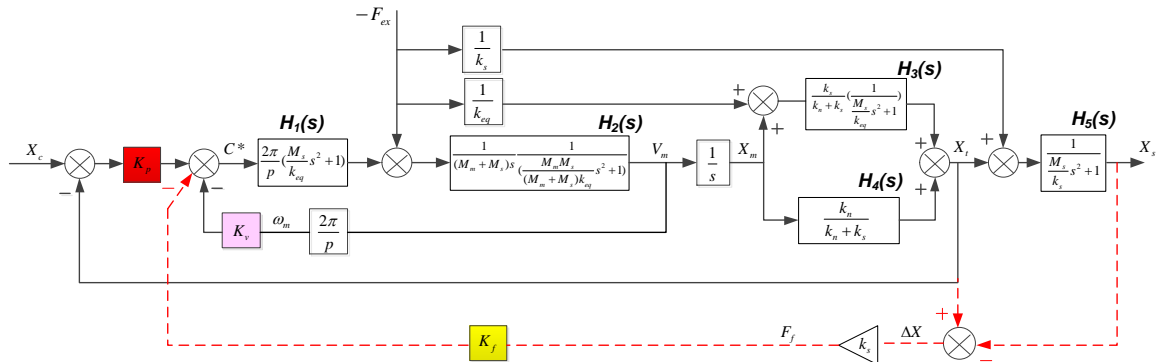


Fig. 2-23 Basic (linear) model for EMA position control with force feedback compensation

where the function of $H_1(s)$ to $H_5(s)$ are defined:

$$H_1(s) = \frac{2\pi}{p} \left(\frac{M_s}{k_{eq}} s^2 + 1 \right) \quad (2.57)$$

$$H_2(s) = \frac{1}{(M_m + M_s)s} \frac{1}{\left(\frac{M_m M_s}{(M_m + M_s)k_{eq}} s^2 + 1 \right)} \quad (2.58)$$

$$H_3(s) = \frac{k_s}{k_n + k_s} \left(\frac{1}{\frac{M_s}{k_{eq}} s^2 + 1} \right) \quad (2.59)$$

$$H_4(s) = \frac{k_n}{k_n + k_s} \quad (2.60)$$

$$H_5(s) = \frac{1}{\frac{M_s}{k_s} s^2 + 1} \quad (2.61)$$

where according to equation (2.51), the equivalent stiffness of EMA is $k_{eq} = \frac{k_n k_s}{k_n + k_s}$

The position controller (K_p and K_v) and transmitted force controller (K_f) can be regarded as two separated loops, because they operate at different frequencies for different goals. For position setpoint tracking X_c (pursuit), the position controller ensures good performance at low frequency and force controller improves good performance around the resonance that is caused by structure compliances.

With compensated by force feedback gain K_f , the characteristic equation $D(s)$, Eq.(2.46), of the closed loop system in Fig. 2-24 is changed to $D'(s)$ as:

$$D'(s) = D(s) + 2\pi p M_s k_{eq} K_f s^2 \quad (2.62)$$

K_f Force feedback controller gain [Nm/N] |

For position pursuit ($F_{ex} = 0$), the closed-loop transfer functions of the rod and load are changed as, respectively:

$$\frac{X_t(s)}{X_c(s)} = \frac{2\pi p K_p k_{eq} \left(\frac{M_s}{k_s} s^2 + 1 \right)}{D'(s)} \quad (2.63)$$

$$\frac{X_s(s)}{X_c(s)} = \frac{2\pi p K_p k_{eq}}{D'(s)} \quad (2.64)$$

For load rejection ($X_c = 0$), the closed-loop transfer function of the rod and load are respectively:

$$\frac{X_t(s)}{F_{ex}(s)} = \frac{p^2 M_m \frac{k_n}{k_n + k_s} s^2 + 4\pi^2 K_v \frac{k_n}{k_n + k_s} s + p^2 k_{eq} + 2\pi p k_{eq} K_f}{D'(s)} \quad (2.65)$$

$$\frac{X_s(s)}{F_{ex}(s)} = \frac{p^2 M_m s^2 + 4\pi^2 K_v s + p^2 k_{eq} + 2\pi p K_p \frac{k_n}{k_n + k_s} + 2\pi p k_{eq} K_f}{D'(s)} \quad (2.66)$$

When incorporating the force feedback, the position errors for rod and for the load under constant external load (rejection function) are respectively:

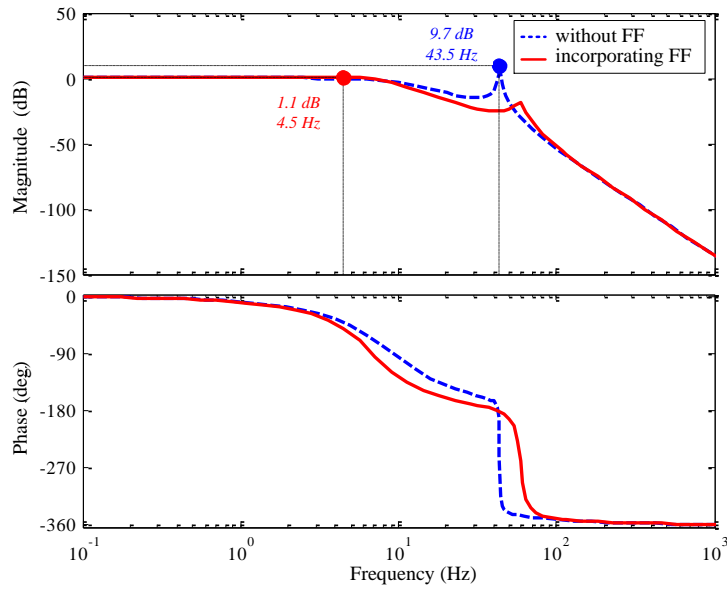
$$\varepsilon'_{dt} = \lim_{s \rightarrow 0} \frac{X_t(s)}{F_{ex}(s)} = \left(\frac{p}{2\pi K_p} + \frac{K_f}{K_p} \right) F_{ex} \quad (2.67)$$

$$\varepsilon'_{ds} = \lim_{s \rightarrow 0} \frac{X_s(s)}{F_{ex}(s)} = \left(\frac{p}{2\pi K_p} + \frac{1}{k_s} + \frac{K_f}{K_p} \right) F_{ex} \quad (2.68)$$

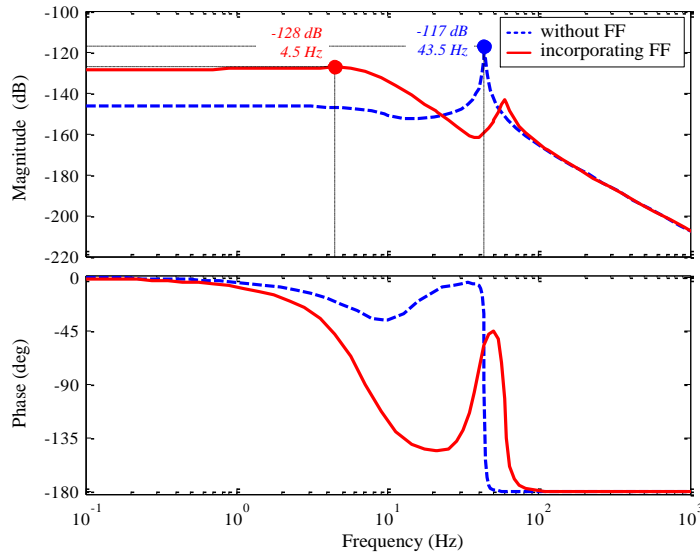
ε'_{dt} Static rod position error with force feedback compensation [m]	$\left \varepsilon'_{ds} \right.$	Static surface position error with force feedback compensation [m]
---------------------------------------------------------------------------------------	------------------------------------	-----------------------------------------------------------------------

Theoretically, the force feedback gain K_f can change the zeros and poles distribution and eliminate the oscillations effects. However, when compared to the no force feedback compensation control system, in Eqs. (2.54) and (2.55), the above two equations (2.67) and (2.68) clearly indicate that K_f decreases the equivalent stiffness of the closed-loop system and causes bigger static errors under constant external load (rejection function).

A numerical study, using the parameters in Table 4-5, is carried out in order to validated the above conclusions. A pure gain is selected for the force feedback controller, $K_f = 0.005$ [Nm/N]. Figure 2-24 compares frequency responses of the load, with and without force feedback. For position pursuit, Fig. 2-24 (a), K_f effectively decreased the resonances caused by compliance effects without impacting system stability. For load rejection, Fig. 2-24 (b), although the load chattering has been decreased, the equivalent stiffness of the closed-loop system became weaker (decreased by 11 dB), so static error for load rejection became much bigger, what may be unacceptable.



(a) Position pursuit



(b) Load rejection

Fig. 2-24 Bode diagram comparison of without/with force feedback for load surface

Additional temporal simulations were carried out to confirm the above conclusions. Using the same physical configuration, three different gains are tested for the force feedback gain: $K_f = 0.005$ [Nm/N], $K_{f1} = 0.001$ [Nm/N] ($K_{f1} = 0.2K_f$) and $K_{f2} = 0.01$ [Nm/N] ($K_{f2} = 2K_f$). Figure 2-25 shows that greater K_f decrease the load oscillations but increase the static error ε_d as well as the first overshoot. Smaller K_f decreases the overshoot and improves the equivalent static stiffness (smaller ε_d) but compensates less the resonance effect due to compliance. Once again the simulation results are well in accordance with the theoretic analysis in Eq.(2.68).

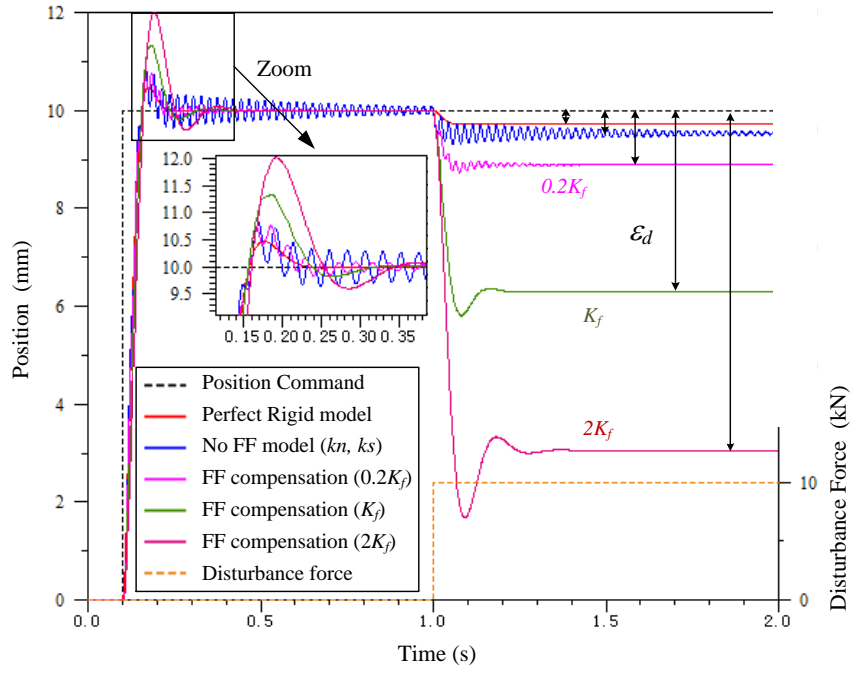


Fig. 2-25 Performance comparison of different force feedback gain K_f

2.6.2 Notch-Filter Force Feedback Controller Design

As shown in the previous section, a simple static force feedback controller is unable to meet all the performance requirements, i.e. decrease the oscillations due to resonance and provide a high equivalent stiffness for the closed-loop system in response to the aerodynamic disturbance force. Therefore, in addition to the proportional control gain K_f , a combination of low-high pass filter can be considered, as shown in Fig. 2-26. The low pass filter is used to decrease the static error under disturbance load, and high pass filter is used to damp the system response (decrease the overshoot).

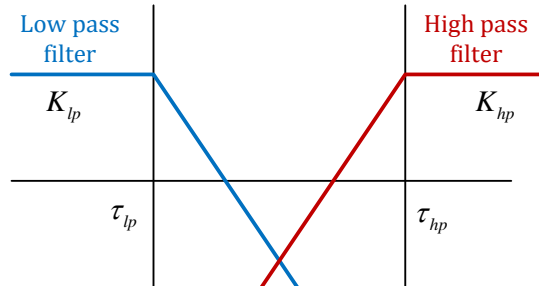


Fig. 2-26 A notch-filter structure (a low pass filter combines to a high pass filter)

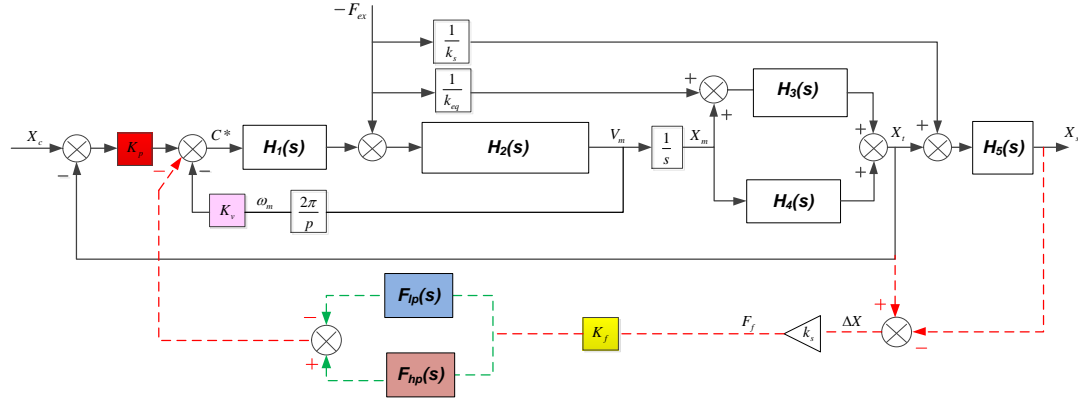


Fig. 2-27 High-low pass filter force feedback control compensation structure

On the basis of Fig. 2-23, the notch-filter (high-low pass filtered) force feedback control compensation structure is shown in Fig. 2-27, in which, the low pass and high pass filter can be expressed as:

$$F_{lp}(s) = K_{lp} \frac{1}{\tau_{lp}s + 1} \quad (2.69)$$

$$F_{hp}(s) = K_{hp} \frac{\tau_{hp}s}{\tau_{hp}s + 1} \quad (2.70)$$

K_{lp} Low pass filter gain [-]
 K_{hp} High pass filter gain [-]

τ_{lp} Low pass filter time constant [s]
 τ_{hp} High pass filter time constant [s]

If the position controlled system has a resonance frequency of f_p [Hz], in practice, the setting rules for low pass filter cutoff frequency f_{lp} and high pass filter cutoff frequency f_{hp} are given:

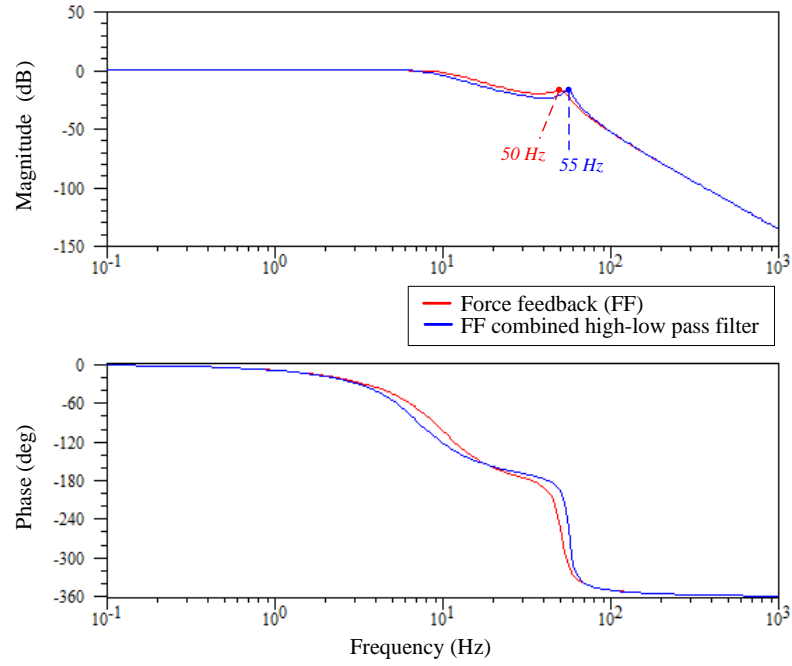
$$f_{lp} = \frac{1}{2\pi\tau_{lp}} = \frac{1}{15} f_p \sim \frac{1}{10} f_p \quad (2.71)$$

$$f_{hp} = \frac{1}{2\pi\tau_{hp}} = \frac{1}{3} f_p \sim \frac{1}{2} f_p \quad (2.72)$$

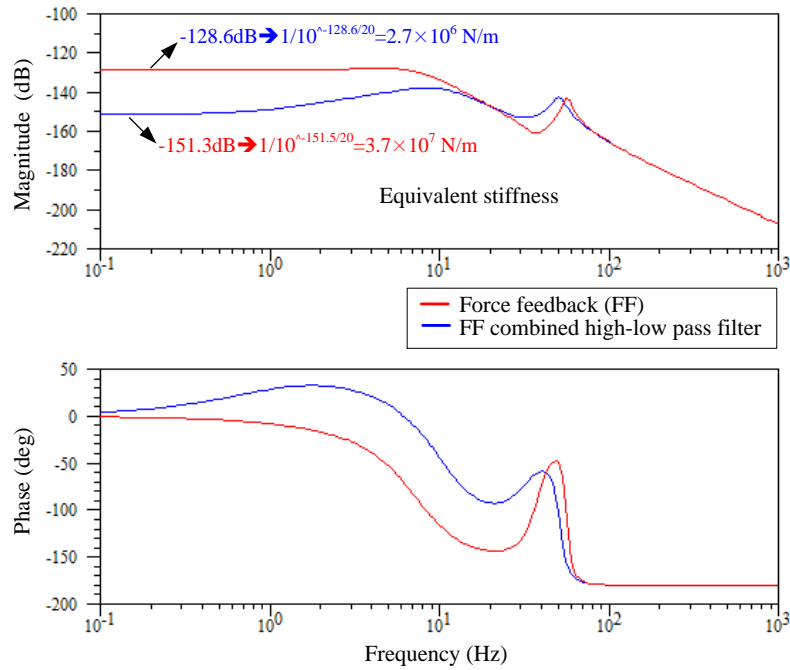
f_p Resonance frequency [Hz]
 f_{hp} High pass filter frequency [Hz]

f_{lp} Low pass filter frequency [Hz]

In addition, the static error under load disturbance can be corrected by the low filter gain K_{lp} , while system rapidity and damped performance (overshoot) can be adjusted by the high filter gain K_{hp} .



(a) Position pursuit



(b) Load rejection

Fig. 2-28 Bode diagram comparison of force feedback (FF) without/with notch filter

As previously, numerical simulations were performed in order to validate the expected performance improvement when using a notch filter force feedback compensation for EMA position control. In our model, the resonance frequency is $f_p = 43.5 \text{ Hz}$, also seen in Fig. 2-25. Thus, according to the setting rules for the filter frequencies, Eqs. (2.71) and (2.72), the

selected frequencies of the filters are $f_{lp} = 3$ Hz and $f_{hp} = 15$ Hz. The gains of the filters were chosen to be $K_{lp} = 0.06$ and $K_{hp} = 0.6$. Figure 2-28 shows frequency response of closed-loop system compensated without and with high-low pass filter. As shown in former Fig. 2-28 (a), for position pursuit, the high-low pass filter still effectively reduces the resonance effect. In Fig. 2-28 (b), for load rejection, when adding the high-low pass filter, the equivalent stiffness of the closed-loop system (K_p , K_v , K_f involved) has been augmented. This means that static error under permanent force disturbance will be smaller.

Time domain analysis, Fig. 2-29, also verifies that system static error decreases when a high-low pass filter is added in the force feedback. This static error can be decreased up to the one obtained with the perfect rigid model (2nd order linear model). The first overshoot is also improved thanks to the high pass filter gain K_{hp} .

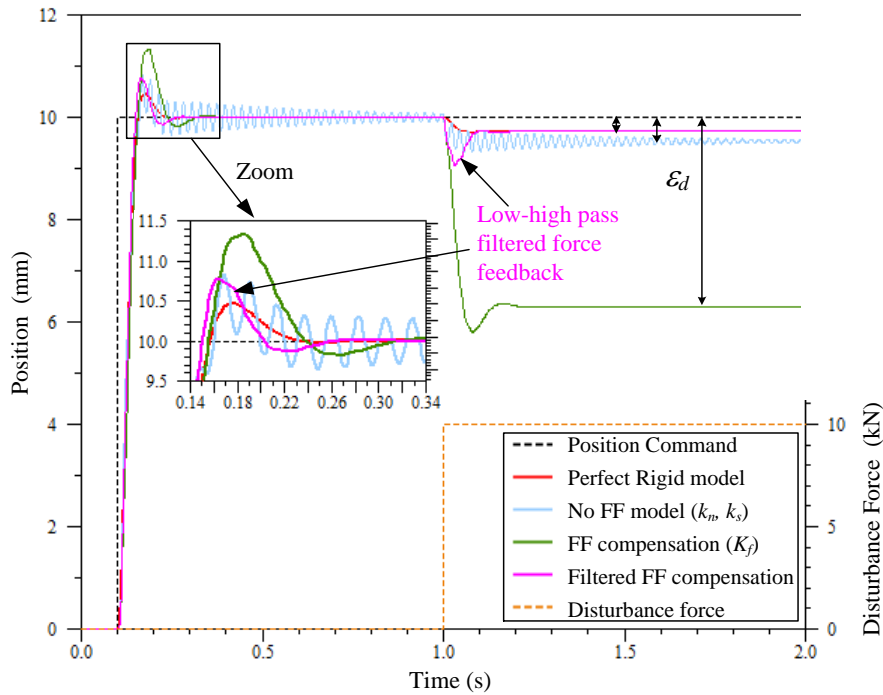


Fig. 2-29 Performance of high-low pass filter feedback compensation

Thus, in addition to the conventional cascade control structure (K_p , K_v), the high-low pass filter force feedback controller (K_f , τ_{lp} , K_{lp} , τ_{hp} , K_{hp}) can improve system performance. This additional controller can be tuned by combining analytic methods and engineering experience.

However, for the design of the force feedback controller, accurate values of the stiffness or compliance of EMAs and structure are crucial. Also, the notch filter force feedback controller needs an additional force sensor.

2.7 Conclusion of Chapter 2

In the present chapter, the individual EMA has been considered with respect to control. The EMA basic physical effects and cascade control structure have been presented firstly. The setting of the controller (position pursuit and rejection of rotor speed) has been studied first considering that the EMA behaves as 2nd order linear system, as often done.

In a second part, it has been shown that this common approach is not sufficient. In particular, this is due to the presence of the power limitation (current and voltage), to the mechanical compliance and to ideal effects of a pure PI current controller. This work enabled generic top-level best practices to be proposed, even in the presence of non-linearity or high order dynamics. It serves the very preliminary design of motor control and position control performance prediction. Control engineers may use these design rules to reduce the number of design iterations through rapid verification of consistency between closed-loop performance requirements and early choices and definition (e.g for mechanical components):

- It has been shown that performance becomes significantly reduced when the torque and speed saturations decrease to about 15% of the values reached in the absence of saturations.

- The motor current loop dynamics is closely linked to the motor electric time constant which suggests the current PI controller time constant. However, it has been shown that stability and speed disturbance rejection are constrained by stability issues and that back-emf compensation is efficient.

- Parasitic compliances of the EMA, load and airframe may have a significant impact on load position control because the controlled position is the EMA extension. This adds another constraint on position and speed controller parameters and may require additional sensor of force to load.

- Notch filter force feedback controller is designed that effectively decreases the resonance

effect and improves control system equivalent stiffness, based on the conventional cascaded control structure for position controlled EMA.

-The proposed best practice rules can also be used by the mechanical or system engineers in order to design the EMA components so that the performance requirements will be achievable once the control loops will be implemented.

References

- [1] C. Renault, "Usefulness of a Force Feedback on Electromechanical Actuator," in *6th International ESA Conference on Guidance, Navigation and Control Systems*, Loutraki, Greece, 2005.
- [2] J. Fu, I. Hazyuk, and J.-C. Maré, "Preliminary design rules for electromechanical actuation systems - effects of saturation and compliances," in *5th CEAS Air & Space Conference*, Delft, Netherlands, 2015.
- [3] M. A. Cooper, C. P. Lawson, D. Quaglia, D. Zammit-Mangion, and R. Sabatini, "Towards trajectory prediction and optimization for energy efficiency of an aircraft with electrical and hydraulic actuation systems," in *28th Congress of the International Council of the Aeronautical Sciences (ICAS)*, Brisbane, Australia, 2012.
- [4] L. Wang, K. Xiao, L. de Lillo, L. Empringham, and P. Wheeler, "PI controller relay auto-tuning using delay and phase margin in PMSM drives," *Chinese Journal of Aeronautics*, vol. 27, pp. 1527-1537, 12// 2014.
- [5] L. Wang, "Force equalization for active/active redundant actuation system involving servo-hydraulic and electro-mechanical technologies," Université de Toulouse, INSA Toulouse, 2012W. Karam, "Générateurs de forces statiques et dynamiques à haute puissance en technologie électromécanique," INSA Toulouse, Université de Toulouse, 2007.
- [6] R. Krishnan, *Electric motor drives: modeling, analysis, and control*, 1st ed. New Jersey, USA: Prentice Hall Inc, 2001.
- [7] Exlar. Exlar Product Catalog, GSX Series Integrated Motor/Actuator [Online]. Available: <http://exlar.com/pdf/?pdf=/content/uploads/2014/09/GSX-Catalog-Section1.pdf>
- [8] R. Krishnan, *Permanent magnet synchronous and brushless DC motor drives*, 1st ed. USA: CRC press, 2010.
- [9] J.-C. Maré and S. Cregut, "Electro hydraulic force generator for the certification of a thrust vector actuator," in *International Conference on Recent Advances in Aerospace Actuation Systems and Components (R3ASC)*, Toulouse, France, 2001, pp. 59-64.
- [10] G. Dée, T. Vanthuyne, and P. Alexandre, "An electrical thrust vector control system with dynamic force feedback," in *International Conference on Recent Advances in Aerospace Actuation Systems and Components (R3ASC)*, Toulouse, France, 2007, pp. 75-79.
- [11] F. Golnaraghi and B. Kuo, *Automatic control systems* vol. 2, 2010.

- [12] B. Carpentier, F. Puel, C. Cros, B. Pin, and L. Gerbe, "Stability analysis using a coupled model of TVC actuator control loop and structural dynamics of a Launch Vehicle," in *4th European Conference for Aerospace Sciences(EUCASS)*, 2011.
- [13] D. E. Schinstock, D. A. Scott, and T. A. Haskew, "Transient force reduction in electromechanical actuators for thrust-vector control," *Journal of Propulsion and Power*, vol. 17, pp. 65-72, 2001.

Chapter 3

Power Drive Electronics and Motor

As explained earlier, EHAs and EMAs combine PDE and EM. Beside the functional physical effects of power modulation and power transformation, some technological imperfections (e.g. PDE power losses of EM rotor inertia) impact performance significantly.

Considering the energy losses in PbW actuators is of prior importance. Firstly, the heat coming from energy losses increases the temperature of PDE and EM. Thus, the thermal balance must be predicted with accuracy for calculating the service life and verifying that the actuator operation remains inside in the safe operating area (SOA). Secondly, the sizing of the electrical power generation and network depends on the mean and peak power, demanded or regenerated, at PDE input. Thirdly, designing greener aircrafts requires better care to wasted energy, even at secondary power users.

For all these reasons, it is proposed in this chapter to develop hi-fidelity modelling and simulation of PDE and EM. The key idea consists in using an incremental process in order to adapt the model complexity to the available data and the engineering needs (control design, DC network stability, energy saving, preliminary sizing, etc.). Non-functional (or parasitic) physical effects models are made optional and replaceable. The objective is to generate through a structured approach the different model levels of PDE and EM, which are generally described by nonlinear equations and sometimes difficult to implement as system-level models.

3.1 Physical Effects in Power Drive Electronics (PDE)

The function of the power drive electronics is to modulate the power transferred between the electric supply bus and the motor by action on the motor windings voltage, according to the switching signals sent to the power transistors. Consequently, the PDE can be seen as at first

as a modulated perfect power transformer. In addition, the PDE is subjected to power losses that come from switching and electrical resistance. Nowadays, with the rapid development of modern semiconductor technologies, power losses are very small and the state-of-the-art efficiencies of power drive electronics can reach the 93 to 95% at rated operation point [1, 2]. However, the power, although relatively small cannot be ignored because it is the major effect that drives the sizing of the PDE for the thermal point of view.

3.1.1 Perfect Power Transformer

The power electronics functionally operates as a perfect modulated power transformer, a MTF in Bond-Graph, seen Fig.3-1.

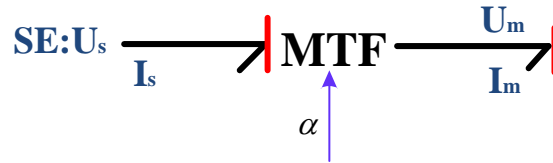


Fig. 3-1 Bond-Graph model of perfect PDE

Between the DC supply and power windings, it is driven by the controller which pulse width modulation function outputs the duty cycle (α), $\alpha \in [-1, 1]$:

$$\begin{cases} U_m = \alpha \cdot U_s \\ I_m = I_s / \alpha \end{cases} \quad (3.1)$$

U_s	DC supplied voltage [V]	I_s	DC supplied current [A]
U_m	Motor windings voltage [V]	I_m	Motor windings current [A]
α	Duty cycle [-]		

3.1.2 Dynamic Torque Function

For preliminary design of controllers, it may be interesting to develop a simplified model that merges the PDE and the motor. At this level, the motor current I_m is linked to the motor electromagnetic torque C_r through the motor torque constant K_t and the dynamics of the current loop is introduced thanks to an equivalent second order model. Therefore, the electromagnetic torque produced by the motor can be calculated as a function of the torque demand C^* by:

$$C_r = \frac{\omega_i^2}{s^2 + 2\xi_i\omega_i s + \omega_i^2} C^* \quad (3.2)$$

$$\omega_i = 2\pi f_i \quad (3.3)$$

C_r	Motor reference torque [Nm]	C^*	Demand torque reference [Nm]
ω_i	Current loop natural frequency [rd/s]	ξ_i	Current loop damping factor [-]
f_i	Current loop frequency [Hz]		

The above parameters can be provided by the PDE supplier (f_i is usually in the range 600~800 Hz while ξ_i is in the range 0.6 to 1). It is important to remark that this model supposes implicitly that the current loop perfectly rejects the disturbance coming from the motor back electromotive force (bemf).

3.1.3 Power Losses

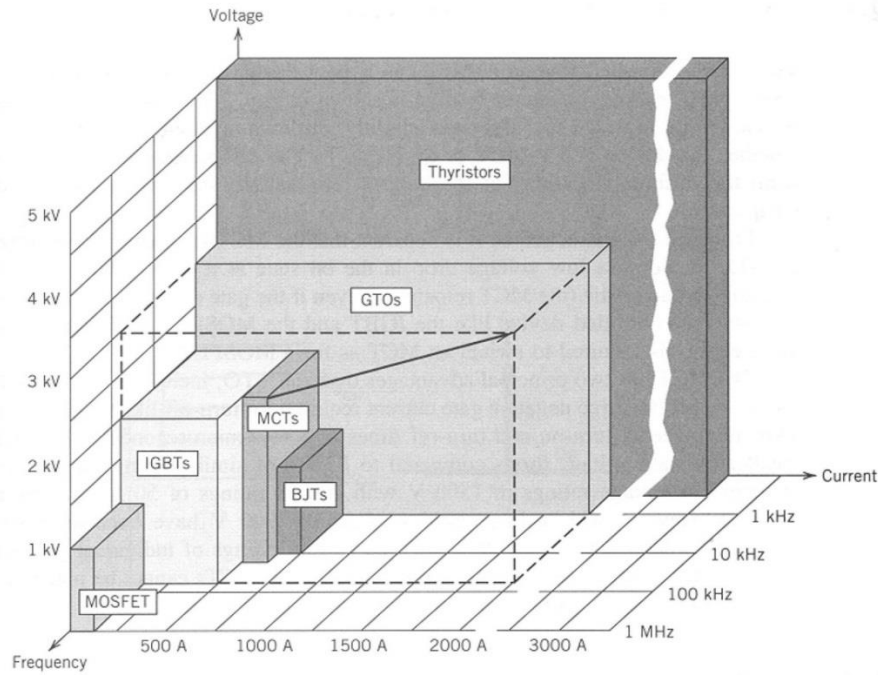


Fig. 3-1 Typical application area for different switch [3]

The commutation circuits of the chopper or the inverter in PDE, each leg is grouping two modules. Each module has a solid-state switch, i.e. Insulated Gate Bipolar Transistor (IGBT) or Metal-Oxide-Semiconductor Field-Effect Transistor (MOSFET). Choosing either IGBT or MOSFET as the switch depends on its different application areas, seen Fig.3-1. The MOSFET is

preferred device for high switching frequency application (> 100 kHz) but cannot suffer high current at high voltages. The IGBT usually operates in the range of 10 kHz IT has higher breakdown voltage and is more suitable for high current applications. In today's aerospace industrial domain, IGBT is widely used and particularly for electrical motor drives with ratings higher than 1 kW [4].

In addition, each module consists of another an anti-parallel or free-wheeling diode to obtain a fully functional switch for energy recovery, Fig.3-2 giving a typical structure of inverter bridge circuit for driving 3-phase motor. For IGBTs, when they drive inductive-resistive load (ex. motor), they can only carry positive current, without the anti-parallel diodes, the inductive current will cease instantly and generate a high voltage peak.

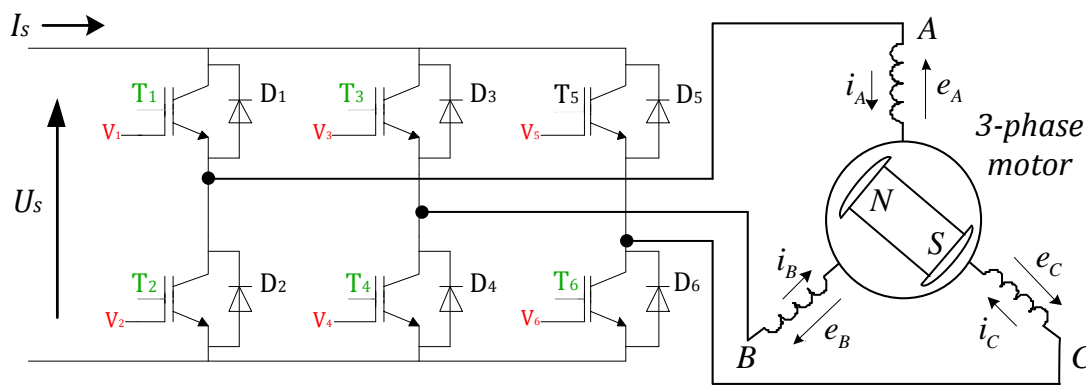


Fig 3-2 Inverter bridge circuit of co-package IGBTs and diodes

Since the structure of the inverter is symmetrical, the shape of the current and voltage curves are the same for IGBTs and diodes, there is only a fixed phase difference between them. The overall energy losses are the summation of each of IGBT and diode. The generated energy losses can be represented by R effect in Bond-Graph. For each IGBT or Diode, the losses can be divided in three types: on-state conduction losses, off-state blocking (leakage) losses, and turn-on/turn-off switching losses. In practice, the off-state blocking losses can be neglected because the leakage currents are extremely low [5].

Conduction Losses

The conduction losses are taking place at on-state mode, when an IGBT or a diode becomes conducting that generates a voltage drop U_d . One approach to determine this voltage drop is to simulate the losses, using device model of [6], given the expression:

$$U_d = a \cdot \left(\frac{i_d}{I_r}\right) + b \cdot \left(\frac{i_d}{I_r}\right)^c \quad (3.4)$$

U_d	Voltage drop by IGBT or Diode [V]	i_d	Operating current for IGBT or Diode [A]
I_r	Rated current for IGBT or Diode [A]	a	Model parameter [V]
b	Model parameter [V]	c	Model parameter [-]

The estimation model in equation (3.4) for device voltage drop has three key parameters, which are not available in documentations and have several percentage errors. Therefore, this model has not been widely applied. Another approach in [7] models the on-state voltage drop by a dynamical resistance R_{on} , and a static forward voltage drop U_0 at zero current, giving

$$U_d = U_0 + R_{on} i_d^\beta \quad (3.5)$$

U_0	Static forward voltage drop by IGBT or Diode [V]	R_{on}	On state resistance for IGBT or Diode [Ω]
β	Model parameter [-]		

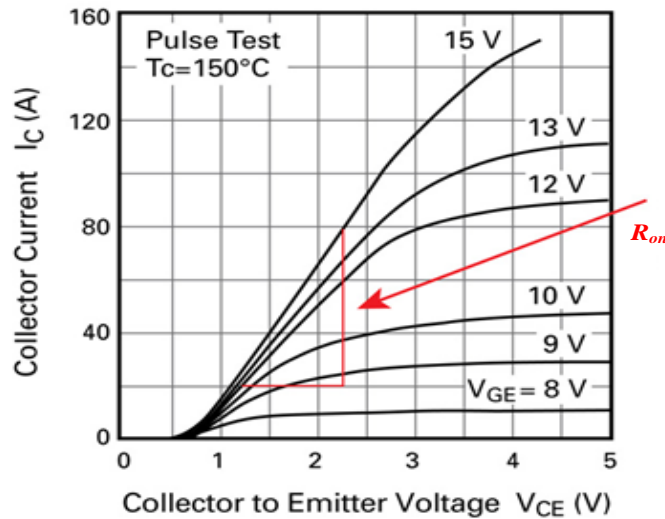


Fig.3-3 Typical output characteristics of IGBT (datasheet RJE65S04DPQ)

For IGBT or diode, the current/voltage characteristic is generally documented in its

datasheet, which can be easily found. In Figure 3-3 and Figure 3-4, respectively show a typical output characteristic of IGBT (datasheet RJE65S04DPQ) [8], and a real output Characteristics of diode [9].

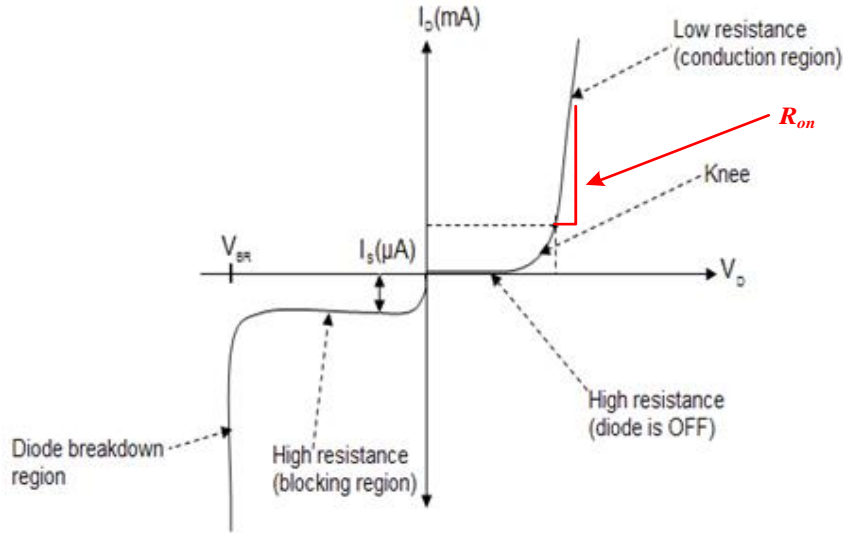


Fig.3-4 Real output characteristics of diode

According to the equation(3.5), when IGBT and diode work on the low current range (< 100 A), the voltage drop by conduction losses can use a first-order linear approximation ($\beta=1$) [10] comprising a zero-current forward threshold voltage U_0 and an “on-state” resistance R_{on} , seen Fig.3-5.

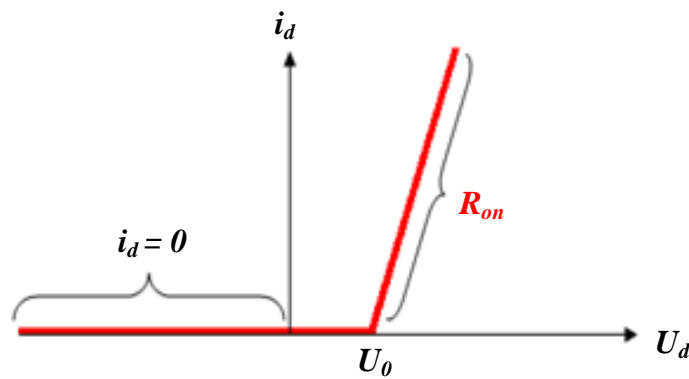


Fig.3-5 Linearized characteristics of the IGBT and diode

Consequently the voltage drop is expressed as:

$$U_d = U_0 + R_{on} i_d \quad (3.6)$$

Then, the average power due to conduction losses that dissipated in the IGBT or diode at fundamental frequency is given by,

$$P_d = U_0 I_d + R_{on} I_d^2 \quad (3.7)$$

P_d	Conduction power losses of IGBT or diode [W]		I_d	Average current flowing through the IGBT or diode [A]
-------	-------------------------------------------------	--	-------	----------------------------------------------------------

Finally the dissipated energy by conduction during a period t_d is

$$E_d = P_d t_d \quad (3.8)$$

E_d	Conduction energy losses of IGBT or diode [J]		t_d	IGBT or diode conduction time [s]
-------	--------------------------------------------------	--	-------	-----------------------------------

Switching Losses

In PDE, switching losses typically contribute to a significant amount of the total power losses. They occur during the transients “turn-on” or “turn-off” because the IGBT and diode cannot switch instantaneously. During switching, a phase lag between current and voltage occurs. The energy losses of switching cannot be neglected when the switching frequency is high (typically in the range of 10 kHz for aerospace EMAs). The switching power losses are the product of switching energies and switching frequency, which are considered continuously dissipated over time [11] for PWM control.

Nowadays, in the modern fast recovery diodes used with IGBTs for bridge circuits, the “turn-on” switching losses can be neglected because they represent less than 1% when compared to the switching “turn-on” losses [5, 12]. Generally, the total switching losses of single module (Co-package of an IGBT and a diode) have the expression,

$$E_{sw} = E_{ton} + E_{toff} + E_{don} + E_{doff} \quad (3.9)$$

E_{sw}	Switching energy losses of an IGBT and a diode [J]		E_{ton}	Switching turn-on energy losses of IGBT [J]
E_{toff}	Switching turn-off energy losses of IGBT [J]		E_{don}	Switching turn-on energy losses of diode [J]
E_{doff}	Switching off energy losses of the diode [J]			

To calculate or estimate the total switching losses, many different methods have been proposed. One way, [5, 13, 14], consists in building a physical model of the IGBT and diode

that provide voltage and current-waveforms during switching turn-on and turn-off modes. For each commutation period, this model is based on transient analysis and needs to know the reverse recovery time and current peak of diode characteristics, the rise and fall time, tail time and tail current of IGBT characteristics and stray inductance factor. In this mode, the energies losses are directly obtained by complex expression evaluations.

The typical diode-turn-off waveforms are shown in Fig.3-6 and the IGBT turn-on and turn-off waveforms are shown in Fig.3-7, more detail developed model is presented in Ref [5].

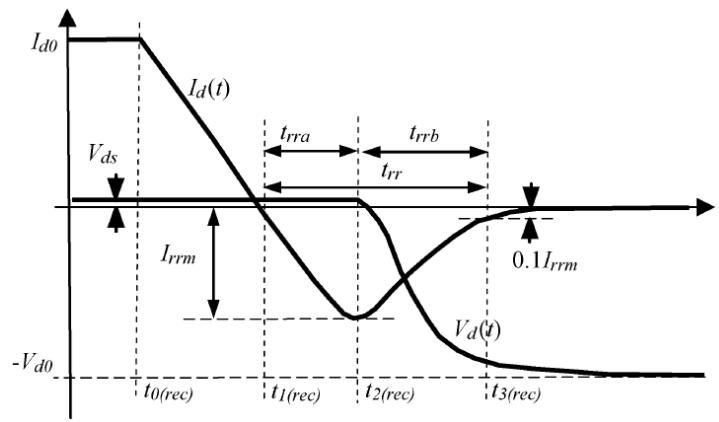


Fig. 3-6 Transient "turn-off" characteristics of diodes [5]

The generic transient calculation of its switching losses in diode,

$$E_{doff} = \int V_d(t) I_d(t) dt \quad (3.10)$$

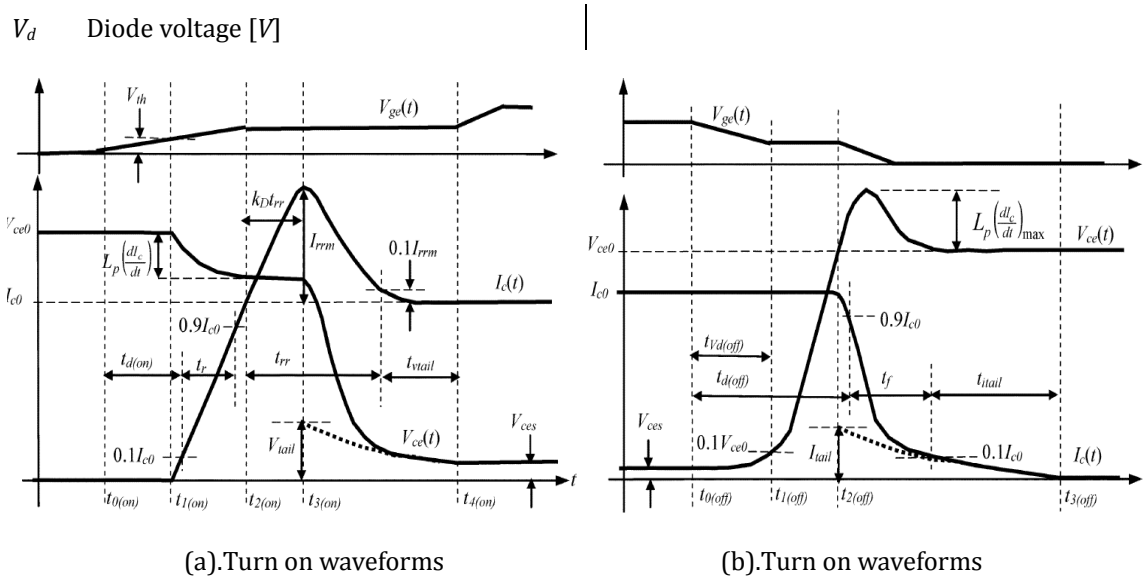


Fig. 3-7 Transient characteristics of IGBTs [5]

For calculating the switching energy losses in IGBT,

$$E_{ton}, E_{toff} = \int V_{ce}(t) I_c(t) dt \quad (3.11)$$

V_{ce} IGBT voltage [V]

Another method is to calculate switching losses analytically on basis of curve fitting [7]. The switching energy losses directly appear as a function of the semiconductor operating current and can be described by a simple equation,

$$E_{sw} = a_{sw} i(t)^{b_{sw}} \quad (3.12)$$

a_{sw} Curve fitting constant [J]

b_{sw} Curve fitting constant [-]

This model can be used for turn-on and turn-off losses of the IGBT as well as the diode. The constants (a_{sw} , b_{sw}) are determined by applying a curve fitting of the measured characteristics. However, this model needs a large number of experimental data to increase the model accuracy of the switching energy losses calculation.

Another look-up table method is proposed in [15, 16]. The estimation combines manufacturers' datasheet information that provides a feasible way to obtain accurate switching loss information. Firstly, in most datasheets of IGBTs and diodes, the turn-on and turn-off energy losses are defined according to the switch characteristics, shown in Fig.3-8.

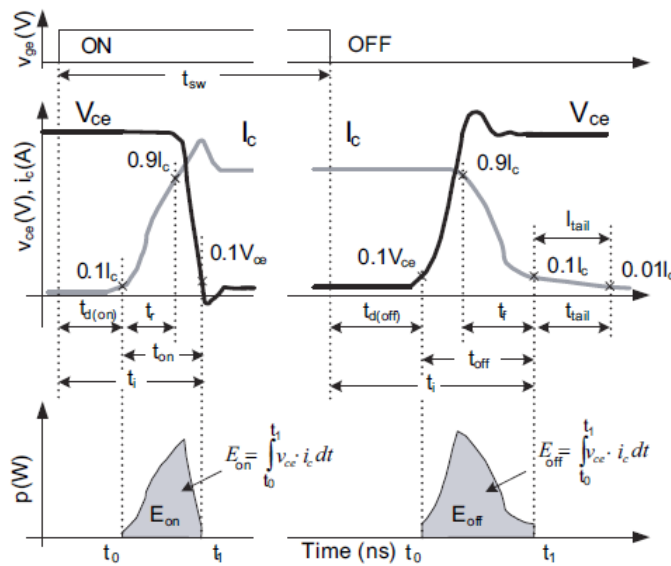


Fig. 3-8 Generic IGBT switching characteristics with switching losses definitions [17]

Based on the look-up table of the datasheets, an easy-to-handle equation assuming linear dependency of the referenced switching losses can be developed. Usually, the IGBTs turn-on and turn-off switching losses are directly given in the suppliers' manufacture datasheet as E_{on} and E_{off} with the conditions of the reference voltage and current, as seen in Fig. 3-9. The diode turn-off energy losses sometimes also are given as the reverse recovery energy. The turn-on energy is usually negligible.

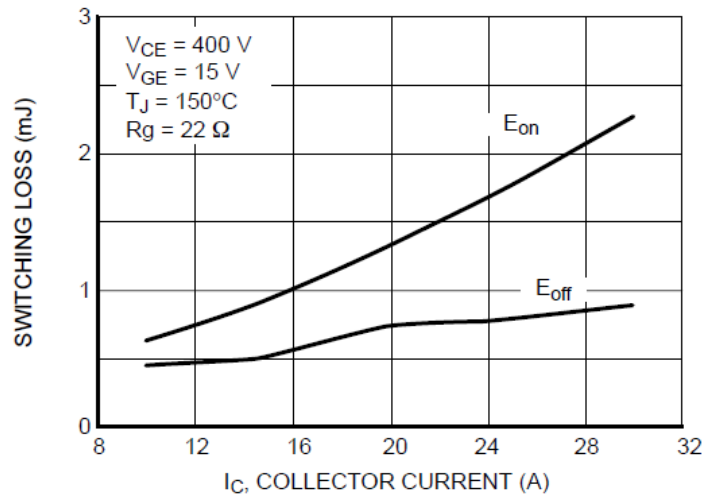


Fig. 3-9 Generic IGBT switching losses from datasheet [18]

By using this method, the switching energy losses of the IGBT or the diode per period at reference voltage and current is the sum of these four energies. They are proportional to supply voltage and input current. These data are sized to the effective operating conditions assuming a proportional sensitivity [11]:

$$E_{on} = E_{ron} \frac{|U_s|}{U_{ref}} \frac{|I_{in}|}{I_{ref}} \quad (3.13)$$

$$E_{off} = E_{roff} \frac{|U_s|}{U_{ref}} \frac{|I_{in}|}{I_{ref}} \quad (3.14)$$

E_{ron}	Reference turn-on energy losses of IGBT or diode [J]	E_{roff}	Reference turn-off energy losses of IGBT or diode [J]
U_{ref}	Switch voltage at reference condition [V]	I_{ref}	Switch current at reference condition [A]
I_{in}	Switch input current [A]		

Therefore, the power loss due to switching effect is equal to:

$$P_{sw} = E_{sw} f_{sw} = (E_{on} + E_{off}) f_{sw} \quad (3.15)$$

P_{sw} Switching power losses [W] f_{sw} Switching frequency [Hz]

In practice, when the DC supply voltage is imposed, the switching losses is viewed as a current leak that is directly proportional to the switching frequency[11], Fig. 3-10.

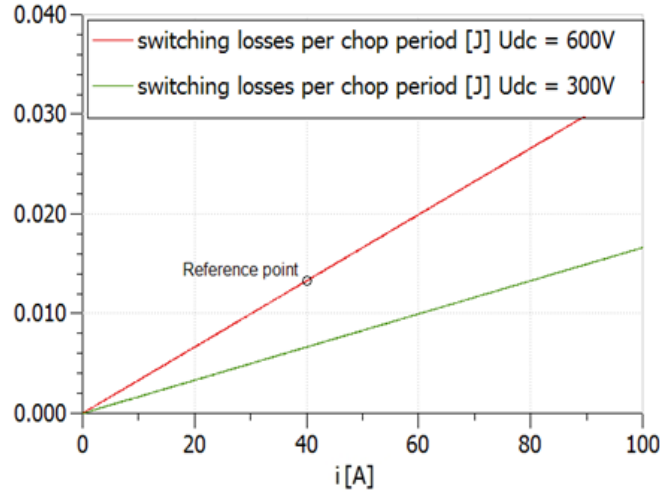


Fig. 3-10 Switching losses as function of current for different DC supply [11]

This gives:

$$I_{sw} = \frac{P_{sw}}{U_s} \quad (3.16)$$

I_{sw} Equivalent current leak by switching in IGBT or diode [A]

3.1.4 Sensitivity to Temperature in PDE

The energy losses of PDE generate heat and make temperature increase. The conduction losses are more sensitive to temperature because of the on-state resistance characteristics in IGBTs and diodes.

Figure 3-10 shows an example of diode forward characteristics with temperature sensitivity. However the switching losses have the weak dependence with temperature, seen Fig. 3-11. Therefore, in this study of PDE temperature sensitivity, the major effects are considered in conduction losses. A RS dissipative resistor in Bond-Graph can be used to present the

temperature effects. Generally, when temperature increases, on-state resistance increases too. This causes a snowball effect. Taking into account the temperature sensitivity, a modulated resistor MRS in Bond-Graph can be adopted to link the conduction losses to temperature.

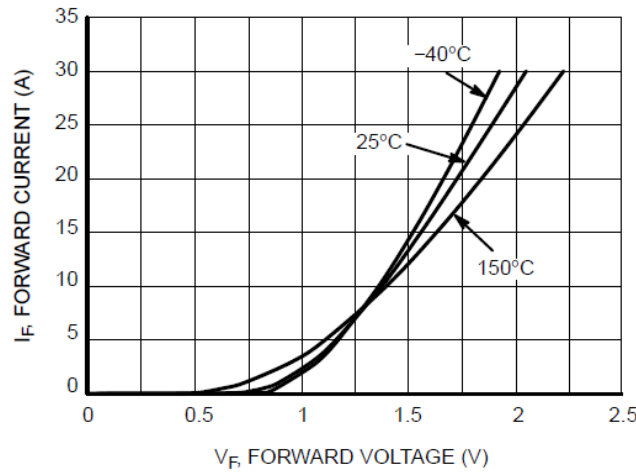


Fig. 3-10 Diode forward characteristics with temperature sensitivity [18]

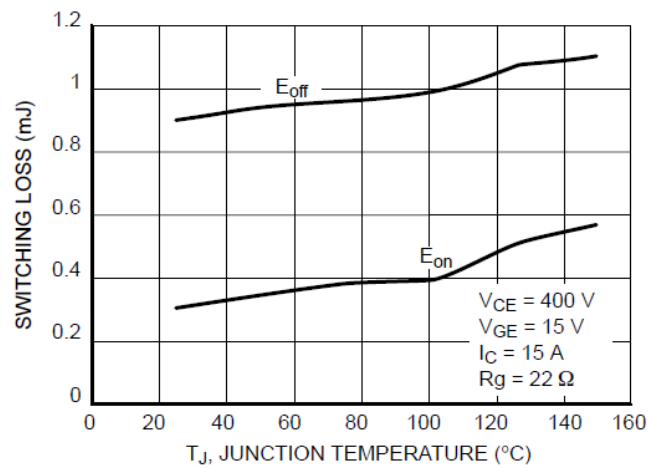


Fig. 3-11 Switching energy losses characteristics with temperature sensitivity [18]

In fact, the accurate effect of temperature for IGBTs and diodes is nonlinear but poorly documented in datasheets of PDE. In the absence of more detailed data, a linear dependence of thermal behavior is assumed for switch on-state resistance:

$$R_{on1} = R_{on0} [1 + \varepsilon_r (\Theta_1 - \Theta_0)] \quad (3.17)$$

R_{on1}	Switch “on-state” resistance at actual operating temperature [Ω]	R_{on0}	Switch “on-state” resistance at reference temperature [Ω]
Θ_1	Actual operating temperature [$^{\circ}\text{C}$]	Θ_0	Reference temperature [$^{\circ}\text{C}$]
ε_r	Temperature dependency of resistance [$1/^{\circ}\text{C}$]		

3.1.5 Causal Bond-Graph Model of PDE

In PDE, The basic element is the perfect and modulated power transformer (MTF). For each switching cell, the conduction losses of IGBTs and diodes are computed from the phase current. They cause the voltage to drop at the motor supplied pins: a 1 junction in Bond-Graph is used to present these efforts relations. The switching losses are considered as a current leak through the switching cell and to the DC supply: a 0 junction is used to present this flow relation. The current (or torque) loop can be included as a dynamic function that affects the torque demand. The conduction and switching losses can be respectively presented as two dissipative modulated resistor fields (MRS) which link to the thermal port. The switching loss (R_{sw}) is modelled as a leakage current at power supply side that is fixed by switching frequency (f_{sw}). The conduction loss (R_{cd}) is modelled as a voltage drop at motor side which is affected by temperature because of mentioned in section 3.5. As displayed by the causal marks, the causal Bond-Graph model of PDE is shown in following Fig.3-3.

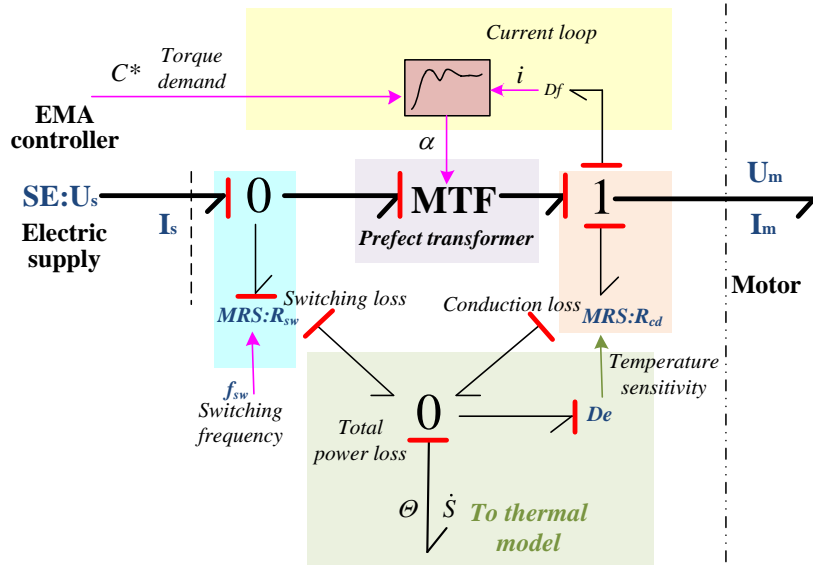


Fig. 3-3 Generic PDE model on basis of Bond-Graph

3.2 Physical Effects at Electric Motor (EM)

The electric motor makes an electromechanical power conversion: input voltage and current are functionally proportional to torque and angular velocity at motor shaft, respectively. The physical principles acting in the motor are multi-domain: electrical, magnetic, mechanical and

thermal. When it is intended to get a realistic and detailed system-level model of the motor, many parasitic effects have to be considered and appear significantly nonlinear. This particularly concerns the iron losses in magnetic domain, which can be predicted through finite element analysis techniques [19, 20]. However, this approach is suitable when the detailed geometry of the motor is known. That is generally not the case for preliminary design and virtual prototyping activities, when only top level motor data are available.

In order to facilitate the analysis of these effects at system-level, a progressive top-down modelling approach is applied. Firstly the electric motor can be seen as a perfect power transformer (the motor shaft torque C_m equals the motor electromagnetic torque C_{em}) in which the torque balance is additionally affected by parasitic inertial torque, dissipative torque and compliance torque:

$$C_m = C_{em} - C_j - C_d - C_{cg} \quad (3.18)$$

C_m Motor shaft torque [Nm]	C_{em} Electromagnetic torque [Nm]
C_j Inertia torque [Nm]	C_d Dissipative torque [Nm]
C_{cg} Compliance torque [Nm]	

3.2.1 Perfect Power Converter

The electric motor is an electromechanical power transformer which functionally links current to torque and voltage to velocity (a gyrator GY in Bond-Graph):

$$\begin{cases} C_{em} = K_t I_m \\ \omega_m = U_m / K_t \end{cases} \quad (3.19)$$

K_t Motor torque constant during operation [Nm/A] or [Vs/rad]	ω_m Angular velocity of motor [rad/s]
-----------------------------------------------------------------	----------------------------------------------

3.2.2 Inertia Effect

The rotor inertia J_m , an inertance I element in Bond-Graph, generates an inertial torque and stator.

$$C_j = J_m \frac{d\omega_m}{dt} \quad (3.20)$$

J_m Motor inertia [kgm^2]

Attention must be paid that the inertial torque involves the absolute velocity of the rotor which is time derived with respect to earth frame. The inertial torque cannot be neglected for three reasons:

- In very demanding applications, e.g. fighters or space launchers, the inertial torque takes the major part of the electromagnetic torque during transients (high rate acceleration or deceleration);
- Under aiding load conditions, it impacts the transient back-drivability of the actuator by opposing torque to the load acceleration;
- At end-stops, the kinetic energy stored by the inertial effect must be absorbed in such a way to not generate excessive force.

EMAs reflect a huge inertia at the load level, typically 10 to 20 times greater than the load itself. Oppositely, however, HSAs only reflect a few percent of the load inertia [21, 22].

3.2.3 Dissipative Effect

Energy dissipation, modelled by R elements in Bond-Graph, comes from copper, iron and friction losses.

a) Electric Domain: Copper loss

The primary source of power losses in the electric domain of motor is the copper losses also called Joule losses. The copper losses are defined as heat loss when electric power flows through the motor windings, which comes from the voltage drop due to the windings resistance to current, given as follows:

$$U_{co} = I_{mw} R_{mw} \quad (3.21)$$

U_{co} Voltage drop due to copper loss [V]

R_{mw} Motor windings resistance [Ω]

I_{mw} Motor windings current [A]

The associated copper loss can be defined as:

$$P_{co} = U_{co} I_{mw} = I_{mw}^2 R_{mw} \quad (3.22)$$

P_{co} Copper losses [W]

b) Magnetic Domain: Iron Losses

The variation of the flux density in the magnetic circuit of the motor causes iron losses. In motor rotor, the magnetic field is rotating with the rotor at the same velocity. Then very little magnetic flux variation generates nearly no iron losses in the rotor. Therefore, iron losses are mainly in motor stator and usually can be divided as eddy current loss and hysteresis loss.

Eddy Currents Loss: Eddy currents are caused by reversing magnetic field in iron. This field induces a voltage that produces eddy currents due to the electrical resistance of iron. As there is not access to the magnetic quantities during measurements, the effect of eddy currents is commonly expressed as an equivalent power loss that reflects in the mechanical domain. This power loss P_{ed} is modelled by the first member of the Steinmetz equation [4] as a function of the eddy current constant k_{ed} , the magnetic flux density B_s and the angular velocity ω_m :

$$P_{ed} = k_{ed} B_m^2 \omega_m^2 \quad (3.23)$$

P_{ed} Eddy current losses [W]

B_m Peak value of the magnetic flux density [T]

k_{ed} Eddy current constant [-]

As a result, the torque loss C_{ed} due to eddy currents takes the form of an equivalent viscous friction torque that is given by

$$C_{ed} = k_{ed} B_m^2 \omega_m \quad (3.24)$$

C_{ed} Equivalent eddy current loss [Nm]

In above equations (3.19) and (3.20), the value of the eddy current constant depends on the lamination magnet material weight, which is determined by information from manufacturer's data.

Hysteresis Loss: Magnetic hysteresis appears within ferromagnetic materials where the hysteresis effect appears between the remanence flux density B and the coercivity H (B - H

curve), which is shown in Fig. 3-5. The area of the hysteresis domains represents the work done (per unit volume of material).

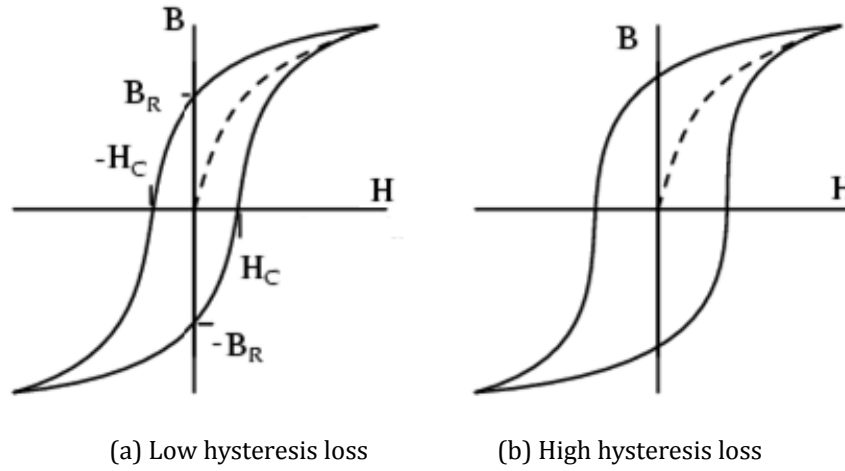


Fig. 3-5 Example of B/H loops with hysteresis loss [23]

For each cycle, the magnetic hysteresis generates an energy loss that directly depends on the motor electrical frequency. The hysteresis power loss P_{hy} can be modelled using the second member of Steinmetz equation [4] that links the hysteresis constant k_{hy} and the magnetic flux density:

$$P_{hy} = k_{hy} B_m^\gamma \omega_m \quad (3.25)$$

P_{hy}	Hysteresis losses [W]	γ	Steinmetz constant [-]
k_{hy}	Hysteresis constant [-]		

In practice, the Steinmetz constant γ is the range [1.5; 2.5] depending on magnetic saturation. Generally, it is set to 2 for ignoring the excess loss in motor.

According to Eq.(3.25), the hysteresis effect can be modelled globally as a pure Coulomb friction torque:

$$C_{hy} = k_{hy} B_m^2 \quad (3.26)$$

C_{hy}	Equivalent hysteresis Torque loss [Nm]
----------	----------------------------------------

c) Mechanical Domain: Friction Loss

Friction loss in motor occurs due to bearing friction and air gap resistance between rotor and

stator. The friction torque generated by the hinge bearing is addressed in the next section. The drag friction torque generated by the gap between the rotor and the stator can be modelled as given in [24].

3.2.4 Capacitive Effect

The variation of the air gap permeance of the stator teeth and slots above the magnets during the rotor rotation generates a torque ripple [25] which is called cogging (or detent) torque. This is an energy storage effect that is equivalent to a spring effect, a C element in Bond-Graph. Modelling the cogging effect may be important for two reasons: firstly, in some actuation applications, the cogging torque can be used as a functional effect to avoid back-drivability; secondly, cogging generates in operation a torque ripple which frequency depends on the relative rotor/stator velocity. This may excite the natural dynamics of the EMAs and its mechanical environment, leading potentially to vibrations and noise emission.

A system-level representation model of cogging torque C_{cg} can be expressed versus rotor/stator relative angle θ_m . It is parameterized by the number n_p of motor pole pairs and the cogging factor λ that applies to the rated torque C_n , equation given [4]:

$$C_{cg} = \lambda C_n \sin(n_p \theta_m) \quad (3.27)$$

λ	Cogging factor [-]	C_n	Motor rated torque [Nm]
n_p	Number of pole pairs [-]	θ_m	Motor rotor angular position [°]

With respect to conversion of energy, cogging does not consume power. Its dependency to angular position denotes a mechanical capacitive effect: the cogging torque generates a spring effect which stiffness is modulated by angle. Nowadays the cogging torque can be reduced to 1% or 2% of the motor rated torque.

3.2.5 Magnetic Saturation

At flux densities drop above the saturation point, the relationship between the current and the magnetic flux in ferromagnetic materials ceases to be linear: a given current generates less magnetic flux than expected, as illustrated by the magnetization curve given in Fig.5.

Consequently, the motor constant reduces in the saturation domain. In addition, inductance of motor windings is also affected by magnetic saturation. Therefore, it is proposed to model the magnetic saturation by modulating the motor constant and the windings inductance as a function of current.

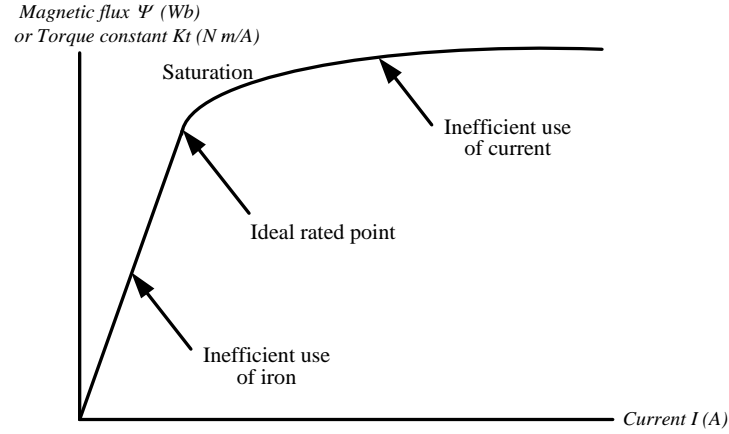


Fig. 3-11 Magnetic flux and current curve by saturation effect

Saturation is the wasteful use of energy associated with using materials at flux densities above the saturation point. Without saturation, and according to the Faraday's Law, the magnetic flux is obtained as follows:

$$\psi = BA_s \quad (3.28)$$

ψ Magnetic flux [Wb] A_s Effective area of core [m^2]		B Magnetic flux density [T]
---------------------------------------------------------------------	--	-------------------------------

Magneto-motive force can be thought of as the magnetic equivalent of electromotive force, seen Eq. (3.16):

$$Hl_m = NI_m \quad (3.29)$$

H Magnetic field strength [A/m] N Number of turns in the coil [-]		l_m Effective magnetic path length [m]
--------------------------------------------------------------------------	--	------------------------------------------

Rearranging the equation (3.15) and (3.16) with flux density equation, gives:

$$\psi = \frac{N\mu_m A_s}{l_m} I_m \quad (3.30)$$

μ_m Magnetic permeability [H/m]		
-------------------------------------	--	--

For electric motor manufacture, the torque constant is a function of magnetic flux. The saturation of magnetic flux-current will influence the motor torque constant:

$$K_t = f(\psi) \quad (3.31)$$

3.2.6 Sensitivity to Temperature in EM

The power losses in EM are caused by multidisciplinary effects mainly in electrical, magnetic and mechanical domains. The heat flow generated by these energy losses produces a looped effect that cannot be neglected. These sensitivities can affect the thermal equilibrium or the service life of the EMA. For this reason, they have to be taken into account for building the advanced EMA simulation models.

a) Influence on Electrical Resistance

Like the resistance effect in power drive electronics, temperature also influences the motor windings resistance:

$$R_{mw} = R_{s0} [1 + \varepsilon_r (\Theta_1 - \Theta_0)] \quad (3.32)$$

R_{s0} Motor windings resistance at reference temperature [Ω]

b) Influence on Magnet

Furthermore, the increase of motor temperature may decrease the performance of the magnets which lowers the electromagnetic torque constant. As done for electrical resistance, this may be generally modelled as a linear dependency to temperature:

$$k_t = k_{t0} (1 + \varepsilon_m (\Theta_1 - \Theta_0)) \quad (3.33)$$

k_{t0} Torque constant at reference temperature [Nm/A]
 ε_m Dependence of material magnet [$1/degree$]

This sensitivity is illustrated in Table 3-3 for common magnet materials[26]:

Table 3-3 Temperature dependency of the magnet material

Magnet material	Value (ε_m)
Ferrites	-0.002
Nd ₂ Fe ₁₄ B	-0.0013
SmCo	-0.0005
AlNiCo	-0.0002

In normal operation, the loss of magnetization is reversible. Oppositely, for high temperature increase, it becomes irreversible. It must be also mentioned that irreversible loss of magnetization can be produced by excessive currents. In general the PDE associated with the motor is designed in order to prevent this risk.

c) Influence on Friction

It is well known that friction hugely depends on temperature. Modelling this effect at system-level has been addressed in details by Mare.[27, 28] It has to be kept in mind that the effect of temperature on friction is poorly documented, including in the suppliers' datasheets.

3.2.7 Causal Bond-Graph Model of EM

The proposed Bond-Graph model of the electrical motor (EM) is presented in Fig. 3-17.

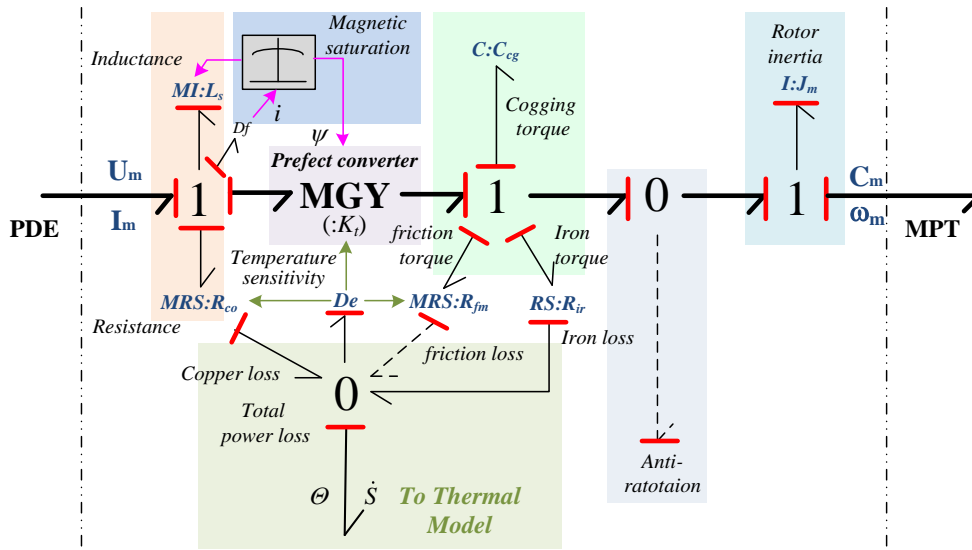


Fig. 3-17 Causal Bond-Graph model of motor considering temperature sensitivity

a) Model Structure

The element GY corresponds to the perfect power transformation between electric and mechanical domains. The global inertia (rotor and screw) and motor friction are modelled as a mechanical inertance J and resistance R_{fm} , respectively. The magnetic saturation can be potentially introduced as a modulating signal. Firstly, by its effects on the perfect power transformation between the current in the field windings and the magnetic flux (gyrator GY

becomes MGY). Secondly, by its effect on inductance of motor windings (inertance I becomes MI). Copper losses are introduced as a resistance element that generates a voltage drop (1 junction) in the electrical domain. According to the proposed models by Eqs.(3.23) and (3.25), iron and friction losses are introduced as two resistor elements that generate torque losses (1 junction) in the mechanical domain. According to Eq.(3.27), the cogging torque is represented by a nonlinear mechanical capacitance (C_{cg}). Any power losses (electromagnetic, electric and mechanical) sum to produce the heat flow at motor heat port. Only one thermal node (0 junction) is considered to make the model simple. As a consequence all effects sensitive to temperature are submitted to the same temperature that is sensed by the De effort detector element. However, if a detailed thermal model of the motor is developed, there is no particular issue in splitting the thermal nodes in different parts associated to windings, magnets, housing, etc.

b) Model causality

The Bond-Graph model of Fig. 3-17 also displays the model's calculation structure by the causal marks. The proposed model structure doesn't neither involve any derivative causality nor algebraic loop. At electrical interface the EM model input is the voltage delivered by the PDE that receives the EM current in response. At mechanical interface, the EM model delivers the rotor angular velocity and receives torque from the downstream mechanical load. There is also a port associated with the motor housing (or stator) that enables reproducing the effect of imperfect anchorage to holding frame (e.g. airframe). At this port, the holding frame imposed the angular position of the stator (ideally as a null position source), while the EM model outputs the torque to be reacted by the holding frame. At thermal interface, the EM model outputs the heat flow generated by EM power losses and receives the temperature that is used internally to reproduce its influence on EM model parameters.

3.3 Incremental Virtual Prototyping

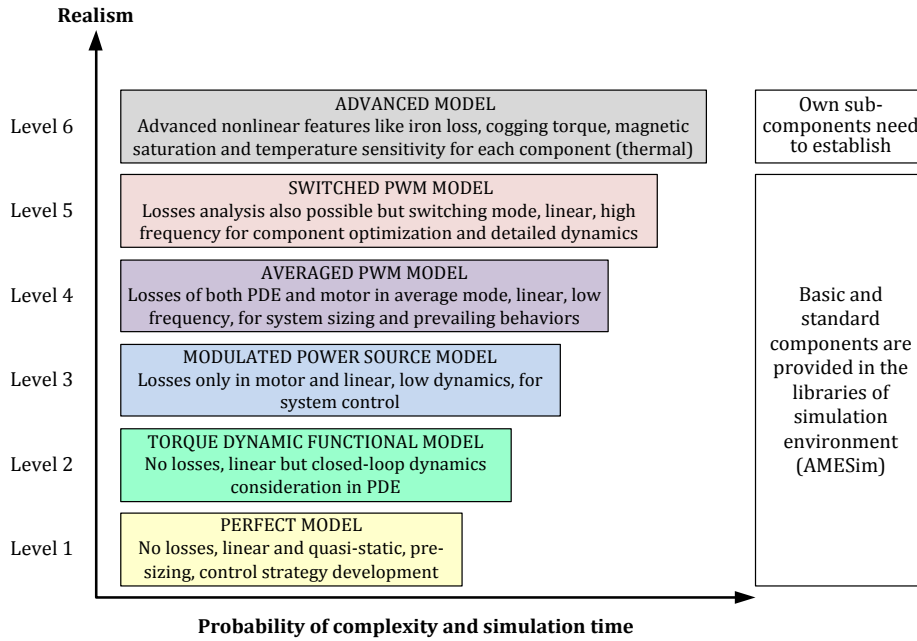


Fig. 3-18 PDE and motor package multi-level modeling and simulation models

An incremental modelling approach is proposed here to progressively analyze the physical effects from sections 3.1 and 3.2. Different modeling levels of different architectures are suggested as a function of the modeling need. Therefore, six generic levels of model package (PDE and EM) can be defined, Fig. 3-18. In this figure, these levels are organized from the simplest one to the most complex one, with the associated impact on accuracy and simulation time cost.

(1) Replaceability: Every package model of PDE and motor can be implemented as a separate replaceable sub-model of the EMA. In this attempt, the same ports and causalities are employed. Taking into account the basic control structure of EMAs system in Chapter 1, for a signal view, same connectors for torque reference and motor velocity feedback are in all models. For the power view, the connectors are identical between models for electrical supply, motor shaft output and heat port of power losses. Of course, some power ports are not involved by the low level models.

(2) Model implementation in a commercial simulation environment: The link between the modelling level (PDE and EM package) and the physical effects to be considered are

summarized in Table 3-4. These models can be built (from existing standard libraries) and developed (from models proposed in the above sections). This particularly applies to the Siemens-AMESim simulation environment that is well established in aerospace industry for multi-physics system-level simulation.

Table 3-4 Choices of motor and PDE for EMAs system-level modelling and simulation

Motor \ PDE	Perfect (TF)	Torque Source	DC bus Supply	Chopper	Inverter	PWM (Average or Dynamic)	Park Transformation	Trapezoidal (back EMF)	Sinusoidal (back EMF)	Hall Sensors	Encoder/Resolver	Power Losses (IGBTs)
Perfect (GY) (Jm)	✓	✓										
DC (Rs, Ls, Jm, Kt)			✓	✓		✓				✓		✓
3-phase/BLDC (Rs, Ls, Jm, Np, ψ_r)			✓		✓	✓	✓	✓		✓		✓
3-phase/PMSM (Rs, Ls, Jm, Np, ψ_r)			✓		✓	✓	✓		✓		✓	✓
Power Losses (Copper, Iron)				✓	✓	✓						✓

Note: ✓ = yes; ✓ = possibility; □ = not applicable (N/A)

(3) Controller structure: The controller structure implemented for simulation of the EMA is based on the cascade multi-loops control strategy, which is presented in Chapter 2, Fig. 3-19, that displays the PDE and EM sub-system under study.

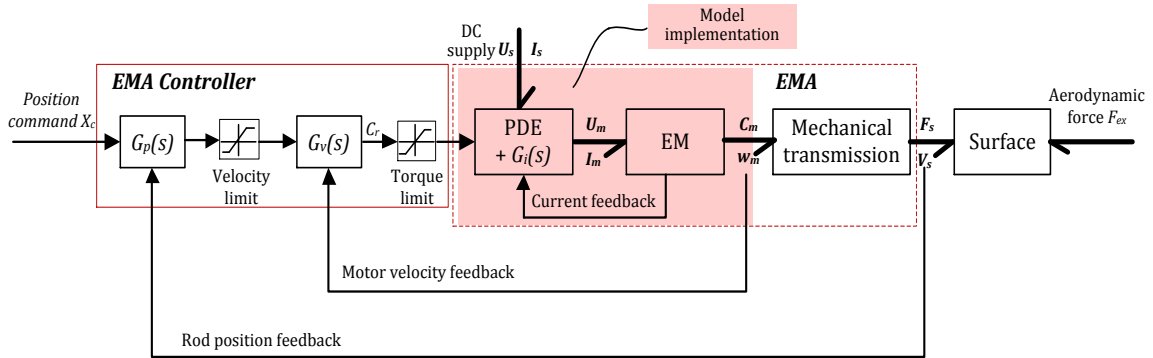


Fig. 3-19 Schematic diagram of EMA system for PDE and EM model implementation

The conventional control method of current loop in motor is preferred to PI corrector, in which an equivalent over-damped closed-loop is set to avoid the overshoot [29]. Generally, a mathematically expressed to get the PI corrector parameters of K_{ip} and K_{ii} are expressed as follows:

$$\frac{K_{ip}}{K_{ii}} = \frac{L_m}{R_m} \quad (3.34)$$

The design rule for EMA controller has been studied and presented in a previous chapter. The implementation of the different levels of the PDE and EM package is detailed below. The detailed study of the mechanical transmission is addressed in the next chapter. In this section, it is modelled as a perfect rotary to linear power transformation, as illustrated in Fig. 3-20. The driven load (e.g. flight control surface) is modelled by combining its inertial effect and the compliance of attachment to the EMA plus the external load, e.g. coming from the aerodynamic forces.

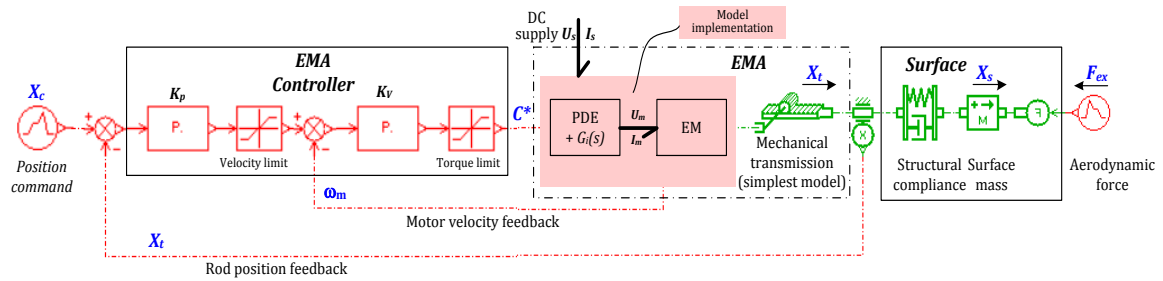


Fig. 3-20 Controller, mechanical transmission and load model Implementation in AMESim

3.3.1 Level 1: Perfect Model of PDE and EM

The perfect package model of PDE and EM is the simplest one. It is linear, without any power loss. However, the rotor inertia, although being a parasitic effect, is not neglected: it is the main driver of closed loop performance and it is required to meet causality requirements. At this modeling level, detailed dynamics, thermal effects and electrical supply are not considered. The torque reference generated by the controller is directly applied to the rotor shaft inertia as a perfect torque source. This means that the current loop, the PDE and the electromagnetic part of the EM are supposed to behave perfectly. This model, Fig. 3-21, suits well system control design or functional simulation engineering activities.

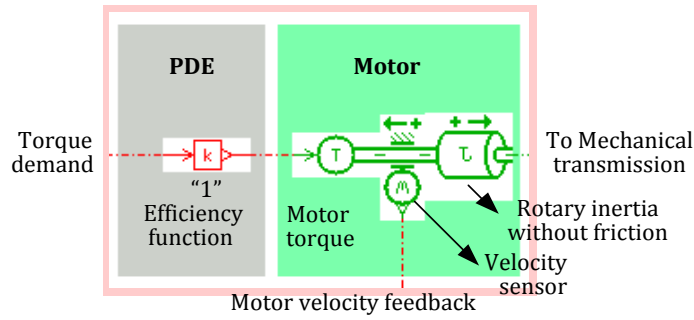


Fig. 3-21 Realization of perfect model of PDE and motor

3.3.2 Level 2: Torque Dynamic Functional Model

When designing the EMA position and speed controllers, the dynamics at which the electromagnetic torque establishes in response to the torque demand cannot be neglected. In this case, the dynamic performance of motor current control loop in PDE can be considered as a first and simple approach, by adding a correctly damped second order system (typically with a natural frequency of a few hundreds of Hz) as shown on Fig. 3-22:

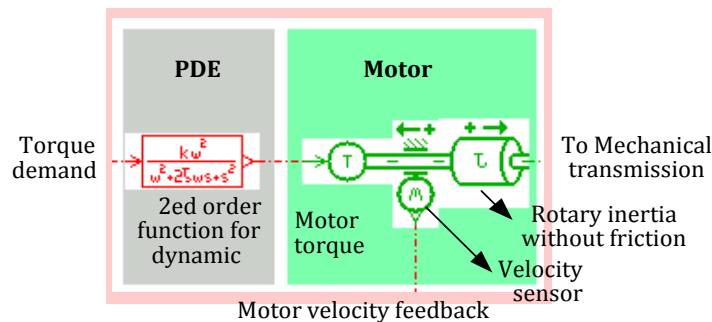


Fig. 3-22 Addition of a simplified model of the torque loop dynamics in the AMESim model

3.3.3 Level 3: PDE as a Perfect Modulated Power Source

In this level, the power losses in PDE (chopper or inverter) are ignored, in order to simplify sizing and control application activities. This is achieved by considering the PDE as a perfect modulated power source. This enables accessing the power drawn for the electrical power supply. The motor model is improved by introducing the resistance and inductance of windings.

Even if the EM is of brushless type (permanent magnet synchronous machine or brushless DC motor), a progressive approach for reducing complexity in controller design consists in

considering first an equivalent brushed DC motor driven by a chopper that implements the H-bridge. The synchronous-type brushless motor, generally 3-phase, driven by the inverter can be introduced in a second step, as illustrated by Fig. 3-23. In both models the control signal is adapted to generate the duty cycle signal α .

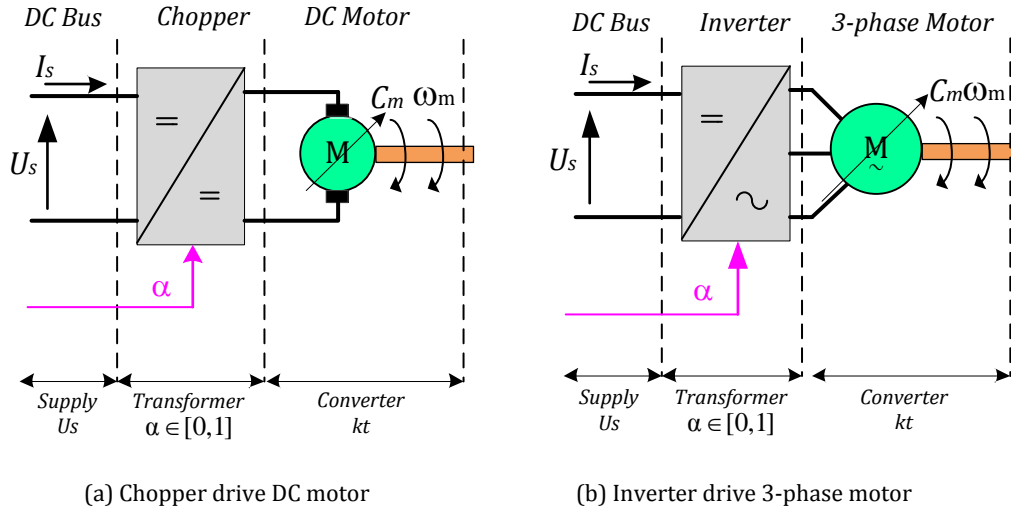


Fig. 3-23 Structure of modulated power source for DC motor and 3-phase Motor

a) Chopper-Driven DC Motor

The chopper driven DC motor is a common model for EMAs system modeling and simulation. Indeed, it can easily implement the structure of the current loop and the effect of copper loss, generally the major power loss, for preliminary analysis of power losses. As shown in Fig. 3-24, the PDE motor can be simplified to a modulated voltage source which is driven by the controller. A current sensor is introduced to enable the inner current loop to be modelled. At this stage, new parameters are introduced: for the motor, resistance, inductance and torque constant, for the torque loop, the PI gains of the current loop. The copper loss in unit $[W]$ can be accessed through the thermal port of the standard DC motor model.

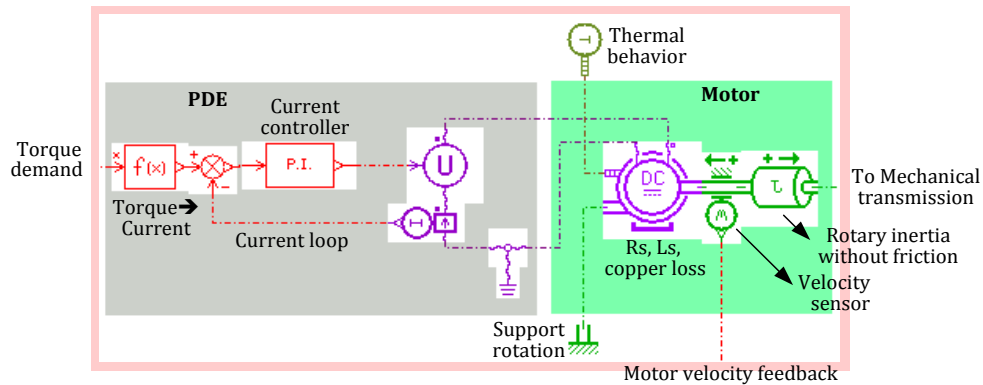


Fig. 3-24 Realization of power source modulated model applied for DC motor

b) Inverter Drive and 3-phase brushless Motor

The intention is now to consider a 3-phase motor, which is nowadays widely implemented in aerospace industry, in particular in EMAs. As for the DC motor, the model from the standard library considers the resistance and the inductance of the windings in addition to the perfect electromagnetic power transformation. The generic block-diagram of the inverter drives the 3-phase motor in Fig. 3-25.

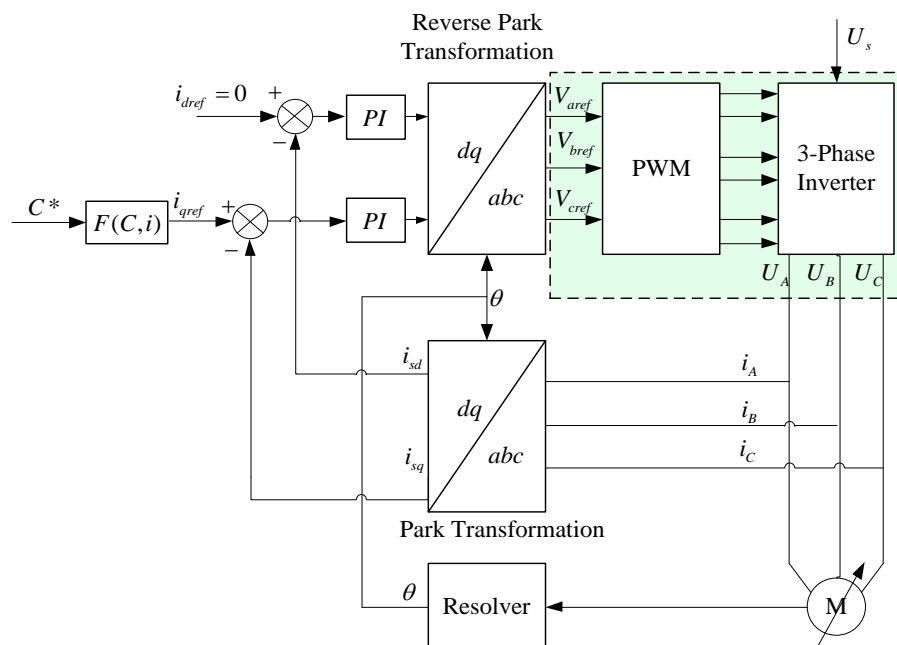


Fig. 3-25 Schematic diagram of inverter drive for 3-phase motor

The 3 legs of the PDE generate the voltages applied to the motor phases, according to the drive signals elaborated by the field-oriented control strategy [30]. This control strategy involves the Park transformation that links the currents in the motor phases (I_A , I_B , I_C) and the

direct /quadratic currents I_{sd} , I_{sq} [31, 32], as a function of the rotor/stator angle. Both I_{sd} and I_{sq} current loop controller are of PI type. Here, the zero direct axis current ($I_{dref}=0$) strategy is used for PMSM control, which is a strategy most popular and simple for application. The direct axis reference current is let to zero leaving only the torque or quadrature axis current in place. So it has the constant direct axis flux linkages to produce a constant motor torque.

As for the perfect inverter model, PWM dynamics and power losses are not to be considered. Each leg is modelled as a voltage source that is modulated by the associated output of the reverse Park transform. The associated model is shown in Fig. 3-26.

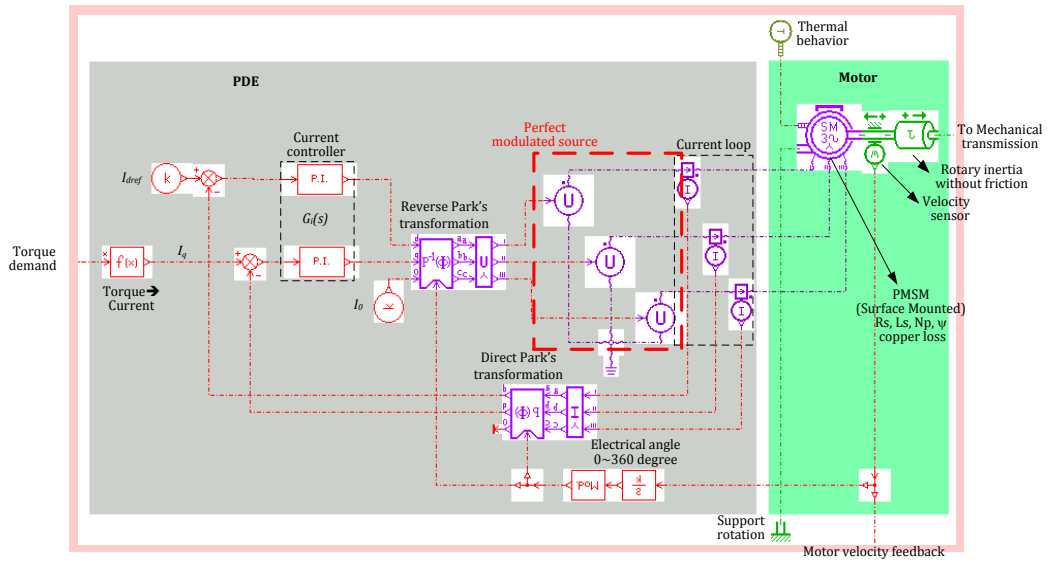


Fig. 3-26 Realization of power source modulated model applied for 3-phase motor (PMSM)

3.3.4 Level 4: Averaged Inverter Model

In fact, the level 3 model is a functional model that does not reproduce the real behavior of the power transistors. In particular, it neglects the switching and conduction losses and it does not explicitly involve the DC supply port of the PDE. Although these losses do not impact significantly the control performance, they cannot be neglected for assessing the thermal balance of the EMA, in particular of the PDE, and the electrical power flowing at the supply port of the PDE. In practice, the commutation cells of the PDE are driven in on/off mode through PWM, in order to not be sensitive to the linearity of the power transistors. The PWM frequency is several times the maximum electrical frequency of the motor in order to

generate winding voltages as close as to possible to a sine wave form. For example, for an EM which has 8 poles and a nominal velocity of 3000 (r/min), for each sine phase the electrical frequency is 400 Hz, using 20 samples per sine, the switching frequency is 8 kHz.

At this level, simulating an on/off switching at such a frequency increases drastically the computational load. For thermal and power consumption analysis, this issue can be removed using an equivalent average model of the PDE. This model is easily achieved because such a model is available in the standard library “Electric Motor and Drive”, leading to the model displayed on Fig. 3-26. Now, the PDE model explicitly involves 2 new power ports, one for the DC electrical supply and one thermal port that outputs the heat generated by the power transistors.

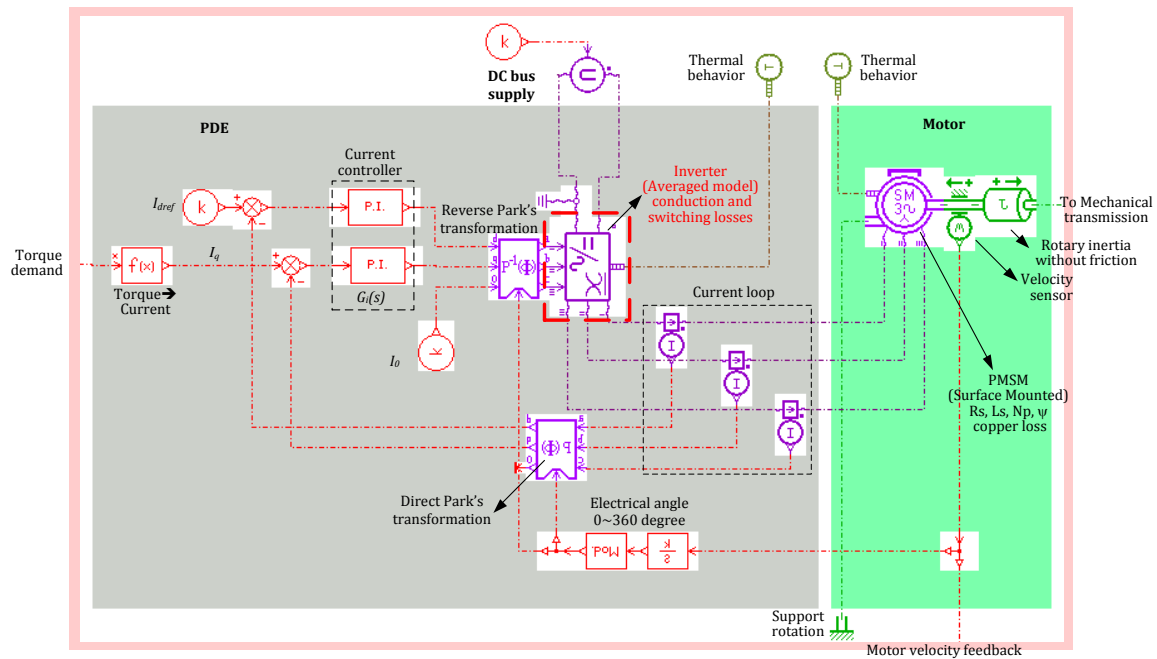


Fig. 3-27 Realization of averaged inverter model applied for PMSM

3.3.5 Level 5: Switched PWM Model

In switched PWM model, the focus is put on the high frequencies dynamics and on pollution of DC supply. For this reason, the high frequency PWM switching shall be modelled and the expense of simulation load shall be accepted. The proposed model re-uses as far as possible the standard library. The PWM module is driven by the Park reverse transformation block and generates the 6 switching orders sent to the power transistors. Each transistor model also

comes from the standard library. It outputs separately the conduction and switching losses. All losses are summed to make the overall PDE power loss that is sent to the thermal port. These changes are displayed in Fig. 3-28.

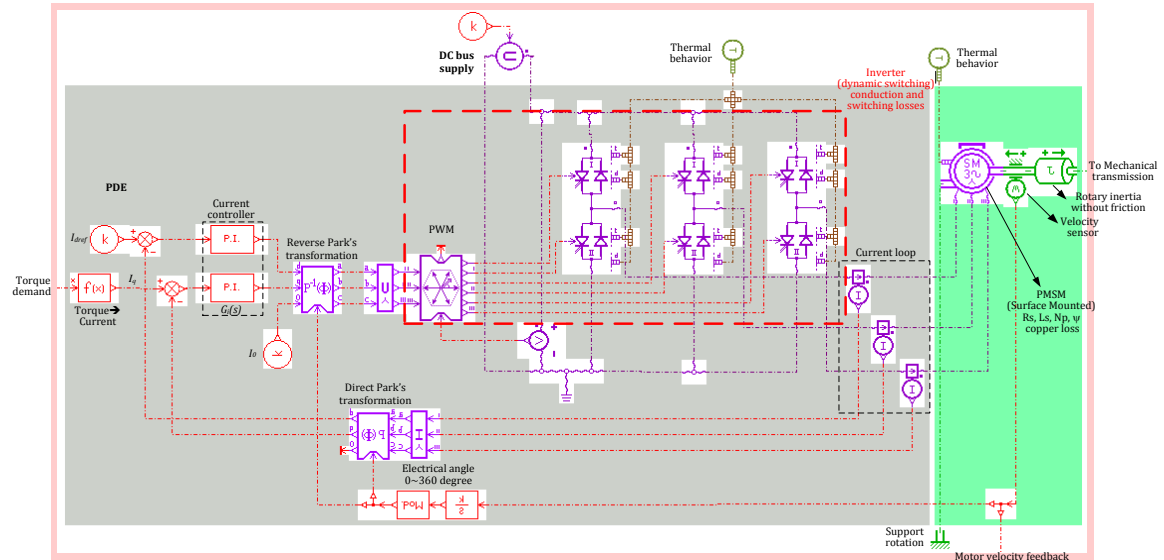


Fig. 3-28 Realization of PWM dynamic behavior of PMSM control

3.3.6 Level 6: Advanced Motor Model

The standard three-phase PMSM motor model is already integrated in the software model library. However, this model does not consider iron losses, cogging torque, magnetic saturation or hysteresis. For making an advanced motor model, these effects must be taken into account. Thus, a subcomponent is designed, Fig. 3-29, which can replace the standard motor model. It implements Eqs. (3.24), (3.26) and (3.27) using standard blocks from the library for signals (functions of one variable) and for mechanics (torque summation, friction, sensors). A specific model is created to provide the speed sum that corresponds to the 0 junctions.

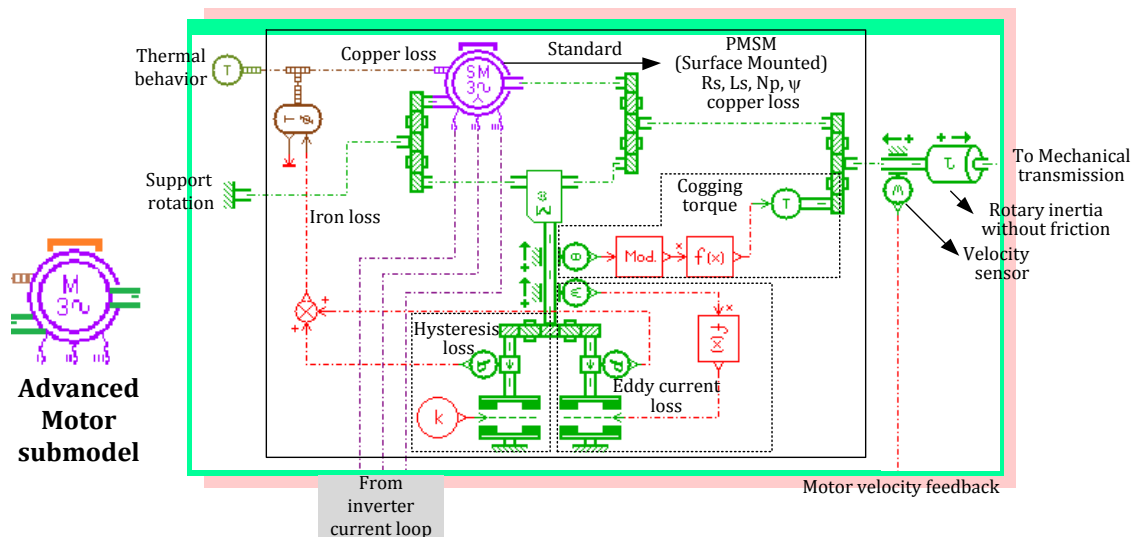


Fig. 3-29 Proposed advanced 3-phase submodel considering iron loss and cogging torque

Of course, the same incremental approach model can be continued, e.g. by introducing

- the current sensors and signal conditioning (e.g. low-pass filters)
- the commutation delays introduced to drive the upper and lower power transistors of each leg
- the passive filters on the supply and motor lines
- the supply rectifier and chopper.

3.4 Numerical Simulation and Analysis

In this section, the object is to illustrate how the PDE and ME models become more realistic when the modelling level is increased. For this reason, a basic model of mechanical transmission is used in all levels. Power losses and compliance are not considered and the inertial effect of the mechanical power transmission is included in the motor rotor inertia parameter. There is no change too in the controller parameters between the different model levels. The parameters of the EMA controller (as in Chapter 2), ideal mechanical transmission and load are listed in Table 3-5.

Table 3-5 EMA controller, mechanical transmission and load parameters

Parameter	Value	Parameter	Value
$G_p(s)$ position P-gain K_p (rad·s ⁻¹ ·m ⁻¹)	4500	Current loop integral gain K_{ii} (V s ⁻¹ /mA)	17.7
$G_v(s)$ velocity P-gain K_v (N·m/(rad/s))	0.47	Lead of roller-screw p (mm)	2.54
Amplifier saturation velocity (rad/s)	314	Structural stiffness k_s (N/m)	5×10 ⁹
Amplifier saturation torque (N·m)	10	Structural damping b_s (N·s/m)	1×10 ⁴
Current loop proportional gain K_{ip} (V/A)	67.8	Equivalent surface mass M_s (kg)	600

Other generic parameters of PDE and EM are listed in Table 3-6, which links to different modeling levels by complexity.

Table 3-6 Parameters of PDE and EM for multi-level modelling and simulation

Parameter	Value	Reference source	Level 1	Level 2	Level 3	Level 4	Level 5	Level 6
Total inertia of rotor and screw J_m (kgm ²)	0.00171	Motor datasheet of Exlar EMA [33]	√	√	√	√	√	√
Current loop damping factor ξ_i (-)	0.7		×	√	×	×	×	×
Current loop natural frequency ω_i (Hz)	600		×	√	×	×	×	×
Motor windings resistance R_{mw} (Ω)	1.77		×	×	√	√	√	√
Motor windings inductance L_m (mH)	6.78		×	×	√	√	√	√
Motor torque constant K_t (N·m/A)	1.65		×	×	√	√	√	√
Motor rated torque C_N (N·m)	10	IGBTs datasheet [34, 35]	×	×	√	√	√	√
Number of pole pairs n_p (-)	4		×	×	√	√	√	√
Supply DC voltage U_s (V)	565		×	×	×	√	√	—
Transistor on-state resistance R_{ton} (Ω)	0.013		×	×	×	√	√	—
Diode forward resistance R_{don} (Ω)	0.0087		×	×	×	√	√	—
Transistor forward voltage drop (V)	1		×	×	×	√	√	—
Diode forward voltage	1.3		×	×	×	√	√	—

drop (V)								
Switching frequency f_{sw} (Hz)	8000		×	×	×	√	√	–
Switching loss energy per period @ 600V/40A E_{sw} (J)	0.0133		×	×	×	√	√	–
Threshold input switch value	0.5		×	×	×	×	√	–
Switching energy dissipation time d_t (s)	2×10^{-7}		×	×	×	×	√	–
Mass of magnetic material stator M_B (kg)	4	Motor datasheet of Exlar EMA [33]	×	×	×	×	×	√
Magnetic flux density B_m (T)	2		×	×	×	×	×	√
Steinmetz constant of hysteresis loss k_{hy} (-)	5.8×10^{-3}		×	×	×	×	×	√
Steinmetz constant of eddy current loss k_{ed} (-)	9.3×10^{-6}	Assumed from literature[4]	×	×	×	×	×	√
Factor of the maximum cogging torque (-)	0.01		×	×	×	×	×	√
Temperature dependency of resistance ε_r (-)	–	unknown	×	×	×	×	×	–
Temperature dependency of materiel magnet ε_m (-)	–	unknown	×	×	×	×	×	–
Saturation function of motor torque and current	–	unknown	×	×	×	×	×	–
Temperature dependency of motor friction (-)	–	unknown	×	×	×	×	×	–

Note: √ : must be applicable; – : may be applicable; × : cannot be applicable

In order to verify the models and compare the interest of multi-level modelling for the PDE and EM, the simulation can support various engineering needs: control design, energy consumption or thermal balance, dynamic performances and pollution of power supply.

3.4.1 Interest for Control Design

EMA model is used to simulate the position-control of a commercial aircraft aileron. The closed-loop performance is addressed in the time domain with a single simulation (duration $t = 2$ s) that combines:

- for the pursuit function, a pilot step demand of 10mm (6% full stroke) occurring at $t = 0.1$ s
- for the disturbance rejection function, an external aerodynamic force disturbance F_{ex} of 10 kN (40% rated EMA output force) occurring at $t = 1$ s.

The responses of levels 1, 2, 3, 4 and 6 (no PWM switching mode, level 5) are compared with respect to control performance in Fig. 3-30. The black dash line is the position command step signal. Level 1 response is that of the basic model that has been used for verifying the correct preliminary setting of the controller parameters and of the EMA functional parameters in Table 3-5. Levels 2, 3, 4 responses correspond to section 3.3.5 that consider different physical effects. All models produce globally the same static accuracy (closed loop static stiffness of 100 kN/mm), stability (overshoot 4.5 to 5.5 %) and dynamics (response time 0.11 s). Level 3 and 4 display no difference in position performance. Meanwhile, as levels 3 and 4 model the PI vector control of the current loop, stability is slightly reduced from models 1 and 2, by the additional dynamics. When the motor losses are considered in addition (level 6), the iron losses increase the power losses and therefore increase the closed-loop damping.

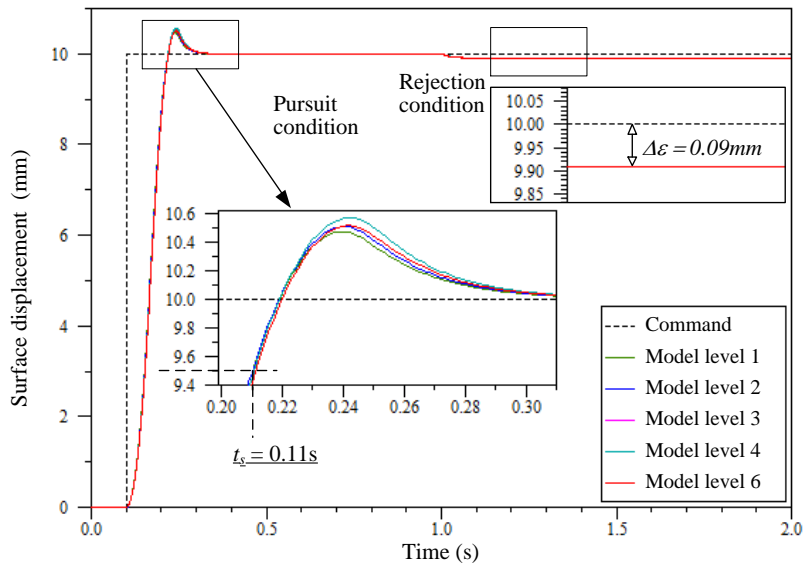


Fig. 3-30 Simulation response of surface position in different model levels

Fig. 3-31 displays the motor torque for the same excitation of Fig. 3-30. The motor torque is plotted versus time to highlight the differences between the different modelling levels. The position command makes the motor current saturating during 40 ms. The Pi gains of the field-

oriented control are set to get globally the same response as the level 2 model. The effect of the motor windings resistance that is introduced since level 3 clearly appears as a reduction of the electromagnetic torque when the current is saturated. The introduction of the cogging torque in level 6 contributes in the same manner to reduce the electromagnetic torque in the saturated domain.

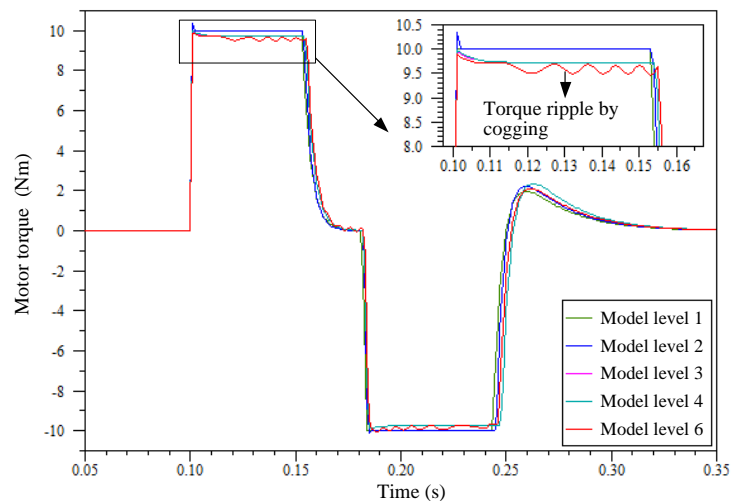


Fig. 3-31 Simulation result of motor torque in different model levels

3.4.2 Interest of PWM Switching Dynamics

The interest of modelling the PWM switching is assessed by comparing the responses of model levels 4 (average) and 5 (switched). The motor phase voltage and current are respectively plotted in Fig.3-32 and Fig. 3-33.

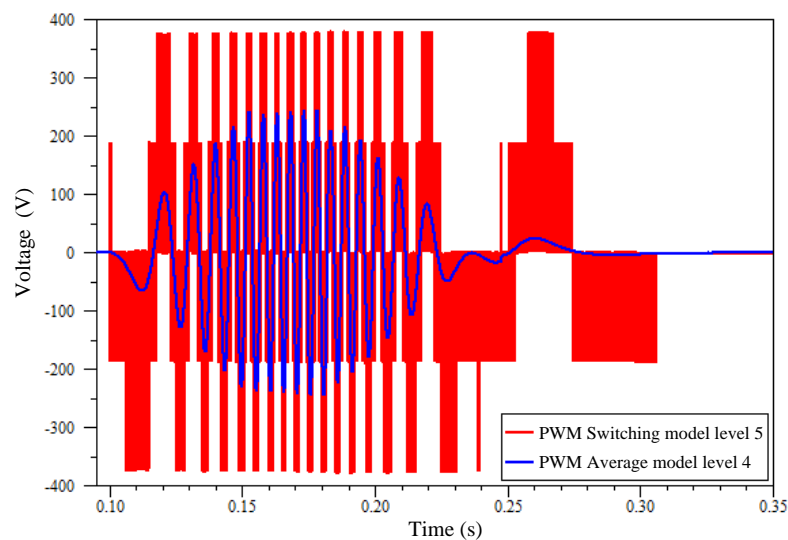


Fig. 3-32 Simulation results with motor phase-A current

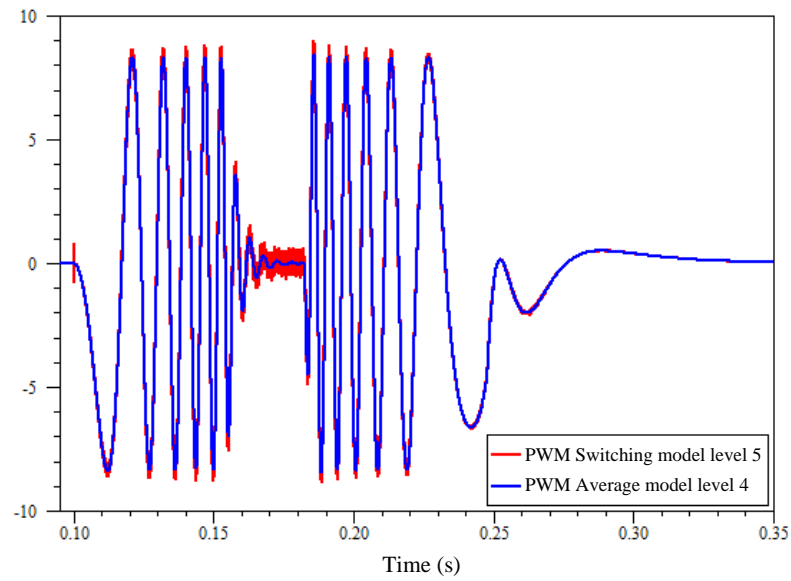


Fig. 3-33 Simulation results with motor phase-A voltage

The d-axis and q-axis currents of the field-oriented control, Fig. 3-34 shows dynamic performance comparison of PWM switching of level 5 and PWM average model level 4. In model level 5, at $t = 0.24$ s the q-axis dynamic current is nearly null, because the surface archives the peak overshoot of displacement and has the whistle stop.

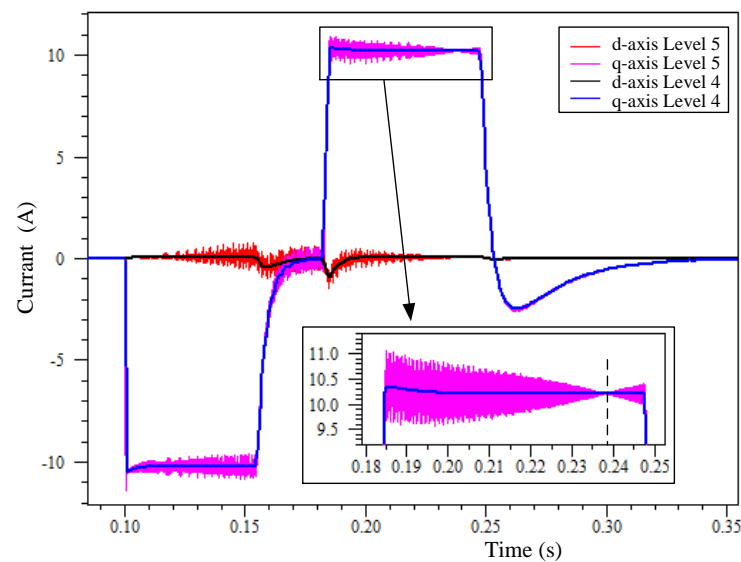


Fig. 3-34 Simulation results with d-axis and q-axis current

3.4.3 Interest for Power Network Pollution Analysis

The effect of high frequency switching for driving the inverter legs with PWM is addressed by comparing the response of the models levels 4 and 5. In level 4, where PWM is replaced by its

low frequency equivalent. The PWM generates current spikes on the DC bus which magnitude can reach 4 times the mean current. For load rejection stability mode, although the average current output from DC supply is 0.1 A, the peak current reaches 5 A, which is 50 times greater and pollutes the DC power network.

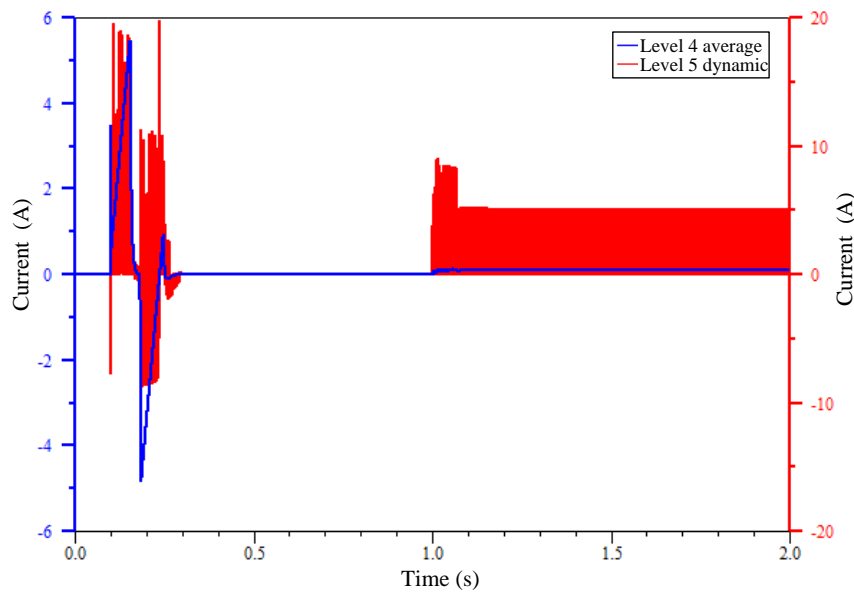


Fig. 3-35 Current pollution network comparison, PWM average and PWM switching

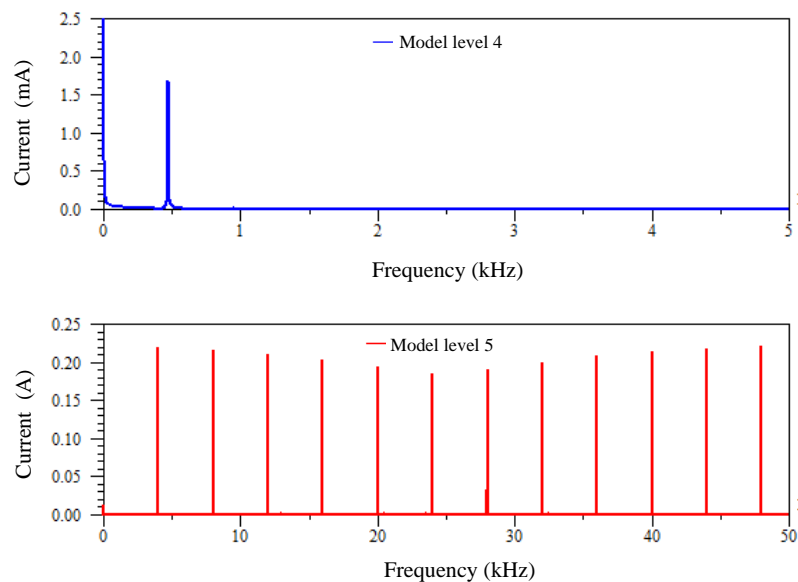


Fig. 3-36 FFT Current pollution network comparison, PWM average and PWM switching

Fig. 3-36 shows the spectrum analysis of the current through a fast Fourier transform (FFT) applied to the time response sampled at 100 kHz in the interval [1 s; 1.5s]. It is reminded that the DC bus supply is considered as a perfect voltage source because its study is out of scope of

the present work. The PWM control generates a rectangular wave current that produces high energy harmonics

3.4.4 Interest for Power Consumption Analysis

The same model excitation is used for comparative analysis of the energy losses and energy consumption. In Fig.3-36, the power losses in PDE and EM are compared for the model level 6. The copper loss (red plot) is always the major contributor. Logically, the iron losses (blue plot) depend directly to velocity. The PDE losses due to switching and conduction (black plot) represent 30% of the copper losses in the saturated part of the pursuit mode, and 80% in the rejection mode. Finally, this plot highlights that none of the PDE, iron and copper losses can be neglected.

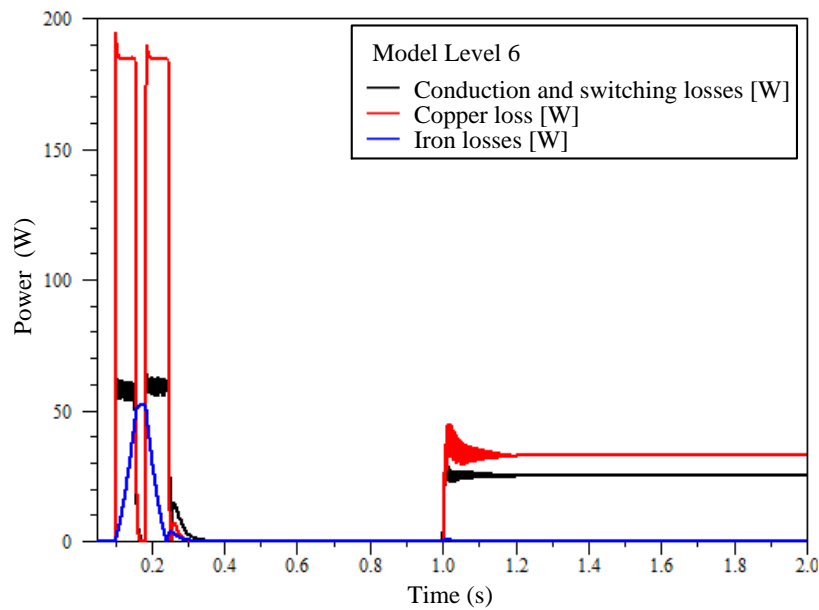


Fig. 3-36 Power losses comparison for EMA system power sizing in model level 6

3.5 Conclusion of Chapter 3

In the present chapter, an incremental modelling approach has been proposed using the Bond-Graph formalism. Starting from the model of a perfect PDE, the physical effects have been progressively introduced: conduction and switching losses for PDE, copper and iron losses plus rotor inertia for the EM, control dynamics and PWM control of the PDE, influence of operating temperature. Causalities have been addressed to enable causal numerical solvers

to be used for model simulation.

It has been shown how the progressive model levels can be implemented in a commercial simulation environment by taking benefit of the available standard libraries. Six modelling levels have been implemented and compared with respect to their impact on the simulated responses using the example of an aileron actuator. It has been shown that the above proposals provide engineers with models that can be developed in an incremental way with the benefit of keeping the same model structure during the various steps of simulation-aided development: control design, PMSM dynamics performance, power consumption and thermal balance. The influence of temperature on PDE and EM has not been implemented totally. However, if any information is available from PDE and EM datasheets, it can be easily introduced in the models according to the model structure and causality defined by the Bond-Graph. The implementation of the temperature effect from the Bond-Graph will be illustrated for friction in the next chapter.

References

- [1] T. P. Dever, K. P. Duffy, A. J. Provenza, P. L. Loyselle, B. B. Choi, C. R. Morrison, *et al.*, "Assessment of technologies for noncryogenic hybrid electric propulsion," 2015.
- [2] W. David, W. Thomas, C. Louis, L. Quinn, B. Wendell, B. Jared, *et al.*, "Dynamic Heat Generation Modeling of High Performance Electromechanical Actuator," in *48th AIAA Aerospace Sciences Meeting Including the New Horizons Forum and Aerospace Exposition*, ed: American Institute of Aeronautics and Astronautics, 2010.
- [3] S. Bęczkowski. IGBT vs. Power MOSFET for switching applications [Online]. Available: <http://electronics.stackexchange.com/questions/68971/igbt-vs-power-mosfet-for-switching-applications-where-to-draw-the-line>
- [4] R. Krishnan, *Permanent magnet synchronous and brushless DC motor drives*, 1st ed. USA: CRC press, 2010.
- [5] A. D. Rajapakse, A. M. Gole, and P. L. Wilson, "Electromagnetic transients simulation models for accurate representation of switching losses and thermal performance in power electronic systems," *Power Delivery, IEEE Transactions on*, vol. 20, pp. 319-327, 2005.
- [6] B. Cassimere, S. D. Sudhoff, B. Cassimere, D. C. Aliprantis, and M. D. Swinney, "IGBT and PN junction diode loss modeling for system simulations," in *IEEE International Conference on Electric Machines and Drives*, San Antonio, TX, USA, 2005, pp. 941-949.
- [7] F. Blaabjerg, J. K. Pedersen, S. Sigurjonsson, and A. Elkjaer, "An extended model of power losses in

- hard-switched IGBT-inverters," in *Industry Applications Conference, 1996. Thirty-First IAS Annual Meeting, IAS '96., Conference Record of the 1996 IEEE*, 1996, pp. 1454-1463 vol.3.
- [8] IGBT Datasheet RfH65S04DPQ [Online]. Available: <http://www.powersystemsdesign.com/igbts-impact-efficiency-and-ruggedness-in-solar-inverter-apps>
- [9] EDV-255 Electronic Devices of Diode [Online]. Available: <http://people.senecac.on.ca/john.kawenka/EDV255/diodes.html>
- [10] G. G. Parma and V. Dinavahi, "Real-Time Digital Hardware Simulation of Power Electronics and Drives," *Power Delivery, IEEE Transactions on*, vol. 22, pp. 1235-1246, 2007.
- [11] L. imagine, "AMESim electrical static conversion library,rev.13," ed, 2014.
- [12] R. L. Libby, T. Ise, and L. Sison, "Switching characteristics of SiC Schottky diodes in a buck DC-DC converter," in *Proceedings in. Electronic and Communications Engineering Conference*, 2006.
- [13] S. Kouro, M. Perez, H. Robles, and J. Rodriguez, "Switching loss analysis of modulation methods used in cascaded H-bridge multilevel converters," in *Power Electronics Specialists Conference, 2008. PESC 2008. IEEE*, 2008, pp. 4662-4668.
- [14] O. Al-Naseem, R. W. Erickson, and P. Carlin, "Prediction of switching loss variations by averaged switch modeling," in *Fifteenth Annual IEEE Applied Power Electronics Conference and Exposition (APEC)*, New Orleans, LA, USA, 2000, pp. 242-248.
- [15] S. Munk-Nielsen, L. N. Tutelea, and U. Jaeger, "Simulation with ideal switch models combined with measured loss data provides a good estimate of power loss," in *Industry Applications Conference, 2000. Conference Record of the 2000 IEEE*, 2000, pp. 2915-2922 vol.5.
- [16] D. Graovac and M. Pürschel, "IGBT Power Losses Calculation Using the Data-Sheet Parameters," I. A. N. V11, Ed., ed, 2009.
- [17] M. Aung and V. Dinavahi, "FPGA-based real-time emulation of power electronic systems with detailed representation of device characteristics," in *Power and Energy Society General Meeting, 2011 IEEE*, 2011, pp. 1-11.
- [18] ON Semiconductor, IGBT datasheet NGTB15N60EG [Online]. Available: http://www.onsemi.com/pub_link/Collateral/NGTB15N60E-D.PDF
- [19] A. Młot, M. Korkosz, and M. Łukaniszyn, "Iron loss and eddy-current loss analysis in a low-power BLDC motor with magnet segmentation," *Archives of Electrical Engineering*, vol. 61, pp. 33-46, 2012.
- [20] B. Frenzell, R. Hanitsch, and R. M. Stephan, "Saturation effects in small brushless DC motors. A simplified approach," in *Power Electronics and Variable Speed Drives, 1996. Sixth International Conference on (Conf. Publ. No. 429)*, 1996, pp. 99-102.
- [21] J. Fu, I. Hazyuk, and J.-C. Maré, "Preliminary design rules for electromechanical actuation systems - effects of saturation and compliances," in *5th CEAS Air & Space Conference*, Delft, Netherlands, 2015.
- [22] L. Wang and J.-C. Maré, "A force equalization controller for active/active redundant actuation system involving servo-hydraulic and electro-mechanical technologies," *Proceedings of the*

- Institution of Mechanical Engineers, Part G: Journal of Aerospace Engineering*, vol. 228, pp. 1768-1787, 2014.
- [23] T. R. Kuphaldt. Lessons in electric circuits; Volume II. [cited 2006 Jan 18] [Online]. Available: http://isc.dcc.ttu.ee/Public/Kuphaldt/AC/AC_13.html
- [24] P. M. Churn, C. J. Maxwell, N. Schofield, D. Howe, and D. J. Powell, "Electro-hydraulic actuation of primary flight control surfaces," in *IEEE Colloquium on All Electric Aircraft (Digest No. 260)*, London, UK, 1998, pp. 3/1-3/5.
- [25] P. C. Krause, O. Wasynczuk, S. D. Sudhoff, and S. Pekarek, *Analysis of electric machinery and drive systems*, 2ed ed. vol. 75. USA: John Wiley & Sons, 2013.
- [26] Temperature dependency of magnet materials [Online]. Available: <http://www.20sim.com/>
- [27] J.-C. Maré, "Friction modelling and simulation at system level: a practical view for the designer," *Proceedings of the Institution of Mechanical Engineers, Part I: Journal of Systems and Control Engineering*, pp. 728-741, 2012.
- [28] J.-C. Maré, "Friction modelling and simulation at system level: Considerations to load and temperature effects," *J. Systems & Control Engineering*, vol. 229, pp. 27-48, / 2015.
- [29] L. Wang, K. Xiao, L. de Lillo, L. Empringham, and P. Wheeler, "PI controller relay auto-tuning using delay and phase margin in PMSM drives," *Chinese Journal of Aeronautics*, vol. 27, pp. 1527-1537, 12// 2014.
- [30] R. Krishnan, *Electric motor drives: modeling, analysis, and control*, 1st ed. New Jersey, USA: Prentice Hall Inc, 2001.
- [31] L. Kien Minh, H. Hung Van, and J. Jae Wook, "A method to improve the accuracy of synchronous control systems," in *Industrial Informatics (INDIN), 2013 11th IEEE International Conference on*, 2013, pp. 188-193.
- [32] S. Baldursson, "BLDC Motor Modelling and Control-A Matlab®/Simulink® Implementation," 2005.
- [33] Exlar. Advantages of Roller Screw Technology [Online]. Available: <http://exlar.com/why-exlar/many-advantages-roller-screw/>
- [34] S. Clemente, A. Dubhashi, B. Pelly, and G. Dokopolous, "Application characterization of IGBTs: International rectifier application note-AN-983," in *International Rectifier Inc*, ed, 2012.
- [35] S. Clemente, "Application characterization of IGBTs: International rectifier application note-AN-990," in *International Rectifier Inc*, ed, 2012.

Chapter 4

Mechanical Power Transmission

Mechanical transmission is a key part of electromechanical actuators (EMA) that are being developed for implementation of more electrical aircraft. In the frame of the model-based design and development of mechanical transmission system, the designers and manufacturers must consider with great care the parasitic effects coming from the imperfection of technology: friction, backlash, compliance, etc. The mechanical friction is a highly nonlinear effect that depends on velocity, transmitted forces and temperature. It plays a significant role because it determines the mechanical efficiency and therefore the motor torque sizing and thermal balance. The compliance comes from deformation of EMA parts under stress. The mechanical stiffness decreases around the null transmitted force where not all the contacts are fully loaded. So, getting a realistic model of mechanical compliance is also important. Depending on design and service, it can show pre-loading or backlash. Both friction and compliance affect the EMA closed-loop performances.

Nowadays, for mechanical transmission system-level modeling and simulation, the most conventional method is to only consider the functional degree-of-freedom that leads to 1-DoF models. In this approach a single kinematic DoF is modelled at each location of power path. Compliance and friction are globally modeled: bearings, joints and end-stop are not explicitly considered. Consequently the simulated responses of a so simplified model have a low realism, which can be sufficient for some very-preliminary engineering activities.

Developing a lumped parameters model with two degrees of freedom (2-DoF) (translation/rotation) can provide a more efficient way to consider, with limited complexity, the coupling between translational (EMA output is translational) and rotational effects (electric motor generates rotational motion). This approach enables the bearings and joints to be added for component-level performance analysis. The key idea consists in decomposing

the EMA into several generic subcomponents with mechanical “quadriport” model that can easily combine the 2-DoF motion. Its development is facilitated by intensive use of Bond-Graph modelling. This provides a useful support for architecture selection, sizing, assessment of response to failure, health monitoring and control design [3]. Besides, the proposed 2-D lumped parameters models are helpful to evaluate thermal balance and to analyze energy losses through system-level thermal modeling and simulation.

4.1 Power Screw Mechanism

In practice, the mechanical transmission is a mechanical subsystem for converting rotary mechanical power from motor output into translational mechanical power. Two technologies are available in EMAs to realize this transformation: ball screws and roller screws. However, the choices are usually along with EMA structure designing. Most ball screw designing concepts are implanted in geared type EMAs which require additional gear reduction due to the low gear ratio (lead) of the screw. Unlike ball-screws, roller screws offer the advantage of a higher gear ratio that enables the gear reduction to be removed. Such a design is usually called direct-drive type linear EMAs.

4.1.1 Ball Screw

A typical ball screw’s mechanical assembly is as shown below in Fig.4-1, and it includes two circular shaped grooves, one is a circular shaped groove that is cut in a helix on the shaft and the other is the nut ball which matches the shaft groove. The balls moving within the groove form the end of the race to turn to the beginning of the race, and the nut is retained in position on the shaft. When the nut rotates relative to the shaft (screw), the balls move in one direction along the groove to support the axial load. The balls are constrained in the return groove start colliding with each other. The balls are therefore being continuously circulated.

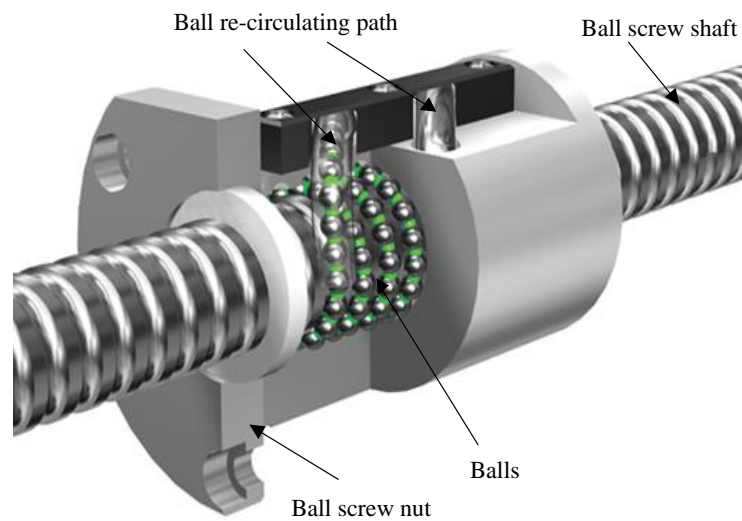


Fig. 4-1 Ball screw with re-circulating device [1]

4.1.2 Roller Screw

Another type of power screw is the roller type, which has the special design for transmitting force to load. A standard configuration of roller screw is shown in Fig.4-2, it has planetary design and travels along the central shaft as it spins. The nut includes a number of special threaded rollers, typically up to more 10 rollers. They are arranged around the central screw shaft, where each roller takes part of the load.

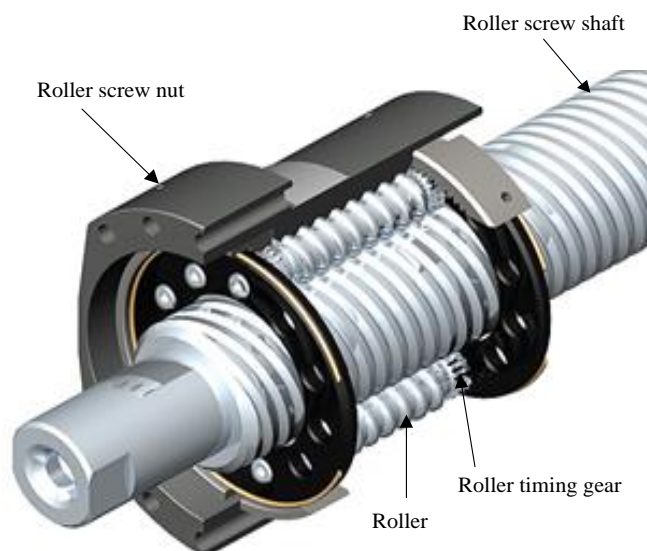


Fig. 4-2 Ground shaft planetary roller screw [2]

4.1.3 Performances Comparison

Compared to the ball screw, the roller screw has many advantages; for instance, Higher stiffness, higher rotational speeds, higher load capacity and quiet operation. However, the increased number of contacts plays against friction and the efficiency of RS is lower than that of BS for the same lead, see examples.

(a). Load Capacity and Efficiency

Roller screws are designed to have larger radius at the point of contact, meaning that more contact points will fit within the same relative space. Because the number of contact points is greater, roller screws have high load-carrying capacities, as well as improved stiffness. This typically means that a roller screw actuator takes up less space in order to meet a designer's load requirement than a similarly sized ball screw [3], seen Fig. 4-3.

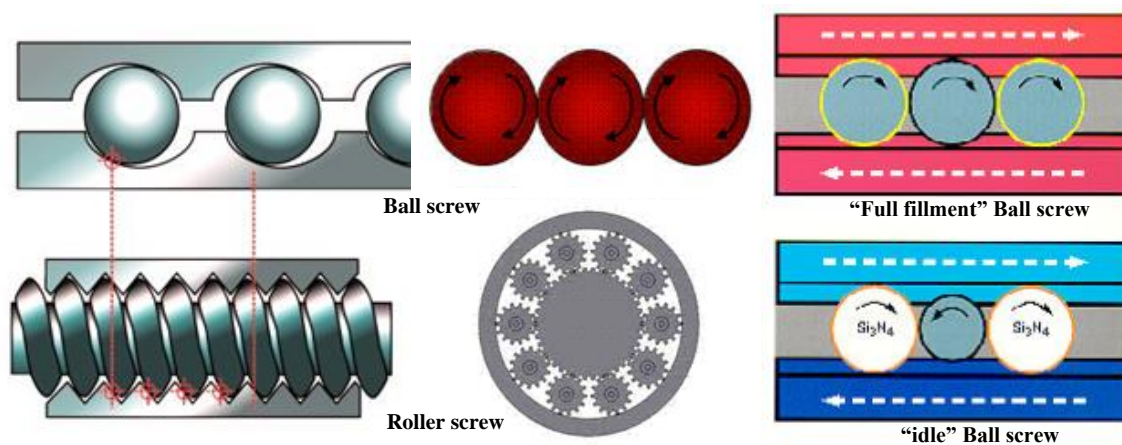


Fig. 4-3 Design comparison of ball screw and roller screw [3, 4]

In addition, because of operational differences between roller screw and ball screw, within a ball screw, the balls contact each other and rotate. The friction will create significant heat and wear as rotational speeds increase. The friction can be decreased for the improvement of the efficiency by special design ceramic balls/alternate filling [4]. This solution is shown in Fig. 4-3 of the “idle” configuration compare with the “full fillment” configuration, which has lower wear even if the maximum contact. In contract, in a roller screw the planetary rollers are all constrained by their journal shafts at each end of the roller. The rollers never touch each other and will prevent such friction.

A ball screw from SKF com catalogue [5], with a nominal screw diameter of 40mm and a lead 5 mm offers a dynamic load rating of 24.1 kN and a static load rating of 63.2 kN. The given theoretical efficiency direct is 0.87 and indirect is 0.85.

For the same screw diameter and lead, a planetary roller screw offers a dynamic load rating of 148 kN and a static load rating of 329 kN. The given efficiency becomes 0.83 for direct mode and is 0.8 for indirect mode. This means that for the same screw shaft (rod) diameter, the load capacity of roller screw is about 5 times greater than that of ball screw while the efficiency is a little decreased.

A planetary roller screw able to withstand with a similar level of dynamic load rating (30.8 kN) and static load rating (71 kN), has a nominal diameter of screw of 18 mm with a minimal lead of 2 mm. Its direct efficiency is 0.82 and indirect efficiency is 0.77. This means that for the same load capacity requirement, the roller screw has much smaller size than ball screw (screw shaft diameter reduced by 55%). This is a significant advantage for aerospace EMAs where the mass is key design constraint.

(b). Rotational Speed Characteristics

Roller screws provide higher rotation speeds than ball screws. One important reason is in roller screws there is no loading and unloading of balls and no sharp turns of ball return tubes where the balls clash with each other, seen above Fig.4-3. Thus, e.g. ball screw speeds are limited to 2000 rpm and less while satellite roller screws velocity are limited to 5000 rpm and higher [2].

4.2 1-DoF Integrated Model

The generic 1-DoF model architecture of MPT shall enable the inertia, compliance and friction effects to be optionally considered if needed. Friction can be made dependent on velocity, load force, temperature and preload. Compliance can include preloading, backlash and nonlinear compliance (e.g. from Hertz theory). As illustrated in [6] of Table 4-1, there are 6 candidate orders of 1-DoF MPT model decomposition. The intention to enable friction to be linked to







preload (if exists) and to the transmitted force to load, which is in favor of options 1 and 2. In cases #1 and #2, locating the frictional effect upstream the compliance effect is found more realistic regarding the dynamics and damping of the rotating and translating parts. This finally leads to select option 1 for 1-DoF modeling.

Table 4-1 Candidate locations of generic effects in a mechanical power transmission device [6]

Solution → Order in the power path ↓	#1	#2	#3	#4	#5	#6
1	Perfect	Perfect	Compliance	Compliance	Friction	Friction
2	Friction	Compliance	Perfect	Friction	Perfect	Compliance
3	Compliance	Friction	Friction	Perfect	Compliance	Perfect

The causality requirement imposes that the MPT model architecture is consistent with any causal situation. For a MPT device (as far as the housing velocity/position are imposed), there are 6 causal cases that are summarized on Table 4-2.

Table 4-2 Causal cases for a 2-ports passive power transmission device [6]

Case	Causal Bond-Graph	Imposed at upstream side	Imposed at downstream side
1		Force	velocity/position
2		velocity/position	force
3		velocity/position	velocity/position
4		Force	force
5		force and velocity/position	-
6		-	force and velocity/position

Therefore, the proposed decomposition involves five effects in series from motor to surface, as shown in Fig. 4-4: a global rotating inertia, a perfect nut-screw, a friction loss, a compliance effect (that can represent backlash, preload, or even pure compliance) and a translating mass. In the proposed MPT architectures, friction and compliance effects are the most significant that can be modeled by different levels of complexity: linear or nonlinear and continuous or

discontinuous. In order to meet causality requirements, it may be necessary to add inertance effects (inertia of rotating part and mass of translating part of the MPT) for two reasons:

- the backlash may be considered as a particular case of compliance effect and imposes the integral causality of the associated C effect,
- as friction has to be made sensitive to transmitted load, in particular in the presence of pre-loading, the causality is imposed on the mechanical power bond linking the friction and compliance models.

Although inertia and mass effects in the MPT can be generally neglected, this explains why they may have to be considered optionally in the MPT model.

The effects of the bearings, joints and end-stop will not be explicitly modeled: they will be embedded in the generic effects considered in the MPT model. Consequently, the proposed generic model of the MPT involves four mechanical power ports (rotation and translation of nut and screw). An additional thermal power port enables the MPT to output the heat generated by power losses. For advanced MPT modelling, the heat port also inputs the temperature to the model, which can be used to influence friction and compliance.

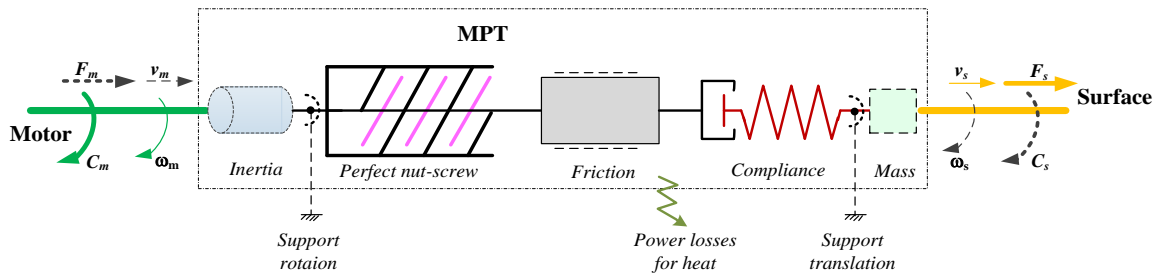


Fig. 4-4. Proposed 1-DoF simplified synoptic model of mechanical transmission

As presented in chapter 1, it is suggested to link engineering needs and physical effects to define different levels of MPT modelling. Thus, four levels of mechanical transmission model were defined, as explained in the next sections.

4.2.1 Functional Model

The nut-screw is considered as a perfect power transmission, Fig.4-4, between the mechanical rotational domain (torque C_m , angular velocity ω_m) and the mechanical

translational domain (force F_s , linear velocity V_s).

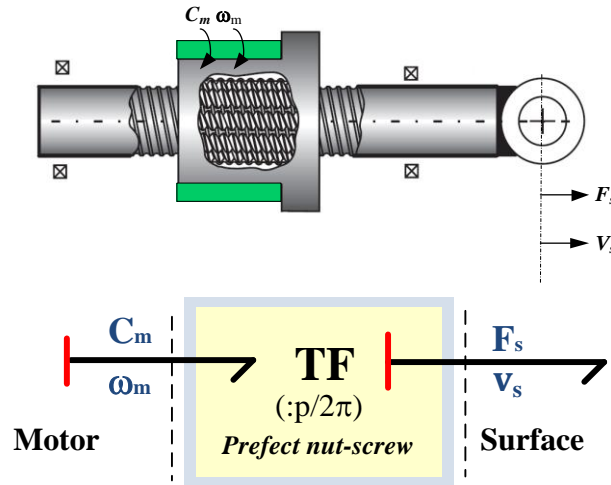


Fig. 4-5 Causal Bond-Graph model of perfect mechanical transmission (Nut-screw)

According to the Bond-Graph formalism, this perfect power transformation can be represented by a TF element that implicitly links the power variables, as given by equations (4.1) and (4.2):

$$F_s = \frac{2\pi}{p} C_m \quad (4.1)$$

$$v_s = \frac{p}{2\pi} \omega_m \quad (4.2)$$

F_s EMA output force [N]
 p Screw lead [m]

V_s EMA output linear velocity [m/s]

Unfortunately, this purely functional view is not sufficient because it does not consider friction, compliance inertia and relative motion, although they may impact significantly EMAs performance.

4.2.2 Basic Model

In this level of modeling, three major parasites are introduced: the screw inertia (J_s), the viscous friction loss (f_e) and the basic compliance effect including the contact elastic force (F_e) and damping force (F_d). The Bond-Graph modeling of these parasites is shown in Fig. 4-6, in which the proposed causalities are consistent with those of the functional model of Fig. 4-5.

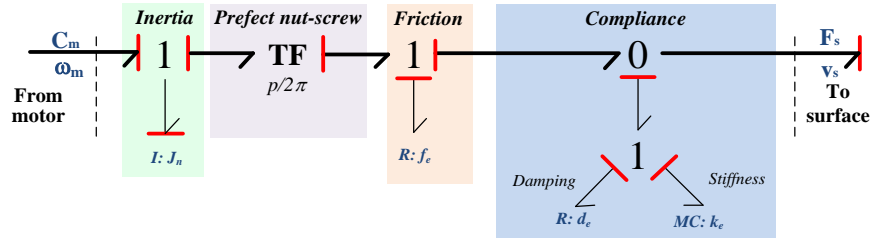


Fig. 4-6 Basic model of MPT in Bond-Graph

(1) Inertia Effect

The screw inertia J_n is inertia I element in the Bond-Graph, which generates an inertial torque:

$$C_j = J_n \frac{d\omega_n}{dt} \quad (4.3)$$

C_j	Inertia torque of MPT [Nm]	J_n	Nut-screw inertia [kgm ²]
ω_n	Nut-screw rotational velocity [rad/s]		

Generally, the screw inertia, like in the roller-screw type direct drive EMAs, is small enough when compared with the rotor/nut inertia, and can be neglected or integrated with the rotor/nut as an overall inertia effect for MPT.

(2) Friction Effect

In MPT, there are several solutions to model the friction loss [7] that depends in practice on both velocity, external load force and operating temperature. From control engineer's point of view, the simplest one is to describe the friction loss as being proportional to the relative velocity (v_r), which is affected by a viscous coefficient (f_v) given:

$$F_f = f_v v_r \quad (4.4)$$

F_f	Friction force in MPT [N]	f_v	Viscous coefficient of translational velocity in MPT [N/(m/s)]
v_r	Relative velocity in nut-screw [m]		

(3) Compliance Effect

Within EMAs, the MPT is not infinitely rigid. This makes it compliant due to the elastic deformation (x_e) of solids under mechanical stress, in particular at contact locations. A basic

compliance model consists of a pure spring (k_e) and a damping (d_e) effects. The elastic force (F_e) can be expressed as :

$$F_e = k_e x_r \quad (4.5)$$

F_e Elastic force of compliance [N]	k_e Pure spring stiffness of nut-screw [N/m]
x_r Relative deformation by compliance [m]	

Although the compliance damping is low, it must be considered in parallel with compliance in order to avoid unrealistic simulated oscillations. As the physical knowledge is very poor, the damping force (F_d) is usually considered as a linear function of the relative velocity (v_r) of damping coefficient (d_e).

$$F_d = d_e v_r \quad (4.6)$$

F_d Damping force of MPT [N]	d_e damping factor of MPT [N/(m/s)]
--------------------------------	---------------------------------------

The main interest of the basic model lies in its linearity. This is useful for preliminary control design based on the linear control theory. This simplicity is balanced by a poor realism, especially regarding load dependent friction and backlash.

4.2.3 Advanced Model

This advanced level of MPT modeling is consistent from the energy balance point of view: Firstly the nonlinear friction model considers the influence of velocity, load force and temperature. It is therefore upgraded to a modulated resistor field (MRS) in Bond-Graph. The nonlinear compliance model may consider pure spring, backlash or preloading effects, both being potentially affected by temperature due to the effect of dilation. For this reason is represented as modulated capacitance element (MC).

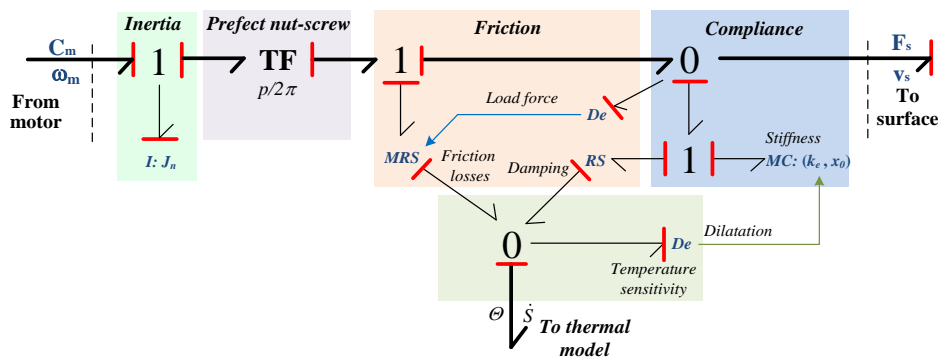


Fig. 4-7 Advanced model of MPT in bond graph

Then, the heat power coming from friction loss (P_f) and structural damping (P_d) can be explicitly introduced by the heat flows and connected a thermal port. Consequently, it becomes possible to use the temperature as a time variable input in the MPT parasitic effects. The introduction of such a thermal port for the MPT makes is ready for the development of a thermal modal at EMA level. Fig. 4-7 describes the Bond-Graph modeling of this advanced MPT model. Once again, it can be remarked that causalities at model's interfaces remain unchanged from previous model levels.

(1) Nonlinear Friction Effect

In a more realistic way, friction can be represented on the contributors considering whether is it mainly velocity and load dependent, or load dependent and load independent [8].

-*Velocity and load dependent friction*: for nut-screw, a five parameter model, equation.(4.7), has been identified by Karam [9]. The friction force introduces a constant Coulomb friction (first part), a Stribeck effect of rapid change of friction at low velocity (second part) and a load and power quadrant dependent Coulomb effect (last part):

$$F_f = \left[F_{cl} + F_{st} e^{-|v_r|/v_{st}} + |F_L| (a + b \operatorname{sgn}(F_L v_r)) \right] \operatorname{sgn}(v_r) \quad (4.7)$$

F_{cl} Coulomb friction force [N]	F_{st} Stribeck friction force [N]
a Mean coefficient of external force [-]	b Quadrant coefficient [-]

-*Load dependent and load independent*: this model is consistent with nut-screw suppliers' datasheets, which provide efficiency (the load dependent friction) as well as the no-load friction under opposite load and the no-drive friction under aiding load (the load independent friction). The velocity effect is added in a second step by introducing its influence on these parameters. The details of this modeling approach based on Bond-Graph have been presented in [6].

For any friction model in MPT, the power loss (P_f) is calculated as

$$P_f = F_f v_r \quad (4.8)$$

P_f Friction power loss [W]	
-------------------------------	--

(2) Nonlinear Compliance Effect

From mechanical engineer's point of view, obtaining a realistic model of compliance is of particular importance because compliance can significantly influence the low-magnitude dynamic performance [10] and the service life of the EMAs. Backlash and preload are two key effects in a realistic compliance model. In the absence of preload and backlash, the axial mechanical stiffness will suffer from such a reduced stiffness around the null transmitted force where not all the contacts are fully loaded, this generates the so-called "lost motion". Fig. 4-8 shows the elastic characteristics of proposed compliance model that can reproduce spring effect, with optional backlash or preload that is defined with a single parameter x_0 :

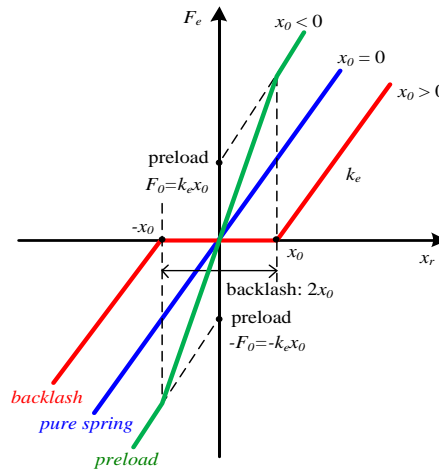


Fig.4-8 Elastic characteristic of proposed compliance model

-*Pure spring effect*: using $x_0 = 0$, the contact force F_c is purely proportional to the relative displacement x_r

$$F_e = k_e x_r \quad (4.9)$$

-*Backlash effect*: using $x_0 > 0$, the model displays a total dead-zone of $2x_0$ and the contact elastic force (F_e) is

$$F_e = \begin{cases} k_e(x_r - x_0) & , \quad x_r > x_0 \\ 0 & , \quad |x_r| \leq x_0 \\ k_e(x_r + x_0) & , \quad x_r < -x_0 \end{cases} \quad (4.10)$$

x_0 Backlash or preload parameter [m]

-*Preload effect*: using $x_0 < 0$, a preload force of $|F_0| = k_e |x_0|$ can be reproduced and the contact elastic force (F_e) is given by

$$F_e = \begin{cases} k_e(x_r - x_0) & , \quad x_r > -x_0 \\ 2k_e x_r & , \quad |x_r| \leq |x_0| \\ k_e(x_r + x_0) & , \quad x_r < x_0 \end{cases} \quad (4.11)$$

For numerical stability and rapidity, it is proposed to implement the compliance model by combining equations (4.9) to (4.11), in such a way as to avoid switches or “if” functions. This is achieved by using :

$$F_e = k_e \left\{ x_r - \frac{x_0}{2} (1 - \text{sign}(|x_0| - |x_r|) \cdot \text{sign}(x_r) - \frac{x_r}{2} \text{sign}(x_0) \cdot [1 - \text{sign}(|x_r| - |x_0|)]) \right\} \quad (4.12)$$

The structural damping at contact can be considered by adding to the elastic contact force a damping force:

$$F_c = F_e + F_d \quad (4.13)$$

|

F_c Compliance contact force [N]

Basically the damping force F_d can be expressed as:

$$F_d = d_e v_e \quad (4.14)$$

where $v_e = dx_e/dt$, x_e is the penetration at contact. However, this generates an issue in case of backlash. When the contact is left, the contact force can become attractive because v_e is negative. This is not realistic. Moreover, at entry into contact with a given velocity, the contact force makes a step due to the structural damping force. This is also not realistic. These issues are fixed if the damping force magnitude is limited to the elastic force magnitude:

$$F_d = \begin{cases} \min(F_e, d_e v_e) & , \quad x_r > x_0 \\ 0 & , \quad |x_r| \leq x_0 \\ \max(-F_e, d_e v_e) & , \quad x_r < -x_0 \end{cases} \quad (4.15)$$

The power loss (P_d) due to structural damping, although generally negligible, can be calculated to make the MPT model exactly balanced with respect to energy:

$$P_d = F_d v_e \quad (4.16)$$

|

P_d Power loss by compliance damping [W]

(3) Temperature Sensitivity:

Temperature influences friction due to viscosity effects and dimensions due to dilation.

-*Influence on friction*: variation of lubricant temperature changes its viscosity and consequently friction. Unfortunately, the effect of temperature on friction is poorly documented in the nut-screw suppliers' datasheets. At system-level modeling, several models have been proposed by Maré [8]. As a consequence, a linear or nonlinear parameter/function ($\tilde{\mu}_f(\Theta)$) can be introduced to modulate the friction force, e.g. using the following model:

$$\tilde{F}_f = F_f \cdot \tilde{\mu}_f(\Theta) = \tilde{\mu}_f(\Theta) \cdot \left(\left[F_{cl} + F_{st} e^{-|v_r|/v_{st}} + |F_L| (a + b \operatorname{sgn}(F_L v_r)) \right] \operatorname{sgn}(v_r) \right) \quad (4.17)$$

\tilde{F}_f Friction force considering temperature sensitivity [N] $\tilde{\mu}_f(\Theta)$ Temperature factor to friction force [-]

-*Influence on dimension*: in MPT especially for roller type the nut-screw that has a very small lead, thermal expansion (dilation) may be not negligible. This leads to variation of dimensions and potentially impacts backlash, preload and friction. Once again, if a model of dilation is developed, this effect is easy to introduce using the temperature variable of the MPT thermal port. For example, the temperature effect to the value of the backlash parameter x_0 can use a linear or nonlinear parameter/function ($\tilde{\mu}_x$) to describe the differential dilation by the following formula:

$$\tilde{x}_0 = \tilde{\mu}_x(\Theta) \cdot x_0 \quad (4.18)$$

\tilde{x}_0 Backlash or preload parameter with temperature sensitivity [m] $\tilde{\mu}_x(\Theta)$ Temperature factor to backlash or preload parameter [-]

4.2.4 Behavioral Model

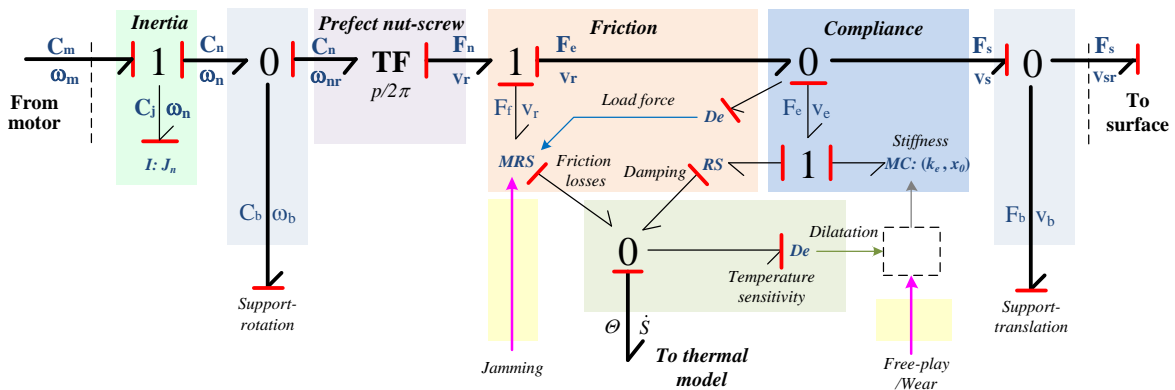


Fig. 4-9 Behavioral model of MPT in Bond-Graph

Again, another step forward in the realism of the MPT model can be made by considering two additional effects, Fig. 4-9: the support motion and the faults due to jamming or free-run

faults.

(1) Support motion

In fact, the power transformation does not operate purely between the motor shaft rotation and the rod translation. Rigorously speaking, it applies to the relative rotational speed between the nut and the screw (or vice-versa) and the relative translational velocity between the screw and the nut (or vice-versa). This can be added in the model by considering the rotational and translational motion of NS support: anti-translation function of MPT rotating part and anti-rotation function of MPT translating part. Consequently, two power interfaces are added (mechanical translational and rotational power bonds in the Bond-Graph model). In this way, it is possible to consider imperfect bearings and joints (e.g. reproducing their compliance and friction) and to access the reaction torque (C_b) and force (F_b) to perform the anti-rotation and anti-translation functions (e.g. within the EMA housing, the airframe or by the load itself. The relative rotational velocity (ω_{nr}) for nut/rotor and relative linear velocity (v_{sr}) for screw to surface are therefore calculated (represented by 0 junction in the Bond-Graph model).

-*Support rotation*: the relative rotational velocity between the rotor/nut and support bearings can be modeled as:

$$\omega_{nr} = \omega_n - \omega_b \quad (4.19)$$

ω_{nr}	Relative rotational velocity between nut and support bearings [rad/s]		ω_b	Support bearing rotational velocity [rad/s]
---------------	-----------------------------------------------------------------------	--	------------	---------------------------------------------

-*Support translation*: the relative translational velocity between the screw and support bearings given:

$$v_{sr} = v_s - v_b \quad (4.20)$$

v_{sr}	Relative translational velocity between screw and support bearings [m/s]		v_b	Support bearing translational velocity [m/s]
----------	--------------------------------------------------------------------------	--	-------	----------------------------------------------

Thus this behavioral model is also the preliminary virtual prototype of MPT for the advanced two degrees of motion (2-DoF) EMAs model that is detailed section 4.2.3.

(2) Failures Injection

Simulating the faults that may occur in the MPT is of prior importance when it is intended to assess the fault-to-failure mechanism and the response-to-failure of the actuation system

involving the faulty MPT. Two main faults are identified: jamming (no possible motion) and free-run (no force transmitted to the load).

-Jamming: Nowadays, many means are proposed in order to make the EMA tolerant or resistant to jamming like in SHAs or EHAs [11, 12]. On one hand is the redundancy concept including several transmission paths to set backup mode. On the other hand is by removing or decreasing the number gear mechanism in EMAs. So, the target to develop direct-drive EMAs using roller screws is currently a hot spot issue. However, despite it is lower in direct drive EMAs, the risk of jamming remains an important source of potential hazard. Being able to assess by simulation the response of the system involving EMAs (e.g. flight controls of landing gears) to a jamming fault in the EMAs is an important target during systems development. It is also important to enable jamming faults to be simulated to assess the merits of health monitoring features. In particular, fault to failure evolution and mechanism is being more understood with resort to real tests. For example, specific tests have been run by Airbus for meeting this objective, Fig.4-10.



Fig. 4-10 Airbus Jamroll project for study jamming issue on roller screw [13]

In the proposed model, jamming can be triggered as a signal input to modulate the friction model parameters (MRS) to force stiction. This approach is preferred against introducing a piloted brake in the model, for two reasons: the brake does not exist physically and increasing friction is consistent with modelling a progressive degradation of mechanical efficiency (e.g. coming from a lack of lubrication).

Consequently, jamming can be modeled by increasing the force in the friction model in response to the jamming signal:

$$F_f^* = F_{jam} + F_f \quad (4.21)$$

$$F_f^* \quad \text{Friction force with jamming [N]} \quad \Bigg| \quad F_{jam} \quad \text{Jamming force [N]}$$

-*Free-play or wear*: Free-run (or even) free-play is another fault caused by mechanical rupture (or huge increase of backlash) It is difficult to control them with a high position of accuracy in a closed loop. Once again, the response of the system involving EMAs to the effect of free-run (or free play) is of particular importance for meeting the safety requirements. Free-run can lead to flutter or shimmy while and excessive free-play can in addition make internal control loops unstable (e.g. EMA speed loop). All these destabilizing effects are very undesirable in aerospace applications. Many activities are focused on estimation and compensation of backlash effect in control strategies [14, 15, 16].

In the proposed model, free-play or free-run can be also triggered using a signal input to change the parameters of the proposed model of compliance (MC): by increasing parameter x_0 , preload can be progressively decreased then backlash can be progressively increased. The compliance parameter x_0 is consequently altered according to the free-run signal input:

$$x_0^* = x_0 + x_w \quad (4.22)$$

$$x_0^* \quad \text{Backlash or preload parameter by wear [m]} \quad \Bigg| \quad x_w \quad \text{Wear parameter [m]}$$

Remark: when x_0 is set to a huge value with respect to the NS stroke, a mechanical rupture is modelled to reproduce free-run.

4.3 2-DoF Decomposition Model

The 2-DoF lumped parameters model has been developed to introduce two new advances to make the EMA model more realistic and versatile. Firstly, the model considers two degrees of freedom, which are the linear motion in the direction of the EMA rod axis and rotation motion around the same rod axis. Secondly, the model is made fully balanced from both energy and mechanical efforts (forces and torques) points of view. These properties enable the strong and multiple couplings in embedded EMAs to be addressed by simulation in order to better

support, as a whole, simulated-aided design: power sizing, energetic/thermal analysis, response to failure, vibration/control design.

4.3.1 Decomposition Process

During the modelling process, one of the most important tasks is to decompose the device under consideration into basic (or generic) components (or functions). As already mentioned, the EMA studied in this thesis is of direct-drive linear type with inverter roller-screw mechanism. For continuity between design steps, it is interesting to define the model structure with the same topology of the EMA hardware. In this attempt, the scheme of decomposition comes directly from the cut-view and it has a similar topology, as suggested in Maré [17]. According to the decomposition rules, the identified generic components are illustrated in Fig 4-10.

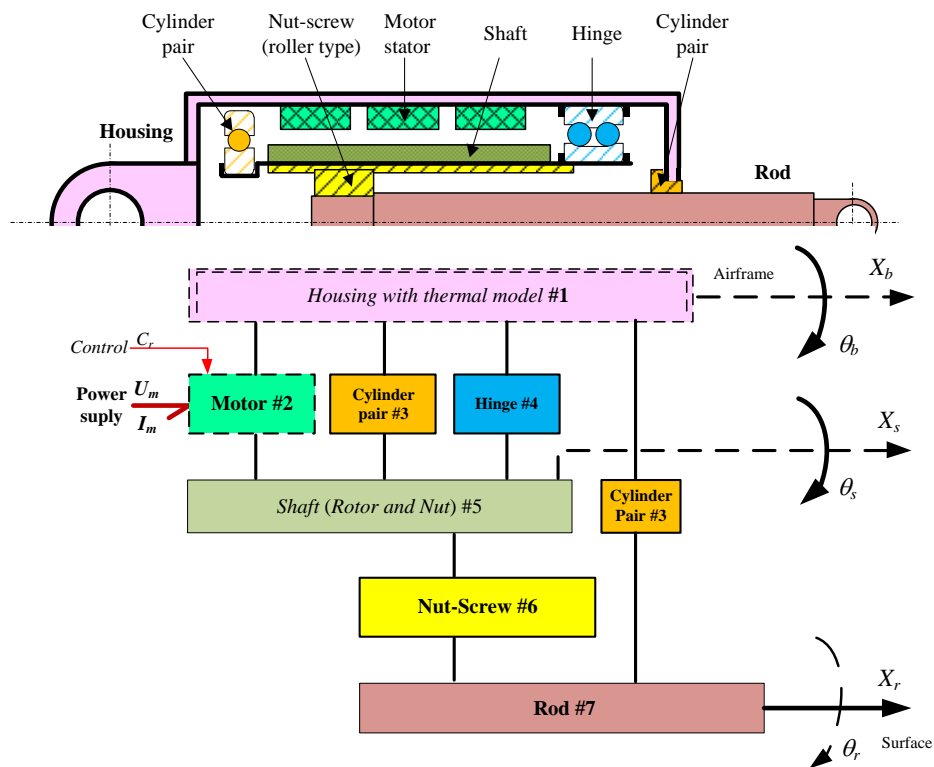


Fig. 4-10 Decomposition of EMA into basic component element [17]

4.3.2 Causalities

Nowadays, the virtual prototyping through numerical simulation still suffers from causality

constraints. Although some new languages (e.g. Modelica) implemented in commercial simulation packages (e.g. Dymola) potentially remove these constraints, a faster and more numerically robust model is obtained if causalities are actively managed during the model development. This is why the proposed models are causal. Consequently, the generic 2-DoF models of mechanical transmission consider causality. This also allows the models to be implemented in causal simulation environments, like AMESim or MATLAB/Simulink. The causal Bond-Graph model of direct drive EMA consisting of the generic subcomponents and junctions is shown in Fig.4-11. The causalities requirements are met by considering separately bodies (housing, shaft and rod) that are linked by generic elements (motor, bearings and joints, nut-screw).

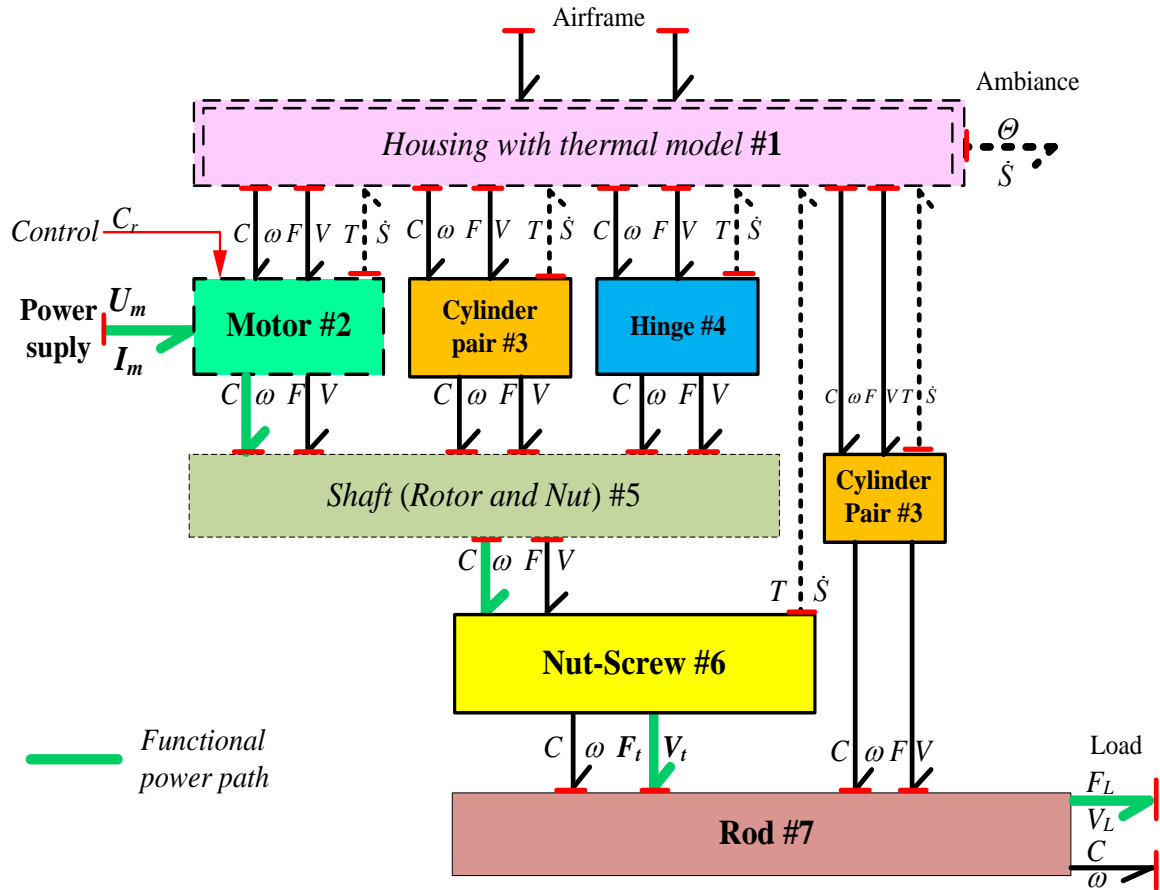


Fig. 4-11 Causal Bond-Graph 2-DoF model of direct drive linear EMA

2-DoF modeling method has a significant advantage when compared to the 1-DoF modeling. Other mechanical joints in MPT, such as bearings can be considered. Also, for advance motor modelling, the mechanical quadric ports also can be introduced in motor model. Taking into

account the loss in each submodel of EMA is important not only to identify of energy conversion efficiency but also to facilitate and improve the thermal simulation accuracy in the whole EMA. It is important to note that on Fig. 4-11, not all the potential thermal bonds are introduced: the figure displays only those involved in a very top level and simple thermal model where the whole EMA is considered as a single thermal body (heat capacitance) lumped at the housing level by transmitting thermal behavior with ambience.

Remark: in the following Bond-Graph, it is found efficient for understanding to use bold bonds for the functional power path. In that manner, parasitic effects are clearly distinguished from functional ones.

4.3.3 Components

a) Generic Elements

The mechanical power transmission mainly consists of nut-screw and kinematic joints (e.g. cylinder pair and hinge). In addition, the electrical motor and also can be considered as a generic quadriport model with a thermal port. In these generic components, the individual inertia is neglected at component level to avoid the numerical derivation or high index implicit loops. For this reason, the inertia effect is considered in bodies' sub-models, this choice being consistent with causality requirements.

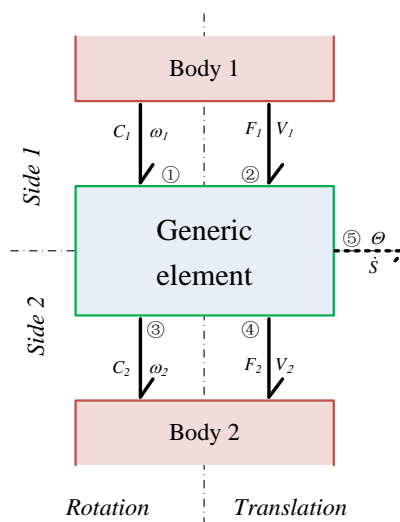


Fig. 4-12 Bond-Graph 2-DoF model of generic element [17]

By using Bond-Graph methodology, a generic four mechanical power ports plus one thermal

port model is proposed in following Fig. 4-12 for each basic component of Fig. 4-11, the calculation structure is addressed carefully through proper causality assignment: each mechanical port of the generic model imposes the mechanical flow variable (velocity) to the sub-model that returns the associated effort variable (force or torque).

As illustrated in Fig. 4-12, it is suggested to use this generic sub-model with four ports (① to ④) to connect two different bodies. The models of each body can be refined according to different simulation objectives. The generic block is able to model the interactions of the four power bonds associated with body 1 and body 2, for rotational and translational motion. In order to ensure energy balance and energy conservation as they represent the energy exchange between subsystems, a fifth thermal port (⑤) is added when the component generates heat. Another possible electrical signal port can also be added for electrically signaled mechanical devices EMA servo drive [17].

Electric Motor

The detailed model of motor is developed in former Chapter 2, with multi domain physical effects considered, like copper loss, iron losses and cogging torque, etc. The 2-DoF model may be used for motor modelling, which generates relative motion between the stator (subscripts 1 in Fig. 4-13) and rotor (subscripts 2).

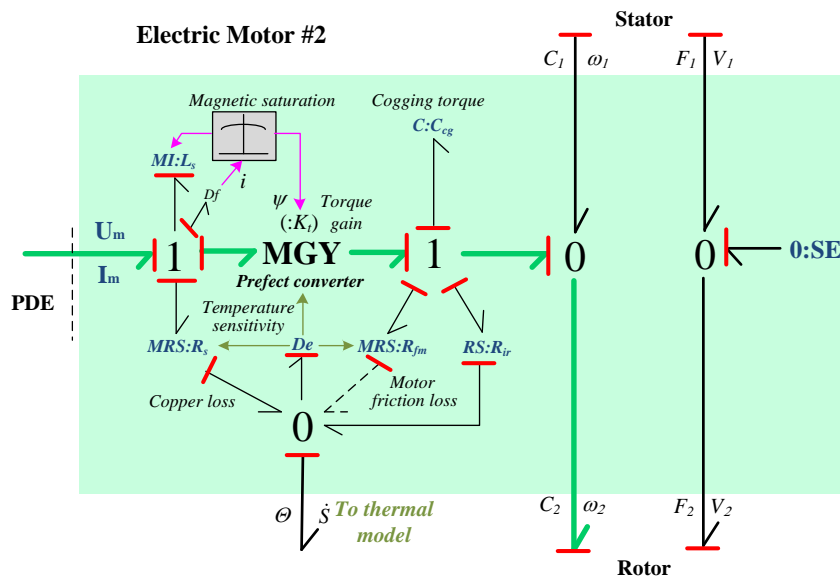


Fig. 4-13 2-DoF Bond-Graph model of EM (advanced motor)

Functionally speaking, the motor stator is rigidly linked to the EMA housing that is not supposed to translate or rotate. In this case, a zero force source should be connected to stator rotational and translational mechanical ports. However, the EMA anchorage to airframe compliance cannot be neglected for some design activities. In that case, the interface between EMA and airframe can be modelled by spring/damper parallel association for each, translational or rotational degree of freedom. Fig. 4-13 confirms that the motor sub-model meets the causality choices at model's interface.

Bearings and Joints

The bearings and joints are used for support rotation and translation in mechanical transmission. The most common components are cylinder pair and hinge pair when the anti-rotation function of the translating part of the EMA is performed by the load. If not, a prism pair function has to be integrated within the EMA to perform internally this function.

Cylinder Pair: The cylinder pair may allow two degrees of freedom, translational and rotational in the same axis. The 2-DoF Bond-Graph model of this type of bearing is shown in Fig.4-14.

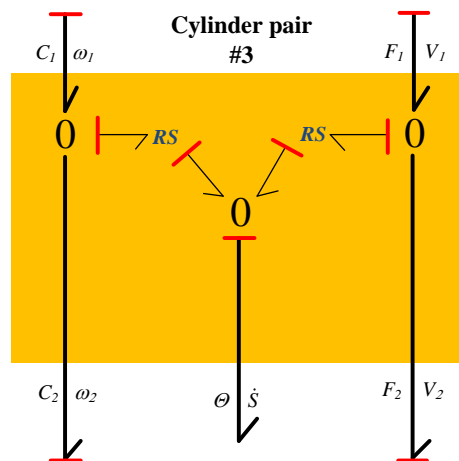


Fig. 4-14 2-DoF Bond-Graph model of cylinder pair

The friction in a cylinder pair is here modeled as a pure function of the relative velocities (linear and angular) since only two degrees of freedom are considered respectively. In fact, the radial forces also impact friction but they are not considered in the 2-DoF model because they are not significant in direct-drive EMAs. Friction is modelled using RS elements, which

are summed to the sub-model thermal port. In that manner, temperature can also be used to reproduce its impact on friction. There is no compliance considered because the cylinder pair offers free motion for the 2-DoF considered.

Hinge: Unlike cylinder pair, the hinge only allows one rotational degree of freedom; it prevents any relative axial motion between the two bodies it links: in the presence of axial forces, it acts as an axial thrust bearing.

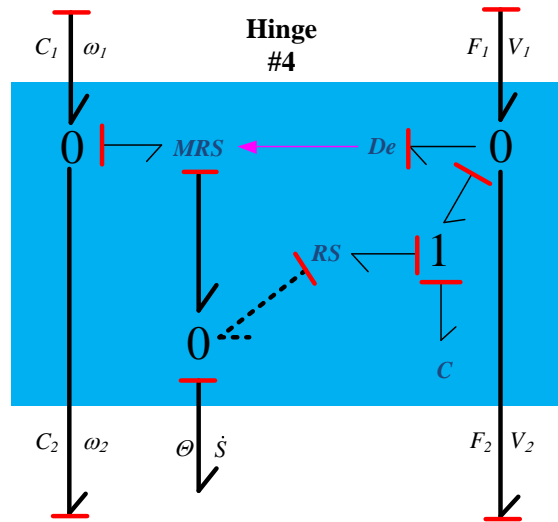


Fig. 4-15 2-DoF Bond-Graph model of hinge

The parasitic effects in hinge joint are friction and compliance. However, the friction torque depends considerably on the axial load. This creates a cross coupling between linear and rotation motions. Structurally speaking, this effect can be modelled, by getting the axial force through a DE detector element and modulating the friction effect that becomes a MRS field for the hinge pair. The axial compliance is introduced using a C element that reproduces the deformation under axial loads. Associated damping can be modelled using a RS field that acts “mechanically” in parallel, i.e. which sums its force to that of the compliant effect (a 1 junction in the translational mechanical domain. A rigorous energy balance is ensured by adding the heat produced by this dissipation, although negligible, to that of the friction effect through a 0 junction in the thermal domain, as shown in Fig 4-15. As the dissipation is negligible in comparison with that of the hinge rotational friction, the bond of the power loss (from RS) is plotted as a dashed line. Once again, it is verified that the internal causalities of the model are consistent with the requirements at its interfaces.

Nut-Screw

According to the decomposition schema in Fig.4-10, the power flows functionally from the rotation of the nut to the translation of the screw. However, strictly speaking, such a mechanical power transformer acts between the relative rotational motion (nut/housing) and the relative translational motion (screw, housing). This cannot be neglected when parasitic motions may occur (due to bearings compliance or to airframe and load motion). For this reason, the relative velocities are explicitly calculated through 0 junctions in Fig.4-16. The parasitic effects affecting nut-screw, which have already been presented in section 4.3 for 1-DoF model. The same effects are introduced in this 2-DoF model with the same order of decomposition (perfect transformer first, then friction followed by compliance). This clearly appears when one follows the functional power path.

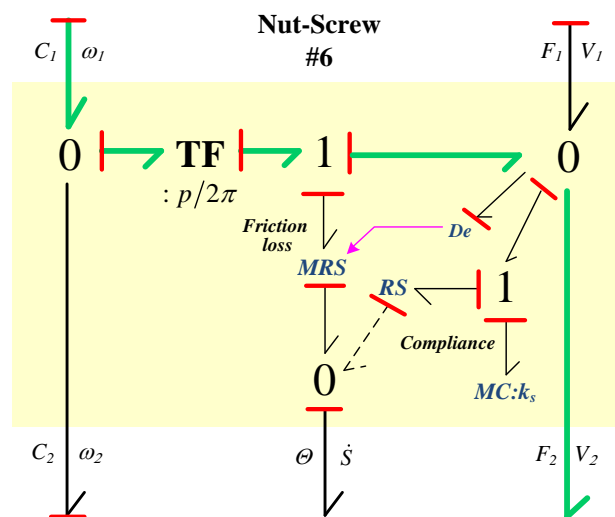


Fig. 4-16 2-DoF Bond-Graph model of nut-screw

As for hinges, nut-screw friction is introduced by a MRS field denoting that friction is made dependent of the axial force transmitted to the load and that friction generates heat. As for hinge joint, the compliance is introduced by a C element with optional parallel dissipative effect. The generic 2-DoF Bond-Graph model of a nut-screw is given by Fig.4-16. It can be noted that causalities are again consistent with requirements at model's interfaces.

b) Bodies and Junctions

The bodies and junctions are connecting the generic submodels of mechanical power transmission (electric motor, nut-screw, bearings and joints, etc.). In the former generic

submodels, the inertia effect is not considered in order to avoid generating causalities issues. The bodies' model is associated with the Newton's second law where the sum of efforts generates the acceleration of the inertial bodies. In term of Bond-Graph, this makes it convenient to represent the bodies as a 1 junction (the sum of mechanical efforts, force or torque) with an I inertance element (the mass or the rotational inertia), seen Fig. 4-17.

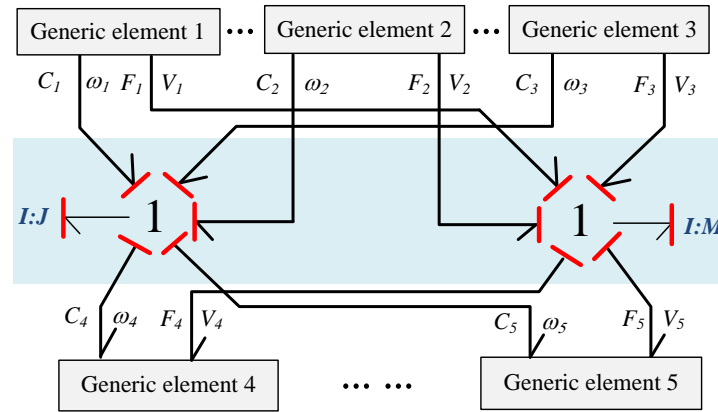


Fig. 4-17 2-DoF Bond-Graph model of body/junction

This approach merges the inertia on a limited number of bodies (the main functional ones). E.g., the inertia and mass of nut and screw are not considered explicitly in the nut-screw sub-model. This is because the nut is integrated with the motor rotor, and the screw is part of the EMA rod: the inertia effects are therefore already considered at rotor and rod bodies' level.

Finally the EMA model involves three models of body or junction that are considered as rigid: the housing, the shaft and the rod, corresponding to the decomposition process of Fig. 4-10.

Housing

Externally, in Fig. 4-18, the 2-DoF housing model connects to the holding frame (two mechanical ports) and to the thermal environment (one thermal port). Internally, it holds the different devices like motor stator, hinge and cylinder pair. Fig. 4-18 shows the housing model and which can be connected to the airframe model through compliance effects (the anchorage compliance). A single rotational inertia I element (J_h) and translational mass I element (M_h) are considered in this 2-DoF model, which merges all the inertial effects having the same motion as the housing (the housing itself, the motor stator, the outer races of the hinge and cylinder pair bearings).

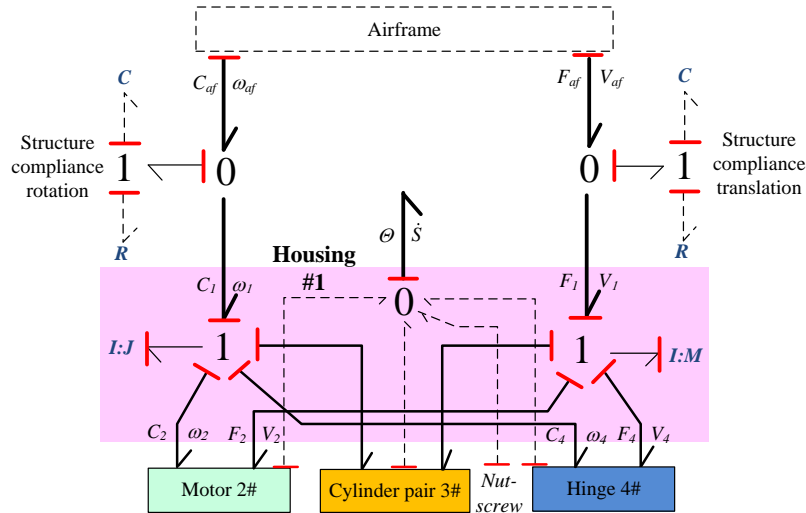


Fig. 4-18 2-DoF Bond-Graph model of housing

From the thermal point of view, a very top level model can consider only one thermal capacity for the whole EMA. In this case the housing can be considered as an single thermal body (C effect) that sums the heat power coming from the EMA elements power losses and the heat flow to ambient (0 thermal junction). Of course, a more detailed model can be developed with multiple thermal bodies [18].

Shaft

From the mechanical point of view, the same approach as that of the housing is used for modelling the shaft body, Fig.4-19. A single equivalent rotational inertia I element (J_s) and equivalent translational mass I element (M_s), the independent 2-DoF model are modelled.

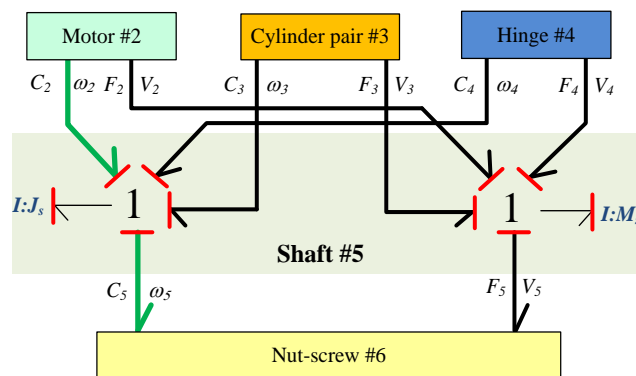


Fig. 4-19 2-DoF Bond-Graph model of shaft

Rod

The same remark applies to the rod body, Fig.4-20. The effects of inertia and mass of screw

and rod the two I elements can be respectively introduced with parameters J_r and M_r , the 2-DoF model. As for the housing, compliance of transmission to load can be optionally considered to link the rod and the load models.

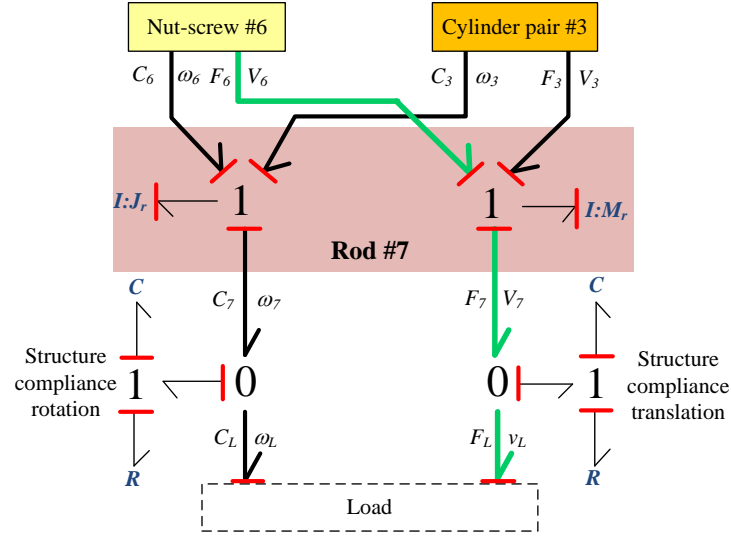


Fig. 4-20 2-DoF Bond-Graph model of rod

4.3.4 Friction Losses Models

Using 2-DoF modeling approach enables the heat generated by power losses in mechanical transmission to be calculated separately for nut-screw and bearings. The power loss in nut-screw is presented in details in the 1-DoF model, which makes friction dependent to transmitted force and relative speed. Meanwhile, with the advantage of the 2-DoF modeling, the heat generation in bearings may be considered. In particular, for high operating speed, bearings losses may be significant and cannot be neglected. As frictional power loss is converted into heat, the bearing temperature increases and in its turn impact the friction on bearing. Therefore, the power loss analysis of bearing is important when intending to model this snowball effect.

Generally, the bearing power loss is the product of the frictional torque and the bearing rotational speed, and it can be calculated using the following equation:

$$P_{bl} = C_{bf} \omega_b \quad (4.23)$$

P_{bl} Bearing power losses [W]

ω_b Bearing rotational speed [rad/s]

C_{bf} Bearing frictional torque [Nm]

Different types of friction models for bearings can be considered: the basic Coulomb friction model, the Palmgren model [19] and the advanced model developed by the SKF bearing supplier [5] model. The models implemented in the libraries of commercial simulation environments are typically based on these 3 types of models. The following sections aim at providing a critical analysis of these models.

a) Rotary Coulomb Friction Model

The rotary coulomb friction model [20] is the easiest method for represent the frictional moment for bearings. Until now, it has been applied in product designing by several companies such as Koyo [21] and NTN [22]. In this model, friction is independent of rotational speed. Friction is calculated assuming the friction coefficient to be constant and dependent on the bearing load (a time variable) and the bearing mean diameter (a constant geometrical parameter coming from design). The equation to calculate the bearing friction is given as follows:

$$P_{bl} = 5 \cdot 10^{-4} \mu_b F_L d_m \quad (4.24)$$

μ_b	Constant coefficient of friction for bearing	F_L	Equivalent dynamic bearing load [N]
d_m	Bearing mean diameter [m]		

In this model, the constant coefficient of friction for bearing is generally set to $\mu_b = 0.0015$ for deep groove ball bearings, and to $\mu_b = 0.002$ for single row angular contact ball bearings. This 1-equation model is the simplest one that can be used to get a first approximation during preliminary sizing. However, its applicability is limited (e.g. good lubrication, medium load and not very high speed operating conditions).

b) Palmgren Model

The Palmgren's bearing friction model [19] is much more detailed, which considers the viscous property of lubricant type and bearing type and operation rotational speed. It has been used by many engineers for a wide range of applications. It enables considering load, speed, mean of lubrication and type of lubricant. Palmgren divided the bearing friction torque (C_{bf}) into two parts, one depending on load (C_{b0}) and the other being load-independent (C_{b1}). The frictional moment in bearing can be expressed as follows:

$$C_{bf} = C_{b0} + C_{b1} \quad (4.25)$$

C_{b0} Load independent friction moment [Nm] | C_{b1} Load independent friction moment [Nm]

where C_{b0} reflects the hydrodynamic lubricant loss and C_{b1} reflects the elastic hysteresis and partial differential slip friction loss. A summary of the analytical description of each loss can be calculated using the empirical formulas in Table 4-2 and Fig.4-21:

Table 4-2 Analytical description of Palmgren model for calculation of bearing friction moment

Conditions	Load independent moment (bearing speed)	Load dependent moment (load)
$\nu n \geq 2000^1$ [$\text{rpm} \cdot \text{mm}^2/\text{s}$]	$C_{b0} = 10^{-7} f_0 (\nu n)^{2/3} d_m^3$	$C_{b1} = f_1 F_L d_m$
$\nu n < 2000$ [$\text{rpm} \cdot \text{mm}^2/\text{s}$]	$C_{b0} = 160 \cdot 10^{-7} f_0 d_m^3$	$C_{b1} = f_1 F_L d_m$

where f_0 the factor depending on the type of bearing and lubricant, ν the kinematic viscosity of the lubricant or grease based oil at the operating temperature [mm^2/s], n the bearing speed [rpm], f_1 the factor depending on the type of the bearing and load, F_L the equivalent load which determines the friction torque.

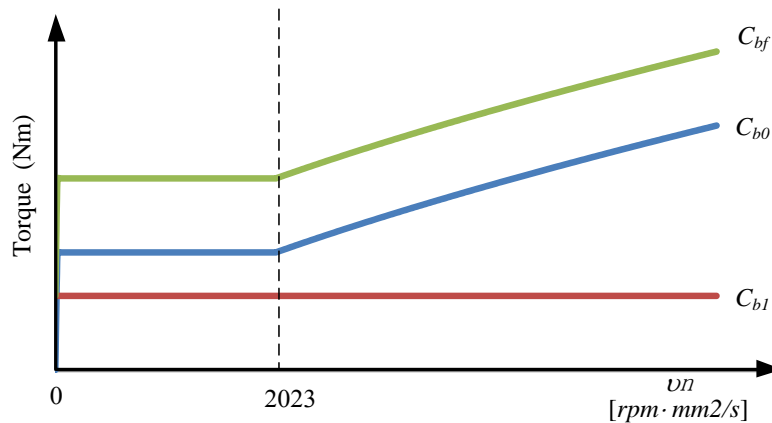


Fig. 4-21 Bearing friction torque of Palmgren model

In terms of dynamic simulation, we propose to represent the structure of this model by separating explicitly the constants that are set by design choices and bearing selection (d_m, f_0, f_1) and the time and operation-point dependent parameters (F_L, ν, n), seen Fig. 4-22.

¹ More accurately speaking, the transition value is that ensure continuity between the two model is 2023.86 [$\text{rpm} \cdot \text{mm}^2/\text{s}$]

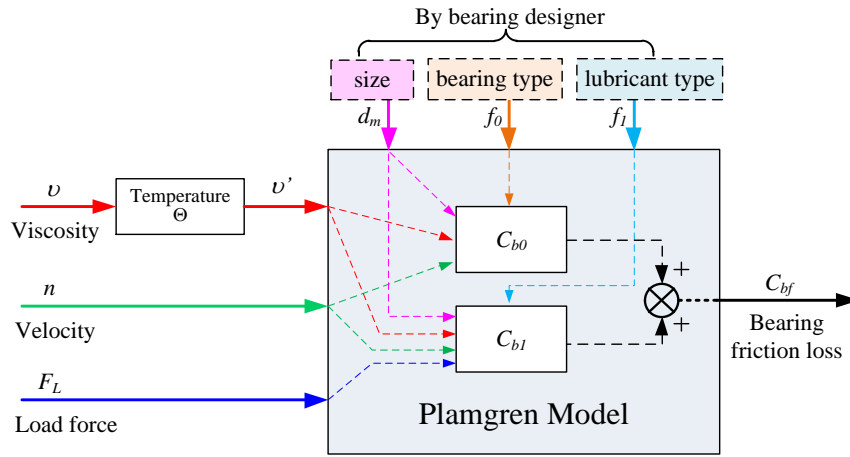


Fig. 4-22 Schematic of Palmgren model for modelling the bearing loss

Nowadays based on Palmgren model, the investigations by Harris [23] and many other companies such as INA/FAG and TIMKEN have modified the model's equations to their use for various types of bearings and applications.

c) SKF Model

SKF has created a more advanced approach which allows more detailed investigations to calculate frictional torque of bearing. SKF takes into account the various coefficients of load, bearing type and size, rotational speed, lubricant and seals. Finally the friction model involves four different terms: rolling frictional moment C_{rr} , sliding frictional moment C_{sl} , frictional moment of seals C_{seal} , frictional moment of lubrication loss C_{drag} . The total moment of friction can be expressed as:

$$C_{bf} = C_{rr} + C_{sl} + C_{seal} + C_{drag} \quad (4.26)$$

C_{rr}	Rolling frictional moment [Nm]	C_{sl}	Sliding frictional moment [Nm]
C_{seal}	Frictional moment of seals [Nm]	C_{drag}	Frictional moment of lubrication loss [Nm]

C_{rr} and C_{sl} represent the torque-dependent losses while C_{seal} and C_{drag} represent the torque-independent losses. A detailed description of different terms of friction loss can be found in [5] and it is summarized in Appendix B.

In the frame of this research work, it has been found important to address with care the architecture, Fig. 4-23, of this friction model, in particular to point out the constant

parameters and the time-dependent quantities.

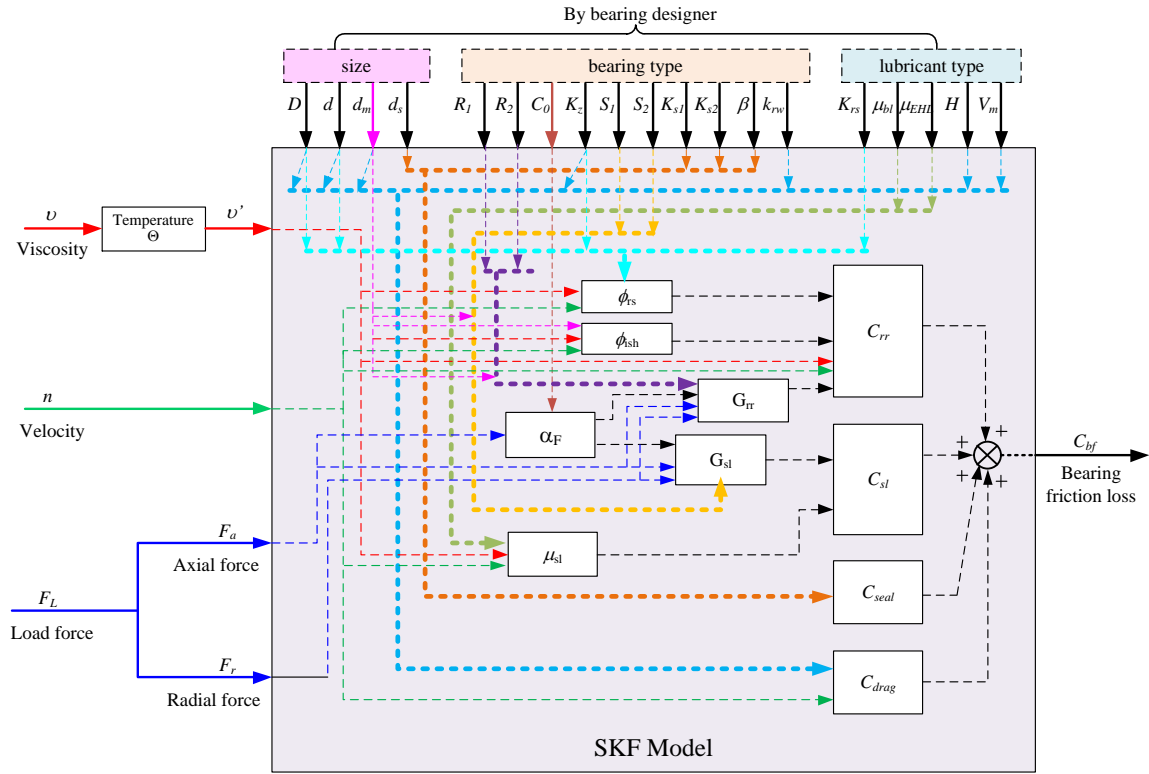


Fig. 4-23 Schematic of SKF model for modelling the bearing loss

The SKF model is the most advanced model which takes all of the discussed contributing factors into account and gives more attention the influence of the lubricant. However, a key consideration has to be kept in mind according to our need: such a model suits well applications where the bearings are continuously rotating in the same direction. This is absolutely not the case for bearings used in position controlled EMAs where the mean velocity is null and where many speed reversals occur. In this situation, it has to be accepted that the model is poorly realistic regarding breakaway torque or establishment of bearing lubricating film.

d) AMESim Bearing Loss Model

LMS AMESim simulation environment, already proposes a bearing loss model[24], which extends the Plamgren model at an intermediate level in comparison to the SKF model. Load dependent friction is explicitly split between axial and radial load effects while “oil” effects denote the load-independent friction:

$$C_{bf} = C_{oil} + C_{rad} + C_{axl} \quad (4.27)$$

C_{oil}	Torque loss due to the oil [Nm]	C_{rad}	Torque loss is due to radial load [Nm]
C_{axl}	Torque loss due to the axial load [Nm]		

The calculation of bearing loss in AMESim is summarized presented as following in Table 4-3:

Table 4-3 Analytical description of AMESim model for calculation of bearing loss

Conditions	Oil torque loss	Radial torque loss	Axial torque loss
$\nu n \geq 2000$	$C_{oil} = 9.78 \times 10^{-8} f_o (\nu n)^{2/3} d_m^3$	$C_{rad} = K_{cof} f_1 (C_0 + C_1) d_m$	$C_{axl} = f_2 F_L d_m$
$\nu n < 2000$	$C_{oil} = 9.78 \times 10^{-8} f_o (2000)^{2/3} d_m^3$	$C_{rad} = K_{cof} f_1 (C_0 + C_1) d_m$	$C_{axl} = f_2 F_L d_m$

where ν the kinematic viscosity of the lubricant or grease based oil at the operating temperature [mm^2/s], n the bearing speed [rpm], d_m the average diameter of the bearing [mm], f_0 the factor depending on lubricant, f_1 the factor depending on radial load, f_2 the factor depending on axial load, C_0 the equivalent static preload [N], C_1 the axial dynamic load [N], K_{cof} the adjustment coefficient load torque, F_r the radial bearing load [N], F_L the axial dynamic bearing load [N].

Once again, the architecture of bearing friction loss of AMESim model can be summed by the schematic diagram in Fig. 4-24.

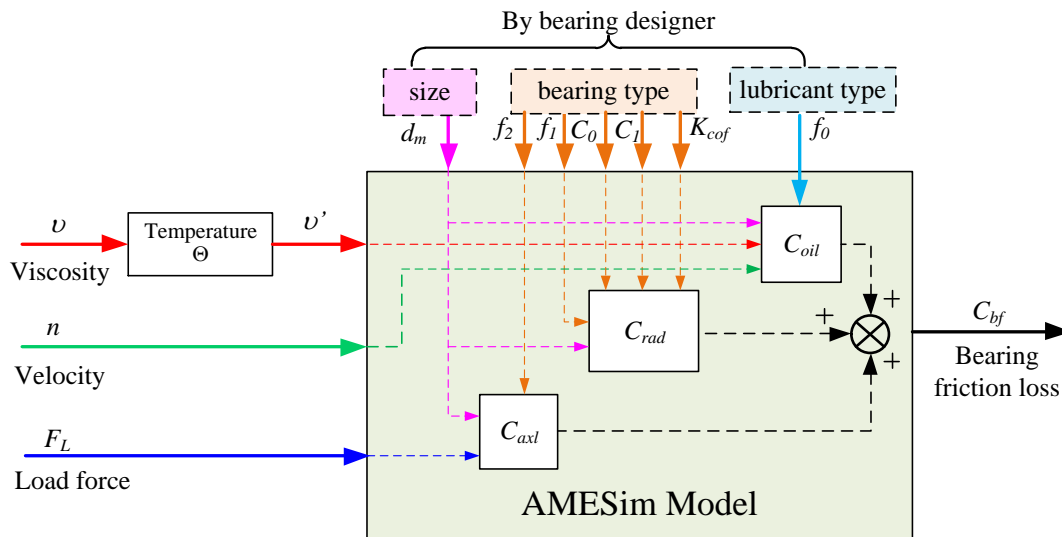


Fig. 4-24 Schematic of AMESim model for modelling the bearing loss

The AMESim loss model considers some of the friction sources but not all of them. For example, the friction due to the seals is not taken into account but cannot be neglected. The

influence of the lubricant is also not sufficient to get a good representation of the total friction torque.

4.3.5 Fault

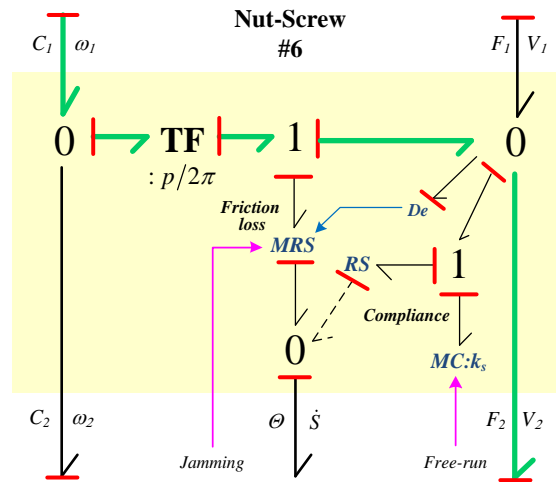


Fig. 4-25 2-DoF causal Bond-Graph model of nut-screw with fault failure

Like in 1-DoF model of MPT, the two major faults considered are jamming and free-run. They can be introduced in 2-DoF model, e.g. at the nut-screw level (there is no practical issue to apply the following developments to the bearing models). The advanced 2-DOF model of nut-screw can consider these two faults as depicted on the Bond-Graph modeling of Fig.4-25.

A detailed 2-DoF model of EMA MPT could have complex structure with numerous contacts between moving bodies (typically at gear teeth, bearings, joints and screw mechanism) in which the jamming of anyone may cause the EMA to jam.

4.3.6 Thermal Behavior

The 2-DoF models of MPT consider the effect of temperature in the same manner as the 1-D model does. The temperature sensitivity to the 2-DoF model of nut-screw is respectively shown in Fig 4-26. The temperature detector (De) is used to introduce the temperature effect on nut-screw compliance (dilatation) by element MC.

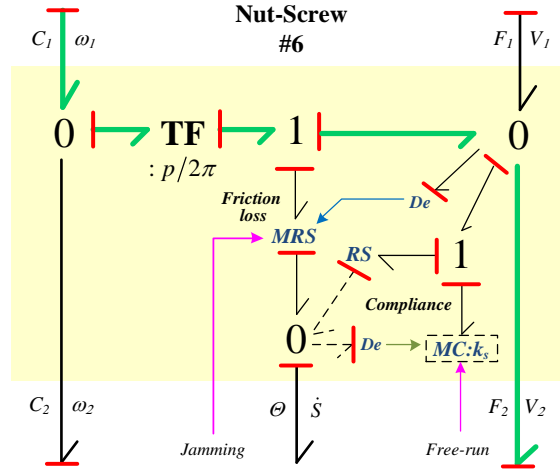


Fig. 4-26 2-DOF causal Bond-Graph model of nut-screw considering thermal behavior

The same modelling approach can be applied to bearings and joints where the thermal effect is also significant. The advanced 2-DOF causal Bond-Graph model is shown in Fig.4-27.

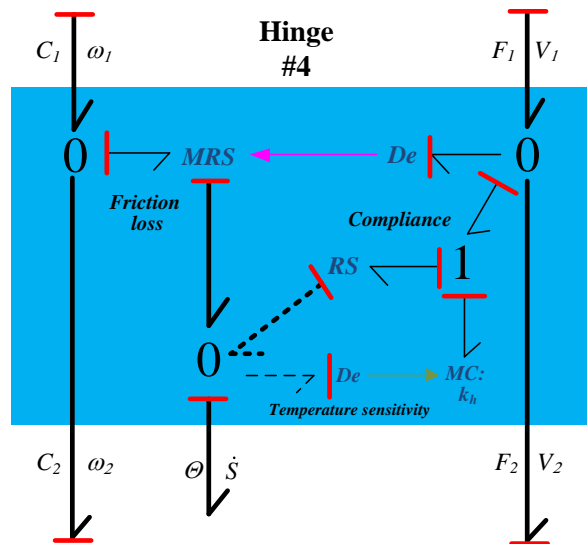


Fig. 4-27 Advanced 2-DOF causal Bond-Graph model of nut-screw considering thermal behavior

In 2-DOF models of EMA system, the friction effects in mechanical transmission are mainly analyzed in generic nut-screw and bearings model according to each sub-assembly function and incorporated structure. Generally, the stiffness of the rod is very high and the compliance effect can be generally ignored.

4.4 Model Implementation

The MPT model also can be regarded as a separate package model as done for PDE and motor

modeling. The schematic diagram of mechanical transmission implementation is shown in Fig.4-28.

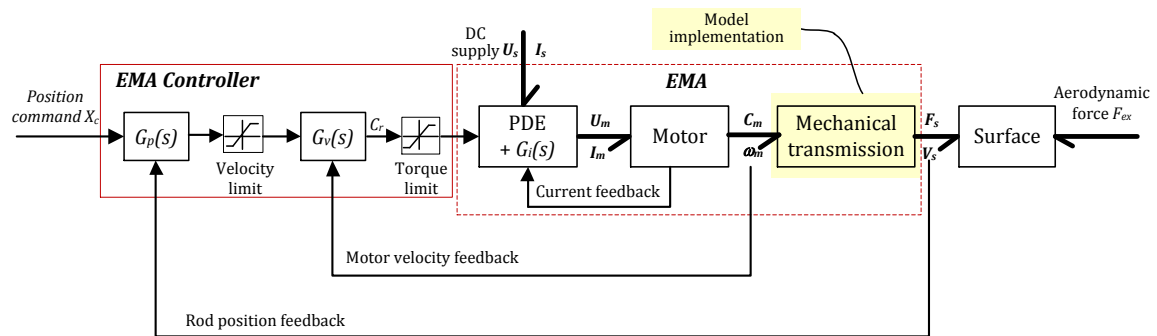


Fig. 4-28 Schematic diagram of EMA system for MPT model implementation

In order to facilitate the reading, the following developments will use simple models of controller, PDE and EM. However, the particular care taken for causalities makes the MPT model compatible with the advanced models developed for PDE and EM in chapter 3. The corresponding structure of the MPT model implementation in AMESim is shown in Fig.4-29. The PDE model uses second order function, which considers motor current loop dynamics. The motor model is assumed to be a perfect power converter, which has no electric parasitic effect but with of rotor inertia.

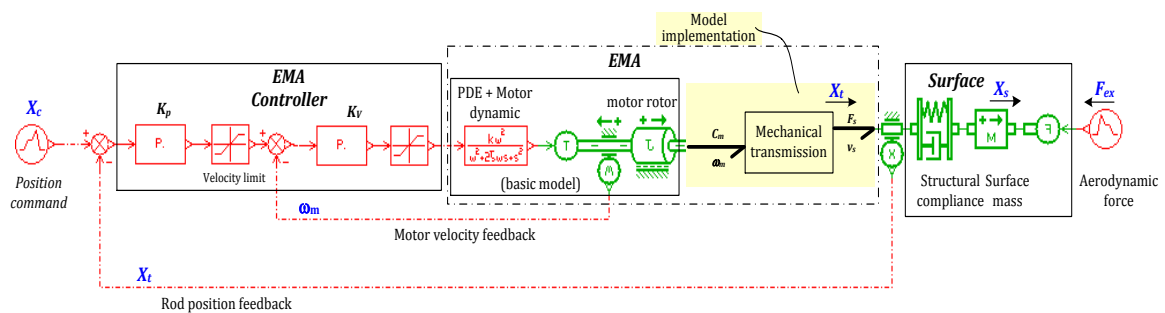


Fig. 4-29 Implementation of MPT model in a full EMA model in AMESim

Two modeling approaches of 1-DoF and 2-DoF have been respectively presented in sections 4.2 and 4.3 using the Bond-Graph formalism. Once again, the attention paid to causalities enables the MPT 1-DoF and 2-DoF models to be implemented in AMESim without causality conflict or algebraic loop.

Remark: attention has to be paid to the position and velocity sensors. Indeed, when parasitic

motion due to compliance effects (e.g. axial motion of nut due to compliance of axial thrust bearing) are considered, the model shall reproduce how the sensors housing and moving part are integrated in the EMA.

4.4.1 1-DoF Modeling

a) Basic MPT Model

The basic model is always simple, low order and linear. Its use is relevant for functional simulation and for preliminary control synthesis. The implementation of this basic 1-DoF model of MPT is shown in Fig.4-30. The motor and nut-screw inertia are merged into a single lumped inertia on which applies a pure viscous friction. The motor power flows to a perfect nut-screw and is transmitted to the load through a compliance effect that is considered using linear spring-damper model. In order to meet causalities requirements at MPT interface with load, a rod mass is also considered.

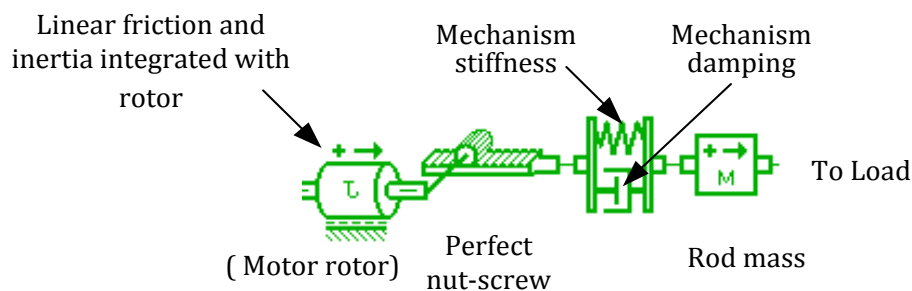


Fig. 4-30 Implementation of 1-DoF basic model of MPT in AMESim

b) Advanced MPT Model

The 1-DoF model of MPT shown in Fig.4-31, implements the major features proposed in section 4.2, Firstly, the former linear models of friction and compliance are replaced by more realistic models:

- the friction model reuses a generic AMESim model in order to take benefit of the various and rigorous implementations of the transition between the stuck and sliding modes (e.g. hyperbolic tangent, Karnopp, Dahl, etc.). The proposed friction model is implemented by making the friction force dependent to transmitted force, temperature and sliding velocity (force and velocity are captured through sensors models). This dependence can be either

defined by parametric functions or by loop-up tables.

- the compliance model of section 4.2.3 is implemented by moving to the “signal” world, separating explicitly the flow and effort variables through a standard AMESim model. The backlash parameter is made dependent on temperature.

Secondly, energy balance and response to fault are implemented as follows:

- a standard AMESim thermal power bond is introduced. It collects the power losses (friction model and structural damping of compliance model) and inputs temperature to the friction and compliance models.

- jamming and free-run faults are optionally introduced by external signal links that affect the friction and compliance parameters, respectively.

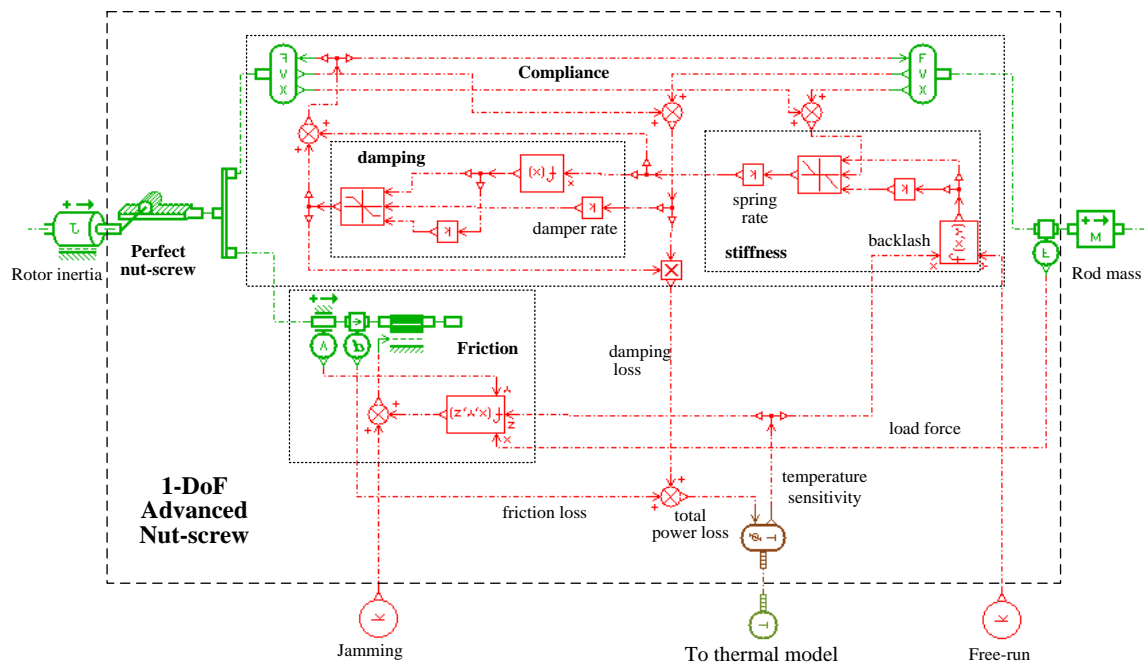


Fig. 4-31 Implementation of advanced submodel of MPT in AMESim

In the future, there is no particular issue to associate the friction and compliance models into extended icons having a similar look as those of Fig. 4.30, on basis of same power flow (motor torque input and force transmission output).

4.4.2 2-DoF Modeling

In this section, the models proposed in section 4.3 are implemented as the advanced MPT

model. Using the 2-DoF has required the mechanical 0 junctions in the translational and rotational domains to be implemented in AMESim, seen Fig. 4-32.

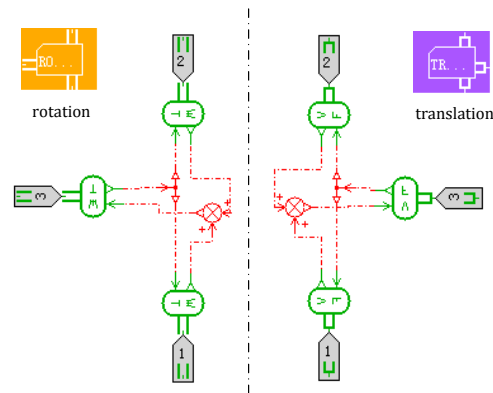


Fig. 4-32 Implementation of mechanical “0” junction of 2-DoF motion in AMESim

a) 2-DoF EM Model

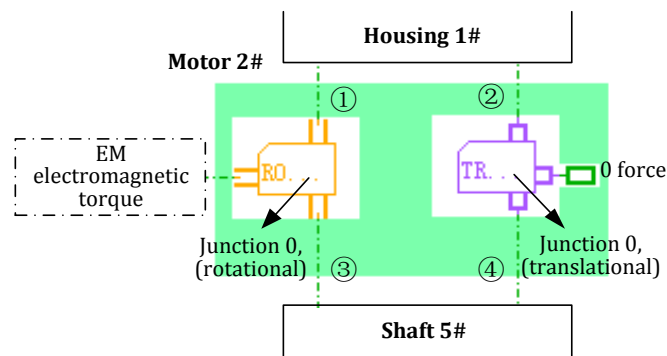


Fig. 4-33 Realization of 2-DoF motor model (perfect) in AMESim

The 2-DoF motor model implements the motor as a source of torque in the rotational domain between the motor stator and the motor rotor, Fig. 4-33. As there is no axial force hold by the motor, a zero force element is connected to the translational speed-summing model. The stator of motor is designed to integrate with housing (1#): they have the same motion movement. The rotor of motor is integrated with the shaft (5#) embedded the nut. It is worth remarking that the motor velocity sensor has to be inserted on the left power bond because it measures the relative rotational velocity between shaft and stator.

b) 2-DoF Cylinder Pair Model

The cylinder pair model Fig. 4-14 is implemented as given in Fig. 4-34. Rotational friction between inner and outer races is not affected by axial force because the cylinder pair offers a

free axial relative motion. However, translational friction can be implemented if necessary. Except that, friction dependency to temperature and velocity is implemented in a similar way as for the nut-screw in section, Fig. 4-31. There is no particular difficulty to consider jamming in the same manner as for the nut-screw through an external signal that can increase friction. The same generic quadriport model of the cylinder pair can be used to link housing (1#) and shaft (5#) or to link housing (1#) and rod (7#) according to Fig. 4-10.

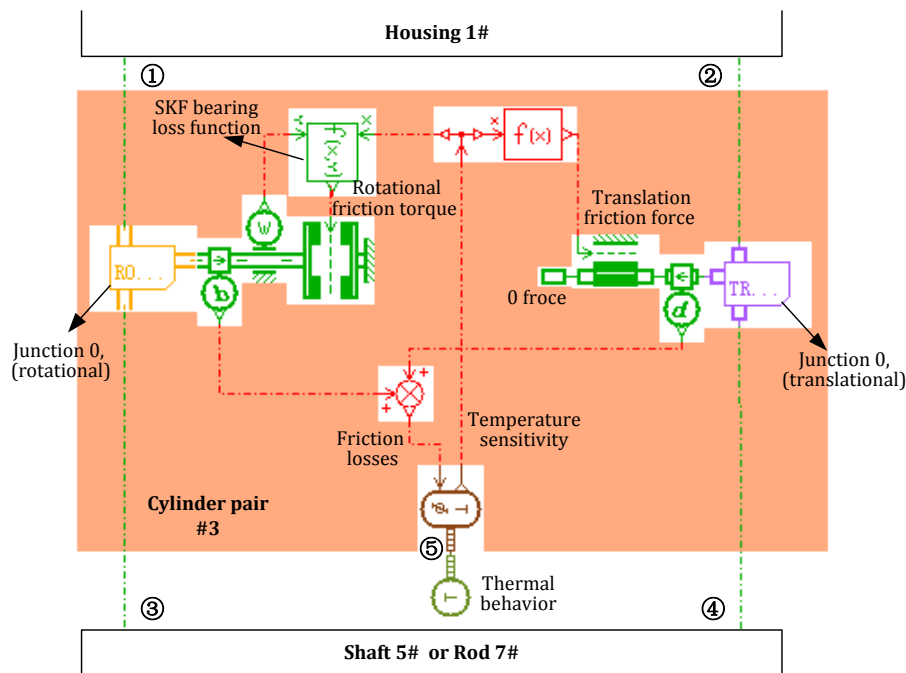


Fig. 4-34 Realization of 2-DoF cylinder pair in AMESim

c) 2-DoF Hinge Model

According to the causal Bond-Graph model in Fig.4-15, the implementation of 2-DoF hinge model in AMESim is shown in Fig.4-35. The hinge pair link housing (1#) and shaft (5#). The friction and compliance models are implemented using globally the same approach as mentioned for the nut-screw in Fig. 4-31. However, to make it simple, the compliance is implemented using the spring and damper models that are available in the AMESim mechanical library. There is no particular issue to use a more detailed compliance model of Fig. 4-27, as explained in the nut-screw model.

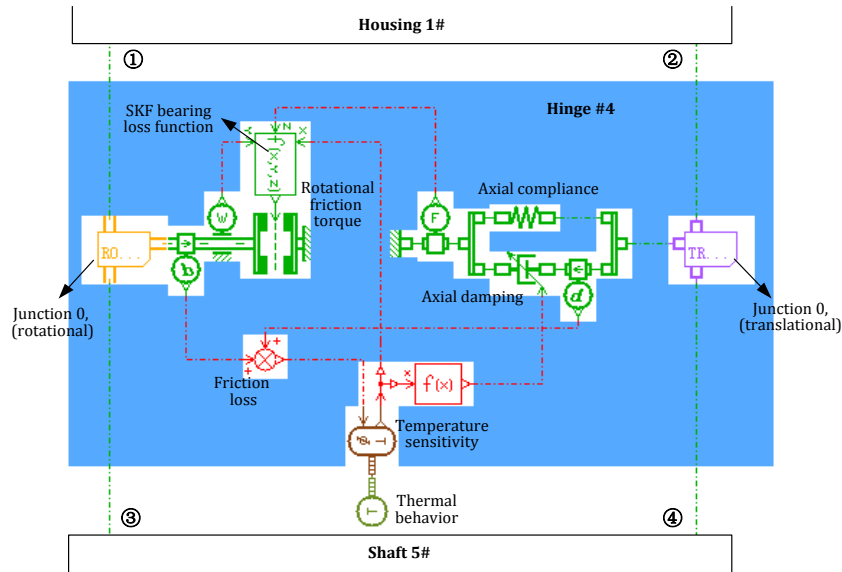


Fig. 4-35 Implementation of 2-DoF hinge in AMESim

d) 2-DoF Nut-Screw Model

Based on the causal 2-DoF model of nut-screw in Fig.4-26, the generic component of nut-screw involves four mechanical ports between shaft (5#) and rod (7#) and one thermal port. The friction and compliance effect in this model is based on the 1-DoF nut-screw model of Fig. 4-31, in which the 2-DoF anti-rotation and anti-translation mechanical ports are added, seen Fig. 4-36. Therefore, for control design the realistic displacement of EMA is available, which is the relative displacement of the airframe deformation and rod displacement.

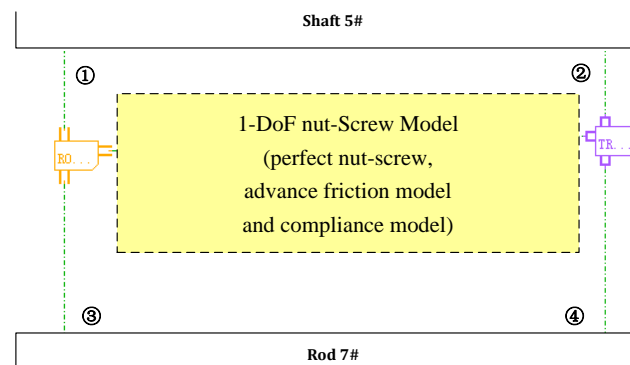


Fig. 4-36 Implementation of 2-DoF nut-screw in AMESim

e) 2-DoF Housing

The EMA housing Bond-Graph model of Fig. 4-18 is implemented as given on Fig. 4-37. According to Fig. 4-10, it interconnects with the airframe, the bearings and the motor stator.

Structural compliances are mentioned for information only and implemented using standard AMESim models. Once again, these models can be upgraded, if necessary, using the approach proposed for the nut-screw compliance, Fig. 4-31. A single inertia and a single mass model merge all the inertance effects of the solids rigidly linked to the housing (outer races of bearings and motor stator). The thermal 0 junction is implemented as a thermal node that sums the heat generated by bearings, motors windings, nut-screw, etc.

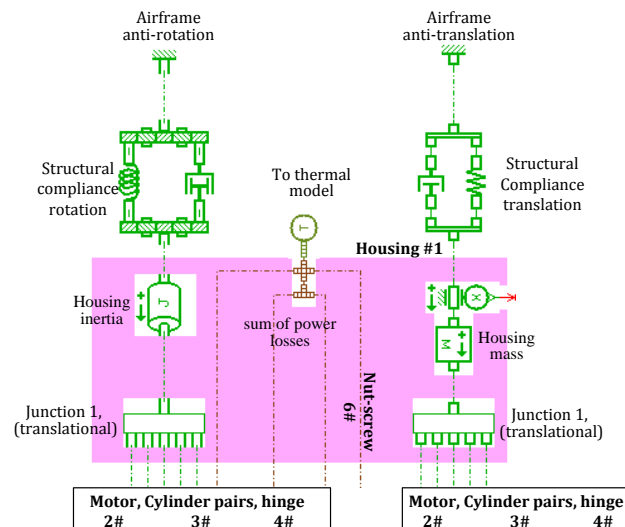


Fig. 4-37 Implementation of 2-DoF housing model in AMESim

f) 2-DoF Shaft Model

The shaft model, 2-DoF Bond-Graph Fig. 4-19, is basically of the same type as the housing model because it acts as a force (translational and rotation) and heat summing body (realistic). However, if the EMA thermal model is basic, the EMA can be considered as a single thermal body lumped at the housing level. In this case, there is no thermal port in the shaft model given on Fig.4-38.

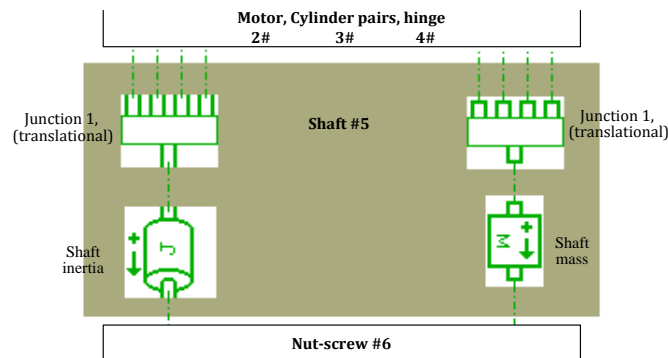


Fig. 4-38 Implementation of 2-DoF shaft model in AMESim

g) 2-DoF Rod Model

The 2-DoF Bond-Graph model of Fig. 20 can be implemented in Fig. 4-39. It has the same structure as that of the housing model.

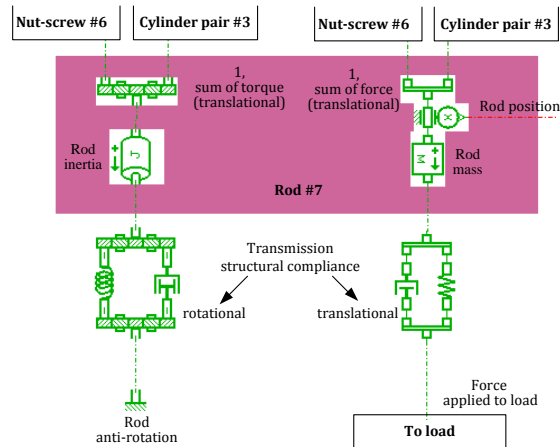


Fig. 4-39 Implementation of 2-DoF rod model in AMESim

4.5 Numerical Simulation and Analysis

The former sections presented the developed of the MPT with or 1-DoF or 2-DoF views. The present section intends to display the influence of the type of model on the simulated responses.

Like in chapter 3, the controller structure and parameters are set on basis of the linear model analysis in Chapter 2 to meet EMA performance requirements. Here, the current loop dynamics is considered in PDE model by a second order function while the electric motor is considered as perfect (efficiency of 100%). Therefore, the parameters of EMA controller, PDE and driven load are listed in Table 4-4.

For 1-DoF modeling and 2-DoF modeling, parameters can be found either in the product datasheets, from former experimental data or assumed for engineering experience. The 1-DoF model parameters are given in Table 4-5, the 2-DoF model parameters are given in Table 4-6. It is worth remarking that these tables explicitly mention the source of information and the uncertainty for the numerical value of each parameter. In practice, this information is of prior interest for concurrent engineering and for performance sensitivity studies, respectively.

Table 4-4 EMA controller, electric power drive electronics and load parameters

Parameter	Value	Parameter	Value
$G_p(s)$ position P-gain K_p ($\text{rad}\cdot\text{s}^{-1}\cdot\text{mm}^{-1}$)	45	Amplifier saturation velocity (rad/s)	314
$G_v(s)$ velocity P-gain K_v ($\text{Nm}\cdot\text{s/rad}$)	0.47	Structural transmission stiffness k_t (N/m)	$5 \cdot 10^9$
Current loop damping factor of PDE ω_i	0.7	Structural transmission damping B_t ($\text{N}/(\text{m/s})$)	$1 \cdot 10^4$
Current loop natural frequency of PDE ξ_i (Hz)	600	Surface equivalent mass M_s (kg)	600
Amplifier saturation torque (Nm)	10		

Table 4-5 Parameters of 1-DoF model

Parameter	Value	Level	Reference source	Confidence
Nut-screw stiffness k_s (N/m)	$3 \cdot 10^8$	Basic	Scaled from former experiments [9]	High
Nut-screw transmission damping B_s ($\text{N}/(\text{m/s})$)	$1 \cdot 10^4$			
Lead of screw p (mm)	2.54		Datasheet of Exlar EMA [25]	High
Rotor inertia integrated with nut-screw (kgm^2)	0.001717			High
Viscous friction coefficient ($\text{Nm}/(\text{rad/s})$)	0.003			High
Rod mass (kg)	1			Medium
Coulomb friction force F_{cl} (N)	7590	Advanced	Scaled from former experiments [26]	High
Stribeck friction force F_s (N)	-4702			
Reference speed for Stribeck friction force v_s (m/s)	0.035			
Mean coefficient of external force a (-)	0.218			
Quadrant coefficient b (-)	-0.13			
Backlash value x_0 (mm)	-		-	Low

Table 4-6 Parameters of 2-DoF components

Parameter	Value	Component	Reference source	Confidence
Rotational spring stiffness to anti-rotation k_{hr} (Nm/rad)	389.6	Housing	Scaled from former experiments [9]	Medium
Rotational damping B_{hr} ($\text{Nm}/(\text{rad/s})$)	1.25			

Translational spring stiffness to anti-rotation k_{ht} (N/m)	$5 \cdot 10^9$			
Translational damping B_{ht} (N/(m/s))	$1 \cdot 10^4$			
Inertia of housing integrated with motor stator J_h (kgm ²)	0.1			
Mass of housing integrated with motor stator M_h (kg)	6			
Motor efficiency	1	Motor	Assumption	Low
Bearing outer diameter D (mm)	60	Cylinder pair for shaft	Angular contact ball bearings	Medium
Bearing inner diameter d (mm)	30			
Sliding friction coefficient μ_{sl} (-)	0.04			
Seal numbers for bearing N_{sb} (-)	0			
Static friction coefficient μ (-)	0.1			
Maximum Coulomb friction force (N)	50			
Translation spring stiffness of bearing k_b (N/m)	$5 \cdot 10^8$	Hinge	Angular contact thrust bearings	High
Initial translational damping of bearing B_{b0} (N/(m/s))	$1 \cdot 10^4$			
Bearing outer diameter D (mm)	80			Medium
Bearing inner diameter d (mm)	40			
Sliding friction coefficient μ_{sl} (-)	0.04			
Seal numbers for bearing N_{sb} (-)	0			
Viscosity of the lubricant for grease ν (mm ² /s) @ 25 °C	220		Mobilith SHC 220 [25]	High
Inertia of shaft integrated with motor rotor and nut J_s (kgm ²)	0.001717	Shaft	Datasheet of Exlar EMA [25]	High
Mass of shaft integrated with motor rotor and nut M_s (kg)	3			
Lead of screw p (m)	0.00254	Nut-screw	Scaled from former experiments [9]	High
Nut-screw transmission stiffness k_n (N/m)	$3 \cdot 10^8$			High
Nut-screw transmission damping B_n (N/(m/s))	$1 \cdot 10^4$			High
Friction and backlash model	-			Medium

parameters seen Table 4-5			
Variable of SKF rolling friction losses G_{rr} (-)	0	Cylinder pair for rod	Plain bearing Medium
Variable of SKF sliding friction losses G_{sl} (-)	0		
Static friction coefficient (-)	0.1		
Maximum Coulomb friction force (N)	50		
Inertia of rod J_r (kgm ²)	0.02	Rod	Datasheet of Exlar EMA [25] High
Mass of rod M_r (kg)	1		Scaled from former experiments [9] High
Rotational spring stiffness to anti-rotation k_{rr} (Nm/rad)	3896.1		
Rotational damping B_{rr} (Nm/(rad/s))	1.766		
Translational spring stiffness to anti-rotation k_{rt} (N/m)	$3 \cdot 10^8$		
Translational damping B_{rt} (N/(m/s))	$1 \cdot 10^4$		

The modelling and simulation study for different models of MPT in this section are run using the same mission profile as used in chapter 3 for EMAs aileron position control. Different levels of simulation models of MPT were respectively assessed: a perfect/ideal 1-DoF model (level 0) without friction and compliance effects, a basic 1-DoF model (level 1), an advanced 1-DoF model (level 2) and an advanced 2-DoF model (level 3).

4.5.1 Interest for Control Design

The performance requirements are expressed in terms of closed-loop stability, dynamics and accuracy for both position pursuit and load rejection. A pilot step demand X_c for aileron position (10 mm at $t=0.1s$, 6.6% full stroke), followed by an external aerodynamic force disturbance F_{ex} (10 kN at $t=1s$, 65% rated output force) are applied in following simulations.

Fig. 4-40 compares the rod position simulated by the different MPT models (level 1, 2 and 3). Both simulated responses are stable. Firstly, it can be seen that the friction effect increases EMA system damping and affects dynamic performances when compared to the model of level 0. In level 3, because bearing friction and nut-screw friction are considered, the system response is slower. Secondly, in 1-DoF models, the perfect model of level 0 considers infinite

stiffness in MPT, while basic (level 1) and advanced models (level 2) introduce realistic nut-screw compliance and 2-DoF model (level 3) adds the contribution of structure compliance. The effects of compliance clearly appear on the load rejection performance, by increasing rod oscillations, especially in models level 1, 2 and 3. The 2-DoF model of MPT (level 3) including bearings compliance is the less stable. In practice, it is difficult to set the right level of structural damping.

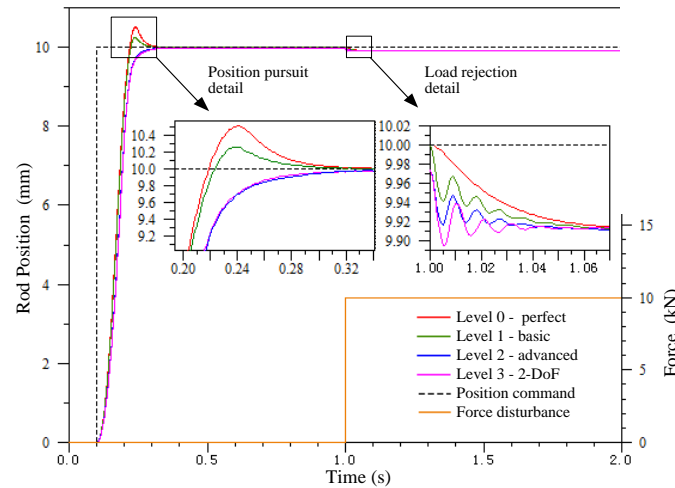


Fig. 4-40 Position responses of EMA with different MPT models of friction effects

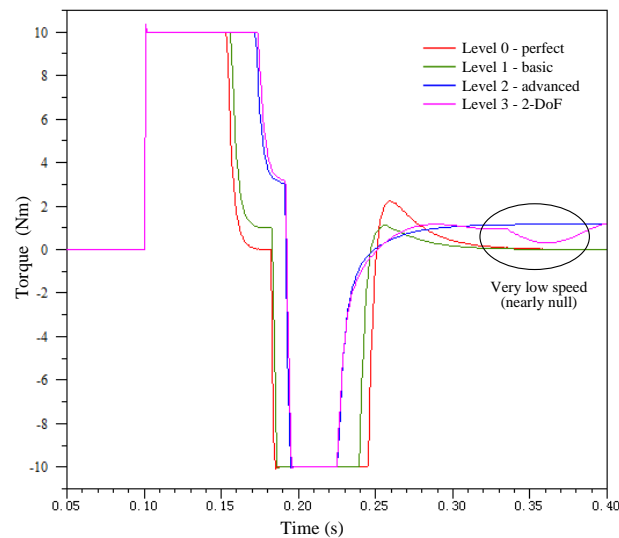


Fig. 4-41 Motor electromagnetic torque of EMA with different MPT models of friction effects

Fig. 4-41 shows the electromagnetic torque of motor versus time to highlight the differences among the MPT models. It can be seen that the motor torque/current is saturated for a longer time when a more realistic friction model is considered. Significant differences in response also appear at very low velocity.

4.5.2 Interest of Relative and Coupled 2-DoF Motion

In MPT models of level 0, 1 and 2, only 1-DoF motion of translation for the screw (rod) or rotation for nut (rotor) can be addressed and the relative motion between EMA bodies or components (bearings or support) is not available. Fig. 4-42 firstly illustrates this when the aerodynamic load has been applied (demanded position 10 mm, load applied 10kN). In the 1-DoF model, e.g. level 0 perfect MPT, only rod (screw) displacement can be plotted. Oppositely, for 2-DoF model (level 3) relative motion are available. It can be remarked that, because of anti-translation of screw by axial thrust bearings, the screw displacement is more realistic (blue curve), being different from the screw position measured by the position control loop sensor (green curve). The rod displacement becomes also more realistic when the structural compliance of anchorage of housing to airframe is considered (pink curve).

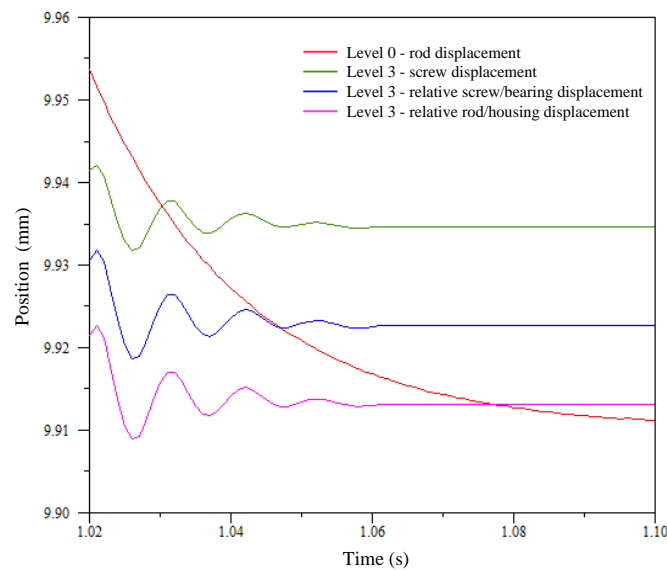


Fig. 4-42 Relative displacement simulated available in 2-DoF MPT model

In addition, the proposed 2-DoF model enables the motion due to reaction forces to be reproduced by simulation. In order to illustrate this advantage, the rotational motions of housing and rod are plotted in Fig. 4-43. It is clearly observed that model level 1 fails to reproduce this effect and no rotation is got. In the presence of aerodynamic load, the motor torque has to be reacted by the holding frame and by the load at anchorage and load attachment, respectively. As simulated by the 2-DoF model, the EMA is mechanically balanced in statics (e.g. after time 1.3 s) where the anchorage and transmission torques are exactly

opposed. The angular parasitic movement is clearly observed and contributes to a loss of load positioning accuracy because the position sensor of the control loop only measures the rod/housing relative displacement.

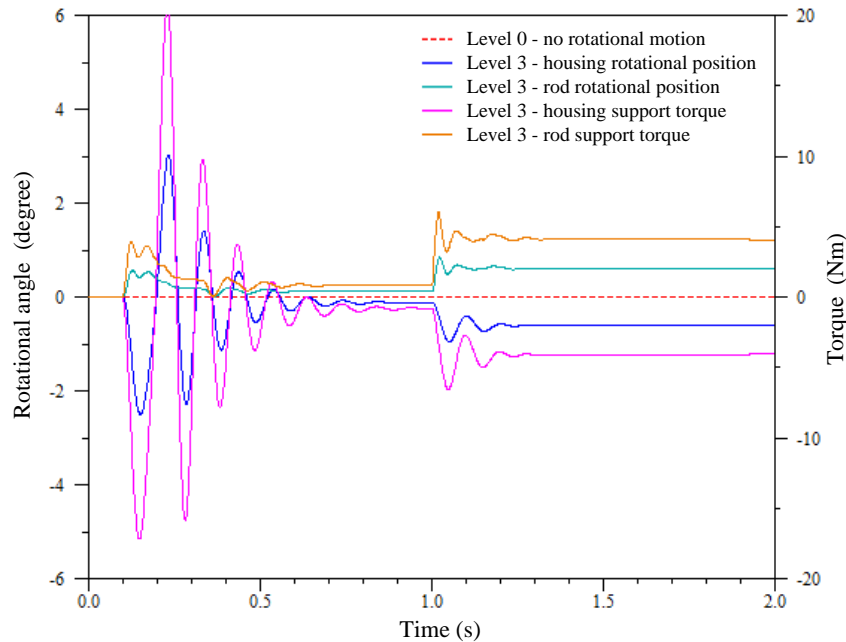


Fig. 4-43 Mechanically balanced 2-DoF MPT model for analyze housing and rod rotational motion

4.5.3 Interest for Power Consumption Analysis

When focus is put on analysis of power losses and energy consumption of MPT, simplest models fail to reproduce the contribution of bearings, while the advanced models enable designers to assess their impact. In order to illustrate this, a specific mission, Fig. 4-44 is applied to the models using trapezoidal shapes for position demand (50 mm) and external load (15 kN). In that manner, 4 zones of interest can be investigated:

- Zone 1: high speed, no load
- Zone 2: null speed, high load
- Zone 3: high speed, high aiding load
- Zone 4: high speed, high opposite load

According to the simulated controller, the maximum position error is 1.3 mm.

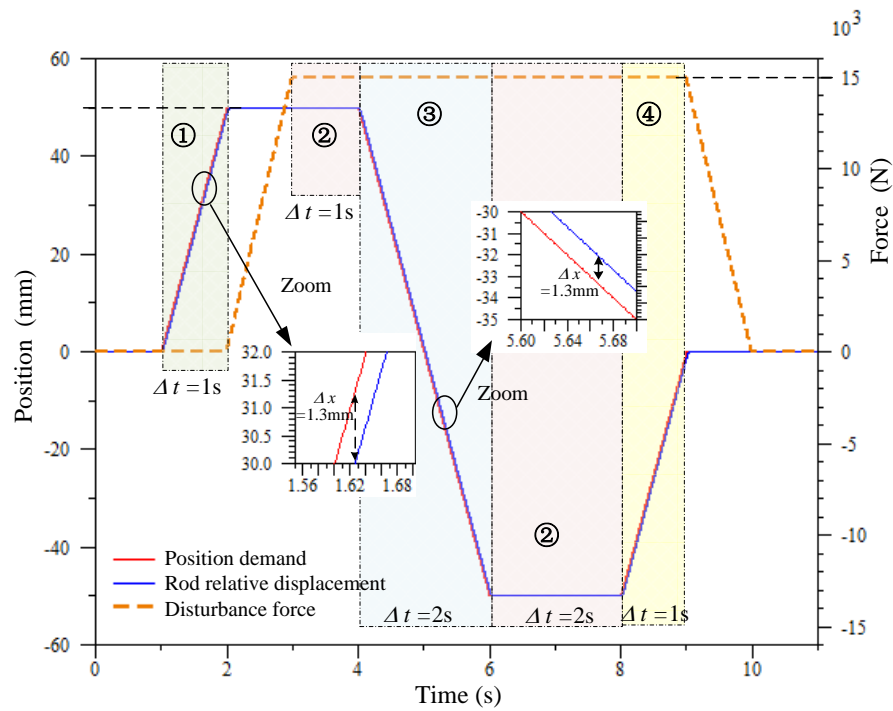


Fig. 4-44 Position demand and rod displacement performance

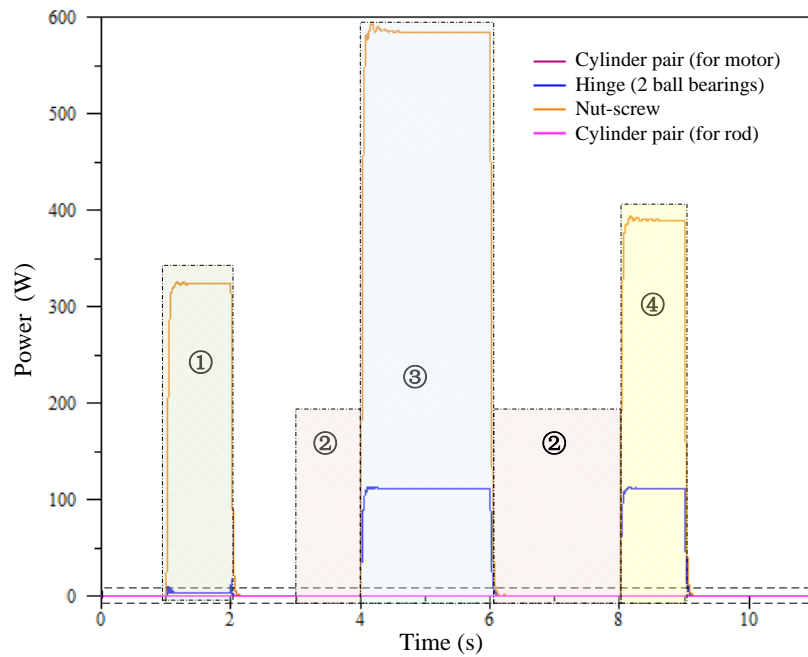


Fig. 4-45 Friction power losses comparison in MPT components

Fig. 4-45 compares the simulated power losses for each zone at cylinder pair, hinge bearings, nut-screw and plain pair bearing. It is clear that the nut-screw friction loss dominates. However, the axial thrust bearing function performed by the hinge bearing is a significant contributor to power (torque) loss as it can represent up to 20% of the total loss. This result is consistent with what has been observed in practice for various research projects.

Other bearing effects remain minor contributors to power loss, as displayed by the zoom, Fig. 4-46. However, introducing their friction models is worth if response to faults has to be investigated. Indeed, as proposed in section 4.3.5, jamming of these elements can be forced by increasing drastically their level of friction.

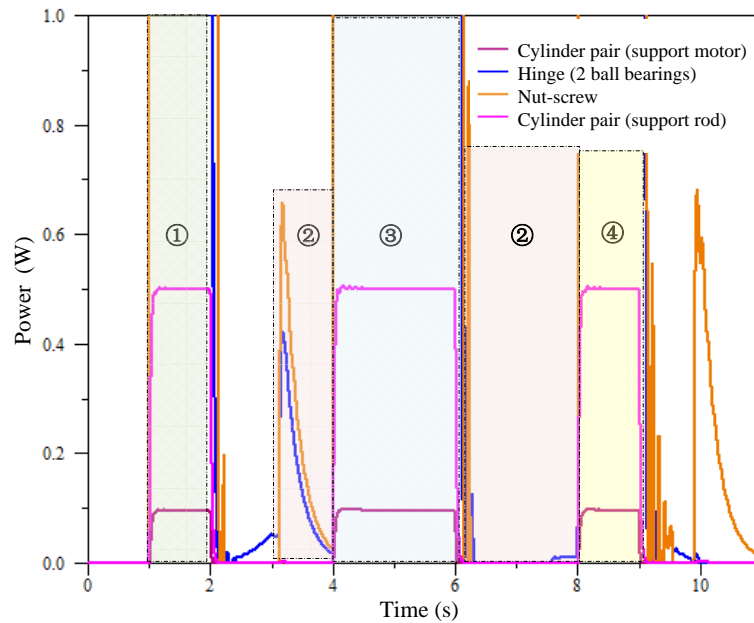


Fig. 4-46 Friction power losses zoom in Fig. 4-44

4.5.4 Interest for Wear/Ageing and Response to Faults

This section illustrates the interest of the proposed models for wear/ageing (increased backlash), and free-run or jamming faults.

-Backlash: the proposed models enable the transmission backlash to be modified dynamically by action on the parameter x_0 , in order to simulate the effect of wear versus service. This feature of the model is illustrated by Fig.4-47 where backlash is changed from null to 60 μm then 0.3 mm. Of course backlash has a little effect when the contacts are loaded in a single direction. This is why only the pursuit part of the EMA response is plotted. As it could have been predicted, in the presence of backlash, a non-linear limit cycle occurs around the demand rod position making the position control unstable.

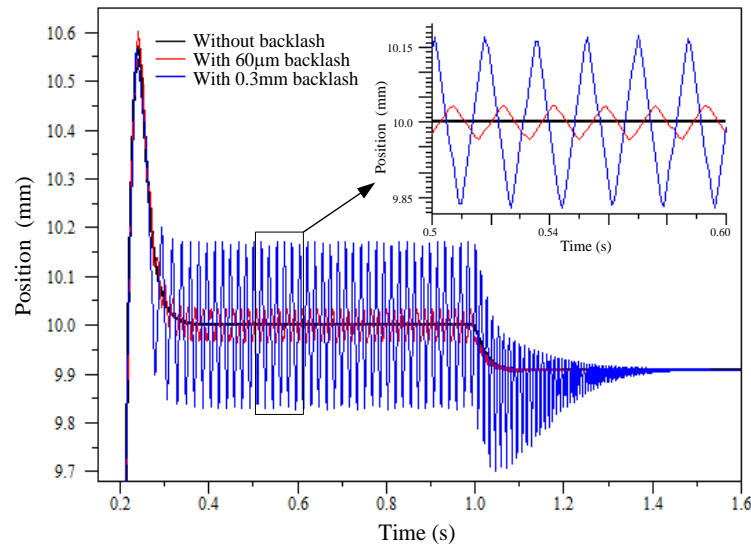


Fig. 4-47 Position responses in advanced model considering backlash

-Free-run: the response to free-run fault can be simulated by setting the backlash to a huge value greater than twice the nut-screw stroke (that of 150 mm). In this manner, there is no more mechanical link between the motor rotor and the load. An example of the simulation result is plotted in Fig. 4-48, in which free-run is initiated at $t = 0.2$ s when speed is fully established. External is null in this simulation.

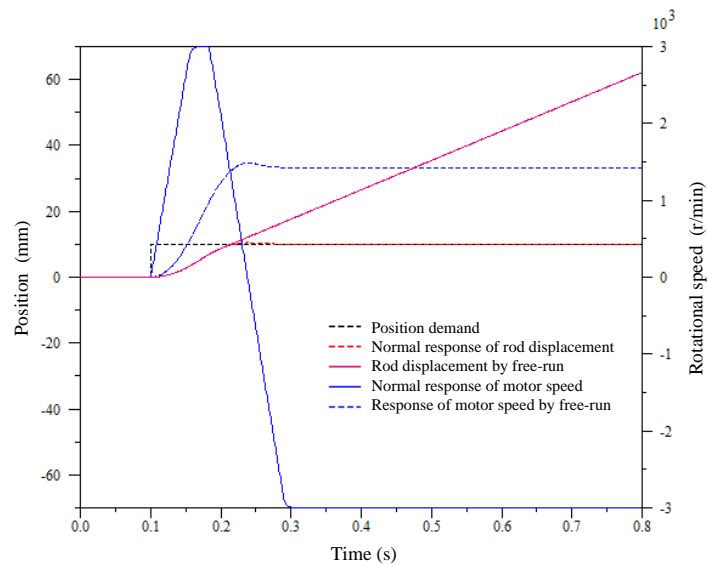


Fig. 4-48 Position responses in advanced model considering backlash

In above Fig. 4-48, the rod displacement is no longer able to follow the position demand and continues moving due to the kinetic energy stored by the rotor that is dissipated into heat by frictional effects. The motor speed becomes rapidly saturated because the controller

increases the demanded torque in response to the wrong position.

-Jamming: in the proposed behavioral MPT models, jamming can be simulated by increasing the friction force parameter (F_{jam}). The response to jamming is simulated, Fig. 4-49 for 4 times at which the jamming fault is triggered: during the rising position (at $t = 0.18$ s, black curve), in the overshoot domain (at $t = 0.24$ s, red curve), in steady position (jamming triggered at $t = 0.65$ s, blue curve) then after application of aerodynamic load (at $t = 1.15$ s, pink curve). As expected, the rod position is locked immediately.

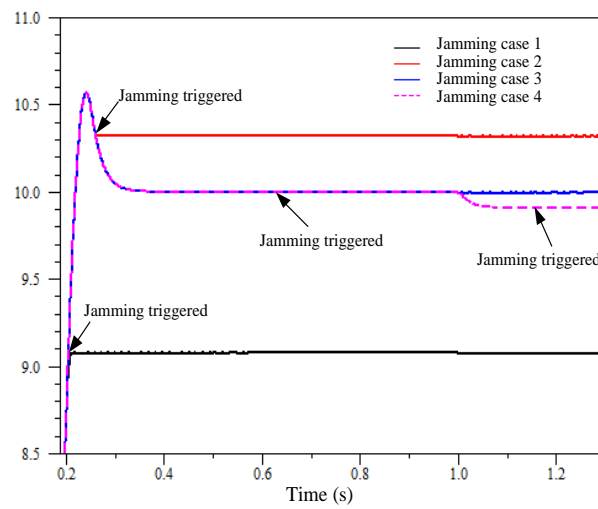


Fig. 4-49 Position responses with friction effect study in mechanical transmission

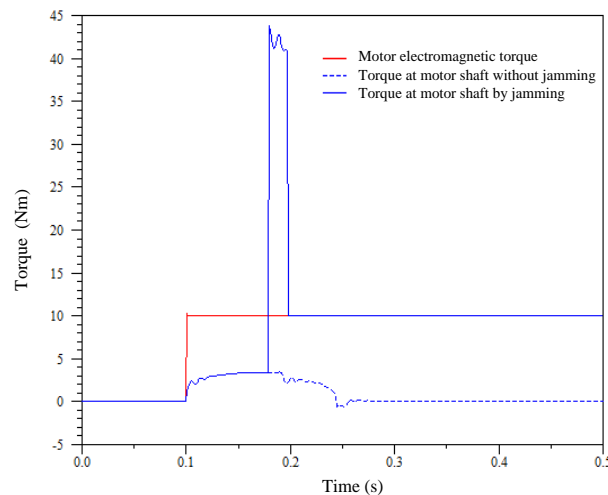


Fig. 4-50 Comparison of the torque response without/with jamming issue

Fig. 4-50 is dedicated to the jamming case triggered during rising position (at $t=0.18$ s). It is interesting to note the huge magnitude to torque transmitted to nut-screw that is 4.5 times

the rated torque, due to the inertial effect of the motor rotor. On its side, the electromagnetic torque remains saturated as the position errors cease to evolve.

4.6 Conclusion of Chapter 4

In the present chapter, the modelling and simulation of the mechanical power transmission (MPT) of EMA has been developed in progressive way, based on system engineering (SE) process and simulation driven design (SDD) approach. By considering successively different physical effects with different levels of details, the 1-DoF and 2-DoF MPT models have been proposed using the Bond-Graph formalism. This enabled defining the model's architecture and causality with rigor. The main advances of the proposed MPT models and their numerical implementation consist in:

- Distinction has been clearly made between perfect effect and parasitic effects (such as inertia, friction, compliance, etc.)

- The structure of decomposition in 1-DoF and 2-DoF ways have been presented to facilitate model-based modelling and simulation. The key effects were incrementally introduced.

- Each MPT lumped-parameter model is energetically and mechanically balanced. The power losses of the MPT are reproduced by advanced friction models (considering sensitivity to transmitted force and temperature in addition to sensitivity to sliding velocity).

- The features of ageing and faults injection (wear, free-run and jamming) are modeled in a simple way without increasing models' complexity and dynamics, in order to facilitate later activity related to the design of health and usage monitoring features.

- All the proposed MPT models are replaceable (same interfaces), the models are ready to be extended for next step thermal simulation and to be integrated in full incremental realistic EMAs virtual prototyping.

In the end, the implementation of mechanical transmission model was found to run rapidly and in robust way, without numerical issues. Although the proposed models have been developed on basis of real tests performed in former research works or from suppliers

catalogues, the next step is obviously to validate the models against real experiments. This objective will be partly addressed in the following chapter that is dedicated to the design of the real testing facility.

References

- [1] High Speed and Large-Lead Model SBK Ball Screw [Online]. Available: <http://www.highprecisionrollingballscrew.com/>
- [2] Exlar. Roller Screw Technology [Online]. Available: <http://exlar.com/resources/>
- [3] Exlar. Advantages of Roller Screw Technology [Online]. Available: <http://exlar.com/why-exlar/many-advantages-roller-screw/>
- [4] F. Perni, L. Pizzoni, and N. Borgarelli, "Ball Screws for the More Electric Aircraft," presented at the International Conference on Recent Advances in Aerospace Actuation Systems and Components (R3ASC), Toulouse, 2004.
- [5] SKF, "SKF General Catalogue," ed, 2006.
- [6] J.-C. Maré, "Requirement-based system-level simulation of mechanical transmissions with special consideration of friction, backlash and preload," *Simulation Modelling Practice and Theory*, 2016.
- [7] J.-C. Maré, "Friction modelling and simulation at system level: a practical view for the designer," *Proceedings of the Institution of Mechanical Engineers, Part I: Journal of Systems and Control Engineering*, pp. 728-741, 2012.
- [8] J.-C. Maré, "Friction modelling and simulation at system level: Considerations to load and temperature effects," *J. Systems & Control Engineering*, vol. 229, pp. 27-48, / 2015.
- [9] W. Karam and J.-C. Maré, "Modelling and simulation of mechanical transmission in roller-screw electromechanical actuators," *Aircraft Engineering and Aerospace Technology*, vol. 81, pp. 288-298, 2009.
- [10] J. Fu, I. Hazyuk, and J.-C. Maré, "Preliminary design rules for electromechanical actuation systems - effects of saturation and compliances," in *5th CEAS Air & Space Conference*, Delft, Netherlands, 2015.
- [11] A. Garcia, J. Cusido, J. Rosero, J. Ortega, and L. Romeral, "Reliable electro-mechanical actuators in aircraft," *Aerospace and Electronic Systems Magazine, IEEE*, vol. 23, pp. 19-25, 2008.
- [12] J. Liscouët, J.-C. Maré, and M. Budinger, "An integrated methodology for the preliminary design of highly reliable electromechanical actuators: Search for architecture solutions," *Aerospace Science and Technology*, vol. 22, pp. 9-18, 2012.
- [13] M. Todeschi, "Airbus-EMAs for flight controls actuation system-perspectives," presented at the International Conference on Recent Advances in Aerospace Actuation Systems and Components (R3ASC), Toulouse, France, 2010.
- [14] M. Nordin and P.-O. Gutman, "Controlling mechanical systems with backlash—a survey," *Automatica*, vol. 38, pp. 1633-1649, 2002.

- [15] R. Merzouki and J. C. Cadiou, "Estimation of backlash phenomenon in the electromechanical actuator," *Control Engineering Practice*, vol. 13, pp. 973-983, 2005.
- [16] M. A. El Sayed and S. Habibi, "Inner-Loop Control for Electro-Hydraulic Actuation Systems," *Journal of Dynamic Systems, Measurement, and Control*, vol. 134, pp. 014501-014501, 2011.
- [17] J.-C. Maré, "2-D lumped paramaters modelling of EMAs for advanced virtual prototyping," in *International Conference on Recent Advances in Aerospace Actuation Systems and Components (R3ASC)*, Toulouse, 2012, pp. 122-127.
- [18] E. Faugère, J.-C. Maré, C. Changenet, F. Ville, and D. Delloue, "Coupling mechanical and thermal lumped parameters models for the preliminary design of power transmissions driven by thermal issues," in *28th International Congress on Aerospace Sciences (ICAS)*, Brisbane, Australia, 2012, pp. 3690-3700.
- [19] A. Palmgren, "Ball and roller bearing engineering," *Philadelphia: SKF Industries Inc.*, vol. 1, 1959.
- [20] J. Brändlein, P. Eschmann, L. Hasbargen, and K. Weigand, *Ball and Roller Bearings: Theory, design, and application*: Wiley Chichester, 1999.
- [21] KOYO. Koyo bearing catalog [Online]. Available: <http://www.koyo.eu/en/products.html>
- [22] NTN, "Ball and roller bearings," ed, 2009.
- [23] T. A. Harris and M. N. Kotzalas, *Essential concepts of bearing technology: rolling bearing analysis*: CRC press, 2006.
- [24] L. imagine, "AMESim powertrain library, rev.13," ed, 2014.
- [25] Exlar. Exlar Product Catalog, GSX Series Integrated Motor/Actuator [Online]. Available: <http://exlar.com/pdf/?pdf=/content/uploads/2014/09/GSX-Catalog-Section1.pdf>
- [26] L. Wang and J.-C. Maré, "A force equalization controller for active/active redundant actuation system involving servo-hydraulic and electro-mechanical technologies," *Proceedings of the Institution of Mechanical Engineers, Part G: Journal of Aerospace Engineering*, vol. 228, pp. 1768-1787, 2014.

Chapter 5

Test Bench and Preliminary Study of Position Synchronization

In the frame of this research work, we have acted as the major contributor to the specification, the design, the integration and the setting of a test bench dedicated to the experimental validation of our modelling and control proposals. The test bench involves two power lines that can be either rigidly connected or made independent. Each power line involves 2 actuators (an EMA and an HSA) in a face-to-face arrangement. This topology enables various configurations to be assessed, e.g. for position synchronization (independent lines) or force equalization (rigidly coupled lines). The first part of this chapter is dedicated to the presentation of the test bench and its virtual prototyping. The second part addresses position synchronization and its preliminary validation through the full EMA's model developed in the former chapters. It is important to recall that the EMA's models are developed using an incremental approach that is driven by engineering needs and real measurements coming from former research projects.

5.1 Description of the Test Bench

5.1.1 Objectives

For safety-critical applications like flight controls, the actuation function has to be redundant to meet the reliability target. When multiple control surfaces are used, e.g. elevators or ailerons, the most common solution consists in driving one surface by two actuators. For this reason, the test bench is developed in order to perform real experiments for the assessment of position synchronization or force equalization in dual-channel actuation. The main objectives of the test bench are:

-to improve the knowledge of parasitic effects, e.g. for EMAs: friction, compliance (including backlash or preloading effects), digital implementation of controllers (signal filtering, sampling, quantization and saturation),

-to allow different combination of actuators to be compared: HSA/HSA, HSA/EMA, EMA/EMA in either active/active, active/damping modes,

-to load the actuators with forces that are representative of real operational conditions, including inertia effects and opposite/aiding airload,

-to validate the proposed control laws for single channel or double channel operation: including position synchronization or force fighting features.

Figures 5-1 (a) and (b) show the functional architectures associated with the position synchronization or force equalization tests, respectively.

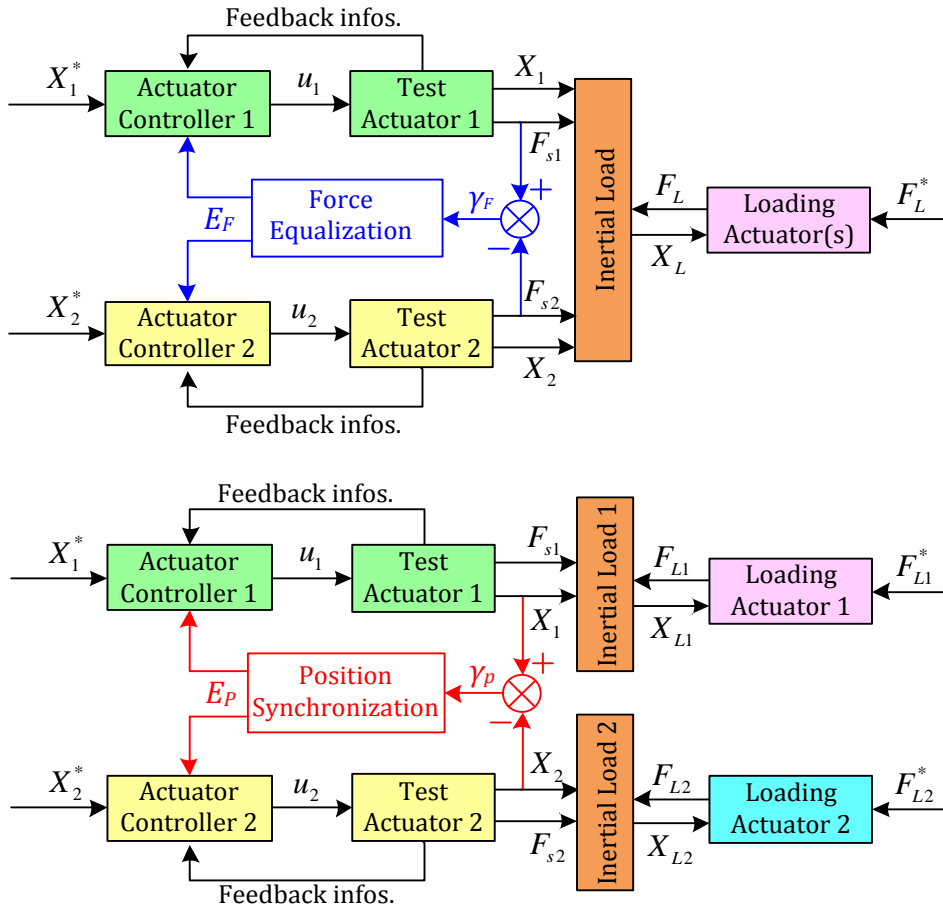


Fig. 5-1 Architecture of the test bench (Top: Force Equalization, bottom: Position Synchronization)

5.1.2 Requirements

According to the above mentioned needs, the following design choices have been made:

a) Type of actuators: two real EMAs + two real HSAs: depending on the need, each type of actuator can be operated either as the tested actuator or as the loading actuator

b) Inertial loads: it is extremely difficult to reproduce pure inertial effect by a loading actuator because it requires a huge bandwidth that cannot be reached due to technological limits. For this reason, the inertial effect is always reproduced by a real inertia. However, in order to minimize the translating mass (M_{eq}) to be mounted, the effective inertia is reproduced with use of a rotational/translational transformer effect (lever arm l) that only requires a small rotating inertia.

$$M_{eq} = \frac{J_L}{l^2} \quad (5.1)$$

For example, a flight control surface inertia of 1 kgm^2 with a lever $l = 50 \text{ mm}$ will translate an equivalent surface mass $M_{eq} = 400 \text{ kg}$. The inertia is varied by adding mass on the rotating arm.

c) Static and dynamic loading: One or two actuators are used as load generator(s) and closed-loop force controlled. The force sensor is mounted between the loading actuator rod and the inertia. It is selected in order to not introduce significant parasitic effects when the actuator is used as the test actuator.

d) Position synchronization or force equalization tests: the two inertias can be decoupled or rigidly coupled.

f) Structural compliances: the compliance of actuator body attachment to airframe and actuator rod transmission to load is reproduced as a single equivalent attachment compliance that can be easily set prior experiments.

g) Control system: A/D and D/A conversion, acquisition and control of all four actuators are performed by a single real time target device that enables rapid prototyping of actuators control, force equalization or position synchronization.

h) Man-machine interfaces: Two PCs are needed and separated. One is in charge of some manual programming (test mode), offline parameters setting. The other is in charge of data collection and servo control realization.

i) Safety: the emergency button is needed and installed to cut-off the actuators powering.

5.1.3 Test Bench Components and Topology

Therefore, some assumptions and choices are presented in detail below:

- Real EMAs, selecting the Exlar commercial industry EMAs as the test actuators.
- Load (surface): For aircraft aileron application, the equivalent translating mass is 600 kg. This is a very large mass to be handled safely in a research laboratory. A compact lumped iron device of 4 kgm² moment of inertia and a transmission lever of 0.08 m length are used to reproduce this inertial effect as the load.
- Disturbance force: Two hydraulic servo actuators (HSAs), symmetrical rod, constant pressure supply and servovalve controlled, are driven in force closed loop to simulate the aerodynamic load. A particular attention is paid to the force control loop in order to reject the effect of load speed (imposed by the position actuator on test) on the force control loop. As well, parasitic compliance (attachment and transmission) are considered with attention.
- Two inertial loads are optionally connected by a rigid linkage (decoupled for position synchronization study, linked for force equalization study).
- Anchorage stiffness: In aerospace, the mass constraints make the EMA attachment to load and anchorage to airframe compliant. This compliance is reproduced on the test bench as a single compliance located at the anchorage of the EMA housing to the test-bench frame. As an example, the stiffness representative of the airframe and surface deformation under load, this typically equals to 1.4×10^7 N/m. The structure of test bench must be sufficient rigidity to not introduce unmanaged compliances. It is usually designed to be 4 to 10 times stiffer (5×10^7 N/m to 1.4×10^8 N/m) than the airframe anchorage to be reproduced.
- Force sensor: the force sensor has to limit the intrusive effect it generates. The selected sensor has a mass of 3 kg that corresponds to 0.5% of the load mass and 0.03% of the

actuator reflected mass. Its stiffness, $8 \cdot 10^8$ N/m, corresponds to 16 times the test bench structural stiffness, 5 times the EMA stiffness ($1.5 \cdot 10^8$ N/m, that of 0.1 mm at 15 kN loading) and that is greater than the test bench frame stiffness.

- Control: the position/speed/current/force loops are implemented in Speedgoat real time target box which is also in charge of taking the measurements.

- Test settings: PC1 is in charge of manual programming (test mode) and EMA offline parameterization. PC2 is in charge of data collection and generation of real time code that is uploaded in the Speedgoat target box.

- Safety: Three emergency stop buttons are available for cut-off the current to EMAs supply and cut-off pressure supply to HSAs. One is placed on the programming desk, another is installed in electric control cabinet and the last one is installed on the test bench.

5.1.4 Test Bench Configuration

The designed test bench is shown in Figure 5-1, and the configuration is in Fig. 5-2:

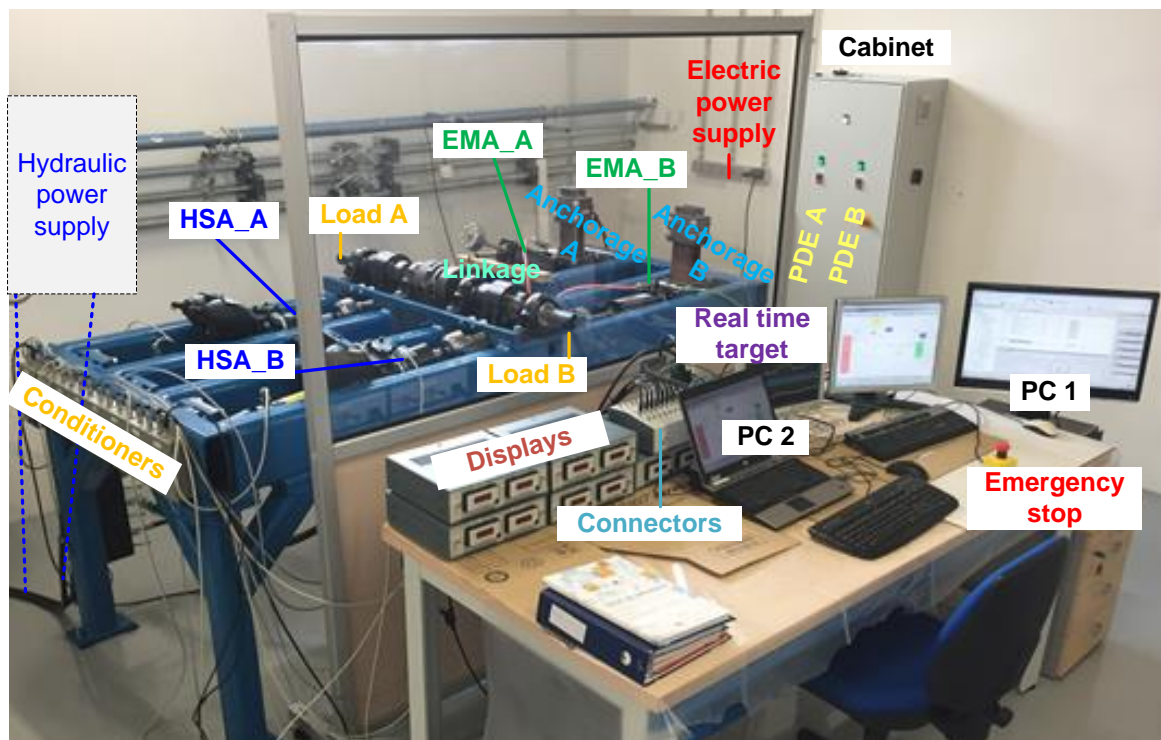


Fig. 5-1 Photograph of test bench

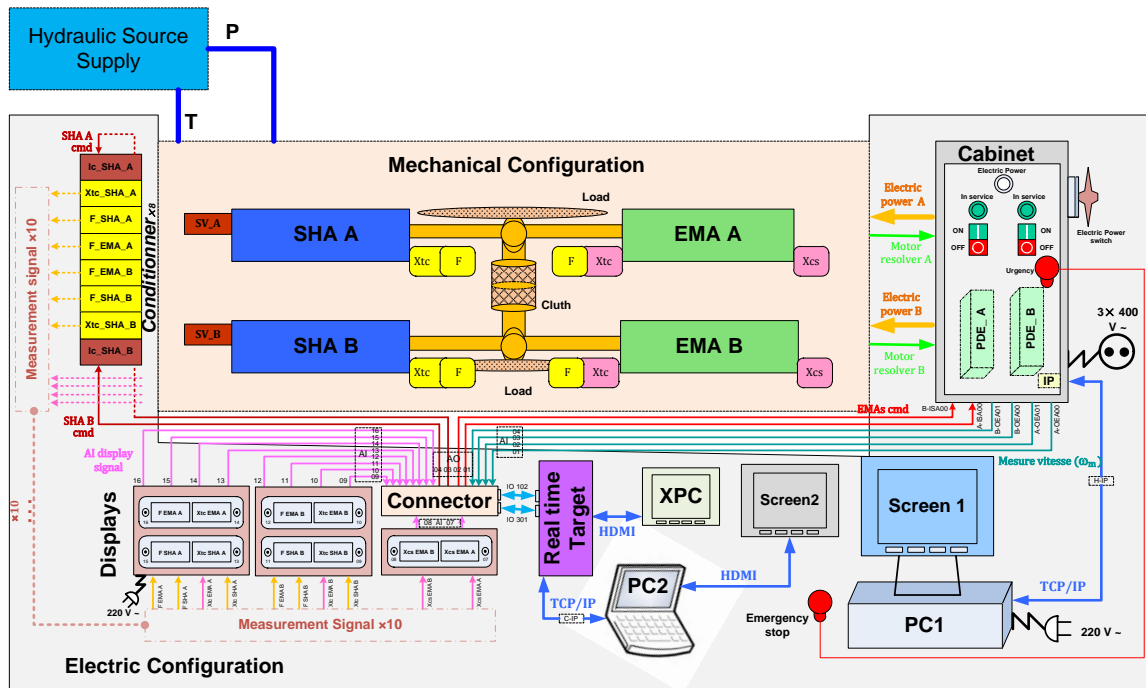


Fig. 5-2 Schematic configuration of test bench

It mainly consists of three parts:

- 1) **Mechanical Structure and actuators:** Two HSAs (A and B) and Two EMAs (A and B) are associated in parallel in two twin channels by the rigid linkage, mechanical structure frame and anchorage mechanism.
- 2) **Electric and Electronic devices:** An electric cabinet with the two motor power drives with the associated the power filters, signals measurement and displays, Speedgoat real time controller, PC1 and PC2.
- 3) **Hydraulic Power Supply System:** Hydraulic oil supply and return, the configuration and function have been presented in [1].

1) Mechanical Configuration

The mechanical configuration of the test bench is shown in Fig. 5-3. Two twins channels (A and B) that may be connected or disconnected by a rigid mechanical linkage. Each channel includes a commercial HSA and commercial EMA, a lever arm transformation to drive the inertial load, a device reproducing the compliance (flight control and airframe).

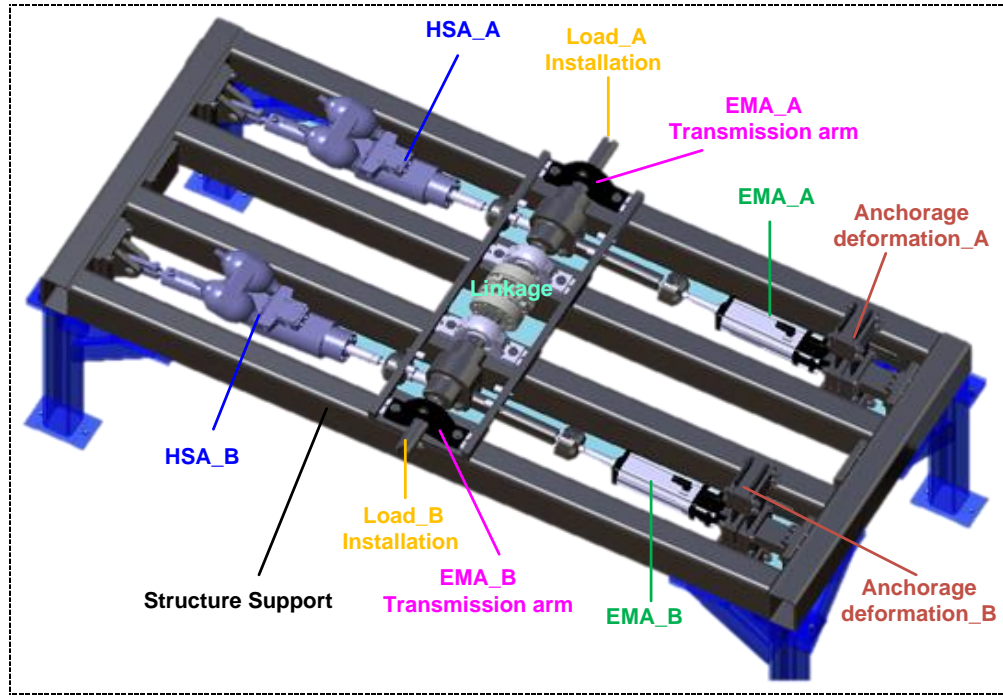


Fig. 5-3 Schematic 3-D view of test bench mechanical structure

The main characteristics of these elements are given in the following Tab. 5-1:

Table 5-1 Main mechanical configuration data of test bench

HSA	EMA	Load
Make: HiFi QUIRI	Make: Exlar	Lever: 80 mm
Stroke: 150mm	Stroke: 150mm	Equivalent translating mass: 600 kg
Max Speed: 500mm/s	Max Speed: 127mm/s	Anchorage stiffness: 1.4×10^8 N/m
Max Force: 30KN	Max Force: 15KN	
Supply Pressure: 14MPa	Supply Voltage: 400V/6.5A	

Remarks:

- HSA housing and EMA housing are respectively fixed on the test bench by two cylindrical pairs. For EMA studies, its anchorage deformation can be measured, as shown in Fig. 5-4.

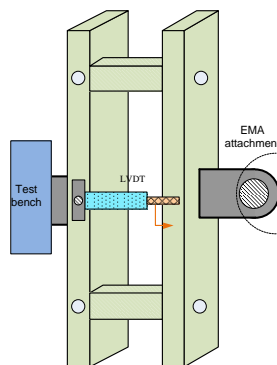


Fig. 5-3 Anchorage stiffness measurements between EMA and frame

- HSA rod and EMA rod are fixed to the lever arm using the spherical plain bearings, seen Fig. 5-4.

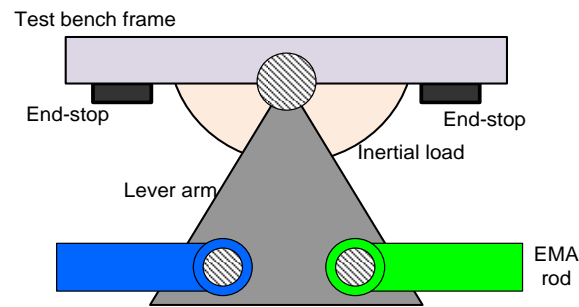


Fig. 5-4 3-point transmission connection of test EMA, loading HSA and inertial load

- A force sensor is mounted in series on the rod end of each actuator (HSA or EMA). It delivers the force feedback signal for force servoloop, force equalization and for force feedback in position control (damping, overload protection, monitoring, etc.).

- Two position sensors are installed: one is between the EMA housing and rod to measure the EMA extension. The other measures the deformation of the compliance device that is representative of the airframe and flight control surface deformation under the transmitted load.

2) Electric Architecture

The electric architecture of test bench includes three parts: electric power supply (from PDE, electric cabinet), signal acquisition, processing and measurement (sensors, conditioners and displays) and command signals (from control computer to PDE of EMA and to servo valve of HSA). The electric system of test bench involves:

a) Electric Cabinet: It integrates the two PDEs (A and B) that are in charge of modulating the power from the electric power supply (network, 3×400V AC) to the EMA motors. The drive configuration is set using TCP/IP Ethernet connection. Setpoint and feedback signals are transmitted in analog form (± 10 V). The hardware connection of power supply and velocity feedback between EMA and PDE is shown in Fig. 5-5.

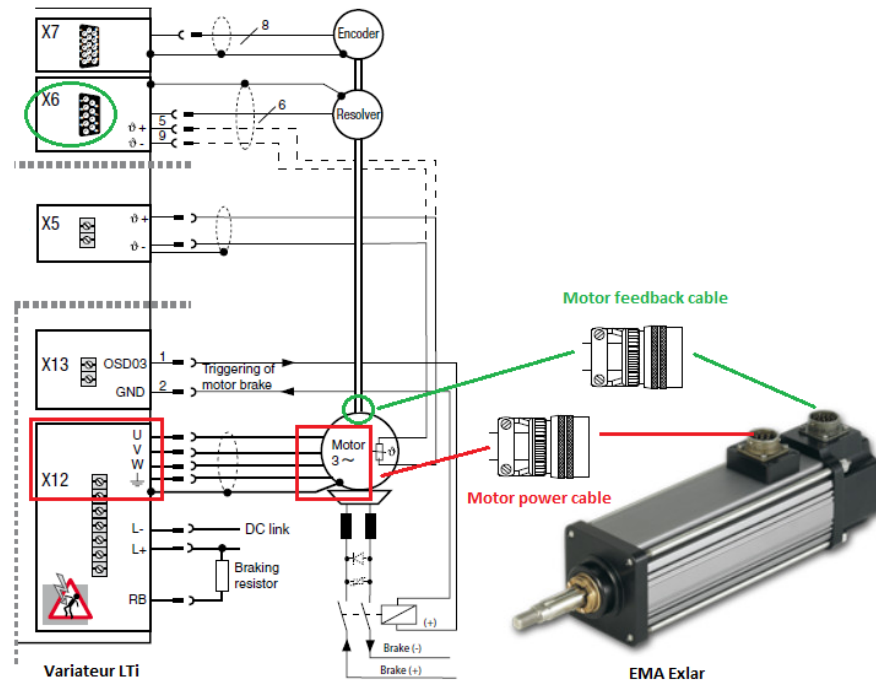


Fig. 5-5 Connection of PDE (mark LTi) and EMA [2]

b) Measurement and Display: It is in charge of conditioning the measurements signals from the sensors and to display the real-time value for monitoring. The connector box enables flexible wiring between the measurement unit, control unit and displays. The main signals involved on the test bench are analog and conditioned for a full range of ± 10 V. The schematic of signals acquisition, processing and measurement system of test bench is presented in Fig. 5-6. The main signals involved on test bench of this figure are summarized in Tab. 5-2.

Table 5-2 Main signals involved on test bench

Description	Symbol	Sensor	Physical Range
EMA Rod Extension (A/B)	X1, X2	RC20-150	-75mm~+75mm
HSA Rod Extension (A/B)	X3, X4	LVDT (integrated)	-50mm~50mm
EMA Motor Velocity (A/B)	ω_A, ω_B	PDE Analog Output	-3000rpm~+3000rpm
EMA Anchorage deformation (A/B)	D1, D2	RC20-25	0~+25mm
EMA Output Force (A/B)	F1, F2	U10M/25	-25KN~+25KN
HSA Output Force (A/B)	F3, F4	U10M/25	-25KN~+25KN
EMA Torque Demand (A/B)	C^*_A, C^*_B	Speedgoat Out 1 (A/B)	-10Nm~+10Nm
HSA Servo valve Amplifier Input (A/B)	I_A, I_B	Speedgoat Out 2 (A/B)	-50mA~+50mA

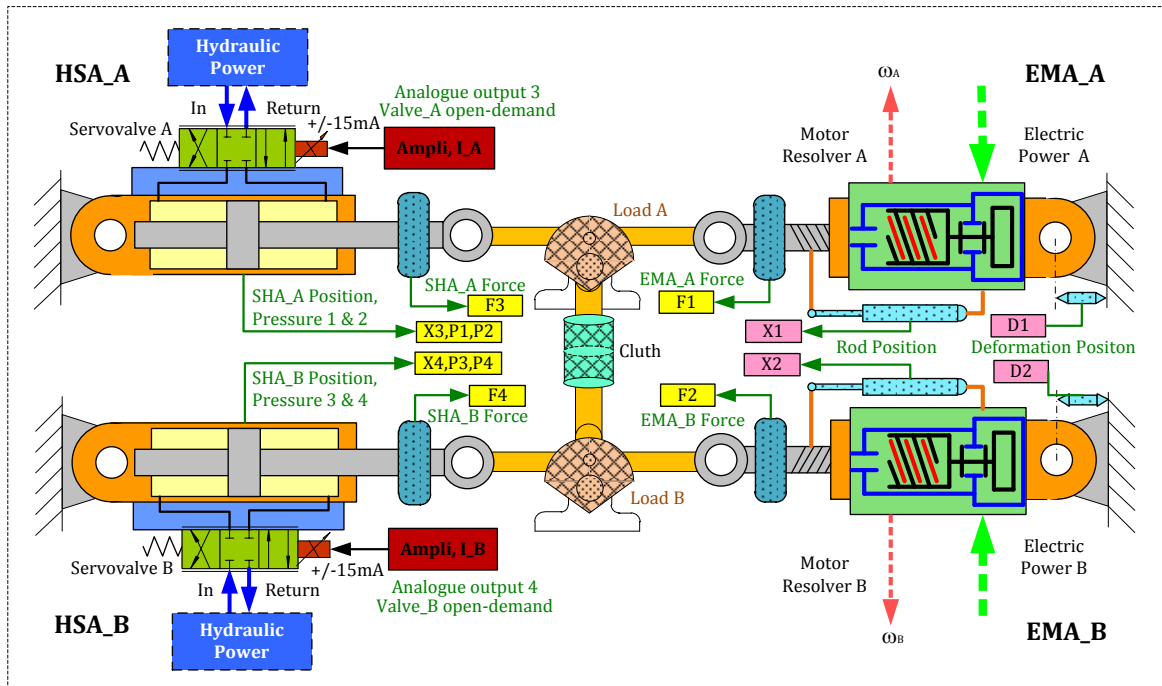


Fig. 5-6 Power flow supply, control and measurements signal schematic of test bench

c) Speedgoat and PCs: It performs the controls and allows setting the test configuration. The real-time controller part performs the servo control of the HSA and EMA, the DA/AD signal conversions and the data storage. It is based on a real time target of Speedgoat A personal computer PC 1 is used for parameters setting of PDEs for EMAs motor control and identification. A second personal computer PC 2 is used for generating the real-time code and for data post processing in MATLAB/Simulink environment.

Speedgoat for Real-time Digital Control: The Speedgoat is an embedded controller, performing the same functions as the former XPC Target box, which is used in the test-bench to simulate the Flight control computer in aircraft. (Speedgoat SN2014, Intel Core i3 2.4 GHz dual-core CPU and Main Board Bus PCI, 32bit/33MHz. Max sampling frequency 50 kHz. I/O modules of one analog card IO 102 and one digital card IO 301. Analog inputs are 32 single-ended/16 differential analog inputs, 16-bit, $\pm 10V$. Analog outputs are 4 single-ended analog outputs, 16-bit, $\pm 10V$. Digital I/O are 16 digital TTL I/O lines). The Speedgoat performs the calculations to apply the control strategies, on the basis of collection of the position, rotational velocity and force information as the closed-loop feedback. It separately elaborates the control signals (range $\pm 10 V$ DC analog) to servovalve voltage/current amplifier for HSA

and to each EMA PDE. The current signal outputted by amplifier (I_A or I_B) can control HSA (A or B) servovalve opening. Meanwhile, the analog output from Speedgoat is transferred as the motor torque demand (C_A^* or C_B^*) to PDE (A or B) as the motor torque/current loop is built and integrated within the PDE as a PI field oriented control.

PCs in Test Bench for Management and Configuration: In test bench system, the PC are not inside the control loops. PC 1 is installed to drive management software of the EMA PDE: programming for manual operation of the EMA, EMA motor and sensor parameters setting, torque loop and protection settings. And the data transmission to PDEs is achieved through by TCP/IP network. PC 2 is connected to Speedgoat also by TCP/IP protocol and programmed in the MATLab/Simulink environment. First function is to collect and process the sensors feedback information. Second is to design the control laws and to upload the associated real-time code to the Speedgoat Target computer. Practically, the experiments results are stored in Speedgoat can be uploaded to PC 2 and can be displayed in real time as shown in Fig. 5-7.



Fig. 5-7 Speedgoat program environment (MATLab/Simulink) and real-time display [3]

5.2 Preliminary Study of Position Synchronization

According to the above configuration of the test bench analysis, each channel, A or B, is independent and available for individual EMA position control or for two EMAs position synchronization. The main concern in this section is to show how the simulation models developed in chapters 2 to 4 can be used for the preliminary study of EMAs position synchronization. The state of the art in position synchronization is firstly reviewed, and then the virtual prototyping approach developed in the former chapters is used to show how it can

support the development of position synchronization strategies.

The control goal is to achieve satisfactory reduction of the position difference between the two independent loads. Ideally, the position control of the EMAs shall ensure at any time:

$$X_{sa} = X_{sb} \quad , \quad \forall F_{LA}, F_{LB} \quad (5.2)$$

X_{sa} EMA_A load displacement [m]	X_{sb} EMA_B load displacement [m]
F_{LA} EMA_A load force [N]	F_{LB} EMA_B load force [N]

In addition, the EMAs for critical application in aerospace should consider safety in response to faults. It means that in the event of one EMA fails, the other EMA shall no more follow the position setpoint but produce the same position as the failed EMA: The two independent EMAs must keep their position synchronized:

$$X_{sa} = X_{sb} \quad , \quad \forall X_{sa, sb} = X_r \quad or \quad X_{sa, sb} \neq X_r \quad (5.3)$$

X_r EMA reference control setpoint [m]	
------------------------------------------	--

Therefore, the strategy of the EMAs position synchronization is to eliminate or reduce the desired synchronization error between the loads. It can be defined as the γ_L difference between the effective positions

$$\gamma_L = X_{sa} - X_{sb} \quad (5.4)$$

γ_L Position synchronization error between two independent loads [m]	
-----------------------------------------------------------------------------	--

However in the test bench (as well as in aircraft actuation system), the desired γ_L cannot be measured directly. Indeed, the measured position is the EMA extension and not the load position with respect to airframe. So the measured position synchronization error γ_t is:

$$\gamma_t = X_{ta} - X_{tb} \quad (5.5)$$

γ_t Position synchronization error between two EMA rods extension [m]	X_{ta} EMA_A rods extension [m]
X_{tb} EMA_B rods extension [m]	

It is not exactly representative of the loads position synchronization error γ_L because of the compliance effect (presented in chapter 2).

5.2.1 Structure of Position Synchronization

Based on the model of the independent individual EMA servo control system, the conventional position synchronization control system is concerned in cross-coupling of position only and designed for twins EMAs experiencing two different levels of load disturbances. The control structure can be viewed in two common ways:

-Case 1, master-slave synchronization. One EMA (the slave) is position controlled to follow the position of the other EMA (the master), as illustrated in Fig.5-9. Also each EMA controller has optionally feedback loops.

$$X_{ca} = X_r, \quad X_{cb} = X_{ta} \quad (5.6)$$

X_{ca} Position command for EMA_A [m] X_{cb} Position command for EMA_B [m]

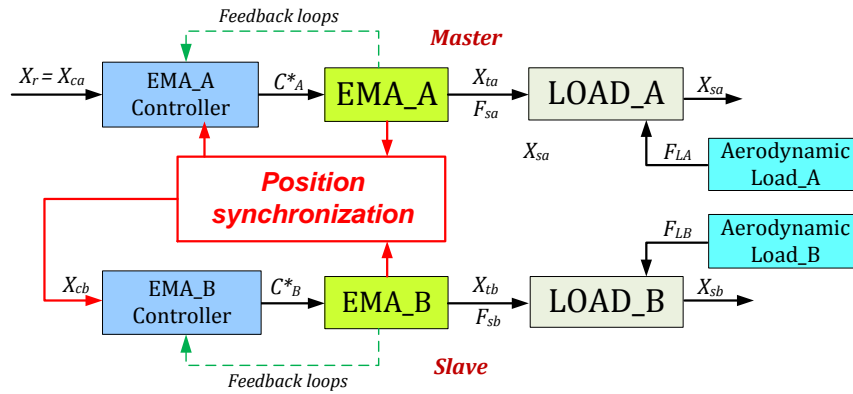


Fig. 5-8 Tandem control structure for EMAs position synchronization

Most of the research works concerning this position synchronization structure are related to synchronized motion control of multi-axis machine tools. In [4], this master-slave control scheme is proposed for biaxial system application, the slave system can follow the master one with high dynamic performance, but the servo delay lag of the slave one cannot be avoided. To improve this shortcoming, a velocity feedforward compensation was considered in [5], seen Fig: 5-9. Furthermore, another master-slave control based on speed and torque coupling was developed in [6].

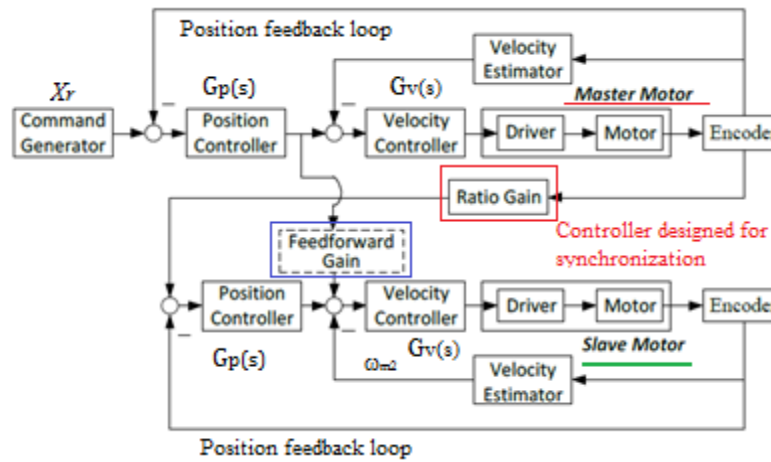


Fig. 5-9 Example of master-slave position synchronization with velocity feedforward compensation [5]

This solution of master-slave structure does not work if an uncertain disturbance or failure occurs in the slave channel. Moreover, the slave load position is always delayed in comparison with the master load due to the dynamics and servo lag of the slave channel. The control compensation is needed, e.g. additional feedforward gain that increases the controller complexity.

-Case 2, cross coupled synchronization: The control structure is strictly identical for each actuator (parallel synchronization control), as illustrated in Fig. 5-10. The two EMAs receive the same position command simultaneously. Each one is closed-loop position controlled independently with additional position synchronization inputs.

$$X_{ca} = X_{cb} = X_r \quad (5.7)$$

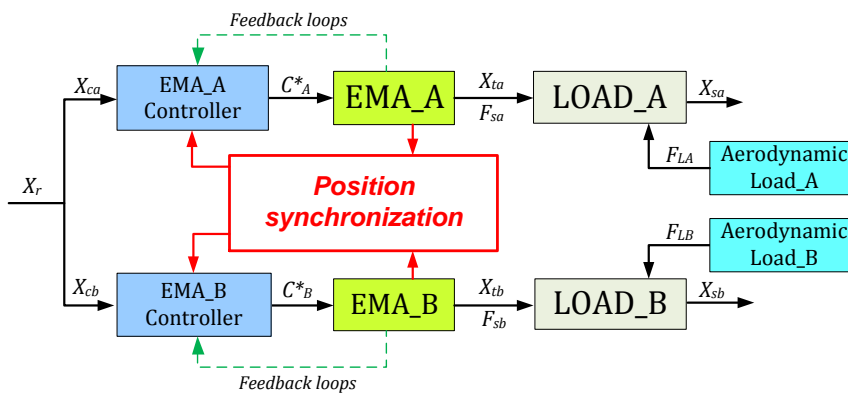


Fig. 5-10 Cross coupled control structure for EMAs position synchronization

This cross coupled synchronization structure is widely used in industry. As a main advantage,

the servo lag delay can be eliminated. In [7], a cross-coupled synchronization design is based on quantitative feedback theory for dual hydraulic motors driven flight simulators, seen Fig. 5-11. The simulation results indicated that this structure could achieve performance specification requirements.

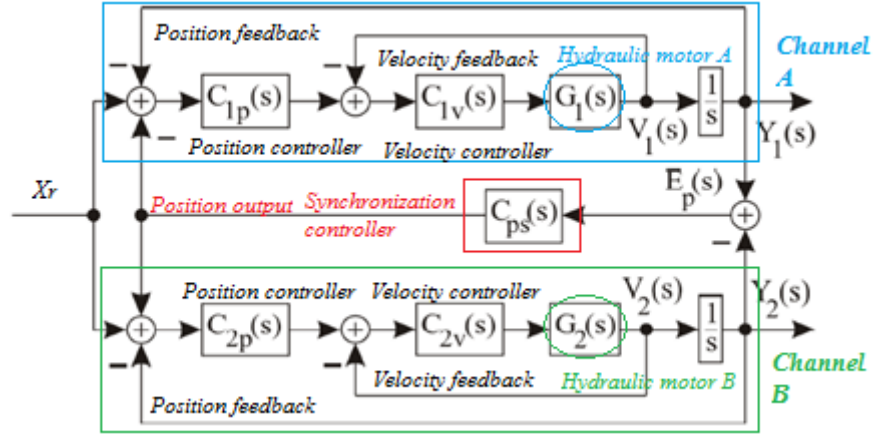


Fig. 5-11 Example of conventional cross coupled control structure for position synchronization [8]

Based on the conventional cross coupled structure, some optimal methods are used to improve the position synchronization accuracy. Firstly, a hybrid velocity and acceleration feedforward controller is added to reduce the synchronization error of dual linear motors simultaneously [9], as shown in Fig. 5-12. Simulation results show the superior synchronization performance than conventional cross-coupled structure.

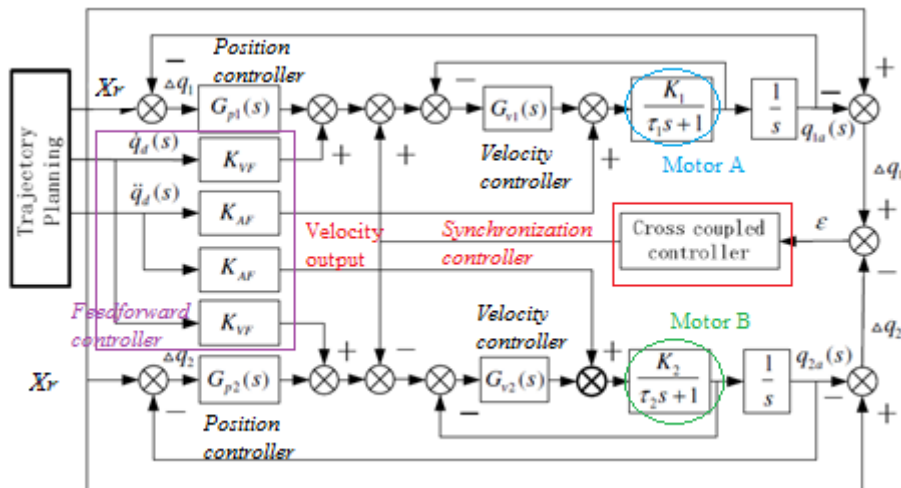


Fig. 5-12 Example of optimal cross coupled control by feedforward compensation [9]

Also a position/velocity hybrid synchronous control is proposed in [10] using this parallel cross coupled concept that also called relative dynamic stiffness motion control. This same

structure is also applied in [11, 12], where an optimal cross-coupled control action is designed for controlling dual-parallel linear servomotors system, as shown in Fig. 5-13. The simulation results show that the synchronization error is reduced when compared to the conventional position synchronization structure. However, the system is modeled as a very simple first order model, all the nonlinear effects being neglected.

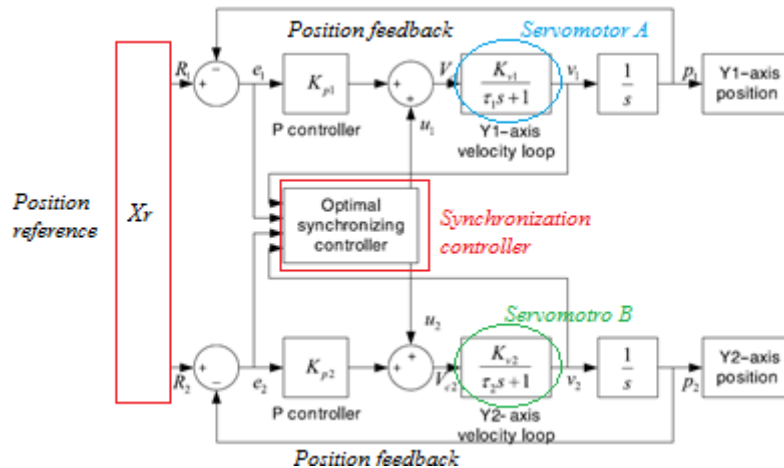


Fig. 5-13 Example of optimal cross coupled control structure for position synchronization [12]

In addition, some intelligent control theories, such as fuzzy control [13] and neural network control [14], can be used to optimize the conventional cross-coupled structure for position synchronization. They have been shown to be effective in handling nonlinearities and parameter uncertainties.

In [15, 16], the author is interested in synchronizing asymmetrical loads in the presence of strong uncertainties and disturbance to an electro-hydraulic actuation system. An integrated approach with hybrid controller for position synchronization is shown in Fig. 5-14. The whole system control consists of two independent controllers for cylinder and a fuzzy logic controller for position synchronization. Experimental results show that the proposed control approach may be effective for enhancing both the synchronization of the movement and positioning. However, the dynamic load application in the whole process has not been studied and analyzed. In addition, the fuzzy logic technology is not reliable enough for aerospace application.

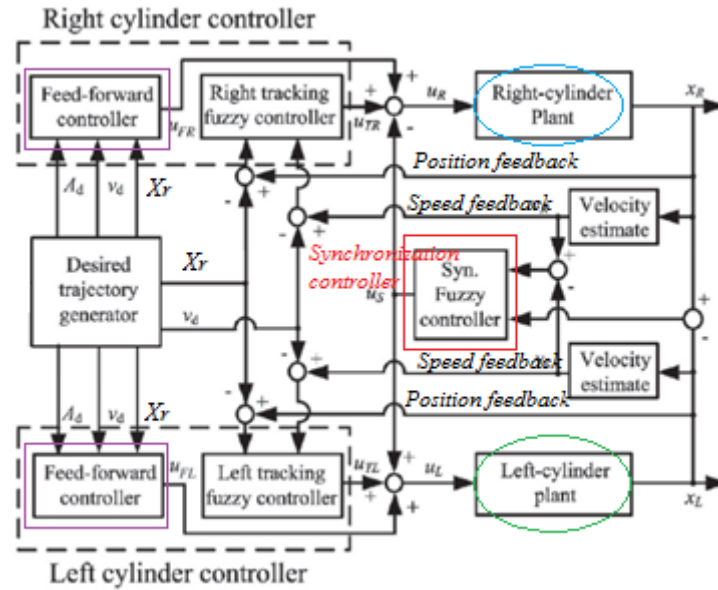


Fig. 5-14 Fuzzy logic optimal cross coupled control structure for position synchronization [16]

An integrated PID-Neural network controller is designed for synchronization control of electro-hydraulic system in [17]. The control system consists of individual cylinder controller and coordinate synchronization controller, as shown in Fig. 5-15. It is clear that the PIDNN controller coordinates the movement of the two cylinders to reduce the synchronization error by injecting correction signals in the position loop. The simulation results show that this method can effectively achieve the position synchronization with absolute maximum synchronization error within 2.6 mm. However, it is not taken into account that the variability of the unbalanced load. The performance is assessed through virtual prototyping by co-simulation in the LMS-AMESim and MATLAB/Simulink environments.

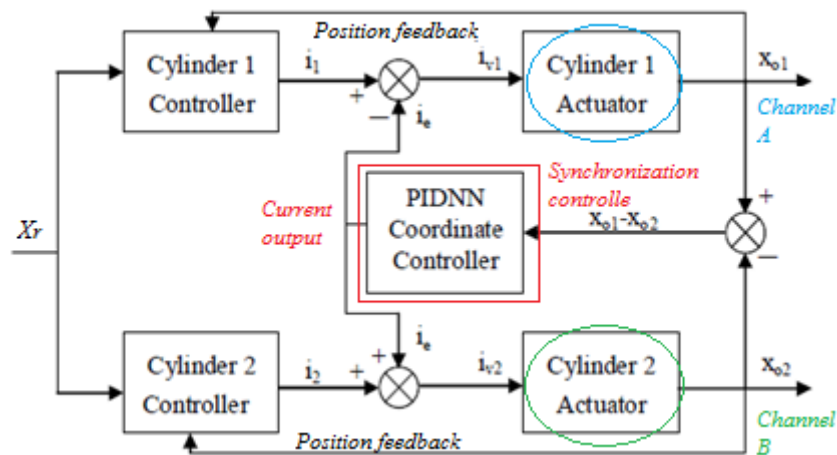


Fig. 5-15 Neural network optimal cross-coupled control structure for position synchronization [17]

Therefore, by comparison of above two position synchronization cases, master-slave synchronization and cross-coupled synchronization, the second one with parallel cross coupled structure is more acceptable for the EMAs, especially for aircraft application. The similar EMAs have similar controllers, and the distributed EMAs for the wing application cannot be classified as a master one or slave one. But it must be kept in mind that the position synchronization performances can be improved by different cross-coupled synchronization design.

5.2.2 Cross-Coupled Synchronization (CCS) Controller Design

The requirements for the CCS controller design are listed below:

R1) The position synchronization function shall eliminate, or as far as possible reduce, position synchronization error (γ_L) to an acceptable level in any case of normal operation,

R2) In case of failure in one channel, the other channel shall be controlled in order to position its load to the same position as that of the failed channel. Therefore, it is accepted that the loads' positions cease to follow the position setpoint,

R3) The closed loop performance (pursuit and rejection) of each EMA shall not be significantly influenced by the position synchronization.

At each EMA control level, position synchronization is implemented introducing a synchronization input. This input is calculated as a function of the sensors signals that are already available for the position control of each EMA (EMA extension, motor speed/position, transmitted force to load). The simplest and most direct approach of design CCS consists in elaborating the position synchronization signal as a dynamic function of the EMAs extensions difference (γ_t). This signal is injected as an additional torque demand (C_s) into each EMA torque reference (C^*). However, as presented in former section, the optimal hybrid structure based on CCS may also introduce the velocity signals. In particular and more directly, it can use the motor speed signals that are used for implementation of the field oriented control (if are available at PDE level). It is also possible to introduce the velocity signals as the differential signals from rod position through the D action. The two candidate CCS structures

are shown in Fig. 5-16 (a) and (b).

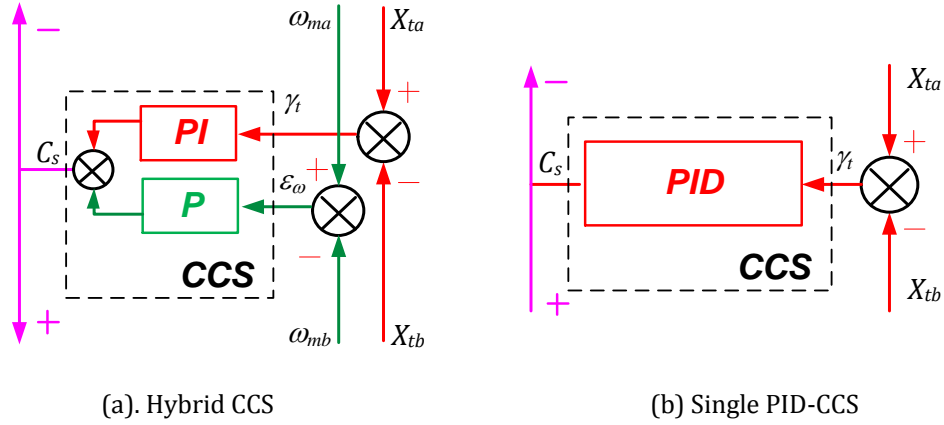


Fig. 5-16 CCS structures for EMAs position synchronization

Figure 5-16 (a) displays the CCS structure that uses both position error (γ_t) and motor velocity error (ε_ω) as input. The γ_t is controlled by a proportion-integral (PI) structure and ε_ω is introduced by a pure proportional action of gain P. That can be given:

$$C_s = (K_{pr} + \frac{K_{ir}}{s}) \gamma_t + K_{p\omega} \varepsilon_\omega \quad (5.8)$$

K_{pr}	PI position proposition gain [Nm/m]	K_{ir}	Position error integral gain [Nm/m s]
$K_{p\omega}$	Speed error proportional gain [Nm/(rad/s)]	ε_ω	Velocity difference between two EMAs motors [rad/s]

The integral action I is added in the synchronization law in order to improve its static accuracy. The C_s dependence on γ_t (gain K_{pr}) can be seen at low frequencies as producing “electrically” a spring effect of stiffness $2\pi K_{pr}/p$ between the two EMAs rods position (friction and other compliances effects are neglected). The C_s dependence on ε_ω can be seen as an “electrical” equivalent rotational damper of coefficient $K_{p\omega}$ connecting the two EMAs motor shafts. Attention has to be paid to the parasitic effects (compliance or backlash) that make the rod velocity and motor velocity not simply proportional. The impact of these nonlinear effects is difficult to assess formally during control design. Oppositely, the proposed virtual prototype models reproduce these effects with realism and provide a useful support for virtual validation of the position synchronization.

The other option, PID-CCS structure, Fig. 5-16 (b), simply uses the EMA extension signals and introduces the velocity difference through the derivative action. In the same manner, the

derivative effect D can be seen as an “electrical” equivalent of a damper connecting the two EMAs rods. The synchronization control law is expressed as:

$$C_s = (K_{pr} + \frac{K_{ir}}{s} + K_{dr}s)\gamma_t \quad (5.9)$$

K_{pr}	Position proposition gain [Nm/m]	K_{ir}	Position error integral gain [Nm/m s]
K_{dr}	Position Derivative gain [Nm/(m/s)]		

When implementing any of these structures, for safety reasons it is important to limit cross-coupling effects between the channels. The authority of the synchronization function can be limited using a saturation effect. As well, the low-pass filtering of the derivative action and anti-windup of the integral action are also need to be considered.

The total control structure of two EMAs for position synchronization according to the PID-CCS position synchronization is shown in Fig. 5-17. The individual EMA controller, the multi-feedback controller (position/speed/force) has been studied and presented in chapter 2. The CCS controller between the two EMAs is clearly evident, by noting the interconnections of synchronization position tracking error of γ_t . The synchronization torque demand (C_s) is summed to the torque demand coming from the individual EMA controller.

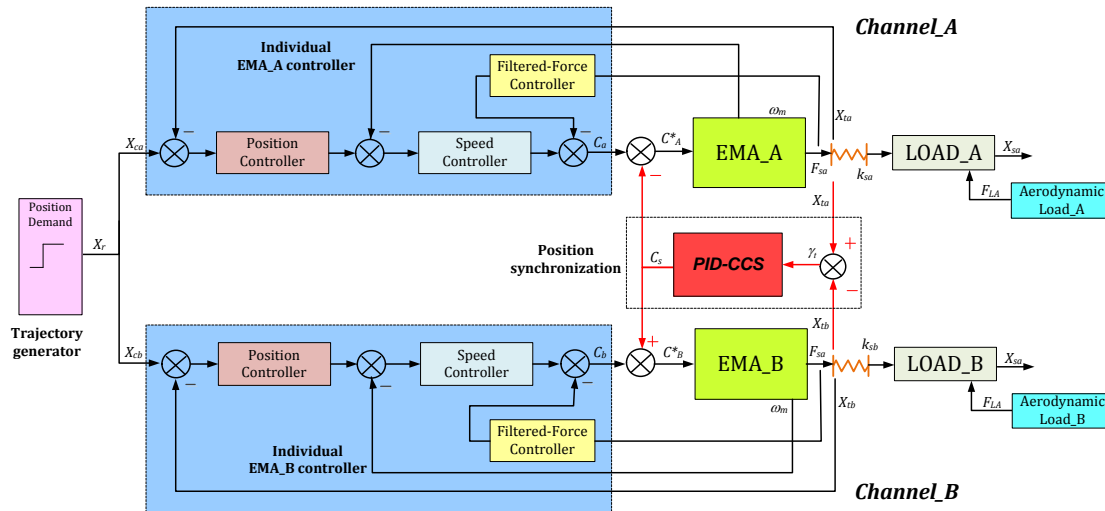


Fig. 5-17 Schematic of overall structure of EMAs position synchronization

The proposed two criterions have to be defined in order to quantify the performance of the load position synchronization by using PID-CCS structure. They are calculated as:

a) E_{ITAE} as the integral of time-weighted absolute error (ITAE) [18]

$$E_{ITAE} = \int_0^{\infty} t |\gamma_s(t)| dt \quad (5.10)$$

b) E_{max} as the absolute maximum value of position synchronization error

$$E_{MAX} = MAX \{ |\gamma_s(t)| \} \quad (5.11)$$

where t is the time.

5.3 Validation of Overall Twin-Parallel EMAs Virtual Prototype

5.3.1 Linear Model

As a first step, a linear approach is used to formally define the structure and to support the parameter setting of the position synchronization function added to the individual position control. The performance, either in frequency or in time domain, can be assessed without numerical simulation through the theory of linear systems. However, it is interesting to also implement the linear model as simulation model to meet the incremental modelling objective. In that manner, the influence of non-linear effects can be easily assessed by replacing the linear model by the advanced model.

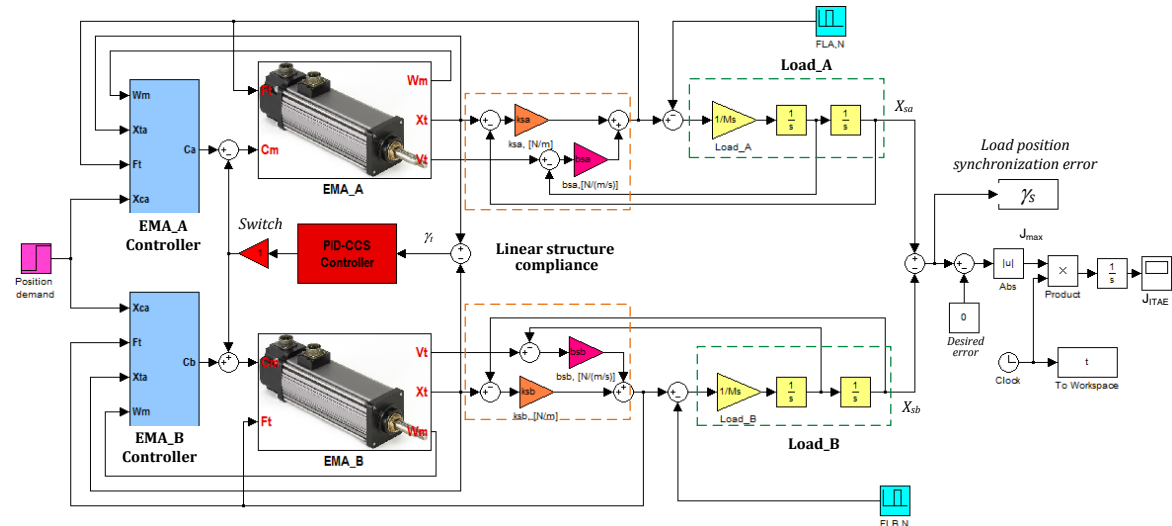


Fig. 5-18 Linear model for EMAs position synchronization in MATLAB/Simulink

Figure 5-18 displays the linear model implemented for simulation in the MATLAB/Simulink environment. All the parasitic effects of PDE dynamics, EM electrical and frictional effects,

MPT inertial and frictional effects, and digital implementation of control (anti-aliasing, sampling, and quantization) are not considered. The compliance effects are taken into account as linear effect because of their impact on force rejection performance (section 2.5 in Chapter 2). The EMA parameters and the position control parameters remain unchanged from chapter 2.

5.3.2 Full Model

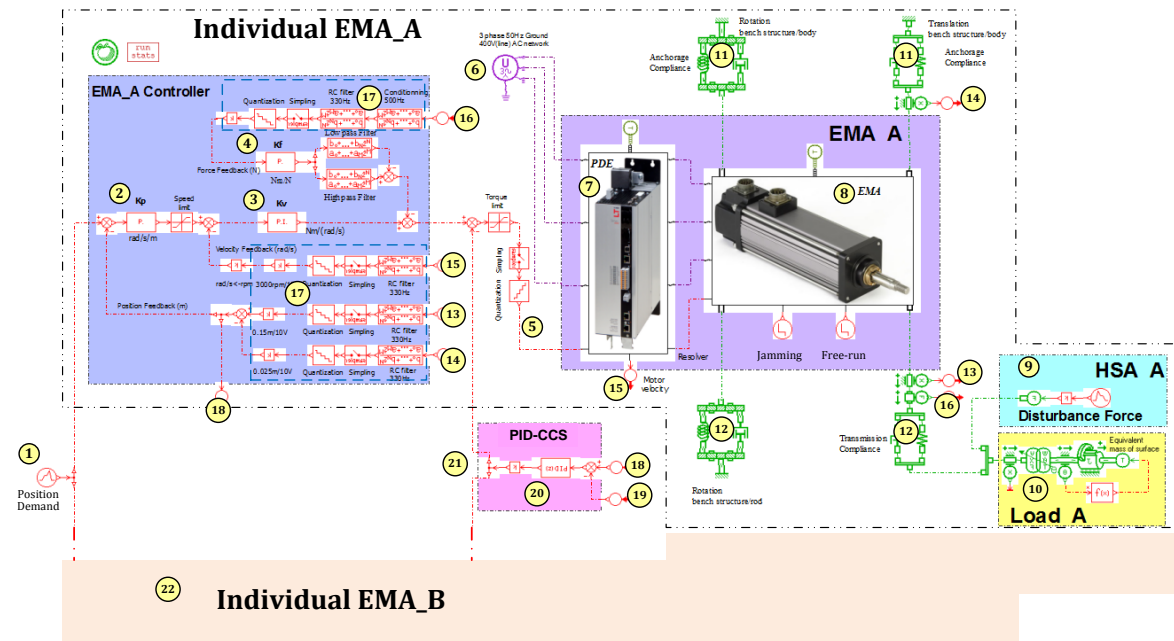


Fig. 5-19 Full model for EMAs position synchronization in LMS-AMESim

Figure 5-19 displays the full virtual prototyping model implemented in the LMS-AMESim simulation environment, including the proposed position synchronization controller (Fig. 5-17). All the former mentioned physical effects (in PDE, EM and MPT) are introduced, according to the developments presented in chapters 2 to 4). Other parasitic effects associated with the test and the instrumentation are also considered. This full model consists of following components:

- 1) Rod position demand generator X_r .
- 2) EMA_A position feedback loop and controller.
- 3) EMA_A velocity feedback loop and controller.
- 4) EMA_A force feedback loop and controller.
- 5) EMA_A torque control reference.

- 6) Electric power supply for EMA_A.
- 7) Power drive electronics (PDE) advanced submodel of EMA_A, in Chapter 3, Fig.3-27.
- 8) EMA_A cylinder 2-DoF submodel (EM and MPT including), in Chapter 4, section 4.4.2.
- 9) HAS_A used for dynamic loading for EMA_A (here an ideal and piloted source of force).
- 10) Inertial load of EMA_A.
- 11) 2-DoF anchorage between EMA_A body and test bench frame.
- 12) 2-DoF transmission compliance between EMA_A rod and inertial load.
- 13) EMA_A rod displacement from LVDT sensor.
- 14) EMA_A anchorage deformation from LVDT sensor.
- 15) EMA_A motor velocity from PDE resolver.
- 16) EMA_A output force to load, from force sensor.
- 17) Sensor dynamics, ADC filter, sampling and quantization, as summarized in Tab 5-6.
- 18) Relative displacement between the EMA_A rod and test bench frame.
- 19) Relative displacement between the EMA_B rod and test bench frame.
- 20) Position synchronization PID-CCS controller.
- 21) Torque compensated out of CCS controller.
- 22) Individual EMA_B system, with same structure of EMA_A.

In Fig. 5-19, according to the test bench, this full model includes the digital control effects, which are neglected in the linear model: filtering, sampling, quantizing and conditioning. It is particularly important to consider them because they may significantly impact performance (phase lag and noise). Moreover, the measured quantities will be the discrete ones. The parameters associated with these electrical signaling effects are summarized in Tab. 5-6,

Table 5-6 Summaries of electric nonlinearity and discrete effects

Items	Description	AMESim Submodels
Filtering	First order low-pass filter placed on any A/D converter input	First order lag : $f_{rc}=330$ Hz
Sampling	Sampling rate for control: 0.5ms (2 kHz)	Zero order hold: $t_s=0.5$ ms
Quantization	Quantization of A/D converter device: 14 bits for ± 10 V full scale	Quantize: 0.001V
Conditioning	Second order low-pass filter for EMAs and HSAs force sensors conditioning	Second order lag: $\omega=500$ Hz, $\xi=0.8$

5.3.3 Parameters Setting and Mission Excitations

Simulations are run to illustrate the capability of the proposed EMA modelling and CCS-PID controller to assess actuation performance. The following mission excitations are applied to linear model in Fig.5-18 and full model in Fig. 5-19. Their key controller parameters are listed in Tab. 5-7.

Table 5-7 Parameters of controllers

Item	Parameter	Value
EMA individual controller	Position proportional gain K_p (Nm/m)	45000
	Velocity proportional gain K_v (Nm/(rad/s))	0.55
	Force controller pure gain K_f (Nm/N)	0.005
	Force controller low-pass filter gain K_{lp} (-)	0.06
	Force controller low-pass filter frequency f_{lp} (Hz)	3
	Force controller high-pass filter gain K_{hp} (-)	0.6
	Force controller high-pass filter frequency f_{hp} (Hz)	15
PID-CCS controller	Position proposition gain K_{pr} (Nm/m)	$1 \cdot 10^5$
	Integral gain K_{ir} (Nm s/m)	$8 \cdot 10^5$
	Differential gain K_{dr} (Nm /(m/s))	$5 \cdot 10^3$
Digital Implementation in full model	Sampling period (s)	0.0005
	Quantization voltage (V)	0.001
	Discrete PID-CCS output torque limitation (Nm)	± 10

(a) Normal Operation under Position Step Demand

A step demand (10 mm position step signal at $t = 0.1$ s) is used to test the position synchronization performance in normal mode, under two different load disturbances. The two external forces are square waves of 0.6 s period. The magnitude for EMA_A is 5 kN (applied at $t = 0.6$) and the magnitude for EMA_B is 15 kN (with a 0.3 s phase delay and applied at $t = 0.9$ s). The mission profile is shown in following Fig.5-20.

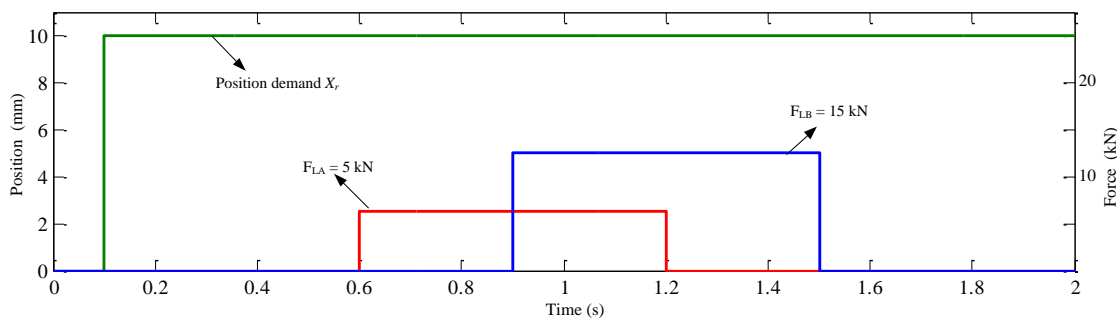


Fig. 5-20 Mission profile of position step demand and disturbance loads

(b) Normal Operation of Position Trapezoidal Demand

A specific mission of trapezoidal position demand is created as between ± 50 mm with a slope of 50 mm/s that represents the maximum velocity input. Two different load disturbances are applied: for EMA_A, a step demand occurring at $t = 0.5$ s with a magnitude of 10 kN. For EMA_B, a trapezoidal force signal that starting at $t = 2$ s with a maximum magnitude of 10 kN, falling at $t = 7$ s a static level of 2 kN. The mission profile is shown in Fig. 5-21.

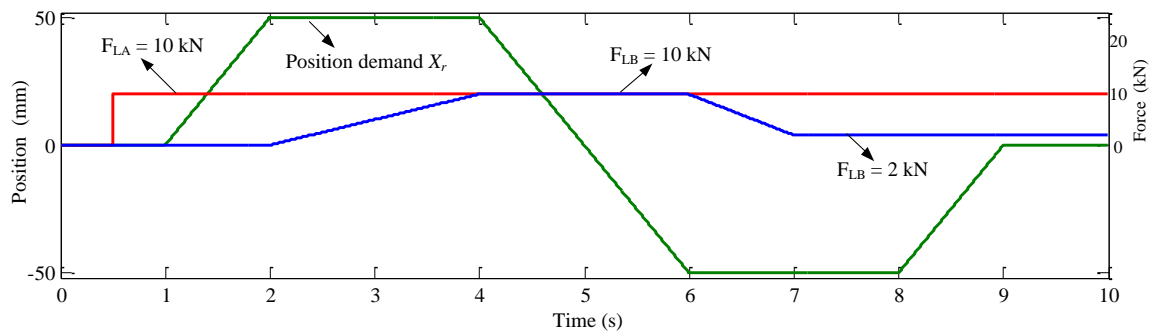


Fig. 5-21 Mission profile of trapezoidal response

(c) Response to Faults

In order to address the response under fault, jamming is triggered on EMA_B. A specific mission consists of two position steps (30 mm from null at $t = 0.1$ s then -15 mm from 30 mm at $t = 3$ s). The external loads are of trapezoidal shape with different phase and level for each EMA. EMA_A always operates normally while EMA_B jams during its motion to reach the 30 mm position setpoint or when the external loads change at $t = 2$ s. Figure 5-22 shows the mission profile with these jamming triggering times.

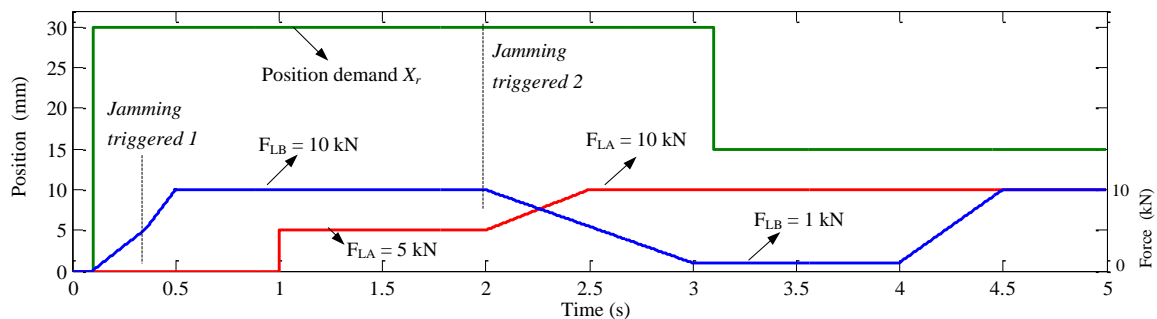


Fig. 5-22 Mission profile of response to faults

5.3.4 Simulation Results and Analysis

The linear model (Fig. 5-18) and full model (Fig. 5-19) are simulated separately, according to the above mission excitations. Jamming is produced in the linear mode by forcing motor speed to null. The synchronization performances are evaluated by using absolute MAX and ITAE criterions. The positions that are considered are the load position with respect to airframe (that is for interest for flight control), although the position controllers use the rod extension signals.

(a) Step Position Responses

Figure 5-23 shows the linear model (top) and full model (bottom) simulation results, in both linear and full models. Figure 5-24 shows the comparison of synchronization errors without/with use of PID-CCS controller.

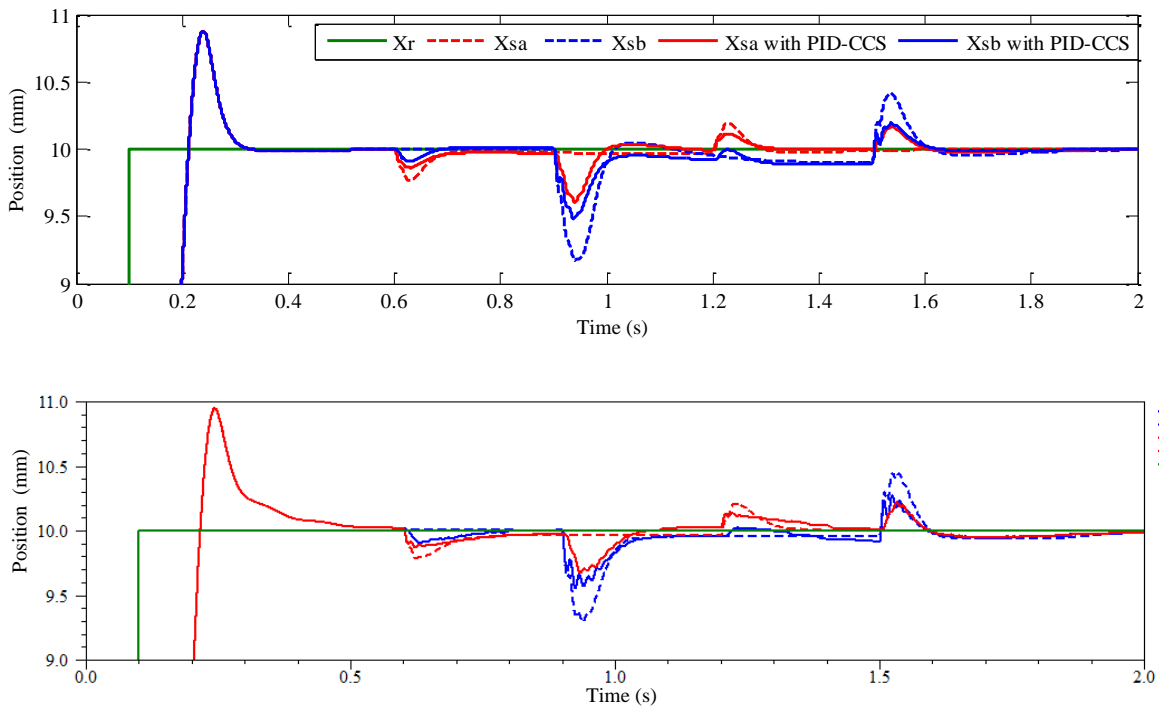


Fig. 5-23 Position step response (top: linear model; bottom: full model)

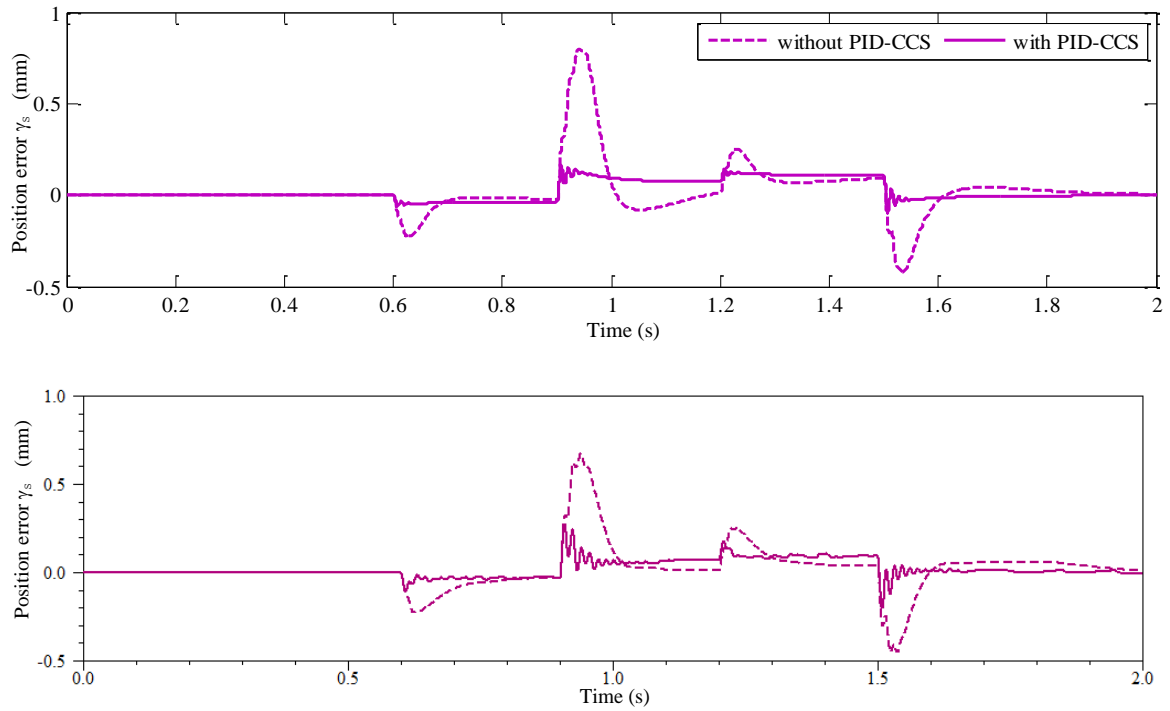


Fig. 5-24 Position synchronization error of step demand (top: linear model, bottom: full model)

The top figures are relative to the linear model simulation results and the bottom ones correspond to the full model. It can be noticed that the position synchronization controller (CCS-PID) has no effect on the pursuit performances (before $t = 0.6$ s). However, in both models, when different disturbance forces are applied (start at $t = 0.6$ s), the position difference clearly appear (the two dashed curves) and cannot be removed without resort to the CCS-PID controller. When introduced PID-CCS controller, the load position can be synchronized and the synchronization error is reduced. However, in the transient phase of the response, the mean value of the two actuators' position remains quite identical with and without the CCC-PID controller. The simulation results in full model show more oscillations and slower responses. This essentially comes from the more realistic friction and compliance models and from the effect of digital implementation of the controllers.

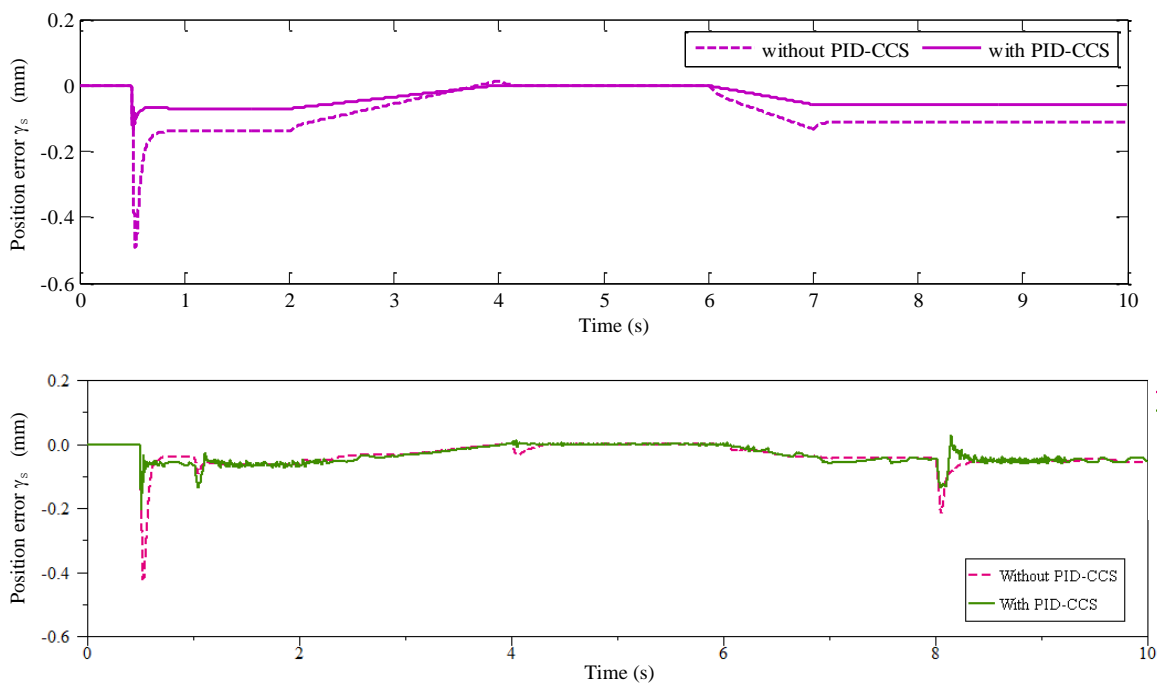
Furthermore, comparisons of the absolute MAX and ITAE criterion performances for position synchronization error in linear model and full model, without/with PID-CCS synchronization controller are given in Tab. 5-8. By using PID-CCS controller, the maximum synchronization error between the two EMAs loads is reduced by 80% (from 0.81 mm to 0.17 mm) in linear model and by 58% in the full model.

Table 5-8 Position synchronization performance comparison of linear and full model-Step response

Mission of step response	Control Schema	Synchronization error γ_s (mm)		Maximum error ratio (%)
		ITAE	MAX	$E_{MAX}/\text{Max travel}$
Linear model	Without PID-CCS control	0.16	0.81	8.1%
	With PID-CCS control	0.09	0.17	1.7%
Full model	Without PID-CCS control	0.16	0.67	6.7%
	With PID-CCS control	0.08	0.28	2.8%

(b) Trapezoidal Position Responses

Load position tracking performance can be easily assessed using this mission profile. The interest is put on the comparison of synchronization errors. Figure 5-25 shows the interest of PID-CCS synchronization. With PID-CCS controller, the synchronization error is significantly reduced in both linear and full models. The full model simulation results show more high frequency/low magnitude oscillations that come from realistic structure compliance between EMA housing and frame., because the position feedback in full model presented the relative displacement of the EMA rod and the housing.

**Fig. 5-25** Position synchronization error of trapezoidal demand (top: linear model, bottom: full model)

Once again, the evaluations of synchronization performance for both the linear model and full

model, has been performed using the absolute MAX and ITAE criterion, Tab. 5-9.

Table 5-9 Position synchronization performance comparison - Trapezoidal response

Mission of trapezoidal position	Control Schema	Synchronization error γ_s (mm)		Maximum error ratio (%)
		ITAE	MAX	$E_{MAX}/\text{Max travel}$
Linear model	Without PID-CCS control	3.8	0.49	0.98%
	With PID-CCS control	1.8	0.13	0.26%
Full model	Without PID-CCS control	1.9	0.43	0.86%
	With PID-CCS control	1.7	0.21	0.42%

(c) Response to Fault

Following the third mission excitation, Figure 5-26 shows the positions responses in the presence of jamming faults when the PID-CCS is active or not. The position synchronization errors are plotted on Fig. 5-27.

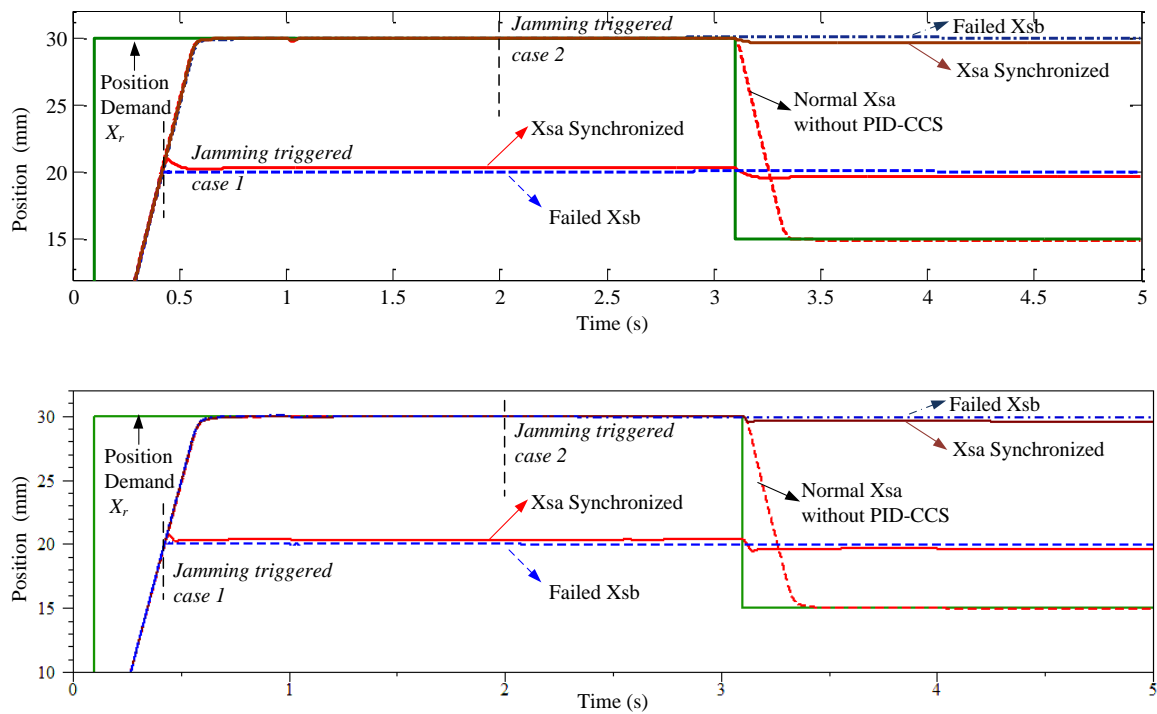


Fig. 5-26 Synchronization responses to 2 cases of faults (top: linear model, bottom: full model)

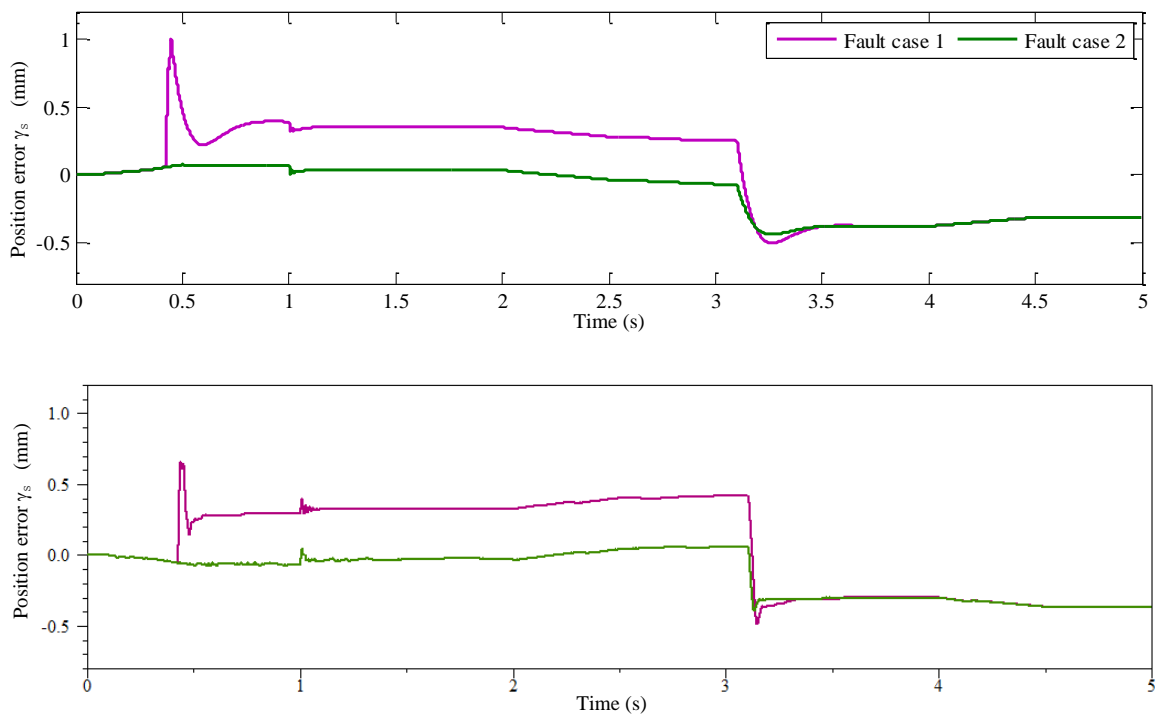


Fig. 5-27 Synchronization errors of 2 cases of faults (top: linear model, bottom: full model)

In both linear and full models simulations, position synchronization cannot be achieved without PID-CCS. Oppositely, the introduction of PID-CCS controller enables the healthy EMA to detect the fault and to synchronize to the faulty EMA, whatever the position demand. Although the position and synchronization controllers have been designed using the linear model, it is observed that they produced good results when applied to the full model that is more realistic.

The absolute MAX and ITAE evaluation performances are listed in Tab. 5-10. The loads position are well synchronized and with very small errors. The ITAE error is significantly reduced by using position synchronization.

Table 5-10 Position synchronization performance comparison – Failures

Mission of failure case 1	Control Schema	Synchronization error γ_s (mm)		Maximum error ratio (%)
		ITAE	MAX	$E_{MAX}/\text{Max travel}$
Linear model	Without PID-CCS control	84.7	10.2	34%
	With PID-CCS control	4.2	0.97	3.2%
Full model	Without PID-CCS control	84.4	9.8	32.7%

Mission of failure case 2	With PID-CCS control	4.1	0.65	2.1%
	Control Schema	Synchronization error γ_s (mm)		Maximum error ratio (%)
		ITAE	MAX	$E_{MAX}/\text{Max travel}$
Linear model	Without PID-CCS control	110.1	15.1	50.3%
	With PID-CCS control	2.9	0.44	1.5%
Full model	Without PID-CCS control	109.2	15	50%
	With PID-CCS control	2.7	0.39	1.3%

5.4 Conclusion of Chapter 5

In the first part of the present chapter, the architecture test bench has been proposed, designed and integrated for the experimental validation of EMAs/HSAs of position synchronization or force equalization. The components and topology have been selected to meet the design requirements. The mechanical configuration and electrical configuration have been presented in details.

The second part of the chapter was dedicated to the exploitation of the detailed modelling proposed in the former chapters for the virtual validation of position synchronization strategies. As a preliminary study, a PID common controller was introduced as an add-on to the individual position controllers to perform the synchronization task. Its parameters were set using the linear model than were applied to the full model's controller. Typical mission excitations were proposed to verify in a qualitative and quantitative way the synchronization performance. It was observed that the proposed PID-CCS controller significantly reduces the synchronization error.

Of course, the next step will be to perform real tests. However, as the full model has been developed mainly through validated models of EMA elements and with particular attention to virtual integration, one can be reasonably trust the simulated responses of the full model. It well be also necessary to address the robustness of the control laws versus parameters uncertainties.

References

- [1] W. Karam, "Générateurs de forces statiques et dynamiques à haute puissance en technologie électromécanique," INSA Toulouse, Université de Toulouse, 2007.
- [2] Exlar. Advantages of Roller Screw Technology [Online]. Available: <http://exlar.com/why-exlar/many-advantages-roller-screw/>
- [3] Mathworks. Using Speedgoat Target Computer Hardware for Simulink Real-Time [Online]. Available: <http://fr.mathworks.com/videos/using-speedgoat-target-computer-hardware-for-simulink-real-time-90982.html>
- [4] P. Sarachik and J. R. Ragazzini, "A 2-dimensional feedback control system," *Transactions of the American Institute of Electrical Engineers, Part II: Applications and Industry*, vol. 76, pp. 55-61, 1957.
- [5] G. T. C. Chiu and M. Tomizuka, "Coordinated Position Control of Multi-Axis Mechanical Systems," *Journal of Dynamic Systems, Measurement, and Control*, vol. 120, pp. 389-393, 1998.
- [6] W.-S. Yao, F.-Y. Yang, and M.-C. Tsai, "Modeling and control of twin parallel-axis linear servo mechanisms for high-speed machine tools," *International Journal of Automation and Smart Technology*, vol. 1, pp. 77-85, 2011.
- [7] Z. Guo, J. Cao, and K. Zhao, "Cross-coupled approach synchronization controller design method based on quantitative feedback theory for dual hydraulic motors driven flight simulators," in *Computer Design and Applications (ICDDA), 2010 International Conference on*, 2010, pp. V3-376-V3-381.
- [8] L. Kien Minh, H. Hung Van, and J. Jae Wook, "A method to improve the accuracy of synchronous control systems," in *Industrial Informatics (INDIN), 2013 11th IEEE International Conference on*, 2013, pp. 188-193.
- [9] G. Zhang, J.-h. Wu, P.-k. Liu, and H. Ding, "Optimal Cross-Coupled Synchronization Control of a Precision Motion Stage Driven by Dual Linear Motors," in *Intelligent Robotics and Applications*, ed: Springer, 2013, pp. 365-374.
- [10] M.-F. Hsieh, C.-J. Tung, W.-S. Yao, M.-C. Wu, and Y.-S. Liao, "Servo design of a vertical axis drive using dual linear motors for high speed electric discharge machining," *International Journal of Machine Tools and Manufacture*, vol. 47, pp. 546-554, 3// 2007.
- [11] J. X. Yang, "The identification and control of a twin linear servo system with mechanical coupling," Department of Mechanical Engineering, National Cheng Kung University, Taiwan, 2003.
- [12] B. Chu, S. Kim, D. Hong, H.-K. Park, and J. Park, "Optimal cross-coupled synchronizing control of dual-drive gantry system for a SMD assembly machine," *JSME International Journal Series C*, vol. 47, pp. 939-945, 2004.
- [13] C.-T. Chao and C.-C. Teng, "A PD-like self-tuning fuzzy controller without steady-state error," *Fuzzy Sets and Systems*, vol. 87, pp. 141-154, 4/16/ 1997.
- [14] A. E. Alemu and Y. Fu, "Neural Network and Extended State Observer Based Sliding Mode Control of Electro Hydrostatic Actuators," 2016.

- [15] C.-Y. Chen, P.-S. Liao, and H.-M. Cheng, "Fuzzy Controller Design for Positioning and Synchronization of Electrohydraulic System," in *Industrial Electronics and Applications, 2007. ICIEA 2007. 2nd IEEE Conference on*, 2007, pp. 971-976.
- [16] C.-Y. Chen, L.-Q. Liu, C.-C. Cheng, and G. T.-C. Chiu, "Fuzzy controller design for synchronous motion in a dual-cylinder electro-hydraulic system," *Control Engineering Practice*, vol. 16, pp. 658-673, 2008.
- [17] Z. Junliang and L. Li, "Synchronization Motion Control for Electro-hydraulic System of Tensioner for Pipelaying Vessel," in *Natural Computation, 2009. ICNC'09. Fifth International Conference on*, 2009, pp. 287-291.
- [18] F. G. Martins, "Tuning PID controllers using the ITAE criterion," *International Journal of Engineering Education*, vol. 21, pp. 867-873, 2005.

Conclusion

As mentioned in chapter 1, “More Electric” and “All Electric” aircraft concepts are becoming widely implemented in aerospace industry. In the next future, EMAs actuation will be preferred to implement these concepts with special focus on safety, costs and environment friendliness. In some applications, the driven load is split into two (or more) parts which positions are to be synchronized: thrust reverser actuation system (e.g. TRAS), secondary flight controls (e.g. flaps/slats) and pylon conversion of tiltrotors (e.g. V22 or AW/BA609). For the time being, the loads of these systems are mechanically linked to ensure safe synchronisation. Therefore, new features could be offered by managing independently the loads positions. In this attempt, the mechanical linkages between loads could be removed and position synchronization could be performed by mean of “electrical” synchronization loops.

In the present thesis, the research work has addressed the system-level virtual prototyping of EMAs for more extensive use of “electrical” position synchronization. Two major considerations have driven the research work:

- The proposed virtual prototyping approach and models shall be consistent with the Model-Based Systems engineering process.
- The proposed models shall reproduce the key effects that drive the energy and mechanical balance and the control performance of EMAs.
- The EMAs model shall support the design of position synchronization even in case of fault.

In order to enable the virtual prototypes to realistically assess the performance of EMA synchronisation, it has been found important to focus firstly on the modelling process. In chapter 1, it has been proposed to drive the virtual prototyping activities by engineering needs and consequent requirements (in particular model’s replaceability). The EMA’s model has been decomposed into generic elements according to the hardware components (power

drive electronics, electric motor and mechanical power transmission). The Bond-Graph formalism has been selected to support the incremental system-level modelling and simulation while satisfying the causality constraints. Along all chapters, it was proposed to:

- Assign causalities in order to enable at the same time the implementation of multi-domain cross-links effects and multi-level models.
- Analyse energy losses that impact the thermal balance of the EMA to reproduce snow-ball effect and therefore components' sizing.
- Systematically associate thermal ports to dissipative effects, it enables thermal modelling and introduces the temperature effects.

In chapter 2, the position control of EMAs has been studied. The individual EMA controller was designed involving position/velocity/force loops on the basis of the linear approach. It was shown that:

- Power limitations of saturation (torque and velocity) have significant effect on control performance when compared to the common 2nd order EMA linear model.
- Motor current loop dynamics was closely linked to its PI controller setting, and the back-emf compensation was efficient for stability and velocity disturbance rejection.
- Compliance effects made a difference of EMA rod extension and load displacement. Introducing force feedback effectively improved the control accuracy of the load position and reduced the resonance effect.

Following that, parasitic effects were introduced to consider with realism of nonlinear models of EMAs. In chapter 3, the virtual prototyping of power drive electronics and electric motor were addressed.

- Physical effects of power drive electronics and motor were progressively modeled on the basis of Bond-Graph, from perfect model to advanced one.
- Conduction and switching losses were considered for the power drive electronics. Copper and iron losses plus cogging torque were considered for electric motor.

- Temperature sensitivity was taken into account for both power drive electronics and motor components.

- Following the proposed incremental modelling approach, 6-level models of combining the power drive electronics and motor were built step-by-step in LMS-AMESim environment and tested with different excitations.

In chapter 4, for mechanical power transmission was addressed and generated the following outputs:

- One degree of freedom integrated model has been proposed based on Bond-Graph theory. Combining perfect nut-screw, parasitic effects (friction and compliance) and fault failures, the functional, basic, advanced and full models have been developed.

- More advanced and realistic two degree of freedom (translational and rotational motion) model has been proposed. Several generic subcomponents were decomposed by considering power flow causalities. Bearing and joints friction losses were modeled and the thermal behavior were considered. Possibilities were made for modelling jamming and free-run faults.

- Each lumped-parameter model was energy balanced and mechanically replaceable (interface). It enabled faults (jamming or free-play) to be simulated.

- The models were implemented in the AMESim simulation environment. It was shown that various steps were addressed for simulation-aided development: conceptual design, control design, thermal balance and analysis of response to faults.

The chapter 5 reported the design of an actuation test bench involving 2 HSAs and 2 EMAs for real assessment of position synchronization. The preliminary position synchronization strategy was then addressed: a PID-CCS controller was proposed and pre-validated by simulation. It was shown that the PID-CCS controller was effective for synchronizing the two loads even for very different load or in the presence of faults in the mechanical transmission.

Regarding the remaining issues in present thesis, the perspectives of future work and investigation improvements can be listed as follows:

-Now in proposed advanced virtual prototype of EMA, the jamming and free-run faults were considered, which are concerning in mechanical domain. However, other types of faults from power drive electronics, motor and sensors are also important, such as open/short circuit of wiring, demagnetization of permanent magnets, etc. Therefore, better model of the EMA faults and evolution of fault detection and identification algorithm for Health Monitoring and Usage (diagnosis and prognosis) should be developed at the system-level.

-The power losses of EMA were modeled in component level independently by introducing a thermal port based on Bond-Graph theory. However, the thermal model and analysis of the complete EMA should be developed and implemented, which should be concerned realistic effect of the heat exchange among the EMA components or between the component and the ambient.

-The proposed position synchronization strategy was preliminary study used a common PID structure. For get better synchronization performance, the control study should be continued. EMAs position synchronization control could be seen as a multiple input multiple output (MIMO) system, mathematic model of transfer function or state space equations should be developed for more advanced position synchronization.

-Based on the test bench, the experimental study should be validated, not only to verify the position synchronization strategy but also to verify the some uncertain parameters and coefficients in virtual prototype, such as temperature sensitivity to friction losses and backlash or preloading to impact the control performance. There is still a lot of work to do, also in this direction.

List of Publications

- [1] Jean-Charles MARE, **Jian FU**. “Best practices in modelling and simulation applied to aerospace electromechanical actuators”, Oral presentation in Siemens PLM LMS-2015-European Aerospace Engineering Conference, Toulouse, France, March 11-12, 2015.
- [2] **FU Jian**, Jean-Charles MARE, FU Yongling and HAN Xu. “Incremental Modelling and Simulation of Power Drive Electronics and Motor for Flight Control Electromechanical Actuators Application”, *In Proceeding of IEEE International Conference on Mechatronics and Automation (ICMA 2015)*, Beijing, China, August 2-5, 2015, pp.1319-1325.
- [3] **Jian FU**, Ion HAZYUK, Jean-Charles MARE. “Preliminary Design Rules for Electromechanical Actuation Systems – Effects of Saturation and Compliances”, *In Proceeding of 5th CEAS Air & Space Conference Challenges in European aerospace (CEAS 2015)*, Delft, Netherlands, September 7-11, 2015 (57) pp.1-14, 2015.
- [4] Ataklti E ALEMU, **Jian FU**, and Yongling FU. “Neural Network and Extended State Observer Based Sliding Mode Control of Electro-Hydrostatic Actuators”, *In Proceeding of The 35th IASTED International Conference on Modelling, Identification and Control (MIC 2016)*, Innsbruck, Austria, February 15-16, 2016, pp.145-152.
- [5] Yongling FU, Ataklti E ALEMU, **Jian FU**. “Radial Basis Function Neural Network and Extended State Observer Based Sliding Mode Control of Electro Hydrostatic Actuators (EHA)”, *In Proceeding of 7th International Conference on Recent Advances in Aerospace Actuation Systems and Components (R3ASC'16)*, Toulouse, France, March 15-18, 2016, pp.75-81.
- [6] Clément COIC, **Jian FU**, Jean-Charles MARE. “Bond Graph Aided Architecting of Models for Virtual Prototyping: Application to the Mechanical Power Transmission of Aerospace Electromechanical Actuators”, *12th International Conference on Bond Graph Modeling (ICBGM 2016)*, Montreal, Canada, July 24-27, 2016, pp.17-24.
- [7] **Jian FU**, Jean-Charles MARE, Yongling FU. “Incremental Modeling and Simulation of Mechanical Power Transmission for More Electric Aircraft Flight Control Electromechanical Actuation System Application”, *ASME International Mechanical Engineering Congress & Exposition (IMECE 2016)*, Phoenix, USA, November 11-17, 2016. [Paper NO: 2016-66436]
- [8] Yiwei WANG, Christian GOGU, Nicolas Binaud, Christian BES and **Jian FU**. “Determination of Paris’ Law Constants and Crack Length Evolution via Extended and Unscented Kalman filter: An Application to Aircraft Fuselage Panels” *Mechanical System and Signal Processing*, Vol. 80, pp 266-281, 2016.
- [9] **Jian FU**, Jean-Charles MARE, FU Yongling. “Modeling and Simulation of Flight Control Electromechanical Actuators with Special Focus on Models’ Architecting, Multidisciplinary Effects and Power Flows”, *Chinese Journal of Aeronautics*, 2016. [doi: 10.1016/j.cja.2016.07.006]

Appendix

Appendix A BLDC vs. PMSM Used for EMAs

This appendix introduces the comparison of two types of 3-phase motor: BLDC and PMSM, the PMSM has more the advantage that is more suitable for aerospace application, and PMSM is considered in this thesis study.

Two ways are most used to separate BLDC and PMSM. From flux distribution communication, the sinusoidal back EMF waveforms type is known as PMSM and the trapezoidal type is called BLDC motor. From arranging magnets structure on the rotor, PMSM can be designed as surface-mounted type (round) or interior periphery of rotor laminations type (salient-pole). But for BLDC prefers to surface-mounted type design. For simplify used, usually the surface-mounted type PMSM we call it BLDC motor.

1) Power factor

Assuming BLDC and PMSM RMS value of the induced EMFs is equal and denoted by E_p , For BLDC the excitation waveforms of the trapezoidal communication, the peak values of the stator currents I_b , only two phase conduct current at any time the power output is contributed by only two phases. On the contrary, the PMSM sinusoidal communication has currents in all its phases, the peak values of the stator currents I_p , and hence the power output is contributed by all the three phase.

For BLDC, the output power output can be calculated using RMS, given as follows:

$$P_{BLDC} = 3E_p \left(\sqrt{\frac{2}{3}} I_b \right) = 2E_p I_b \quad (A.1)$$

For PMSM, the output power output can be calculated using RMS, given as follows:

$$P_{PMSM} = 3 \frac{E_p}{\sqrt{2}} \frac{I_p}{\sqrt{2}} = \frac{3}{2} E_p I_p \quad (A.2)$$

From equation (A.1) and (3.31), if to equal the copper losses in BLDC and PMSM, the BLDC have 15% higher power density than the PMSM. If to equal the power density for PMSM and BLDC, the PMSM have the more the power losses in motor and power drive, because it need more the phase current. So higher cooling of the devices in the power drive and in the PMSM are needed to enhance the thermal reliability of the motor control system [1].

2) Device needed

For trapezoidal communication, the signals are derived from a position sensor whose resolution has to be only six times the fundamental frequency of the motor, i.e., usually using Hall sensor. By contrast, the sinusoidal drive system has to have position information continuously to construct the sinusoidal current command, which needs to determine the resolution of the position sensor, i.e., usually the 8, 10 and 12 bits position per revolution encoder or resolver is needed, which has high cost and more complicated installation as against the Hall application.

3) Torque ripple

Regarding flux distribution in BLDC, the trapezoidal communication control is to get the trapezoidal flux distribution for obtain the ideal square wave current and the ideal back EMF trapezoidal waveform. If the stator windings with star connection, and no midline, the stator phase currents are constrained to be balanced:

$$i_A + i_B + i_C = 0 \quad (\text{A.3})$$

Generated electromagnetic torque is given by:

$$T_m = \frac{n_p}{\omega_m} (e_A i_A + e_B i_B + e_C i_C) \quad (\text{A.4})$$

The relationship of angular position and angular velocity can be obtained by following equation:

$$\theta = n_p \int \omega_m dt \quad (\text{A.5})$$

But the actual induced EMFs do not have sharp corners as shown in trapezoidal functions but have rounded edges like sinusoidal wave, the equation is given:

$$\begin{cases} e_A = \psi_f \omega_m \sin(\theta) \\ e_B = \psi_f \omega_m \sin\left(\theta + \frac{2\pi}{3}\right) \\ e_C = \psi_f \omega_m \sin\left(\theta - \frac{2\pi}{3}\right) \end{cases} \quad (\text{A.6})$$

ψ_f Permanent magnet flux linkage [Wb] |

By substituting equation (A.6) into (A.4), the electromagnetic torque can be modified as:

$$T_m = n_p \psi_f \left(i_A \sin(\theta) + i_B \sin\left(\theta + \frac{2\pi}{3}\right) + i_C \sin\left(\theta - \frac{2\pi}{3}\right) \right) \quad (\text{A.7})$$

In equation (A.7), the currents in BLDC are trapezoidal in shape, so the electromagnetic torque has the torque ripple. While PMSM offers the sinusoidal flux distribution, the severity of such pulsations is absent in the sinusoidal EMF type PMSM as their currents are sinusoidal. According to equation (A.7), the torque ripple will not take place on the electromagnetic torque, which can be considered a constant torque.

Therefore in theory, PMSM has a constant electromagnetic torque can be controlled and modeled as an equivalent DC motor. In addition, in high-performance an application, torque ripple is always becomes unacceptable. So nowadays application for aerospace EHA, EMA actuation system, when the position control precision is strict the sinusoidal back EMF waveforms PMSMs are preferred to the trapezoidal type BLDCs.

4) PMSM Control Strategy

The sinusoidal flux distribution PMSM motor is preferred to study in this thesis. Vector control proves and provides the decoupling between torque and flux channels [1]. To analyze the PMSM control, the d-q reference frames model is most developed. This method not only can be used for analysis of PMSM steady-state performance, and can also be used to analyze transient performance. The relation of reference frames (ABC-dq) is shown in Figure A-1.

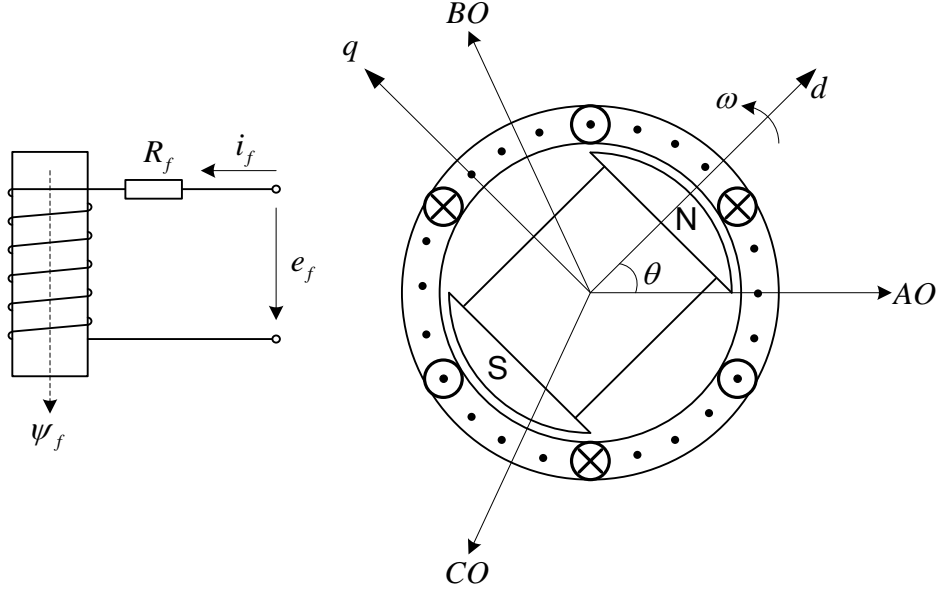


Figure A-1 Relation of reference frames (ABC-dq) of 8 poles PMSM motor

When using constant power constraints coordinate Park's transformation, as seen from the actual three-phase motor current to d-q coordinate current, which gives as:

$$\begin{bmatrix} i_d \\ i_q \\ i_0 \end{bmatrix} = \sqrt{\frac{2}{3}} \begin{bmatrix} \cos \theta & \cos(\theta - \frac{2\pi}{3}) & \cos(\theta + \frac{2\pi}{3}) \\ -\sin \theta & -\sin(\theta - \frac{2\pi}{3}) & -\sin(\theta + \frac{2\pi}{3}) \\ \sqrt{\frac{1}{2}} & \sqrt{\frac{1}{2}} & \sqrt{\frac{1}{2}} \end{bmatrix} \begin{bmatrix} i_A \\ i_B \\ i_C \end{bmatrix} \quad (\text{A.8})$$

With inverse Park's transformation, as seen from d-q coordinate current to the actual three-phase motor current, which is given by:

$$\begin{bmatrix} i_A \\ i_B \\ i_C \end{bmatrix} = \sqrt{\frac{2}{3}} \begin{bmatrix} \cos \theta & -\sin \theta & \sqrt{\frac{1}{2}} \\ \cos(\theta - \frac{2\pi}{3}) & -\sin(\theta - \frac{2\pi}{3}) & \sqrt{\frac{1}{2}} \\ \cos(\theta + \frac{2\pi}{3}) & -\sin(\theta + \frac{2\pi}{3}) & \sqrt{\frac{1}{2}} \end{bmatrix} \begin{bmatrix} i_d \\ i_q \\ i_0 \end{bmatrix} \quad (\text{A.9})$$

Using Ohm's law for the various phases in the PMSM, the stator phase A,B,C tension are then replaced by fictive phases d, q tension can give as follows:

$$\begin{cases} U_d = R_s i_d + \frac{d\psi_d}{dt} - \omega_m \psi_q \\ U_q = R_s i_q + \frac{d\psi_q}{dt} + \omega_m \psi_d \end{cases} \quad (\text{A.10})$$

The fluxes can be expressed in the Park's transformation, a rotating reference whose position is given by the electrical angle. The stator phases A, B, C are then replaced by fictive phases d, q can give as follows:

$$\begin{cases} \psi_d = L_d i_d + \sqrt{\frac{3}{2}} \psi_f \\ \psi_q = L_q i_q \end{cases} \quad (\text{A.11})$$

The electromagnetic torque equation is given by:

$$T_m = n_p \sqrt{\frac{3}{2}} \left[\psi_f i_q + (L_d - L_q) \cdot i_d i_q \right] \quad (\text{A.12})$$

For surface-mount type PMSM, the stator cyclic inductances are defined as follows:

$$L_d = L_q = L_s \quad (\text{A.13})$$

By substituting equation (A.11) into (A.12), the electromagnetic torque can be modified as:

$$T_m = n_p \sqrt{\frac{3}{2}} \psi_f i_q \quad (\text{A.14})$$

The stator current can be given as:

$$I_s = \sqrt{i_d^2 + i_q^2} \quad (\text{A.15})$$

Therefore, the stator current, tension and electromagnetic torque performance can be described in following Figure A-2.

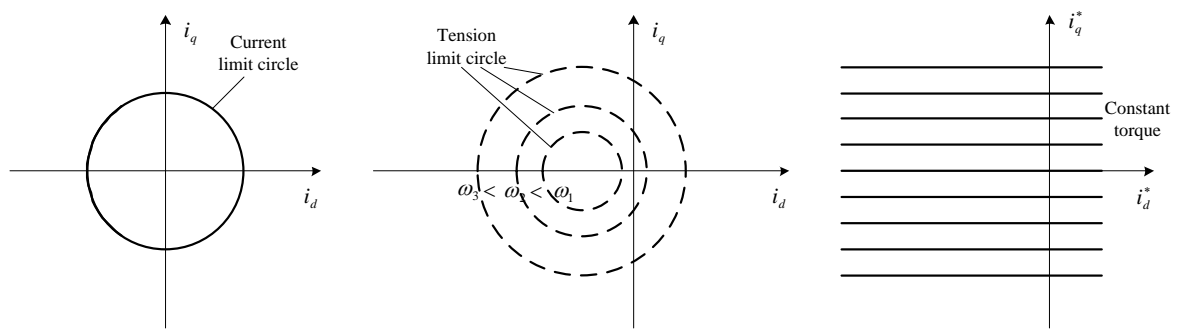


Figure A-2 Equivalent performance of stator current, tension and electromagnetic torque

Appendix B SKF Bearing Loss Model

The SKF total moment of friction can be expressed as:

$$C_{bf} = C_{rr} + C_{sl} + C_{seal} + C_{drag} \quad (B.1)$$

C_{rr}	Rolling frictional moment [Nm]	C_{sl}	Sliding frictional moment [Nm]
C_{seal}	Frictional moment of seals [Nm]	C_{drag}	Frictional moment of lubrication loss [Nm]

Rolling frictional moment C_{rr}

The rolling frictional moment is calculated from the equation:

$$C_{rr} = \phi_{ish} \phi_{rs} G_{rr} (\nu n)^{0.6} \quad (B.2)$$

G_{rr}	Variable represents the influence of the bearing type [-]	ϕ_{ish}	Inlet shear heating reduction factor [-]
ϕ_{rs}	kinematic replenishment/ starvation reduction factor [-]		

In EMA system, the deep groove ball bearings are mostly used. The design coefficients and coefficients for the calculation can be taken from the SKF Catalog. The rolling friction variable G_{rr} for the deep groove ball bearing is given by

$$G_{rr} = R_1 d_m^{1.96} \left[F_r + \frac{R_2}{\sin \alpha_F} F_a \right]^{0.54} \quad (B.3)$$

F_r	Radial load [N]	F_a	Axial load [N]
-------	-----------------	-------	----------------

The R_1 and R_2 are the geometry constants for rolling frictional moments and are dependent on the bearing type. The angle α_F is defined as:

$$\alpha_F = 0.429 \left(\frac{F_a}{C_0} \right)^{0.24} \quad (B.4)$$

C_0	Maximum static force [Nm]
-------	---------------------------

However, the rolling friction is affected by two key factors: ϕ_{ish} and ϕ_{rs} . For ϕ_{ish} , in a lubricant flow, the lubricant is exposed to shear forces caused by the movement of the rolling elements. This produces heat and therefore reduces rolling moment of friction due to the negative sensitivity of viscosity to temperature. So ϕ_{ish} is calculated by:

$$\phi_{ish} = \frac{1}{1 + 1.84 \times 10^{-9} (nd_m)^{1.28} v^{0.64}} \quad (B.5)$$

For ϕ_{rs} , the constant rolling action squeezes excess lubricant away from the contact zone of the rolling elements. This reduces the thickness of lubrication film and therefore reduces the rolling moment of friction. So ϕ_{rs} is calculated by:

$$\phi_{rs} = \frac{1}{e^{\frac{[K_{rs} \eta n (d+D) \sqrt{\frac{K_z}{2(D-d)}}]}{K_{rs}}}} \quad (B.6)$$

e	Base of natural logarithm equals 2.718 [-]	K_{rs}	Replenishment/starvation constant for grease equals 6×10^{-8} [-]
d	Bearing bore diameter [mm]	D	Bearing outside diameter [mm]
K_z	Bearing type related geometric constant [-]		

Sliding frictional moment C_{sl}

Sliding friction is between the rolling elements of the bearings, when surface to surface contact of the balls in the races, and from the contact between the balls and the surfaces of the cage (or separator) of the bearing. It is calculated from the equation:

$$C_{sl} = G_{sl} \mu_{sl} \quad (B.7)$$

G_{sl}	Rolling friction variable [-]	μ_{sl}	Sliding friction coefficient [-]
----------	-------------------------------	------------	----------------------------------

For deep groove ball bearings, the rolling friction variable G_{sl} is given by:

$$G_{sl} = S_1 d_m^{-0.145} [F_r^5 + \frac{S_2 d_m^{1.5}}{\sin \alpha_F} F_a^4]^{1/3} \quad (B.8)$$

S_1	Geometry constant for sliding frictional moment [-]	S_2	Geometry constant for sliding frictional moment [-]
-------	-----------------------------------------------------	-------	-----------------------------------------------------

With S_1 and S_2 are dependent on the bearing type. μ_{sl} the sliding friction coefficient normally assumed to be constant. For more accurate, an equation is given by SKF the total friction coefficient coming from shearing the oil and from asperity contacts:

$$\mu_{sl} = \phi_{bl} \mu_{bl} + (1 - \phi_{bl}) \mu_{EHL} \quad (B.9)$$

ϕ_{bl}	Weighting factor for the sliding friction coefficient [-]	μ_{bl}	Coefficient depending on the additive package in the lubricant [-]
μ_{EHL}	Sliding friction coefficient in full film		

conditions [-]

The ϕ_{bl} has the calculated function:

$$\phi_{bl} = \frac{1}{e^{2.6 \times 10^{-8} (nv)^{1.4} d_m}} \quad (B.10)$$

In addition, with μ_{bl} , generally equals 0.15. μ_{EHL} , the values are 0.05 for lubrication with mineral oils, 0.04 for lubrication with synthetic oils and 0.1 for lubrication with transmission fluids.

Frictional moment of seals C_{seal}

To protect the rolling elements and races from the operating spaces, the bearings are fitted with contact seals, the seals frictional loss are generated by the bearings. To estimate the seals loss using:

$$C_{seal} = K_{s1} d_s^\beta + K_{s2} \quad (B.11)$$

K_{s1}	Constant depending on the bearing type and size [-]	K_{s2}	Constant depending on the bearing type and size [Nm]
d_s	seal counter face diameter [mm]	β	Exponent depending on the seal and the bearing type [-]

Frictional moment of drag loss C_{drag}

The frictional moment of drag loss is only caused by flow, churning, and splashing during oil bath lubrication or oil jet lubrication. The drag loss produced by lubricating greases tends to zero because of the oil bath level H is zero, seen Fig. B-1.

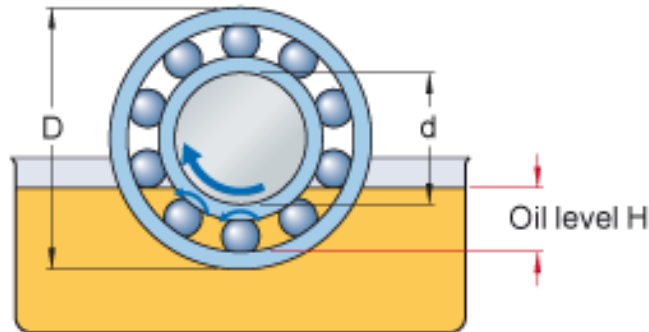


Fig. B-1 Oil level H [2]

The drag loss shows that when a large amount of fluid is present in the bearing races, it has a

disturbing effect on the rotation speed. The definition of C_{drag} for ball bearing is given by:

$$C_{drag} = V_M K_{ball} d_m^5 n^2 \quad (B.12)$$

The ball element related constant which related to its geometry is defined as:

$$K_{ball} = \frac{k_{rw} K_z (D+d)}{D-d} \times 10^{-12} \quad (B.13)$$

k_{rw} Number of ball rows [-] H Oil bath level [mm]

The parameter V_m is as a function of the oil bath level H , has been shown in Fig.B-2 as following:

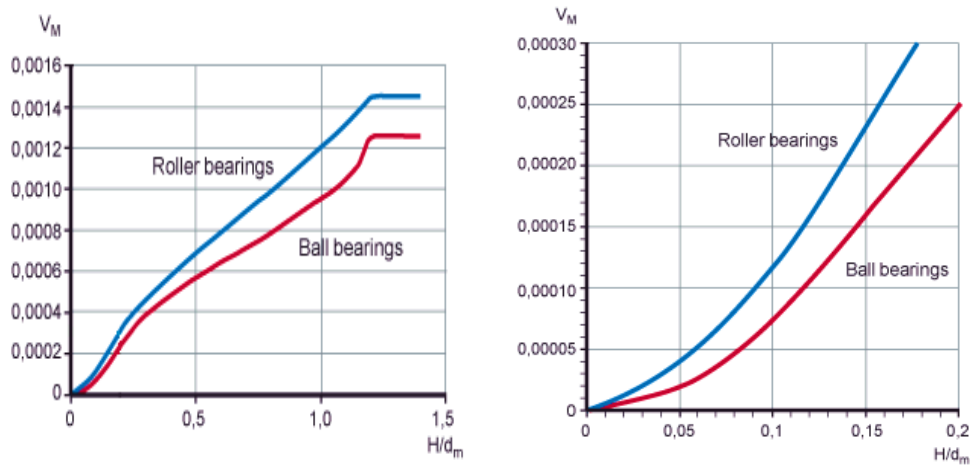


Fig. B-2 V_M in function of the oil level and bearing mean diameter [2]

References

- [1] R. Krishnan, *Permanent magnet synchronous and brushless DC motor drives*, 1st ed. USA: CRC press, 2010.
- [2] SKF, "SKF General Catalogue," ed, 2006.

Résumé

Dans le domaine de l'aéronautique, les concepts basés sur l'usage étendu de l'électricité dans les avions plus électriques (MEA) et même tout électriques (AEA) font appel à des actionneurs électromécaniques (EMA) en remplacement des actionneurs servo-hydrauliques conventionnels (HSA). Lorsque les EMA sont utilisés pour des applications d'actionnement critique comme les commandes de vol, certains problèmes spécifiques liés à l'équilibre thermique, l'inertie réfléchie, le mouvement parasite dû aux élasticités structurelles, la réponse aux fautes (grippage et rupture) et la synchronisation d'EMA actifs sur charges indépendantes ne peuvent être ignorés. La simulation apporte un support indéniable à la conception pour l'évaluation et la validation des concepts. A cet effet, il est nécessaire de développer des prototypes virtuels des EMA avec une vision système et de façon structurée pour répondre aux besoins des ingénieurs. Malheureusement, les phénomènes physiques qui apparaissent dans les EMA sont multidisciplinaires, couplés et fortement non linéaires. De nombreux logiciels commerciaux de simulation système multi-domaines sont désormais disponibles. Cependant, le processus de modélisation et les besoins des ingénieurs sont rarement pris en compte selon une vision globale, en raison du manque d'approches scientifiques pour la définition d'architectures, la modélisation incrémentale et l'amélioration de l'implémentation numérique des modèles. Dans cette thèse, le prototypage virtuel de l'EMA est adressé en utilisant le formalisme Bond-Graph. De nouvelles approches sont proposées pour permettre la modélisation incrémentale de l'EMA en vue de fournir des modèles pour la synthèse de la commande, l'évaluation de la consommation d'énergie, l'analyse thermique, le calcul des forces de réaction, la simulation de la pollution du réseau d'alimentation électrique, la réponse aux fautes et l'influence de la température. L'intérêt des modèles proposés est illustré sur l'exemple de la synchronisation de position de deux EMA actionnant des charges indépendantes.

A partir de ces situations, ces travaux de thèse sont organisés en cinq chapitres. Dans le

Chapitre 1, les besoins techniques et les exigences ont été proposés pour les activités de prototypage virtuel (en particulier, bonnes propriétés pour les modèles). Le modèle de l'EMA a été décomposé en éléments génériques selon les composants matériels (électronique de puissance, moteur électrique et transmission mécanique). Le formalisme Bond-Graph a été sélectionné pour soutenir la modélisation incrémentale au niveau système tout en satisfaisant les contraintes de causalité. Dans ce chapitre 1, il a été proposé de:

- Gérer activement les causalités pour permettre de combiner plusieurs types d'effets (fonctionnels/parasites) ainsi que des modèles multi-objectifs (dynamique, thermique, etc.).
- Analyser les pertes d'énergie qui influent sur l'équilibre thermique de l'EMA pour reproduire l'effet boule de neige et donc le dimensionnement de composants.
- Associer systématiquement les ports thermiques aux effets dissipatifs, ce qui permet au passage de prendre en compte l'influence de la température sur ces phénomènes.

Chapitre 2 est dédié à la commande en position des EMA. Le correcteur de type cascade met en œuvre des boucles position / vitesse / couple et est prédéterminé sur la base d'un modèle linéaire associé à un faible nombre de non-linéarités. Les travaux ont montré:

- L'impact des limitations de puissance (comme les saturations de couple et vitesse) sur la performance de la commande par rapport à un modèle linéaire pur.
- L'impact sur la dynamique de la boucle de courant du moteur du réglage de son correcteur PI, en particulier concernant la stabilité et le rejet des perturbations de tension contre-électromotrice liées à la vitesse du moteur.
- L'effet du jeu de transmission sur la chaîne mécanique entre le moteur de l'EMA et la charge. L'introduction d'un retour de force a nettement amélioré la précision de la position de charge et réduit l'effet de résonance.

La suite du travail a consisté à introduire les différents effets parasites pour améliorer les réalisme des modèles, qui deviennent alors fortement non-linéaires. Le Chapitre 3 a porté sur le prototypage virtuel de l'électronique de puissance et du moteur électrique :

- Les différents effets ont été progressivement introduits à partir d'une modélisation incrémentale à l'aide du formalisme Bond-Graph, depuis le modèle parfait jusqu'au

modèle de niveau avancé.

- Les pertes de conduction et de commutation ont été considérées pour l'électronique de puissance. Les pertes Joule, fer (hystérésis et courant de Foucault) ainsi que le couple de détente ont été pris en compte pour le moteur électrique.
- La sensibilité à la température a été introduite tant pour l'électronique de puissance que pour le moteur.
- Suivant l'approche de modélisation incrémentielle proposée, 6 niveaux de modèles ont été proposés et implémentés dans l'environnement de simulation LMS-AMESim. Ils ont été testés et vérifiés pour différentes excitations.

De son côté, le Chapitre 4 a concerné la transmission mécanique :

- Un modèle intégré à 1 de degré de liberté a été proposé sur la base d'un modèle Bond-Graph. Il combinait un système vis-écrou parfait à des effets parasites (frottement et jeu), permettant l'introduction possible de défaillances. Cette approche 1D a permis de proposer des modèles de complexité croissante (de purement fonctionnel à expert).
- Un modèle plus avancé et réaliste à deux degrés de liberté (translation et rotation) a ensuite été proposé. Plusieurs sous-composantes génériques ont été décomposées en considérant les causalités et la généricité des modèles. Les pertes de frottement des roulements et des joints ont été modélisées et le comportement thermique a été considéré. Le modèle améliore le réalisme des réponses vis-à-vis du jeu, du frottement et de l'injection de fautes (grippage, usure).
- Chaque modèle à paramètres globaux, conservait les mêmes interfaces quel que soit son niveau de détail. Il était équilibré du point de vue énergie et actions.
- Comme pour la partie électrique les modèles ont été implémentés dans l'environnement de simulation LMS-AMESim. A travers divers exemples, il a été montré comment ces modèles étaient adaptés à des tâches d'ingénierie diverses, comme par exemple la conception, la synthèse de la commande, l'analyse de l'équilibre thermique et la réponse aux fautes.

actionneurs servo-hydrauliques et 2 actionneurs électromécaniques. Ce banc est destiné à évaluer expérimentalement les stratégies de synchronisation de position lorsque de EMA doivent actionner de façon synchrone deux charges indépendantes. La stratégie préliminaire de synchronisation de position a ensuite été abordée a permis de définir une fonction de synchronisation de type PID (PID-CCS) qui a été validée par simulation. Il a été en particulier montré que la synchronisation était efficace pour des charges très différentes ou en présence de défauts dans la transmission mécanique.

Suite à ces travaux de thèse, les voies d'amélioration et les perspectives de travaux futurs peuvent être énumérées comme suit:

- Développer un meilleur modèle des fautes de l'EMA et proposer des modèles d'évolution de ces fautes pour permettre la mise en œuvre d'algorithmes de Health-Monitoring (détecter, identifier les fautes et prévoir leur évolution dans le temps).
- Améliorer le modèle et l'analyse thermiques de l'EMA complet pour être plus prédictif en simulation, en fonction de la mission et de l'environnement de l'actionneur.
- Poursuivre l'étude sur la stratégie de synchronisation de position en intégrant notamment l'aspect robustesse.
- Exploiter le banc d'essais pour valider expérimentalement les différents travaux de modélisation, de commande et démontrer la robustesse des approches vis-à-vis des incertitudes paramétriques.